

12-7-2015 12:00 AM

A new technique for interpreting depolarization measurements using the CRL atmospheric lidar in the Canadian High Arctic

Emily M. McCullough, *The University of Western Ontario*

Supervisor: Prof. R. J. Sica, *The University of Western Ontario*

A thesis submitted in partial fulfillment of the requirements for the Doctor of Philosophy degree in Astronomy

© Emily M. McCullough 2015

Follow this and additional works at: <https://ir.lib.uwo.ca/etd>



Part of the [Atmospheric Sciences Commons](#)

Recommended Citation

McCullough, Emily M., "A new technique for interpreting depolarization measurements using the CRL atmospheric lidar in the Canadian High Arctic" (2015). *Electronic Thesis and Dissertation Repository*. 3418.

<https://ir.lib.uwo.ca/etd/3418>

This Dissertation/Thesis is brought to you for free and open access by Scholarship@Western. It has been accepted for inclusion in Electronic Thesis and Dissertation Repository by an authorized administrator of Scholarship@Western. For more information, please contact wlsadmin@uwo.ca.

A NEW TECHNIQUE FOR INTERPRETING DEPOLARIZATION
MEASUREMENTS USING THE CRL ATMOSPHERIC LIDAR IN THE
CANADIAN HIGH ARCTIC

(Thesis format: Monograph)

by

Emily McCullough

Graduate Program in Astronomy, Specialization in Planetary Science

A thesis submitted in partial fulfillment
of the requirements for the degree of
Doctor of Philosophy

The School of Graduate and Postdoctoral Studies
The University of Western Ontario
London, Ontario, Canada

© Emily Madill McCullough 2015

Abstract

Linear depolarization measurement capabilities were added to the CANDAC Rayleigh-Mie-Raman lidar (CRL) at Eureka, Nunavut, in the Canadian High Arctic. This upgrade enables inferences of the phases (liquid versus ice) of cold and mixed-phase clouds, including during polar winter. A rotating-polarizer module was installed in the lidar, and depolarization measurements were calibrated according to existing methods. An alternate calculation technique, using the lidar's existing visible Rayleigh elastic channel in combination with the new rotating polarizer channel, was developed. A detailed mathematical description of both methods and their calibrations is presented. The new method is superior to the traditional method for the CRL: It has lower uncertainty, and gives depolarization parameter values at higher spatial-temporal resolution.

Keywords: Lidar, Atmosphere, Depolarization, Polarization, Arctic, Calibration, Ice, Polar Clouds, Eureka, CRL

Acknowledgements

I wish to extend my sincere thanks to several people without whom this work would not have been possible, and to those without whom it would have been much less enjoyable.

First, my advisor Prof. R. J. Sica. I deeply appreciate that Bob encourages graduate students to take on new challenges and to learn as much as possible. He trusts them to live up to the highest level of scientific integrity. Arctic atmospheric science, and lidar, are not topics that I stumbled across on my own; Prof. Sica threw all of my academic plans off course in the best possible way, and then supported me throughout the work for this thesis.

I also thank my Academic Advisory Committee. Prof. G. Osinski and Prof. P. Wiegert were instrumental in helping me find the line between sufficient research and way too much scope. Both were supportive of my participation in planetary science activities, some of extended duration, while a student. These experiences have been enriching and extraordinarily valuable.

As a result of Prof. Sica's participation with the Canadian Network for the Detection of Atmospheric Change, I have had the opportunity to do much of the work for this thesis on site at the PEARL laboratory at Eureka, Nunavut. The Canadian High Arctic is a most wonderful place, and I'm truly grateful for the chance to experience it in person.

CANDAC has also led to interactions with many other atmospheric scientists. Critique from, and discussions with, these professors and government scientists has been invaluable. CANDAC-supported meetings has meant getting to know many of my peers who are normally scattered across the country, and to benefit from their experiences. I anticipate that many among them will continue to be my colleagues for years to come.

Close work with Prof. T. J. Duck's Atmospheric Optics group at Dalhousie University was essential to this thesis. I thank Tom for graciously inviting me to work with the CRL lidar. Initial instruction from Dr. G. Nott was vital in learning how to operate and care for the instruments. He provided detailed guidance for the depolarization channel installation.

Prof. K. A. Walker from the University of Toronto has been a wonderful mentor for many years. Discussions with Kaley have been a tremendous form of support. She has also included the CRL lidar group in the yearly Canadian Arctic ACE/OSIRIS Validation Campaigns which were crucial for getting the depolarization channel up and running.

Funding for this project comes from many sources, including: The NSERC CREATE Training Program in Arctic Atmospheric Science, NSERC grants to the professors of CANDAC, Ontario Graduate Scholarships, and The Northern Scientific Training Program.

With an experimental project which includes equipment at a remote site, and spans several years, there are lots of opportunities for others to provide assistance, ideas, and encouragement. At Eureka, help came in the form of the CANDAC PI J. Drummond, site manager P. Fogal, operators P. Leowen, A. Khmel, A. Harret, K. MacQuarrie, M. Maurice, O. Mikhailov, and M. Okraszewski, and all of the campaign participants, including: C. Adams, K. Baibakov, J. Franklin, G. Gamache, S. Gamage, D. Griffin, L. Ivanescu, F. Kolonjari, S. Kristoffersen, R. Lindenmeier, Z. Mariani, T. McElroy, J. Mendonca, C. Perro, C. Pike-Thackray, V. Savastiouk, K. Strong, A. Tikhomirov, S. Tran, Z. Vaziri, D. Weaver, and X. Zhao. Help came equally from the staff of the Environment Canada Weather Station: J. Allen, A. Bouchard, S. Carpenter, M. Edwards, J. Fonger, A. Gaudet, M. Lane, D. Lavallée, R. LeCotey, B. MacInnis, J. MacIver, D. McLaughlin, D. Prior, J. Roberts, E. Saul, M. Wallmann, and D. White. I thank them for their hospitality and friendship, and for assistance with the lidar. Without these people, the CRL would not have a calibration lamp that worked. I would not have been able to spend so much time with the wolves and muskoxen, either.

My lidar labmates from Western and Dalhousie, past and present, are the people who fully understand the joy of aligning lasers at 3 AM in the freezing cold or from thousands of kilometers away. Seeing how they each approach lidar with their different strengths has helped me to learn so much. Thanks to: Andy Moss, Paul Doucet, Blessing Iserhienrhien, Robin Wing, Peter Argall, Chris Perro, Graeme Nott, Colin Pike-Thackray, Jason Hopper,

Jon Doyle, Jaya Khanna, Frans Olofson, Justin Bandoro, Sean Hartery, Meike Rotermund, Ali Jalali, Shannon Hicks, Sham Gamage, Ghazal Farhani, and Jeff Vankerkhove.

Planetary science friends Marianne Mader, Bhairavi Shankhar, Haley Sapers, Annemarie Pickersgill and the others from CPSX have been there through the interdisciplinary adventures with robots and impact craters, long hours, lots of writing, and odd science questions.

Thanks in particular to my dear friend Annemarie Pickersgill for her friendship. She has given support of all kinds, company while analyzing data, extensive amounts of very careful editing on short notice (even while on vacation on the other side of the planet). Writing Camp produced reams of pages, mostly fueled by excessive amounts of tea and cake.

To my Mum, Bridget Madill, and my Dad, Brian McCullough, and to my brothers Ben and Nathan, I owe a lot of gratitude. They made me curious, and were forever making me look things up and figure things out. They valued books, and gave me the freedom to explore in a house full of them. They also made me stubborn, and it looks like tenacity has been just as important in getting this thesis done as anything else. They've always supported my education, while helping me to keep things in perspective.

To Chad Bennett, my fiancé, I owe more thanks than it is possible to express. He has stood beside me during this process without doubt or hesitation, and with a lot of love. He would not have thought less of me for quitting, but understood why I did not want to, and encouraged me when things were difficult. He shares the curiosity, and the drive to learn more about the world. He holds our household together as I finish this academic endeavour, and is exceedingly patient. I appreciate all the time he has spent as a sounding board for ideas as I talk my way through (especially the math) problems. I thank him, too, for keeping the interesting conversations going when my brain was too full of calibrations for me to think up anything neat to talk about. Thanks for being fantastic. I'm looking forward to our next adventures!

Contents

Abstract	i
Acknowledgements	ii
Contents	v
List of Figures	xv
List of Tables	xxxi
1 Introduction	1
1.1 Overview	3
1.2 Major contributions of this thesis	5
2 Literature Review and Background	7
2.1 Scientific motivation: Polar clouds	7
2.1.1 Clouds and the radiation budget of Earth’s atmosphere	7
2.1.2 Scientific questions regarding mixed-phase clouds	8
2.1.3 Types of Arctic cloud measurements and their challenges	10
2.1.3.1 Aircraft observation	10
2.1.3.2 Satellite observation	11
2.1.3.3 Ship-based observations	11
2.1.3.4 Ground-based observations	12

2.1.3.5	Human observation	13
2.1.3.6	Multimethod intercomparisons	13
2.1.3.7	Models	16
2.2	Background physics for polarization and lidar	18
2.2.1	Physics of Polarization	18
2.2.2	Polarization in scattering events	20
2.2.3	The Elastic Lidar Equation	21
2.3	Technical context for this thesis: Depolarization lidar	24
2.3.1	The traditional depolarization ratio: δ	24
2.3.1.1	Development of the equation for δ	24
2.3.1.2	δ in terms of light intensities	25
2.3.2	Early depolarization ratio measurements	27
2.3.3	Depolarization lidar configurations	28
2.3.4	Calibrations	30
2.3.4.1	Careful design reducing calibration	31
2.3.5	Interpretation of depolarization ratio δ measurements	31
2.3.5.1	The shape of nonspheres, and their sizes	33
2.3.5.2	More ambiguous cases and a few solutions	34
2.3.5.3	Something to be aware of when coadding	35
2.3.6	Using d instead of δ	35
2.3.7	The scope of this thesis	37
3	The CRL Lidar at Eureka	39
3.1	The Lab	40
3.2	Transmitter	41
3.3	Receiver	43
3.4	Measurement “channels” used in this thesis	45
3.5	CRL operations	47

4	Installation of the CRL lidar depolarization channel	50
4.1	Situation of depolarization channel within the CRL	51
4.2	The Polarotor	53
4.3	Advantages to a rotating polarizer design	54
4.4	The pellicle beamsplitter	54
4.5	Interference Filter Specifications	55
4.6	Calibration Equipment	55
4.6.1	Calibration light sources	56
4.6.2	Depolarizing calibration optics	57
4.6.2.1	Calibration tests of the optical qualities of glassine waxed paper	59
4.6.2.2	Practical considerations when using glassine	61
4.6.3	Polarizing calibration optics	63
5	Low-level data processing for depolarization channels	66
5.1	Introduction to low level data analysis	66
5.2	Analysis software and languages	67
5.2.1	Python programming at Dalhousie University	67
5.2.1.1	Python Data Acquisition	67
5.2.1.2	Python Data Analysis	68
5.2.2	MATLAB at the University of Western Ontario	68
5.3	Reading in data files	69
5.3.1	Handling Analogue channel overflow flags	70
5.3.2	Handling Photon Counting channel overflow flags	71
5.3.3	Removal (or not) of the flagged values	71
5.4	Turning altitude bins into metres	73
5.4.1	Removing counts outside of appropriate altitude range	74
5.5	Photon counting signals, uncertainties, and corrections	74

5.5.1	Photon Counting raw signals and uncertainty	75
5.5.2	Turning photon count rates into MHz	76
5.5.3	Dead time correction for photon counting channels	80
5.5.4	PC deadtime uncertainty	84
5.5.5	Coadding to improve signal to noise	85
5.5.6	PC uncertainty in coadding	86
5.5.7	Background subtraction from the sky	87
5.5.8	Determining the PC background value	88
5.5.9	PC background uncertainty	89
5.5.10	Subtracting background from PC profiles	90
5.5.11	Uncertainty in background-subtracted PC profiles	91
5.5.12	Photon counting uncertainty: Relative sizes of contribution from all sources	91
5.6	Analogue signals, uncertainties, and corrections	92
5.6.1	Raw analogue signals	93
5.6.2	ADC error for CRL	93
5.6.3	Analogue shot noise uncertainty	94
5.6.4	Turning analogue count rates range-scaled units	96
5.6.5	Uncertainty in turning analogue count rates into range-scaled values	98
5.6.6	Dark Counts	99
5.6.7	Types of dark counts	99
5.6.8	Measuring the dark count profiles in PC channels	100
5.6.9	Measuring the dark count profiles in Analogue channels	101
5.6.9.1	Effect of flashlamps on dark counts	104
5.6.9.2	Effect of laser trigger on dark counts	104
5.6.9.3	Overall trend of the dark count profiles	106
5.6.10	Choosing a dark count profile to remove for each analogue channel .	107

5.6.10.1	Mean profiles for other years	109
5.6.11	Removing the dark counts profile	109
5.6.12	Uncertainty in ANA dark count removal	110
5.6.13	Demonstration of dark count removal on example data	111
5.6.14	Discussion regarding prevention of analogue dark signals	112
5.6.15	Determining ANA background values	113
5.6.16	Analogue background uncertainties	113
5.6.17	Uncertainty in removing the background from ANA profiles	114
5.6.18	Conversion of ANA to the same units as PC	115
5.6.18.1	Linearity limits used for determining gluing coefficients	117
5.6.18.2	Linear fits to determine gluing coefficients	119
5.6.18.3	Conversion of ANA signals to MHz	121
5.6.18.4	Conversion of ADC error to virtual counts and MHz	122
5.6.18.5	Analogue dark count uncertainties in MHz	123
5.6.19	Uncertainty contributions: Relative sizes from all the sources, ANA	124
5.7	Gluing: Combining the ANA and PC channels	124
5.7.1	Choice of profile to use at each point	125
5.7.2	An example night of gluing: 12 March 2013	127
5.7.3	Glued profile uncertainties	129
5.7.4	Other gluing options not used by CRL	129
5.8	Statistical vs. systematic uncertainties	133
5.9	Conclusion of low level data processing chapter	134
6	Traditional Depolarization Method	135
6.1	Traditional Depolarization Method Theory	135
6.1.1	Lower uncertainty expression for depolarization parameter d	136
6.2	Traditional Method Calibration	138
6.2.1	The contents of k : Making gains realistic for CRL	139

6.2.2	Are gains sufficient? Is k a constant for CRL?	140
6.2.3	Method for k calibration	141
6.2.4	Sample Detailed Calibration Test from 1 November 2013 (laser; glassine above window)	142
6.2.4.1	Calibration tests with various resolutions	145
6.3	Which optics contribute most to the k value? Testing depolarizing material at various locations	146
6.3.1	Setup for testing k at various locations in the detector	148
6.3.2	Results for k from various positions	151
6.3.3	Impact on future CRL design and calibration decisions	151
6.4	Traditional Method Sample Calibrated Measurements from 20130312 . . .	153
6.5	Caveats on Traditional Method and motivation for other methods	156
7	More Complete Depolarization Parameter Method: Mathematical Description	157
7.1	Matrix description of signals in each channel	158
7.1.1	Describing the behaviour of the lidar as matrix equations	159
7.1.2	Choice of laser light transmitted Stokes vector	160
7.1.3	Choice of atmospheric scattering matrix	162
7.1.4	Choice of instrument matrices	163
7.1.4.1	Matrices for optics upstream of the analyzing polarizers .	164
7.1.4.2	Matrices for optics upstream of the analyzing polarizers: Simplified case	165
7.1.4.3	Polarizer matrices	166
7.1.4.4	Matrices for optics downstream of the analyzing polarizers	167
7.1.4.5	A note about gains	168
7.1.5	Signals available in each detector	168
7.1.5.1	Signals in Parallel channel	169
7.1.5.2	Signals in Perpendicular channel	170

7.1.5.3	Signals in Rayleigh Elastic channel	171
7.1.6	Signals if a simplified lidar is assumed	172
7.1.6.1	Physical description of a simplified lidar	172
7.1.6.2	Signals in Parallel channel: simplified lidar	178
7.1.6.3	Signals in Perpendicular channel: simplified lidar	180
7.1.6.4	Signals in Rayleigh Elastic channel: simplified lidar	181
7.1.7	Summary of signals received in each detector	182
7.2	Deriving an expression for the depolarization parameter d in terms of observables	184
7.2.1	Option 1: Use only S_{\parallel} and S_{\perp} measurements	184
7.2.2	Option 2: Use only S_{\parallel} and S_R measurements	185
7.2.3	Option 3: Use only S_R and S_{\perp} measurements	186
7.2.4	Option 4: Use all three S_R , S_{\perp} and S_{\parallel} measurements	187
7.3	Summary of the equations for d and calibration constants needed	188
7.4	Choices of methods to pursue	190
7.5	Caveats regarding these matrix derivations of d	191

8 Calibration for Full-Matrix Expression d , Option 1: Parallel and Perpendicular Signals 193

8.1	Calibration setup for Option 1	194
8.2	Finding $\frac{M_{10}}{M_{00}}$, setting $d = 1$	197
8.2.1	Development of the calibration expression for $\frac{M_{10}}{M_{00}}$	197
8.2.2	Sample Detailed $\frac{M_{10}}{M_{00}}$ Calibration Test	201
8.2.3	$\frac{M_{10}}{M_{00}}$ values when testing from various locations in the detector	203
8.3	Finding $\frac{M_{01}}{M_{00}}$, $\frac{M_{10}}{M_{00}}$, and $\frac{M_{11}}{M_{00}}$ together	205
8.3.1	Development of the calibration signals for $\frac{M_{01}}{M_{00}}$, $\frac{M_{10}}{M_{00}}$, and $\frac{M_{11}}{M_{00}}$	205
8.3.2	Simplifications of the calibration signal expressions for $\frac{M_{01}}{M_{00}}$, $\frac{M_{10}}{M_{00}}$, and $\frac{M_{11}}{M_{00}}$ when allowed by calibration results	207

8.3.2.1	First simplification: Symmetry, $M_{02} = 0$ and $M_{12} = 0$. . .	207
8.3.2.2	Second simplification: Zero-signals, $M_{10} = M_{01}$ and $M_{00} =$ M_{11}	210
8.3.3	Method for determining $\frac{M_{10}}{M_{00}}$ once we have made both simplifications	211
8.3.4	Method for determining $\frac{M_{01}}{M_{00}}$, $\frac{M_{10}}{M_{00}}$, and $\frac{M_{11}}{M_{00}}$ if we allow the first as- sumption, but not the second.	212
8.3.5	Caveats regarding the calibration signal expressions for $\frac{M_{01}}{M_{00}}$, $\frac{M_{10}}{M_{00}}$, and $\frac{M_{11}}{M_{00}}$ for CRL	214
8.3.6	Sample Detailed Calibration Test from 20140305 with a lamp and cube polarizer rotated downstream of focus stge	214
8.3.6.1	Physical setup for 20130405 cube rotation calibration test	215
8.3.6.2	Measurements during the 5 March 2014 cube rotation calibration	216
8.3.6.3	Verifying first simplification: $M_{02} = 0$ and $M_{12} = 0$	218
8.3.6.4	Verifying second simplification: $M_{10} = M_{01}$ and $M_{00} =$ M_{11}	219
8.3.6.5	Example calculation of $\frac{M_{10}}{M_{00}}$ with fully-simplified conditions	220
8.3.6.6	Example model and comparison measurements to deter- mine $\frac{M_{10}}{M_{00}}$, $\frac{M_{01}}{M_{00}}$, and $\frac{M_{11}}{M_{00}}$ with partially-simplified conditions	221
8.3.7	Other calibration tests attempted	224
8.4	Conclusions regarding Option 1 calibration constants	224

9 Calibration for Full-Matrix Expression d , Option 2: Parallel and Rayleigh

Elastic Signals	226
9.1 Sample Calibration Test from 5 March 2014 with a lamp and cube polarizer rotated downstream of focus stage: Rayleigh channel	227
9.1.1 Simplifications of the calibration signal expressions for T_{01} and T_{02} when allowed by calibration results	227

9.1.2	First simplification: Symmetry, $T_{02} = 0$	228
9.1.3	Second simplification: Constant signal with angle, $T_{01} = 0$	229
9.1.4	Final equation for Option 2 depolarization parameter d_2	229
9.1.5	Calibration method for determining $\frac{G_{PMTR}O_R(z)}{G_{PMT\parallel\perp}O_{\parallel\perp}(z)} \frac{T_{00}}{M_{00}}$	230
9.1.6	Units of $\frac{G_{PMTR}O_R(z)}{G_{PMT\parallel\perp}O_{\parallel\perp}(z)} \frac{T_{00}}{M_{00}}$	231
9.2	Sample Calibration Test from 10 March 2013 to determine $\frac{G_{PMTR}O_R(z)}{G_{PMT\parallel\perp}O_{\parallel\perp}(z)} \frac{T_{00}}{M_{00}}$	232
9.2.1	Signals and uncertainties in each channel	232
9.2.2	Depolarization parameter d as determined by Option 1 procedures	233
9.2.3	Calculations of $\frac{G_{PMTR}O_R(z)}{G_{PMT\parallel\perp}O_{\parallel\perp}(z)} \frac{T_{00}}{M_{00}}$ for each data point	234
9.2.4	Combining individual measurements into a single $\frac{G_{PMTR}O_R(z)}{G_{PMT\parallel\perp}O_{\parallel\perp}(z)} \frac{T_{00}}{M_{00}}$ for the night	235
9.2.5	Variation in the profile with changing coadding resolution and with different dates	238
9.3	Sample determinations of d using Option 2	239
9.4	Comparing the d_1 and d_2 results to verify validity of Option 2	240
9.5	Demonstration of calibration and calculation of d_2 for other dates	242
9.5.1	Calculation of d_2 for 14 March 2013	242
9.5.2	Calculation of d_2 for 11 March 2013	248
9.5.3	Conclusions regarding the validity of Option 2	250
10	Determining the CRL's optimal depolarization measurement scheme	251
10.1	Example day 1 showing the advantages of d_2 : 10 March 2013	253
10.2	Example day 2 showing the advantages of d_2 : 29 March 2013	258
10.3	Using uncertainties to choose between d_1 and d_2	261
10.4	Summary of advantages of d_2 over d_1 and recommendations	262
11	Conclusions	264
11.1	Summary of major results	264

11.2 Future work	266
Bibliography	268
Curriculum Vitae	282

List of Figures

3.1	Location of Eureka in the Canadian High Arctic on Ellesmere Island [1], and a photograph of the CRL in operation at the ØPAL laboratory during polar night.	39
3.2	CRL lidar container with roof hatch open	41
3.3	Schematic of the CRL lidar including transmitter and receiver modified from [2]. The light from two lasers is combined and directed to the sky. Backscattered lidar returns are collected in the telescope and are focused into the polychromator. Within the polychromator, the light is sorted by wavelength and measured by eight photomultiplier tube detectors (PMTs), in nine measurement channels. Detection channels of particular note for this thesis are the Visible Rayleigh Elastic channel (“VIS el.” in the figure), and the two depolarization channels, Parallel and Perpendicular (“depol.” in the figure, sharing a photomultiplier tube).	42
3.4	Visual representation of the manner in which all lidar channels involved in depolarization parameter calculations relate to one another. Each hardware channel makes measurements in several measurement channels. Pairs of measurement channels are combined to create the glued profile channels.	46

- 4.1 The 50/50 pellicle beamsplitter is visible below the blue anodized polarotor in the depolarization channel. It lies between the visible long wave pass (VLWP) filter leading to the Rayleigh Elastic channel (on the right), and the mirror leading to the 607 nm Nitrogen channel (on the left). The other visible wavelength channels are also seen at the right of the photograph. The optics for the ultraviolet channels are located on the other side of the back wall in this photograph, and are not seen in this image. 51
- 4.2 Polarotor (large blue anodized object at the bottom of the stack) and its associated beamtube optics and photomultiplier tube (small blue cylinder at the top) installed in its current position on top of the polychromator. The electronics rack is visible in the background. 53
- 4.3 Diagram of the test used to verify that Glassine waxed paper is an effective depolarizing optic. The lamp and first linear polarizer are held fixed. Zero, one or two sheets of glassine are held fixed (depending on the test). The second polarizer is rotated through various angles θ . The light through these optics is measured using a photodiode, which is read out on a voltmeter. The voltage is directly related to the intensity of the light measured by the photodiode. 60
- 4.4 Results of the calibration test to verify that glassine does depolarize light, set up according to Figure 4.3. The red data points do not include glassine. The shape of Malus' law for two polarizers is evident. The dark blue data points demonstrate the considerable depolarizing effect of one glassine sheet placed between the polarizers. The black points demonstrate the complete depolarization possible when two glassine sheets are layered orthogonally to one another. 60

- 5.1 Demonstration of the effect of increased photon count numbers on absolute and relative uncertainty due to shot noise. Absolute uncertainty (blue) is small at low count rates N , but it is of the order of the same size as the count rate itself (grey), and equal to it for $N=1$ photon. Therefore the relative uncertainty (red) is high: 100%. At high count rates N , the absolute uncertainty is larger, but it has not grown at the same rate as the signal. The relative uncertainty is therefore smaller: 10%. Relative uncertainty continues to decline with increased count rate. The decrease in relative uncertainty is the reason that longer integration times and coadding, or binning, of photon counts is advantageous for lidar measurements. 75
- 5.2 Effect of dead time on measured signal rate. As more photons per unit time arrive at the PMT, a corresponding number more photons should be measured by the PMT (grey line). Dead time effects cause fewer photons to be counted (black line) than have arrived at the PMT. Dead time effects are important for CRL above true count rates of approximately 20 MHz. 81
- 5.3 Dead time correction demonstration. Example measured count rates from 0 to 100 MHz were dead time corrected. Upper panel: The 1:1 line for the plot (light grey) corresponds to the uncorrected values. Corrected values using the best known dead time value of 3.7 ns (0.0037 μ s) are plotted in black. Corrected values using best known dead time value, plus 5% (red), and minus 5% (blue) show that the uncertainty in the dead time estimate is inconsequential on the scale of the correction itself. Centre panel: Percent difference between the corrected and uncorrected count rates. Lower panel: Detail of the centre panel, for measured count rates between 0 and 30 MHz. CRL never uses photon counting measurements above 20 MHz count rate. The correction there is less than 8%, with dead time uncertainty contributing less than 0.3%. 83

5.4	One minute profile from 12 March 2013 to illustrate the relative contributions of various uncertainty terms to the photon counting data. Left: Photon counting signal in MHz units. Right: Dead time correction (grey) and Shot noise uncertainty. Shot noise is by far the largest contributor to the overall analogue uncertainty when integrating for a single minute.	92
5.5	Photon counting channel dark count profiles for Rayleigh Elastic (left), Parallel (centre), Perpendicular (right). These are all given in units of raw photon counts, and all have on average fewer than one photon per altitude bin per minute. Therefore, no correction is made for dark counts in photon counting channels.	100
5.6	Left: Dark counts in the Rayleigh Elastic analogue channel. Right: Detail of low altitude region. All profiles offset by 100 counts from one another for better visibility.	102
5.7	Left: Dark counts in the Parallel analogue channel. Right: Detail of low altitude region. All profiles offset by 100 counts from one another for better visibility. Test 1 not included because the polarotor is required to rotate for Parallel measurements (without lidar modifications).	103
5.8	Left: Dark counts in the Perpendicular analogue channel. Right: Detail of low altitude region. All profiles offset by 100 counts from one another for better visibility. Test 1 not included because the polarotor is required to rotate for Perpendicular measurements (without lidar modifications).	103
5.9	Comparison of Rayleigh Elastic channel dark count profiles from tests with two different triggers: Test 4 used the laser's internal trigger. Test 5 used the polarotor as the laser trigger. The oscillations of the profile in altitude attributed to the flashlamps are identical for both triggering setups.	105

5.10	Comparing the effect of triggering on Parallel (Left) and Perpendicular (Right) dark count profiles. The ringing is worse with the polarotor acting as trigger (Test 5) than it is with the internal laser acting as trigger (Test 4).	106
5.11	Examining the overall shape of the dark count profiles for Rayleigh Elastic (Left), Parallel (Middle), Perpendicular (Right). The Rayleigh Elastic profiles appear linear. The Parallel and Perpendicular profiles appear to curve, and are larger at low altitudes than at high altitudes. The shape of the Parallel and Perpendicular profiles does not appear to be the same.	107
5.12	Dark count profiles for each analogue channel. Each coloured line is a single profile. Black lines are means; grey lines are the mean \pm the standard deviation. The Rayleigh Elastic mean profile is nearly constant. Neither the Parallel nor the Perpendicular mean profiles are constant.	108
5.13	Before and after removal of dark counts profiles from 3 March 2013 in the Rayleigh Elastic channel (left), Parallel channel (centre) and Perpendicular channel (right). Note that in the case of the Rayleigh Elastic channel, the dark count correction is so small that the uncorrected black profile is completely hidden behind the corrected blue profile.	111
5.14	Gluing regions for the Rayleigh Elastic channel. Regions of linearity for photon counting (red profile) and for analogue (blue profile) are indicated. The linear region in common for both channels is the gluing region. The PC values are given here in MHz units as the specification sheets provided by Licel indicate gluing cutoffs in these units.	118

- 5.15 Test for the Rayleigh Elastic channel to determine its gluing coefficients. Dark grey circles are all 5 gluing coefficient days' PC measurement plotted as a function of their ANA counterparts. The light grey dots clustered at lower left indicate which of these data points are in the gluing region determined in Section 5.6.18.1. The light grey points are used to create a linear regression, which is plotted as the line. The slope and offset of this line give the gluing coefficients a and b . In actuality, there are three lines plotted: The fit, and the fit plus and minus its uncertainty. Although there is a decently large spread in the measurements, the uncertainty in the fit itself is very small; all three lines are indistinguishable from each other at the scale of this plot. 120
- 5.16 One minute profile from 12 March 2013 to illustrate the relative contributions of various uncertainty terms to the analogue data. Left: Analogue signal in MHz units. Centre: Dark count (orange), Gluing uncertainty (black), Shot noise (magenta) and ADC least significant bit error (light blue) are plotted. Right: Expanded view of centre plot to see detail in the smaller quantities. Shot noise is by far the largest contributor to the overall analogue uncertainty when integrating for only one minute. 124
- 5.17 One minute glued profile of data from the Rayleigh Elastic channel. The origins of each of the glued data points, from PC (red) and from ANA (blue), are indicated. Uncertainties are also plotted, but they are so small at these scales as to be difficult to see in the plot. A detailed section of the small peak at 4350 m is also provided. Here, the glued profile (dots) begins using the PC profile, switches to the ANA, and then goes back to the PC. The peak at 4350 m is saturated for the photon counting channel, but is still responding well for analogue. 127

6.1	Plot in units of depolarization parameter which compares the absolute uncertainty propagated through both expressions for depolarization parameter d . The x-axis gives the depolarization ratio test input values, δ . The y-axis gives the depolarization ratio uncertainty test input values, σ_δ . For each combination, uncertainties were propagated through the equations 6.2 and 6.4 for d . The colourbar indicates the difference between these two uncertainties: $\sigma_{dG1} - \sigma_{dG2}$. The many positive (red) values indicate that uncertainties for d_{G2} are most often smaller than those for d_{G1} . Therefore, d_{G2} is the preferable expression for the traditional calculation method of d	138
6.2	Photographs of the glassine-covered lidar window. Left: Looking upward from inside the lab, sunlight is visible coming through the glassine-covered receiver window. Right: Looking down into the lidar hatch with the glassine securely installed for calibration tests.	142
6.3	Colour plot of perpendicular channel coadded and corrected photocounts. Black box indicates region of interest to be used in the calibration analysis.	143
6.4	Parallel and perpendicular channel corrected photocounts within the calibration region of interest, with their associated signal-to-noise ratios plotted beneath. Top right panel shows the ratio of the counts for each time-altitude point (k), with the associated uncertainties in k shown at bottom right.	144
6.5	Calibration constant values of k from various time and altitude coadding trials detailed in Table 6.1 from 20131101. The mean of the values is indicated by the solid grey line, with uncertainty in the mean indicated by dashed lines. Visually, the results when using the summed values are equal to within their errorbars. The mean value is $k = 21.0 \pm 0.2$	146

6.6	The waxed paper sheet was placed at various locations within the CRL’s de- tector system, and count rates were measured in the parallel and perpendicular channels. Test locations, numbered 1 through 8, are indicated in the schematic (top) by coloured lines, which correspond to the coloured boxes in the plot of the measurements (below). Tests 1 and 4 are at the same location (green). The test numbers correspond to those in Table 6.2, which includes some discussion of the results.	149
6.7	Contour plot of traditional depolarization results. Left plots show the depolar- ization ratio, its associated absolute uncertainty, and its relative error. The right plots show the same for the depolarization parameter.	154
6.8	Plots from 20130312 demonstrating the depolarization parameter and ratio with associated uncertainties. The top four panels have eliminated any points with relative uncertainty greater than 25%. The bottom four panels have in- stead eliminated any points with absolute uncertainty greater than 0.2. The difference between the top panels and the bottom panels shows the difference in confidence expressed for depolarization values based on the interpretation and use made of the calculated uncertainty. This is discussed in further detail in the current section.	155
8.1	Left panel: Calculations of $\frac{S_{\perp}}{S_{\parallel}}$ for each data point. Middle panel: Associated uncertainties in this quantity. Right panel: Histogram illustrating the most probable value of $\frac{S_{\perp}}{S_{\parallel}}$. Spline and 6th order polynomial fits are indicated. Note that the most probable value, in cyan, is not the same as the mean value, in red.	203
8.2	The extra polarizer is a linearly polarizing cubic prism. It is placed immedi- ately downstream of the focus stage and is rotated by hand. The glassine sheet ensures that all light entering the cubic prism is unpolarized. The calibration lamp is securely bolted onto the telescope frame.	216

- 8.3 Polarized calibration measurements as a function of incident light polarization angle. The cube polarizer was initially placed at an arbitrary angle to ensure that photons were visible in each channel. It was then rotated through a number of steps, spending several minutes at each angle. In total, it was rotated through just more than one full rotation, or 2π radians. All measurements for each angle θ have been combined for this plot. Photocounts are indicated in units of photons per 7.5 metre altitude bin per 1 minute time bin. Parallel measurements are light blue circles. Perpendicular measurements are magenta points. Their respective mean values are indicated by the blue and red points. The curves are not fits, but trace out straight segment to show the path of the mean. 217
- 8.4 Histograms of perpendicular photocount rates for various cube polarizer angles. Note that the most probable value is zero counts at angles surrounding 0 radians, while the average (mean) value reports a value somewhat higher. . . . 218
- 8.5 Histogram using 50 bins, keeping only the values far from angles where either channel's signal was near zero. The peak value is 0.77 and the standard deviation in this histogram is 0.18. 220
- 8.6 Light grey curves are all valid model curves from this test. The solid darker line is the best fit curve based on a weighted least squares comparison between the modeled curves and the measurement data (black circles). The best fit line falls well within $\pm 1\sigma$ of the measurement, and is occurs with values $\frac{M_{01}}{M_{00}} = 0.81$, $\frac{M_{10}}{M_{00}} = 0.81$, $\frac{M_{01}}{M_{00}} = 1$. The dashed line is the curve computed when using the value $\frac{M_{10}}{M_{00}} = 0.77$ calculated in Section 8.3.6.5. 222

- 8.7 Log of weighted least squares error between the measured and modeled data is plotted for various combinations of calibration constants. In each panel, one $\frac{M_{11}}{M_{00}}$ is chosen, and the $\frac{M_{10}}{M_{00}}$ and $\frac{M_{01}}{M_{00}}$ vary within the plot. Any white squares indicate a combination of M_{xx} which is not applicable to the quantity being plotted. At higher values of $\frac{M_{11}}{M_{00}}$, there are fewer valid values of $\frac{M_{01}}{M_{00}}$ and $\frac{M_{10}}{M_{00}}$ to choose from. 222
- 8.8 Polarized calibration measurements as a function of incident light polarization angle. Angle $\theta = 0\pi$ is completely parallel; $\theta = 0.5\pi$ is completely perpendicular. The best fits to parallel measurements (black dots) and perpendicular measurements (grey dots) are shown for the case in which $\frac{M_{10}}{M_{00}} = \frac{M_{01}}{M_{00}} = 0.81$ and $\frac{M_{11}}{M_{00}} = 1$. The best fit determined by using the Perpendicular signal's least-squares is given by the dashed line. Note that this fit does not fit the Parallel channel at all well. The best fit determined by using the Parallel channel's least-squares fit is given by the solid black line. The best overall fit, using a combination of least squares error from both channels, is indistinguishable from the solid black line as the Parallel channel dominates the fit. The best fit lines fall entirely within $\pm 1\sigma$ of the measurements (light grey). 223
- 9.1 Polarized calibration measurements as a function of incident light polarization angle for all channels. Note the broken axis; the Rayleigh Elastic measurements (grey circles and black line) are an order of magnitude larger than the Parallel (light blue circles and blue line) and Perpendicular (pink points and red line) measurements. Here, the measurements are all plotted in MHz, so the difference in measurement repetition rate between the channels has already been accounted for. 228
- 9.2 These are photocounts from 10 March 2013. The uncertainties are all in units of photon counts. Any locations with signal to noise ratios smaller than 1 have been removed and are coloured white. 233

9.3	Left: The d_1 depolarization values from 10 March 2013. Centre: The uncertainties associated with the d_1 values are all in units of depolarization parameter. Right: The relative uncertainties are in units of percent. Physical interpretation of the measurements: The high depolarization parameter values in the cloud at daynumber 69.2, at 5500 m altitude, indicate that the cloud is composed of particles which are not homogeneous spheres; in context, this means that the cloud is likely composed of ice particles. The uncertainty in this region of the cloud is approximately 12%. For the small cloud at daynumber 69.3, there is less certainty. There, the d_1 values indicate a mix of high and low depolarization varying between 0.4 and 0.8 in a rather noisy fashion. The uncertainty in this small cloud is ± 0.25 or higher, indicating more than 30% relative uncertainty. The edges of all clouds have high uncertainty as well. While a general interpretation of icy clouds in a clear atmosphere is possible, depolarization parameter measurements with higher resolution and/or smaller uncertainty would be better. If there are any clouds at all above 6000 m altitude, d_1 is not sensitive to them because of the low count rates in the perpendicular channel.	234
9.4	Left: The $\frac{G_{PMTRO_R(z)}}{G_{PMT\parallel\perp}O_{\parallel\perp}(z)} \frac{T_{00}}{M_{00}}$ calibration values from 10 March 2013 individually for each data point. Right: Uncertainties in the calculated individual values of $\frac{G_{PMTRO_R(z)}}{G_{PMT\parallel\perp}O_{\parallel\perp}(z)} \frac{T_{00}}{M_{00}}$	235
9.5	Left: The $\frac{G_{PMTRO_R(z)}}{G_{PMT\parallel\perp}O_{\parallel\perp}(z)} \frac{T_{00}}{M_{00}}$ calibration values from 10 March 2013 with the fits to the night's measurements. Right: Zoomed-in portion of the plot on the left to show differences between the lines.	238
9.6	Plots of 2nd order power law fits to the calculated profiles of $\frac{G_{PMTRO_R(z)}}{G_{PMT\parallel\perp}O_{\parallel\perp}(z)} \frac{T_{00}}{M_{00}}$ for the test dates and resolutions listed in Table 9.1	239

9.7	Left: The d_2 depolarization values from 10 March 2013. Centre: The uncertainties associated with the d_2 values are all in units of depolarization parameter. Right: The relative uncertainties are in units of percent. Note the better coverage of time and space using this method as compared to using Option 1 for d_1	240
9.8	Compare depolarization results from both methods. Left: d_2 (from Option 2) - d_1 (from Option 1). Right: Determining whether the differences are significant, taking uncertainties into account. Compare differences in d values to the total combined uncertainty for both methods.	241
9.9	Left: The d_1 depolarization values from 14 March 2013. Centre: The uncertainties associated with the d_1 values are all in units of depolarization parameter. Right: The relative uncertainties are in units of percent.	243
9.10	Top: Context plot of all individual $\frac{G_{PMT\parallel}O_R(z)}{G_{PMT\parallel\perp}O_{\parallel\perp}(z)} \frac{T_{00}}{M_{00}}$ values for 14 March 2013. Box A indicates the region included in the nightly profile which includes all measurements (Bottom left). Box B indicates the region included in the nightly profile which excludes any regions with thick clouds (Bottom right).	244
9.11	Left: The d_2 depolarization values from 14 March 2013, using all data available for that day to influence the calibration profile. Centre: The uncertainties associated with the d_2 values are all in units of depolarization parameter. Right: The relative uncertainties are in units of percent.	245
9.12	Left: The d_2 depolarization values from 14 March 2013, using only clear sky and regular cloud data (thick clouds excluded) to influence the calibration profile. Centre: The uncertainties associated with the d_2 values are all in units of depolarization parameter. Right: The relative uncertainties are in units of percent.	245
9.13	Comparisons of the results for $d_2 - d_1$ 14 March 2014 calculated using the default setting of the entire time-altitude range for calibration.	246

9.14	Comparisons of the results for d_2-d_1 14 March 2014 calculated using only clear sky and regular cloud data (thick clouds excluded) to influence the calibration profile.	246
9.15	Left: The d_1 depolarization values from 11 March 2013. Centre: The uncertainties associated with the d_1 values are all in units of depolarization parameter. Right: The relative uncertainties are in units of percent.	249
9.16	Left: Context plot of all individual $\frac{G_{PMT} O_R(z)}{G_{PMT} O_{\parallel}(z)} \frac{T_{00}}{M_{00}}$ values for 11 March 2013. The black box indicates the region included in the nightly profile (Right); this excludes regions with thick clouds.	249
9.17	Left: The d_2 depolarization values from 11 March 2013, using only clear sky and regular cloud data (thick clouds excluded) to influence the calibration profile. Centre: The uncertainties associated with the d_2 values are all in units of depolarization parameter. Right: The relative uncertainties are in units of percent.	249
9.18	Left: Difference between d_1 and d_2 values for 11 March 2013. Right: Significance plot showing regions in which the difference between d_1 and d_2 exceeds the sum of their respective uncertainties. Differences of that magnitude and larger are deemed to be significant.	250
10.1	The d_1 depolarization values from 10 March 2013, with (t20,z1) resolution, excluding anywhere with more than 0.2 uncertainty in depolarization parameter units. Left: d_1 values. Centre: The uncertainties associated with the d_1 values in units of depolarization parameter. Right: The relative uncertainties are in units of percent.	254

10.2	The d_2 depolarization values from 10 March 2013, with (t20,z1) resolution, excluding anywhere with more than 0.2 uncertainty in depolarization parameter units. Left: d_2 values. Centre: The uncertainties associated with the d_2 values in units of depolarization parameter. Right: The relative uncertainties are in units of percent. The calibration profile is based on (t20,z1) resolution calculations.	254
10.3	The d_1 depolarization values from 10 March 2013, with (t10,z1) resolution, excluding anywhere with more than 0.2 uncertainty in units of depolarization parameter. Left: d_1 values. Centre: The uncertainties associated with the d_1 values in units of depolarization parameter. Right: The relative uncertainties are in units of percent.	255
10.4	The d_2 depolarization values from 10 March 2013, with (t10,z1) resolution, excluding anywhere with more than 0.2 uncertainty in depolarization parameter units. Left: d_2 values. Centre: The uncertainties associated with the d_2 values in units of depolarization parameter. Right: The relative uncertainties are in units of percent. The calibration profile is based on (t20,z1) resolution calculations.	256
10.5	The d_1 depolarization values from 10 March 2013, with (t2,z1) resolution, excluding anywhere with more than 0.2 uncertainty in depolarization parameter units. Left: d_1 values. Centre: The uncertainties associated with the d_1 values in units of depolarization parameter. Right: The relative uncertainties are in units of percent. These plots look empty because almost none of the perpendicular measurement bins have enough counts to make it above the SNR thresholds required.	257

10.6	The d_2 depolarization values from 10 March 2013, with (t2,z1) resolution, excluding anywhere with more than 0.2 uncertainty in depolarization parameter units. Left: d_2 values. Centre: The uncertainties associated with the d_2 values in units of depolarization parameter. Right: The relative uncertainties are in units of percent. The calibration profile is based on (t20,z1) resolution calculations.	257
10.7	The d_1 depolarization values from 29 March 2013, with (t20,z1) resolution, excluding anywhere with more than 0.2 uncertainty in depolarization parameter units. Left: d_1 values. Centre: The uncertainties associated with the d_1 values in units of depolarization parameter. Right: The relative uncertainties are in units of percent.	258
10.8	The d_2 depolarization values from 29 March 2013, with (t20,z1) resolution, excluding anywhere with more than 0.2 uncertainty in depolarization parameter units. Left: d_2 values. Centre: The uncertainties associated with the d_2 values in units of depolarization parameter. Right: The relative uncertainties are in units of percent. The calibration profile is based on (t20,z1) resolution calculations.	259
10.9	The d_1 depolarization values from 29 March 2013, with (t20,z5) resolution, excluding anywhere with more than 0.2 uncertainty in depolarization parameter units. Left: d_1 values. Centre: The uncertainties associated with the d_1 values in units of depolarization parameter. Right: The relative uncertainties are in units of percent.	260

10.10	The d_2 depolarization values from 29 March 2013, with (t20,z5) resolution, excluding anywhere with more than 0.2 uncertainty in depolarization parameter units. Left: d_2 values. Centre: The uncertainties associated with the d_2 values in units of depolarization parameter. Right: The relative uncertainties are in units of percent. The calibration profile is based on (t20,z1) resolution calculations.	260
10.11	Compare uncertainties for both depolarization methods $\sigma_{d2} - \sigma_{d1}$. Positive values indicate that the Traditional Method is more precise; Negative values indicate an improvement using the Option 2 method.	262

List of Tables

5.1	Dark count profile test conditions	102
5.2	Mean dark count values for each analogue channel with their associated standard deviations.	108
5.3	Gluings coefficient results from 5 nights of measurement in 2013. The coefficients are similar for the Parallel and Perpendicular channels which share a PMT, and are different for the Rayleigh Elastic channel. These are for background subtracted measurements, and were calculated in units of photon counts per bin per minute. They can be used to convert ANA signals into units of virtual count rates; not MHz.	120
5.4	Gluings coefficient results from 19 November 2013. The values of a do not change between the background-subtracted and the non-background-subtracted cases. The offsets b do change. These are in units of photon counts per bin per minute, and not MHz.	121
6.1	Calibration constant values of k from various time and altitude coadding trials .	145
6.2	Measuring calibration constant k using a depolarizer at various locations in the polychromator. The VIS LWP filter and collimating optics contribute most. Comparison with the overall $k = 21$ value for whole system indicates that calibration tests must include all optics. The (un)polarization generating calibration optic must precede the roof window.	150

7.1	Summary of more complete expressions for depolarization parameter d	188
7.2	Summary of simplified expressions for depolarization parameter d	189
8.1	$\frac{S_{\perp}}{S_{\parallel}}$ and $\frac{M_{10}}{M_{00}}$ values using the first procedure, via histogram fitting.	203
8.2	Measuring calibration constant $\frac{M_{10}}{M_{00}}$ using a depolarizer at various locations in the polychromator. Test numbers correspond with those from Chapter 6. See that chapter also for a diagram.	204
8.3	Parallel and perpendicular signals for angles diagnostic of symmetry in the measurements. Each signal is effectively the same at 0.25π and 0.75π radians and integer multiples thereof.	219
9.1	Fitting coefficients and goodness of fit for various days and resolution in March 2013 in the determination of $\frac{G_{PMTRO_R(z)}}{G_{PMT\parallel\perp}O_{\parallel\perp}(z)} \frac{T_{00}}{M_{00}}$ Days marked with “*” used only a portion of the data available for that day: clear sky or thin clouds only.	239

Chapter 1

Introduction

Clouds are one of the most poorly understood atmospheric phenomena, particularly in terms of their effect on the radiation balance of Earth. They contribute to cooling through reflection of short wave radiation by the cloud tops. They contribute to warming by trapping long wave radiation from Earth. These competing effects are strongly linked to the phase of the particles which make up the cloud: liquid water droplets, versus frozen ice particles. An understanding through survey measurements of how many of each type of cloud there are, and in which locations, during each part of the year, will help elucidate an understanding of the overall contribution of clouds to the radiation budget of the atmosphere.

In the Arctic, and particularly during Polar Night, there are few long-term observations which are able to quantify and explore the particle phase of the clouds (ice particles versus water droplets). This study seeks to add lidar depolarization measurements of cloud particle phase to the information available about winter clouds at Eureka, Nunavut in the Canadian High Arctic. This will allow more realistic representations of cloud radiation effects in climate model parameterizations, and thus eventually allow a greater understanding of the extent to which cloud feedback influences the overall radiation budget of the Earth.

Lidar (LIght Detection and Ranging) is the primary technique employed in this thesis as it provides high spatial-temporal resolution cloud data, even in the absence of sunlight.

For lidars such as the CANDAC Rayleigh-Mie-Raman lidar (CRL) at Eureka, pulses of polarized visible and UV laser light are directed upward to the sky above the laboratory. The light interacts with molecules and other particles in the atmosphere at various altitudes above the lidar, and is scattered in all directions. Any light which is scattered directly back down into the laboratory is collected with an optical telescope and is directed into photon counting detectors. The telescope is coaligned to the emitted laser beam such that it receives the maximum possible signal from backscattered laser light. A profile of backscattered photon counts is retrieved as a function of altitude.

For a depolarization lidar, profiles of photon counts are retrieved individually for the components of the backscattered light in each of two orthogonal planes of polarization: One parallel to, and the other perpendicular to, the polarization plane of the outgoing laser beam. The depolarization of the returned beam, expressed as the depolarization ratio, δ , or the depolarization parameter, d , is indicative of the phase of particles in the atmosphere with which the lidar beam has interacted. Values close to zero indicate spherical particles, or an absence of cloud particles altogether. Higher values, up to 1, are indicative of frozen particles or aerosol layers.

Lidar depolarization measurements cannot differentiate the ambiguous results alone, nor can other instruments on their own. For scientific interpretations, lidar depolarization measurements are taken in cooperation with measurements from other lidar channels, and other instruments (e.g. radar, starphotometer, etc.). Together, distinctions may be made. A depolarization-capable lidar with high temporal and spatial resolution which can measure long-term is therefore a valuable addition to any suite of remote sensing atmospheric instruments.

1.1 Overview

This thesis includes the installation, calibration, testing and use of a depolarization channel at the CANDAC Rayleigh-Mie-Raman Lidar (CRL) at Eureka, Nunavut, Canada. Because the CRL is somewhat different than other depolarization lidars, a good deal of mathematical work was also done to verify the traditional analysis method for the CRL, and to provide an additional technique which is superior to this method for the CRL.

Chapter 1: Introductory chapter.

Chapter 2: A literature review including background information and context for this thesis is given in Chapter 2. Therein is included: Scientific motivation for having a lidar depolarization channel, mainly focusing on polar clouds and the radiation balance of the atmosphere (Section 2.1.1), a small amount of background description about polarization physics itself as it pertains to lidar depolarization measurements (Section 2.2.1), lidar measurements in general (Section 2.2.3), and finally a section regarding the present state of the depolarization lidar community (Section 2.2) and some examples of scientific situations in which depolarization lidar measurements can be of use (Section 2.1.3).

Chapter 3: Specifications about the laboratory, up to but not including installation of the depolarization channel, are given in Chapter 3.

Chapter 4: Details of the installation process of the depolarization channel hardware within the lidar are given in Chapter 4.

Chapter 5: Information on low level data processing required to turn raw photocount signals into corrected lidar profiles for each channel is provided in Chapter 5.

Chapter 6: The initial calibration of the depolarization channel, and some example calibrated depolarization results, are given in Chapter 6. The calculations in this chapter

follow the standard “traditional method” for depolarization parameter measurements and their calibrations.

Chapter 7: Extra testing was deemed necessary to ensure that the equations for processing depolarization data using the traditional mathematical method of Chapter 6 were valid for use with CRL data. A more mathematically complex derivation of the signals in each lidar channel is developed in Chapter 7, with the resulting equations for depolarization products in Section 7.2.

Chapter 8: Calibrations in Chapter 8 demonstrate that the traditional method (from Chapter 6) is acceptable to use for CRL measurements.

Chapter 9: Through the developments of the latter two chapters (7 and 8), the idea came about to try an alternate procedure for gleanng depolarization information from the CRL. The traditional method uses two depolarization measurement channels (parallel and perpendicular). The perpendicular count rates at the CRL are extremely low, leading to low signal to noise ratios, and low resolution final depolarization products. The CRL, like many visible wavelength lidars, contains a Visible Rayleigh Elastic measurement channel (without polarizers) in addition to the depolarization measurement channels. It was thought that perhaps this channel, combined with the parallel measurement channel, could provide an alternate method for calculating depolarization parameter and depolarization ratio. The results of mathematical derivations to this effect are included in Section 7.2, and this procedure is referred to in this thesis as the “Option 2” method. The calibrations required to take these equations for d into effect are provided in Chapter 9. The perpendicular channel measurements are important in determining the calibration profiles used in Option 2. Validation of Option 2 was carried out, and it was found to be a valid approach to calculating the depolarization parameter (d) for CRL.

Chapter 10: In Chapter 10, a few example days of measurement demonstrate the advantages of using Option 2 over using the traditional method alone. It has lower uncertainty, better signal to noise, and is useable at much higher spatial-temporal resolution than is the traditional method. To keep the different values of d clear in the thesis, d_1 is used to express depolarization parameter calculated using the traditional method with parallel and perpendicular photocounts, and d_2 to express the depolarization parameter calculated using the “Option 2” method with parallel and Rayleigh Elastic photocounts.

Chapter 11: The concluding Chapter 11 summarizes the major results, and indicates likely directions for future work.

1.2 Major contributions of this thesis

This thesis provides two major contributions to the scientific community:

1. The first contribution of this thesis is the availability of routine, long-term lidar depolarization parameter measurements, in a location where such measurements, to date, are scarce. The CRL’s new depolarization channel provides capability for a multi-year data set with cloud phase (ice vs. water vs. mixed phase) and cloud coverage information. These are required inputs to global atmospheric models. The calibrated depolarization data sets provided by the CRL are also desired by the experimental scientific community for comparison with the output of other atmospheric science instrumentation such as radars and starphotometers. Intercomparison studies will help to reduce ambiguous results in cloud and aerosol measurements from Eureka.

2. The second major contribution of this thesis is the development of the new depolarization measurement technique. This technique allows measurements of the depolarization parameter at higher spatial-temporal resolution, with lower uncertainty, and measurements to higher altitudes than those allowed by the traditional technique. As climate model res-

olution increases, physical processes are introduced instead of parameterizations. Most relevant to this thesis is the introduction of cloud microphysical equations to models which previously used a parameterization for the overall radiation contribution from all global clouds together. This requires long-term, high-resolution measurements of the state and extent of the clouds, and the processes which occur within them, for clouds above all regions of the Earth. The higher resolution depolarization measurements developed in this thesis allow more a detailed examination of the small-scale processes within the clouds which are important for climate and which are missed by lower-resolution traditional measurements. Importantly, this new technique can be applied to existing data sets from CRL and from other lidars around the world which have measurements in a non-polarized Rayleigh Elastic channel in addition to their traditional depolarization measurements.

Chapter 2

Literature Review and Background

2.1 Scientific motivation: Polar clouds

2.1.1 Clouds and the radiation budget of Earth's atmosphere

Clouds have a significant effect on the local radiation budget of Earth's surface [3]. Their high albedo can lead to cooling, their absorption of longwave outgoing radiation contributes a warming effect and these competing mechanisms are not easily untangled [4]. Today, there remains uncertainty in the extent of cloud cover over Earth's surface, particularly in Arctic regions. The average cloud cover in the Arctic is generally reported to be high, although estimates vary between 30% and 85% [5].

Still less is known about the microphysical properties of the clouds themselves. In order to model a realistic climate projection, realistic inputs of physical processes are required [3]. In the IPCC 2007 Fourth Assessment of the Intergovernmental Panel on Climate Change [6], cloud feedback is reported to have the largest uncertainty of all components considered in the global average of radiative forcing. While the data record is long for some climate processes in certain regions, there is much left to be understood in the Arctic.

During polar winter, in the absence of incoming solar radiation, effects of cloud albedo cease to be a factor in the radiation budget. Only the long-wave radiation from the ground,

and clouds' interactions with it, will contribute. Clouds can then dominate the radiation budget, so the ability to understand their radiative impact during the polar winter season is essential if a correct estimation of Earth's climate is to be produced ([7] after [8] and [9], [10]). This is of global importance, with cloudiness and radiation being one of the main priority areas for climate research identified by the World Climate Program ([11], [12]).

The atmospheric radiation balance is particularly sensitive to cloud particle phase because liquid and solid cloud phases usually have different scattering properties. Several models adequately describe warm clouds at low and mid latitudes, where many years of continuous measurement are available, and where the water in the cloud is all in the liquid phase. Cold cirrus clouds made up entirely of ice particles are more difficult to understand because of the multiple freezing processes involved in their formation. Particularly challenging to model are mixed-phase clouds. Mixed-phase clouds are low-level clouds which persist over extended time periods at atmospheric temperatures between 242 and 271 K (-31°C to -2°C) [13]. Ground-based observations show supercooled water in discrete layers on top of, or within, a layer of ice crystals [14], but many configurations are possible. The ice particle size and concentration in mixed-phase clouds is different from in ice-only clouds because mixed-phase clouds involve a complex interaction of three phases of water (vapour, liquid, and ice) coexisting in the same cloud. Models are still not capable of adequately predicting particle size spectra within clouds, and those which currently predict cloud height, depth and water content will benefit from further measurements which parameterize the cloud optical properties in terms of liquid and ice water content [11].

2.1.2 Scientific questions regarding mixed-phase clouds

In the Arctic, mixed phase clouds dominate the low level atmosphere during winter and thus play a significant, and complex, role in determining the surface energy budget [15]. Radiatively, the supercooled liquid in these clouds is known to increase cloud surface long-wave flux, reducing net surface cooling by up to 40 to 50 Wm^{-2} [16], [13], and differences

in ice particle shape can modify the ice cloud albedo by up to 30% [17],[18]. Understanding the partitioning between the three phases inside the cloud becomes very important if one is going to model mixed-phase clouds, or indeed all clouds, and their radiative effects correctly ([19] and [20] in [14]). There is still great uncertainty in the relative abundance of particles of each phase, in the morphology of solid particles, and in precipitation rates ([21], [22]).

As a mixed-phase cloud develops, ice formed in the mixed-phase layer gradually grows and precipitates out of the cloud [21]. Various ice-formation processes are understood in isolation, but their relative contribution to mixed phase cloud processes is still not known. One such process is the Wegener-Bergeron-Findeisen process, in which ice crystals grow at the expense of liquid water droplets in the cloud, causing mostly-liquid clouds to dissipate quickly [5]. Another is the Hallett-Mossop process or Rime Splintering, whereby cloud ice content can be enhanced when liquid water is rimed onto ice particles. This results in higher ice particle fall speeds than those observed for pristine ice crystals ([14], [23]).

Many questions remain regarding the evolution of a mixed-phase cloud: How much ice is nucleated in the liquid water layers? How does that ice evolve and fall out? How does the supercooled liquid persist in spite of the vapour flux to ice? [24]. How does the transformation of low clouds from liquid to ice depend on temperature and aerosols, and how do these processes vary with season? [16]. Understanding the growth mechanisms of mixed-phase clouds will allow an understanding of what makes these clouds persistent over such a long time in the atmosphere. Such a study will involve a good understanding of the particle phase partition within the cloud as a function of time.

Arctic clouds are complicated still further through the contribution of aerosols. During polar winter, sulphates represent an important aerosol species, and are expected to inhibit ice nucleation [25]. Studies as recent as 2008 have modeled the effects of aerosols on warm clouds, but the general effect of aerosols on cold clouds is still poorly described in global

circulation models [23]. Long term measurements of such properties during winter are required. Depolarization lidar measurements are one useful tool in this regard.

2.1.3 Types of Arctic cloud measurements and their challenges

Some disagreement in the numbers for cloudiness, etc, stems from the logistical challenges presented by doing research in the Arctic at any time of year, plus the many complications to making measurements during the Arctic winter. Observations of clouds are made by satellite and aircraft, as well from the surface on ships and at ground-based laboratories. The best measurements are made in coordinated efforts, or are made in such a way that the measurements may be coordinated with others later.

2.1.3.1 Aircraft observation

Aircraft can make cloud observations in situ by flying through the cloud, and they may have profiling instruments such as lidars to examine clouds below the aircraft. Instruments on aircraft can be flown to the geographic location of interest in order to make measurements where there is no surface observatory.

When used as a profiler, these aircraft measurements are just as “remote sensing” a technique as those which are surface based. As for in situ measurements, aircraft should not fly in very adverse or unsafe weather conditions. This misses many opportunities to observe interesting cloud effects. Aircraft also generally fly on a campaign basis, rather than continuously for weeks or years.

Early airborne lidar depolarization measurements were made by Spinhirne et al in 1982 [26], who at the time of publication suggested that the aircraft measurements be used as an instrument testbed and preparations for flying lidars in space on the shuttle or other satellite, which had not yet been tried by that date.

Aircraft campaigns continue to be run regularly. Usually, they operate as part of comparison campaigns with ground- or ship- based instruments.

2.1.3.2 Satellite observation

Satellites allow survey-style cloud detection at various wavelengths. Infrared measurements are common, and work well at low- and mid-latitudes. Those which orbit the poles have high spatial coverage, at the expense of temporal resolution for data over any single geographic region. Geostationary satellites do not observe the poles well, and never directly.

The NASA multinational “A-Train” constellation of satellites contains several launched between 2002 and 2006 which are of particular importance to cloud observations: Aqua (with radiometers for cloud investigation, including aerosol contributions), The Cloud-Aerosol Lidar and Infrared Pathfinder Satellite Observations (CALIPSO, which contains a depolarization lidar similar to CRL, and several imagers), and CloudSat (a cloud profiling radar) [27]. These satellites fly in formation with several others, and can produce combined data products because of their nearly-simultaneous measurements.

In locations where the weather can change quickly, satellite measurements alone may not occur frequently enough to track all of the changes. Compounding the problem are the low-level temperature inversions common to the arctic which make it difficult for passive infrared satellites to distinguish between surface emissions and those from clouds (Grenier and andand Rodrigo Munoz-Alpizar, 2009), and to distinguish single layers of clouds from multiple layers. Hence, cloudiness during the dark winter months may be underestimated.

Further, any satellite data set is only worth its surface validation. There must be surface stations groundtruthing the satellite data in the regions for which the data is to be used.

So far, large discrepancies remain between satellite and ground-based climatologies, and this is an area of active research.

2.1.3.3 Ship-based observations

The polar regions are more easily reached for surface operations during the warmer sunlit months when ships are able to travel than they are during the frozen winter. In order to

make surface-based winter measurements, a location is needed from which to make the measurements, and equipment is required which is able to withstand the harsh conditions of polar winter including high winds and extremely low temperatures.

One solution is to freeze a ship into the ice pack, as was done by the SHEBA campaign [28]. The motion of the ship through the winter is determined by the motion of the ice pack. Thus, the laboratory's geographic location is not perfectly repeatable year after year. The campaign-like nature of such projects does have the advantage of nearly continuous measurements for the duration of the project.

2.1.3.4 Ground-based observations

There are several permanent weather stations in the Northern regions of many polar countries, such as the National Oceanic and Atmospheric Administration (NOAA) Earth System Research Laboratory Global Monitoring Division laboratories at Barrow, Alaska [29] and Summit, Greenland [30], [31], and the Tiksi Hydrometeorological Observatory in Russia [32]. There is some collaboration between independent observatories through organizations such as IASOA (International Arctic Systems for Observing the Atmosphere), which includes the aforementioned sites, as well as others in Canada (Alert and Eureka), and in other countries (at Cherskii, Ny-Alesund, Oliktok, Pallas-Sodankyla, and Villum) [33].

The Eureka Weather Station at Eureka, Nunavut, Canada, is ideally situated for winter Arctic research. This is the site of the CRL lidar used for this thesis, so is more fully described in Chapter 3. At Eureka, experiments are run year-round. Notably, these include radar, several lidars of various capabilities, radiometry measurements, and twice-daily radiosonde launches, among other instruments belonging to organizations including Environment Canada, NOAA, CANDAC (Canadian Network for the Detection of Atmospheric Change).

The SEARCH (NOAA Study of Environmental Arctic Change) projects High Spectral Resolution Lidar [34], which begun circular depolarization lidar measurements in Barrow,

Alaska [35] (including with the M-PACE Mixed-Phase Arctic Cloud Experiment), continued such measurements at Eureka from 2005 through 2009 [36]. These were the first depolarization lidar measurements at Eureka. Further lidar depolarization measurements at Eureka now continue with the addition of the linear depolarization channel to the CRL lidar, as discussed in this thesis. The CRL is also capable of measuring aerosols and water vapour mixing ratio profiles.

These ground-based permanent observation sites are able to be run long-term, whether for extended campaigns, or for measurements repeated during the same dates each year. Combined campaigns with simultaneous aircraft measurements are quite valuable.

2.1.3.5 Human observation

Human weather observers are employed by Environment Canada to make hourly estimates of cloud cover, among other weather observations, at Eureka, Nunavut. Similar observations are made worldwide by other national weather services. This provides a very extensive data set of cloud coverage around the globe, but has several drawbacks for Arctic wintertime clouds: Thin ice clouds at high altitudes tend to be subvisual, and any cloud measurement is difficult during the 24 hour darkness of polar night; even estimates of clouds of high optical depth are not trivial when the observer cannot see the clouds at all [37]. Not many of the stations worldwide are in the Arctic, and fewer still are staffed with observers.

Beyond the obvious other advantage of getting vertical profile information, the main advantage to using the active sensing technique of lidar is that a lidar makes its own light; it can “see” in the dark.

2.1.3.6 Multimethod intercomparisons

Multimethod intercomparisons have produced the most fruitful measurements of mixed-phase clouds in the Arctic ([14]). This is partly because each measurement location has its

own strengths. While aircraft observations are clearly better suited to making in-situ, direct measurements of cloud properties, remote sensing by lidar and radar observations have the advantage of long time series at high temporal resolution with good vertical coverage. At mid-latitudes and during the sunlit portion of the Arctic year, satellite measurements can also be of help. The importance of multimethod intercomparisons is also because a mixed-phase cloud is a vastly complicated system which has many different properties to understand; each of these properties is best investigated by a different tool. To date, there have been many individual measurements made of specific properties of mixed phase clouds, and large-scale cooperative multi-instrument projects, but very few campaigns in the Arctic have extended longer than one season. A brief description of some recent campaign-based projects follows:

- SHEBA: Surface Heat Budget of the Arctic Ocean. 15 Sept 1997—1 Nov 1998. SHEBA was a year long ice camp including an icebreaker frozen into the drifting arctic ice pack. Most measurements were oceanographic in nature, but lidar measurements were made between 1 Nov 1997 and 8 Aug 1998 [28].
- FIRE-ACE: First ISCCP regional Experiment Arctic Cloud Experiment . April—July 1998 in conjunction with the SHEBA experiment [38]. FIRE-ACE focused on all aspects of Arctic clouds, flying four research aircraft over the SHEBA ground sites [39].
- MPACE: Mixed-Phase Arctic Clouds Experiment. 27 Sept—22 Oct 2004. MPACE included four surface sites in Alaska with radiosonde, tethered balloon, lidar, and radar capability. An aircraft component of the campaign added cloud microphysics and radiation measurements both in situ and from above ([40], [41]). One example of comparisons with campaign data made at a later date is the 2008 validation comparison by Turner and Eloranta [42], in which ground-based high spectral resolution lidar is used to validate the optical depth retrievals in mixed-phase clouds from measurements by Atmospheric Emitted Radiance Interferometer (AERI) during MPACE.

- ASTAR: Arctic Study of Tropospheric Aerosol, Clouds and Radiation. March and April 2007. ASTAR was conducted in Ny-Alesund, Svalbard with two ground-based lidars (one micro pulse lidar and one Raman lidar) and one airborne elastic lidar [5].
- SEARCH: Study of Environmental Arctic Change. 2005—2010. Since 2005, the National Atmospheric and Oceanographic Administration (NOAA) and the Canadian Network for the Detection of Atmospheric Change (CANDAC) have collaborated through SEARCH to make measurements at Eureka, Nunavut. This is the longest data set of its kind in the Arctic, and includes a high spectral resolution lidar (HSRL), a millimeter cloud radar and radiosonde measurements [13], [43]. The Eureka site has many co-located instruments and is an ideal location for continued measurements. Eureka is the location of the work in this thesis.

Because these campaigns were made at different times of year in different regions of the Arctic, their data are not always comparable. As an example, the results show that liquid water fraction increases with increasing temperature (MPACE, vertically integrated), decreases with increasing temperature (MPACE, in situ measurements), and does not depend strongly at all on temperature (SEARCH) [13]. Clearly, this would be difficult to parameterize in a model. Similarly, several experiments were carried out below -35°C to figure out rate of ice crystal formation. Lohmann 2002, in the lab, varied saturation with respect to ice, with the parameterization of ice crystal size found by Ou and Liou 1995, in which ice crystal effective radius is a function of temperature. In the field, Kristjansson et al. (2000, [44]), Ivanova (2001, [45]) and Boudala (2002, [46]) measured the same properties, but these relationships deviate quite substantially from each other for certain temperature intervals [23]. Again, this data is obtained from field campaigns in vastly differing environments.

It is desirable to continue with long-term measurements at specific locations to reduce similar uncertainty in the data products of this and other microphysical properties. To date, various independent measurements have been made of ice water content, liquid water

content, ice particle effective radius, particle number density, cloud optical depth, particle phase and other complementary measurements. Getting an idea of the processes within these clouds is more difficult because each of these properties depends on all the others.

One must know or make assumptions about crystal shape before an effective size can be calculated [23]. That is not complicated for warm clouds where every particle is a spherical liquid droplet, but becomes orders of magnitude more difficult to ascertain in an ice or mixed-phase cloud.

The influence of aerosols is also not to be neglected, and there is little agreement on their effect on the radiative impact of the clouds in which they reside. Storelvmo, Kristjansson and Lohmann [23] points out that lab experiments by Pruppacher and Klett (1977, [47]) show that lower temperatures are required to freeze the small aerosol-nucleated cloud droplets, while Lohmann and Karcher (2002, [48]) suggests that the increase in cloud droplet number concentration as a result of those same aerosols could promote freezing. Again, more measurements are required in order to definitively understand these competing effects.

2.1.3.7 Models

Several models have been used to simulate mixed-phase clouds, and none to date has been able to adequately include cloud microphysics; several authors claim that it is not even possible to do so at this time, without detailed parameterization from more measurements of these clouds ([14], [15]). The difficulties with modelling mixed-phase clouds are many: a bimodal particle size distribution is required, the models must be multidimensional with microphysical properties calculated at a very fine scale, and major limits are imposed by the lack of data in this research area [49]. All these requirements must be adequately met before a model will be able to produce the relative importance of the competing processes (including phase transitions) taking place within mixed-phase clouds.

Data from the MPACE experiment has been compared to the NASA Goddard Institute

for Space Studies global circulation model (GISS). GISS is a single-column model coupled to a bin-resolved microphysics scheme which was written specifically to address mixed-phase clouds and cloud-aerosol interactions. This state-of-the-art model qualitatively simulates ice crystal concentration and the soluble and insoluble contents of hydrometeors. When compared to MPACE data, it fails quantitatively. It overestimates particle effective radius by about 50%, and vertical profiles are not well-represented [49]. The overall outcome of the model is to demonstrate that when including ice nucleation in the model, both freezing from water vapour and freezing from supercooled liquid droplets are important.

MPACE data has also been compared to the models CAM3 (Community Atmosphere Model) and AM2 (Developed at Geophysical Fluid Dynamics Laboratory (GFDL)). CAM3 is the sixth generation of the National Center for Atmospheric Research (NCAR) atmospheric general circulation model. Traditionally, it uses a single-moment microphysical scheme. The number concentration of liquid droplets and ice are specified to be functions of temperature, but this does not give particularly realistic results. Improvements in CAM3 come from an improved, more physically-based cloud microphysical scheme which takes an ice nucleation scheme (CAM3LIU) into account rather than making assumptions that the particle phase partition is based solely on temperature [15]. Under this method, the comparisons were improved. The modeling requirements lead back to a set of observational questions regarding the particle size and phase for liquid droplets and for ice crystals, the number densities of both kinds of particles, and the mechanisms by which ice crystals form in these clouds (there are many; ice nucleation is difficult to predict).

The polar winter lidar depolarization measurements developed in this thesis will contribute to the increasing fidelity of the role of clouds in atmospheric models such as those listed above.

2.2 Background physics for polarization and lidar

Lidar depolarization measurements are an ideal technique for making long-term studies of mixed-phase clouds, particularly in the Arctic, particularly in polar night. Measuring the magnitude by which an atmospheric particle depolarizes an incident light beam gives some information regarding particle shape, and hence the particle phase which is so important for climate modelling. The required background information about polarization theory is given here, followed by specific details for depolarization lidar.

2.2.1 Physics of Polarization

Light may be described as a transverse electromagnetic wave. Such a wave travelling in the z -direction at time t may be composed of the sum of two electric fields oriented in two orthogonal directions, x and y [50]:

$$E(z, t) = E_x(z, t) + E_y(z, t) \quad (2.1)$$

$$E_x(z, t) = iE_{ox} \cos(kz - wt) \quad (2.2)$$

$$E_y(z, t) = jE_{oy} \cos(kz - wt + \epsilon) \quad (2.3)$$

where:

E_{ox} is the amplitude of E_x

E_{oy} is the amplitude of E_y

k is the wavenumber

w is the angular frequency

ϵ is the relative phase difference between the waves.

When E_x and E_y are in phase ($\epsilon = 0$), $E(z, t)$ is linearly polarized. This resultant electric field vector oscillates as a cosine in time along a tilted line with respect to E_x and E_y . Considered in reverse, this is to say that any plane-polarized wave can be separated into two linearly polarized orthogonal components.

When these waves are measured (for example by a photomultiplier tube in a lidar detector) it is their irradiance, and not their electric field directly, which is detected. Hence, it is noted that irradiance, I , the power per unit area per unit time of the beam incident on the detector may be described as:

$$I = \frac{1}{2} \epsilon_o c E_o^2. \quad (2.4)$$

When a polarizing device is inserted between the original beam and the detector, only the component of light polarized parallel to the device is allowed through. Malus' law describes how the irradiance received at the detector, I , behaves with respect to angle θ between the polarizing device and the polarization plane of the original beam $I(0)$:

$$I(\theta) = I(0) \cos^2(\theta). \quad (2.5)$$

The cosine dependence demonstrates that as the polarizer completes one rotation, the irradiance passing through will have a maximum value of $I(0)$ when the polarizer and the polarization plane of the incident light are parallel, and will have a minimum of zero when they are placed at 90° to one another (crossed-polarization).

The same equation can be applied to the individual components of a light beam such that the total polarization of the beam may be determined. Orientation alternately at the $\theta = 0$ degree angle with respect to x (call this "parallel") will allow through only the I_x component, and at $\theta = 90$ degrees to that angle (call this "perpendicular"), will allow through only the I_y component, such that each component may be measured individually.

When applied to the CRL, these labels (parallel and perpendicular) will be in reference to the polarization state of an outgoing laser beam, to which the polarization state of the received lidar backscatter signal will be compared.

2.2.2 Polarization in scattering events

By measuring the two orthogonal polarization components of the scattered light, and comparing them to the polarization of the incident beam, one can glean some information about the shape of the scattering particle if the scattering mechanics are understood for each type of particle. These scattering mechanics are now described briefly.

Lorentz-Mie scattering theory describes an analytical solution to Maxwells equations for electromagnetic radiation scattering by spherical particles. It was first described in 1908 [51], and has been re-visited several times since in the literature (e.g. [52] and [53]). The small particle size limit of Mie theory is succinctly described by Rayleigh scattering theory. This is applicable when the wavelength of light is much larger than the particles upon which it is incident, and is preferred, when applicable, for its ease of implementation. In the large-particle regime, Rayleigh-Gans-Debye theory, or geometric optics with ray-tracing, describes things fully. In between, the more general Mie theory is required, and that will be discussed briefly here.

Mie scattering is not wavelength-dependent, and becomes somewhat simpler when only the backscattering case ($\theta = 180^\circ$) is considered. Scattering is prominent in the forward direction ($\theta = 0$). For spheres which are homogenous in terms of refractive index, such as water droplets in the atmosphere, the backscattered polarization state is identical to that of the incident light wave, so there is no change in polarization, or certainly no more than 3 to 4 % ([54] after [55]) even with multiple scattering. A full development of this theory may be found in such references as van de Hulst, subsection 4.4 [52]. For aspherical and asymmetric particles such as ice the backscattered polarization will be changed (i.e. a depolarization will be induced in the signal). For example, ice clouds can depolarize as much as 30% [54] to 80% [56]. Mixtures of ice and water produce depolarization ratios of about 10% to 20% [54].

Mueller matrix algebra will be used in Chapter 7 to describe the scattering processes

in the atmosphere. This approach is not new; it is routinely used by [57] and many others. This algebra will be explained in detail later in the thesis.

2.2.3 The Elastic Lidar Equation

The lidar equation is the single equation upon which all lidar operations are based. The lidar equation will produce a signal equation for each channel of the lidar. These will be different from each other depending on their overlap functions, their detector efficiencies, and any differences in transmission through the atmosphere for the photons associated with each detector.

The CANDAC Rayleigh-Mie-Raman lidar (CRL) depolarization measurements make use of lidar signals which have undergone Rayleigh Elastic Scattering (no change of wavelength) in the atmosphere. The Elastic Lidar Equation describes the lidar backscatter signal as measured by the lidar receiver. There is a corresponding equation for use with Raman scattering processes, but this is not relevant to the discussion in this thesis.

The Lidar Equation makes two fundamental assumptions: a) single scattering events only; and b) independent scattering only. This means that the lidar equation is not valid in regions of overly thick cloud, etc. The lidar equation takes all instrument and atmospheric parameters into account to express the received signal as a function of range from the lidar. In the case of the upward-pointing CRL, the range (r in the equations here), is the altitude z in the atmosphere. The lidar equation can be written in its simplest form (as described in [58]) as:

$$P(R) = KG(R)\beta(R)T(R) \quad (2.6)$$

where:

$P(R)$ is the power received from range R

$K = P_o \frac{c\Delta t}{2} A\eta$ describes the performance of the lidar system

$G(R) = \frac{O(R)}{R^2}$ contains the range-dependant measurement geometry

$\beta(R) = \frac{n(R)\sigma}{4\pi}$ is the backscatter coefficient at altitude z

$T(R) = e^{-2 \int_0^R \alpha(r) dr}$ is the transmission term for the atmosphere

in which:

P_o is the laser power (J)

c is the speed of light (m/s)

t is the laser pulse length (s)

A is the area of the receiver (m^2)

$\eta(R)$ is the overall receiver efficiency at range R

$O(R)$ is the overlap function for the laser beam and the receiver field of view

R is the range (m)

$n(R)$ is the number density of air at range R

σ is the scattering cross section

$\alpha(r)$ is the extinction coefficient, in which the factor of -2 in the exponent of the transmission function indicates inclusion of both the upward and downward transmission coefficients, assumed to be identical for elastic scattering when measuring the whole signal. The transmission function depends on polarization state, and has not been well studied in this regard in the lidar wavelength-regime, but is generally assumed to be unchanging as well.

From these substitutions, the lidar equation now has the following form:

$$P(R) = P_o \frac{c\Delta t}{2} A \eta \frac{O(R)}{R^2} \frac{n(R)\sigma}{4\pi} T(R) \quad (2.7)$$

or

$$P(R) = P_o \frac{c\Delta t}{2} A\eta \frac{O(R)}{R^2} \beta(R) T(R). \quad (2.8)$$

For photon counting systems, it is preferable to express the lidar equation in terms of numbers of detected photons rather than in terms of power. The received power term on the left hand side of the equation is the power received per laser pulse *which is measured*, so may be replaced by a function of energy per photon, hc/λ , at wavelength λ , number of photons received per laser pulse, $N(R)$, and the duration of the received pulse, Δt , because power is energy per unit time:

$$P(R) = \frac{N(R)(hc/\lambda)}{\Delta t} \quad (2.9)$$

Remembering that $\Delta R = \frac{c\Delta t}{2}$, because the light must travel up from the lidar to range R and back down again in time Δt ,

$$N(R) = P_o \Delta R A \eta \frac{O(R)}{R^2} \beta(R) T(R). \quad (2.10)$$

Because it will be referred to again later in Chapter 6, the lidar equation is also presented here rearranged to solve for backscatter coefficient $\beta(R)$:

$$\beta(R) = \frac{N(R)}{P_o \Delta R A \eta T(R)} \frac{R^2}{O(R)}. \quad (2.11)$$

Once profiles of photocounts as functions of altitude are determined, many derived products may be calculated: Temperature, density, and pressure of the atmosphere chief among them. The main derived product for this thesis is the depolarization parameter.

2.3 Technical context for this thesis: Depolarization lidar

The advances presented in this thesis have mainly to do with the manner in which the lidar depolarization parameter is measured and calculated. Hence, some context for these developments is presented here, beginning with the history of the field and its depolarization ratios.

2.3.1 The traditional depolarization ratio: δ

The depolarization ratio, δ , is the most traditional manner used to express the extent of depolarization. Measurements are made using two polarization-dedicated measurement channels. The depolarization ratio is calculated as the ratio of the backscatter coefficient in two polarization planes, one parallel and one perpendicular to the plane of polarization of the transmitted laser light.

2.3.1.1 Development of the equation for δ

The development begins with the following ratio of backscatter coefficients:

$$\delta = \frac{\beta_{\perp}}{\beta_{\parallel}}. \quad (2.12)$$

Substituting in from the Lidar Equation (Equation 2.11), this may be re-cast in terms of observables, i.e. the intensity or power received in each of these channels. Many of the values (such as outgoing laser power, overlap function of the telescope, etc.) cancel out as they are identical for both channels. The transmission function, $T(z)$, has been well studied in radar applications, but not at the particle size-range applicable to lidars [59]. In general, it is omitted for depolarization studies.

$$\delta = \frac{\beta_{\perp}}{\beta_{\parallel}} = \frac{\left(\frac{N_{\perp}(R)}{P_o \Delta R A \eta_{\perp} T_{\perp}(R)} \frac{R^2}{O_{\perp}(R)} \right)}{\left(\frac{N_{\parallel}(R)}{P_o \Delta R A \eta_{\parallel} T_{\parallel}(R)} \frac{R^2}{O_{\parallel}(R)} \right)} \quad (2.13)$$

$$= \frac{\left(\frac{N_{\perp}(R)}{P_o \Delta R A \eta_{\perp} T_{\perp}(R)} \frac{R^2}{O_{\perp}(R)} \right)}{\left(\frac{N_{\parallel}(R)}{P_o \Delta R A \eta_{\parallel} T_{\parallel}(R)} \frac{R^2}{O_{\parallel}(R)} \right)} \quad (2.14)$$

$$= \frac{\left(\frac{N_{\perp}}{\eta_{\perp}} \right)}{\left(\frac{N_{\parallel}}{\eta_{\parallel}} \right)} \quad (2.15)$$

$$= \frac{\eta_{\parallel}}{\eta_{\perp}} \frac{N_{\perp}}{N_{\parallel}} \quad (2.16)$$

$$= k \frac{N_{\perp}}{N_{\parallel}} \quad (2.17)$$

Any remaining effects can be rolled into one calibration constant, k , which will modulate the ratio of numbers of photon counts N counted by the PMT, which is the signal in the detector. The calibration constant indicates the ratio of the overall receiver efficiencies in each channel. It includes the quantum efficiencies of the photomultiplier tube detectors and any depolarization caused by optics in the receiver chain. For this thesis, these efficiencies will be called “Gains” regardless of whether they have a value of less than, or greater than, 1.

It is not necessary to solve the entire lidar equation (twice) to obtain the depolarization ratio. A simple ratio of two measured powers suffices when multiplied by one calibration constant.

2.3.1.2 δ in terms of light intensities

Another way to look at the depolarization ratio is in terms of the intensities of light which hit the telescope:

$$\delta = \frac{\text{Intensity of light that is polarized perpendicular when it hits the telescope}}{\text{Intensity of light that is polarized parallel when it hits the telescope}} \quad (2.18)$$

$$= \frac{I_{\perp}}{I_{\parallel}} \quad (2.19)$$

In the Parallel channel, *all* of the light which remains polarized linearly in the same plane as it was emitted by the laser when it is backscattered to the lidar ($I_{pol.}$), and *half* of the light which has become unpolarized through the backscattering process ($\frac{1}{2}I_{unpol.}$), are admitted through the analyzing polarizer (the polarotor, in the case of CRL) [60]. $I_{\parallel} = I_{pol.} + \frac{1}{2}I_{unpol.}$. This results in a signal of:

$$S_{\parallel} = G_{\parallel}(I_{pol.} + \frac{1}{2}I_{unpol.}), \quad (2.20)$$

which has been reduced by the (smaller than 1) gain of the Parallel channel's optics and photomultiplier tube.

In the Perpendicular channel, only *half* of the light which has become unpolarized through the backscattering process ($\frac{1}{2}I_{unpol.}$), is admitted, and *none* of the polarized light [60]. $I_{\perp} = \frac{1}{2}I_{unpol.}$. This results in a signal of:

$$S_{\perp} = G_{\perp}(\frac{1}{2}I_{unpol.}), \quad (2.21)$$

which has been multiplied by the (smaller than 1) gain of the Perpendicular channel's optics and photomultiplier tube.

The equations for traditional depolarization ratios δ are thus:

$$\delta = \frac{I_{\perp}}{I_{\parallel}} = \frac{\frac{1}{2}I_{unpol.}}{I_{pol.} + I_{unpol.}} = \frac{\frac{S_{\perp}}{G_{\perp}}}{\frac{S_{\parallel}}{G_{\parallel}}} = \frac{G_{\parallel}}{G_{\perp}} \frac{S_{\perp}}{S_{\parallel}}. \quad (2.22)$$

Again allowing $k = \frac{G_{\parallel}}{G_{\perp}}$ as a calibration constant, the following is the equation used in practice to calculate the depolarization ratio:

$$\delta = k \frac{S_{\perp}}{S_{\parallel}}, \quad (2.23)$$

which makes sense because the signal measured in a PMT is the number of photons that it counts.

2.3.2 Early depolarization ratio measurements

Depolarization-capable lidars have now been in operation for more than 40 years. The advent of the laser allowed lidar depolarization measurements, which were attempted with searchlight beams in the 1930s, to really begin in earnest [61]. One of the first of these was used by Schotland et al. in 1971 [62] to measure several types of clouds above the United States. They report publications on the subject from similar time periods by [63] and [64].

The general technique used then remains the same today, and is the technique described in Section 2.3.1.1: Compare the number of photons which are backscattered with polarization properties similar to those of the laser to the number of backscattered photons whose polarization is now oriented orthogonally to that of the laser.

In principle, in an atmosphere with no particles, or with only spherical water droplets, most light will return with its polarization unchanged. In the case of nonspherical particles which have corners, much of the laser light will have been depolarized, and the signal in the orthogonal polarization plane will increase. Thus, the ratio δ is small (near zero) for spheres, and large (nearer to 1) for nonspheres.

Total depolarization ratios are used in this thesis. The full contribution to the depolarization of the laser beam comes from: molecular depolarization (less than 1%), aerosol depolarization (larger in regions where aerosols are present), and the depolarization from hydrometeors in the clouds. Some studies attempt to isolate these values. This is not required for the CRL. The reason is that, as shown in [64] and explained in [62], the volume cross section of the molecular atmosphere is many times smaller than that of any cloud. Since CRL is interested in clouds, the molecular contribution does not matter appreciably in the regions of interest.

2.3.3 Depolarization lidar configurations

Since the first depolarization lidars, various configurations of equipment have been tried in order to obtain the two signals required for the measurement. Several are described here.

One detector, rotating polarizer

Schotland et al. [62] used a linear sheet polarizer on a rotatable mount, installed directly in front of the detector. Measurements were made with the polarizer first in the “parallel” position, and then in the “cross polarized” position. Because there is but one PMT in such a system, many of the factors which contribute to the calibration constant cancel out. For example, the PMT for the parallel measurements is the same PMT used for the perpendicular. Therefore, its efficiency will not influence the depolarization ratio.

The CRL lidar, which is the subject of this thesis, uses a similar system, albeit with a prism polarizer and operating at a much higher repetition rate than was possible with the ruby laser of the Schotland system.

Another setup for using a single PMT to measure both parallel and perpendicular returns is to use a polarizing beamsplitter to divide the light, and use mirrors to provide optical paths for each of these polarized beams to reach the PMT, with a final mirror on a motorized mount blocking one or the other at any given time [65]. This reduces the PMT-specific calibrations, but requires extra optics for one measurement channel versus the other, which will induce different calibration effects.

Two detectors

A conceptually simpler setup uses two detectors and requires no moving parts. Indeed, many depolarization lidar groups make use of this configuration. A polarization beamsplitter splits the returned beam of backscattered laser light into two separate paths, each with their own photomultiplier tube. One path allows light polarized parallel to the emitted

laser beam, and the other path allows light polarized in the perpendicular plane. Testing is carried out during setup to ensure that the beamsplitter is oriented truly parallel to the polarization of the transmitted laser beam. In this configuration, measurements are made simultaneously in both channels. The tradeoff is that the calibration will include PMT efficiencies, as the PMTs for each channel may have different properties.

To aid with the calibration, some two-detector systems have a built in capability to rotate the entire set of detectors on its axis; that is, to force the detectors to trade places with each other, to examine the biases between the channels [66].

Three measurement channels

As early as 1973, Pal and Carswell [67] were using a three-channel receiver for depolarization measurements. Each channel had its own polarizer which could be aligned with any of the parallel, the perpendicular, and the 45° angles. The orientations could be repeatedly changed by hand. This led to more calibration and measurement possibilities than are available for a two channel system in which nothing moves.

A different application which uses three channels is described by Reichardt et al. at the RAMSES lidar in Germany [68]. There, a parallel, a perpendicular, and an unpolarized channel are all available in the same UV wavelengths. This system is interested in normalizing all of the lidar signals to a known value at some altitude in the atmosphere. This three-channel system allows better access to such a normalization value.

Biele et al. [69] use two beamsplitters, and work in terms of “polarized backscatter ratios”, which are the Rayleigh plus aerosol contributions to backscatter coefficient, divided by the Rayleigh backscatter coefficient. These authors also include the concept of a total backscatter coefficient being the sum of the parallel and perpendicular backscatter coefficients. The lidar is described in [70], and uses one or two polarizers (depending on the year) to separate the light into s-polarized and p-polarized beams, but does not have any polarization-independent Visible Rayleigh Elastic channel.

The new technique developed in this thesis for the CRL also uses three channels: Parallel, perpendicular, and unpolarized. However, the calibrations made are quite different to those in [68], as described in Chapter 9. Ultimately, the CRL uses the parallel and perpendicular channels together to create a calibration constant which can be used with the Rayleigh Elastic channel to make improved depolarization measurements.

2.3.4 Calibrations

Whatever the physical setup of the depolarization lidar, calibration measurements are required in order to determine k which is used in the equation for depolarization ratio. Calibrations generally involve putting light of a known polarization state into the receiver, and determining the biases in each channel either relative to an absolute value, or relative to each other.

White light calibrations involve shining unpolarized light into the detector chain. In this case, both polarization channels should measure identical values. In practice, they will not, and this discrepancy determines the calibration factor for the system. As most systems are designed specifically for depolarization measurements, and use separate PMTs for each channel, the major contribution to the calibration factor is simply the difference in gains of the different PMTs. The calibration factors for single-PMT systems are dominated by the effects of optics upstream of the polarizer within the receiver.

Frequently, the “clear, aerosol-free” sky is used as a “known” depolarization value. Measurements are normalized to this known value at a particular altitude, and calculations proceed from there. There are a host of problems with this, chief among them being that it is difficult to accurately know this normalization value. This can be helpful if there is a desire to separate the effects of molecular from aerosol depolarization, but this is not the case for CRL.

2.3.4.1 Careful design reducing calibration

David et al. [71] took great care with each optic when designing their aerosol depolarization lidar for use at visible and UV wavelengths. Optics were selected such that the instrument transfer matrix would be diagonal.

Hayman and Thayer [72] performed calibration measurements on a circularly polarized micropulse lidar to determine the retardance and depolarization contributions of the instrument optics. This was done by transmitting four polarizations with the laser beam. Optics were then added to the system to compensate for the large retardance effects, leaving smaller quantities to be calibrated out in software.

Where CRL calibrates out instrument effects after the fact, these lidars prevent the effects in the first place. Because for CRL the depolarization channel was added in after the rest of the lidar had been in operation for many years, the proactive approach to preventing large calibration values is not possible for the CRL.

David et al. has also followed the work of Alvarez [73] in accounting for misalignment in angle between the laser beam polarization and the analyzing polarizers in the receiver. Sassen et al., too, take care of imprecise alignment of the detector by including a subtractive calibration term to their equation for δ in addition to k [74].

2.3.5 Interpretation of depolarization ratio δ measurements

Having well calibrated depolarization ratios mean that measurements from one laboratory can be compared with those from another laboratory, either elsewhere on Earth, or on an aircraft or satellite. What is not so easy to determine is what exactly the depolarization ratios *mean*, by themselves, in an absolute sense. Using them as a relative measure (A is icier than B) is safer, and safer still is using them with other measurements to provide some boundary conditions on the atmosphere. This was apparent by 1991 in the community [75].

In a diffuse scattering medium, the depolarization ratio, δ , is expected to range between:

- $\delta = 0$ for all the laser light remaining linearly polarized in the parallel direction. No perpendicular photons hit the telescope; interpreted as clear sky or spherical atmospheric particles (i.e. liquid water droplets).
- $\delta = 1$ for all the laser light having been depolarized; equal numbers of parallel and perpendicular photons hit the telescope; interpreted as non-spherical atmospheric particles (i.e. ice or aerosols).

There is lack of consensus in the field regarding the cutoff values for when cloud particles are considered to be frozen or not, probably because there is not a very good general rule for all situations, but almost every lidar group has some convention for their data. In-
tieri et al. in 2002 uses $\delta = 0.11$ as the cutoff between water droplets (low depolarization) and ice particles (high depolarization) at the DABUL lidar during the SHEBA project [76]. Sassen 1977 [77] found that despite some complications discussed below, most snowfall typically has values of approximately $\delta = 0.5$. A 1991 review article by Sassen [75] summarizes a few typical values. In snowfall and most cloud: $\delta = 0.2$ to 0.8 , but mostly closer to 0.4 or 0.5 . Sassen reports some ice clouds with depolarization ratios as low as 0.03 , while others exceeding all expected values at $\delta > 1$. The icy low values are easily confused with supercooled water droplets. Sassen advises examining quick changes in depolarization ratio with altitude for clues as to the particle phases within the cloud.

Intermediate values of δ indicate mixtures of particle phases and composition, and particles whose shape is somewhat between that of a sphere and a fully-depolarizing non-sphere. There is great ambiguity in the microphysical cloud results when examining lidar depolarization ratios by themselves. Either cloud ice particles, or aerosols, or multiple scattering, may be the cause of depolarization of the lidar beam, one must take care not to misinterpret the depolarization ratio measurements, nor to draw conclusions about the state of the atmosphere with no other context. Such context can take the form of backscatter coefficient plots to examine cloud and aerosol layer morphology, radar measurements, etc.

2.3.5.1 The shape of nonspheres, and their sizes

A limitation to the depolarization lidar approach is that it is currently impossible to classify solid particle shape based solely on depolarization measurements [62]. In 1995, Mishchenko and Hovenier attempted to theoretically derive and validate numerically general relationships for the elements of the backscattering matrix and the linear depolarization ratio for non-spherical particles in random orientation. They conclude, after extensive calculations, that although depolarization is a good indicator of particle nonsphericity, it is not a universal measure of the degree to which a particle is non-spherical, nor does it indicate particle size.

Calculations showed the possibility of maximum depolarization at both large and small particle sizes. This is contrary to assumptions made early-on in the field of polarization lidar, when the then-few measurements available seemed to point to an ability to use the depolarization ratio to classify particles into three groups according to shape (platelike, columnlike, and irregular). This work was begun by Sassen in 1977 [77] and furthered in studies by Noel et al. in 2001 [78], comparing measurements with the results of ray-tracing simulations. In 2004, Noel et al. [79] specified the following groupings of depolarization ratio values: 1) $\delta < 0.25$: spheres and thin, oriented plates; 2) $\delta > 0.5$: Columns; 3) $0.25 < \delta < 0.5$: irregular shapes.

Sassen has pointed out that depolarization increases as particles are very small [80]. This group also takes known behaviour of ice crystal growth as a function of temperature and humidity into account, and pull in other measurements to combine them with depolarization data.

Lab measurements are a vital piece of the depolarization ratio puzzle. These take known samples and measure the depolarization ratios. Sakai et al. have measured the following in their laboratory chamber: $\delta = 0.39$ for Saharan minerals larger than one micron, $\delta = 0.14$ to 0.17 for those smaller, $\delta = 0.08$ for sea salt particles, $\delta = 0.004$ for ammonium sulfate, and $\delta = 0.01$ for liquid droplets containing ammonium sulfate or sea salt [81]. To make

direct use of these values one would need to constrain numerous other variables in the atmospheric system in question.

2.3.5.2 More ambiguous cases and a few solutions

A good solution to many depolarization lidar problems is to make the measurements together with radar, lidar extinction, temperature, observational and as many other instruments as possible. In the company of these other tools, the depolarization lidar can be the tool which does what was hoped it could do alone, originally: Differentiate ice from water

Multiple scattering is one of the largest complications in depolarization lidar. This has been investigated via ray tracing code by Noel et al., but in a rather limited fashion: Only hexagonal particles are considered, particle size cannot be taken into account, all particles were assumed to be randomly oriented, and in cases for which the depolarization ratio was low, only those for which the temperature unambiguously indicated ice phase were kept in the simulation [82]. Keeping the field of view of the lidar very small is one method for combatting multiple scattering. Another is to observe only events which do not involve any optically thick clouds.

Complications to the depolarization approach to phase determination arise when solid particles are oriented with their flat faces perpendicular to the incoming radiation such that they produce specular reflection rather than Mie scattering (therefore no polarization change) and can be confused with spherical droplets [59]. This is only a problem for a zenith-oriented lidar. Recent advances in hardware have led to an ability to deal with these issues by tilting the lidar off-zenith (even by as little as 2.5° [59]), by rotating the direction of polarization of the laser beam or the receiver by 45° .

Hayman et al. [83] present two cases in which an off-zenith lidar pointing was beneficial: flattened falling raindrops, and an ice cloud. Both situations presented preferentially-oriented particles which would have provided ambiguous results with a zenith-pointing lidar, but which could be understood with the lidar tilted off-zenith.

A group at the Colorado Center for Astrodynamics Research, operating lidars at Summit, Greenland, uses a full Mueller matrix approach to measurement. The CAPABL lidar measures not only depolarization, but also diattenuation, retardance, and cross-talk [84]. The CRL instead makes use of the Mueller matrix idea not for increased kinds of measurements, but for an improved calibration procedure for the lidar.

The NCAR group has done significant work measuring all Mueller matrix elements of the sky (all elements of the volume backscatter phase matrix) [83], following the work of Kaul [85]. Working with circular polarization, a single quarter wave plate is used to rotate the polarization of both the transmitted and the received beams.

The Arctic Lidar Observatory for Middle Atmosphere Research (ALOMAR) in Norway avoids the problem during the Cooperative ALOMAR Bistatic Lidar Experiment (CABLE) by viewing the vertical ALOMAR lidar beam not from the ALOMAR lidar receiver itself, but from a separate receiver 2 km away [61]. This distant receiver was able to scan through different viewing angles and thus 1) reduce the ambiguities in the measurements which are present for a zenith-looking monostatic lidar with its 180° scattering geometry, and 2) gain information regarding particle shape and orientation.

2.3.5.3 Something to be aware of when coadding

One thing to be aware of, which is helpfully pointed out by Sassen and Benson [74] is that one must be very careful about the lengths of time over which depolarization measurements are coadded. The average value of a measurement might lead one to infer particles each with depolarization-ratio-inducing values of some intermediate value. However, the truth might be a bimodal distribution, particularly with pockets of oriented planar crystals.

2.3.6 Using d instead of δ

There is a growing convention of expressing depolarization measurements as depolarization parameter d rather than depolarization ratio δ . The two quantities are directly related to one

another. This shift is lead by Flynn (“ d is related to propensity of the scattering medium to preserve incident polarization”) [86] and Gimmestad (“ d ... which is a more physically meaningful and interesting quantity”) [60], and is also used extensively by Hayman et al. (“... the fraction of light no longer polarized after the scattering process is given the symbol d ”) [72].

The CRL calculations here follow Gimmestad’s lead in this regard.

Gimmestad (2008) has a good approach to calculating the depolarization properties of the atmosphere using backscatter lidar. Gimmestad defines d to mean “The fraction of the received light that has become unpolarized by the scattering process”:

$$d = \frac{I_{unpol}}{I_{pol} + I_{unpol}}. \quad (2.24)$$

This depolarization factor d can range between:

- $d = 0$ for all the laser light remaining linearly polarized in the parallel direction. No perpendicular photons hit the telescope; interpreted as clear sky or spherical atmospheric particles (i.e. liquid water droplets).
- $d = 1$ for all the laser light having been depolarized; equal numbers of parallel and perpendicular photons hit the telescope; interpreted as non-spherical atmospheric particles (i.e. ice or aerosols).

Intermediate values of d indicate mixtures of ice/aerosol and liquid particles. One major difference sets apart the depolarization ratio and the depolarization parameter: The depolarization parameter d is “linear in the quantity of interest”. As stated by Gimmestad (2008), it is “a measure of the propensity of the scattering medium to depolarize the incident polarization”. This parameter is related to physical processes in the atmosphere, and is thus a more desirable target for our studies than the legacy ratio δ . It is easier to understand plots of d as each “percent” is equal in magnitude (in terms of how much the atmosphere depolarized the laser light) to each other “percent”.

As before, it is necessary to express d in terms of observable signals. As given in [60], the depolarization parameter d is calculated assuming that the only instrument effect is a constant difference ratio in detector gains (just as before, for δ).

Conveniently, d and δ are related by a simple equation. Depending on which is the quantity of interest, one can link them in terms of the unpolarized fraction of light (d), or of the remaining-polarized fraction of light ($1 - d$):

$$d = \frac{2\delta}{1 + \delta} \quad (2.25) \quad 1 - d = \frac{1 - \delta}{1 + \delta} \quad (2.26)$$

Equation 2.25 on the left is given in the same format as the depolarization factor equation given by Van de Hulst ([52], page 81).

Taking a calibration factor k into account, this becomes:

$$d = \frac{2k \frac{S_{\perp}}{S_{\parallel}}}{1 + k \frac{S_{\perp}}{S_{\parallel}}}. \quad (2.27)$$

Every caveat which exists for δ exists for d , too. Complementary measurements are still required for best practice.

2.3.7 The scope of this thesis

Where the CRL differs from many depolarization lidars is that it was not built with depolarization as a priority data product. It operated first for a number of years with no depolarization channel at all. It was the work of this thesis to add the depolarization channel to the lidar, and to get it operating correctly. Essentially, the CRL has been retrofit to allow such measurements. Many other non-depolarization-capable lidars exist around the world, and it was worth putting some thought into the complications to calibration or analysis which may come up when retrofitting existing lidars. This may allow the addition of some depolarization measurements without compromising the continuity of measurements

made with other channels. Much of the mathematical development in Chapter 7 is done in this regard.

Finally, the work in this thesis has opened the possibility of using a single polarized channel in concert with an unpolarized channel to make depolarization measurements. While still calibrated using a second polarization channel for the purposes of this thesis, methods to calibrate using externally polarized calibration light are possible, and are discussed. It is hoped that this will be helpful in developing future upgrades for systems in which installing two additional polarization channels, or polarization channels with moving parts, is unfeasible.

The CRL's new depolarization channel does not solve any of the problems with the interpretation of d or δ which are mentioned in the previous section. Instead, it makes d measurements as good as those which exist elsewhere. Located at Eureka, it is also in very good company, with the suite of numerous colocated instruments, many of which can operate in polar night along with the lidar.

Chapter 3

The CRL Lidar at Eureka

The Canadian Network for the Detection of Atmospheric Change (CANDAC) Raylie-Mie-Raman Lidar (CRL) was installed during 2008/2009 at Eureka, Nunavut, Canada ($79^{\circ}59'$ N, $85^{\circ}56'$ degrees W, Figure 3.1). This versatile lidar is installed at the Zero Altitude Polar Environment Atmospheric Research Laboratory (PEARL) Auxiliary Laboratory (ØPAL), whose elevation of 10 m above sea level facilitates measurements from as close to sea level as reasonably possible, allowing measurements of the lower portions of the troposphere.

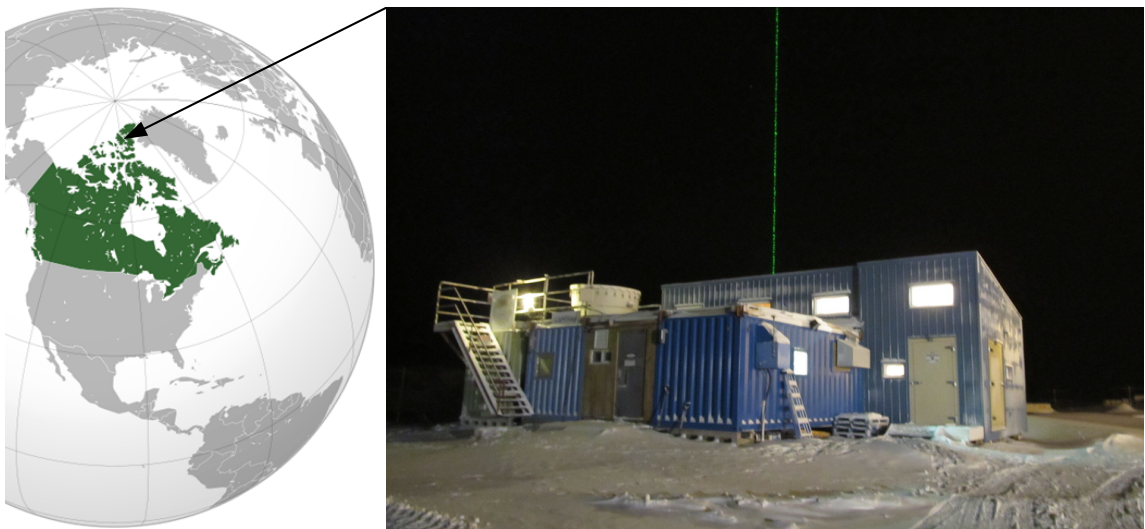


Figure 3.1: Location of Eureka in the Canadian High Arctic on Ellesmere Island [1], and a photograph of the CRL in operation at the ØPAL laboratory during polar night.

The CRL consists of a two-laser transmitter, a telescope receiver and associated photomultipliers, and counting electronics, the latter held in a multi-channel free-space polychromator. The combination of the ultraviolet and visible wavelength lasers allows measurements of backscatter and extinction coefficient profiles, tropospheric temperature, stratospheric temperature, and profiles of extinction and water vapour mixing ratio. The remote location of the CRL at Eureka prompted the design to be fully remotely operable by an operator off-site. Keeping an operator on-site for long-term data acquisition would be prohibitively expensive, and the system was designed to be fully operable over a low-bandwidth satellite data link. Upgrades are underway to move the lidar to fully autonomous operations.

A depolarization channel installed in the CRL in 2010 allows profiles of the linear depolarization ratio to be measured. The installation of hardware for this channel, and the resulting measurements, form the focus of this thesis.

3.1 The Lab

The CRL is housed in a 20-foot modified shipping container. An optical table holds the lasers, transmitter optics, and the polychromator. The telescope mirror is suspended through a hole at one end of the table below a borofloat window with a laser-quality anti-reflection insert at the centre to allow the transmission of the outgoing laser beam to the sky. The 1.5 metre tall cube atop the container blocks some sunlight from entering the receiver and opens to the sky through a motorized roof hatch (see Figure 3.2). An electronics rack and shelving forms a room divider with a small office area at the end. Everything from the lasers to the hatch is remotely operable. Full details of the CRL are described in Nott et al. 2012 [2]. A schematic diagram of the lidar, after [2], is given in Figure 3.3.



Figure 3.2: CRL lidar container with roof hatch open

3.2 Transmitter

The CRL transmitter contains two lasers, one operating in the visible and the other in the UV. Both are Continuum Surelite III-10s with a fundamental frequency of 1064 nm and with a repetition rate of 10 Hz. One laser is frequency doubled to 532nm (visible) and the other is frequency tripled to 355 nm (UV). The visible laser is sometimes seeded with a temperature-stabilized fiber laser to ensure stable, precise Raman temperature measurements. Because the CRL is operated in the Arctic, it was important to choose lasers with low power consumption and no external water cooling. The Surelite III-10s consume only 2.1 kW each while producing ample power in both the visible (380 mJ/pulse) and the UV (240 mJ/pulse). The lasers are coaligned, then directed through a x6 beam expander and three folding mirrors which direct the beams to the sky, aligned to the telescope's field of view. The final folding mirror has computer-controlled actuators for beam steering.

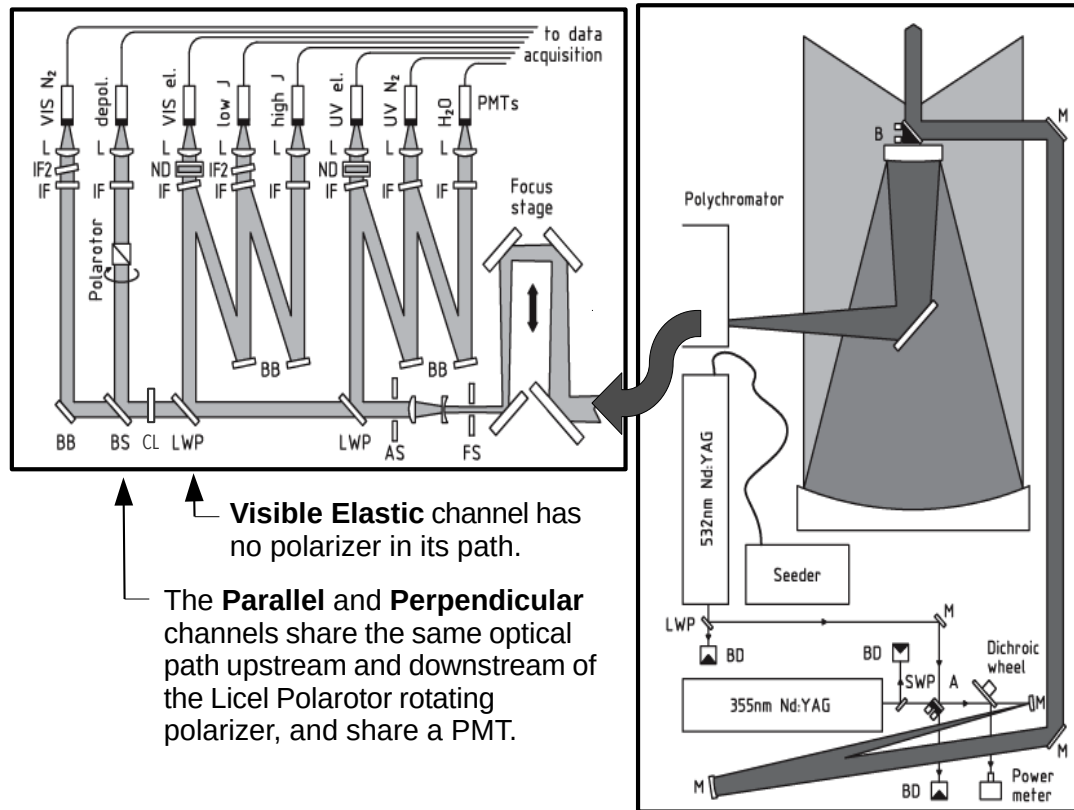


Figure 3.3: Schematic of the CRL lidar including transmitter and receiver modified from [2]. The light from two lasers is combined and directed to the sky. Backscattered lidar returns are collected in the telescope and are focused into the polychromator. Within the polychromator, the light is sorted by wavelength and measured by eight photomultiplier tube detectors (PMTs), in nine measurement channels. Detection channels of particular note for this thesis are the Visible Rayleigh Elastic channel (“VIS el.” in the figure), and the two depolarization channels, Parallel and Perpendicular (“depol.” in the figure, sharing a photomultiplier tube).

3.3 Receiver

The CRL receiver consists of a telescope, a polychromator, and associated data acquisition electronics.

Telescope

The custom 1-m diameter Dall-Kirkham telescope was made by Optical Structures Inc (Rancho Cordova CA, USA) and is installed in a cut-out of the optical table at one end of the lab. Light from this telescope is directed by a tertiary mirror into the polychromator in which all other receiver optics and detectors are contained.

Polychromator

The computer-controlled polychromator is illustrated in Figure 3.3 and was built by Spectral Applied Research (Richmond Hill, ON, Canada). It contains eight photomultiplier tube (PMT) detectors, each with its own interference filter and focusing lens. Long wave pass filters are used to separate the light from the telescope by wavelength. Three detectors are dedicated to channels in the UV (354.7 nm, 386.7 nm and 407.6 nm), and five detectors are dedicated to six measurement channels in the Visible (528.8 nm, 531.2 nm, 532.1 nm Rayleigh Elastic, 532.1 nm depolarization, and 607.5 nm). The 532.1 nm depolarization detector measures light in two planes of polarization on alternate laser shots. In this way, one PMT is the basis of two measurement channels: Parallel, and Perpendicular. Technically, of course, the 532.1 nm depolarization measurements in the parallel and perpendicular channels are both visible Rayleigh Elastic measurements as well, but when a “Rayleigh Elastic” or “Visible Rayleigh Elastic” channel is mentioned in this thesis, it is the 532.1 nm channel *without any polarizer* which is meant. The others will always be specified with either “depolarization”, “parallel”, or “perpendicular”, to keep them straight.

The light is not evenly distributed between the channels in the polychromator. Some channels are afforded a much larger portion of the telescope's beam than others. Particularly important to note is that the Visible Rayleigh Elastic channel obtains approximately 97 percent of all 532 nm light entering the polychromator. When the lidar was designed, there was no depolarization channel, or indeed any other green-light channel, downstream of the Visible Rayleigh Elastic. Thus, at the time, it was sensible to direct as much light as possible into that PMT. With the depolarization channel now installed downstream of the visible long wave pass filter, the depolarization pellicle beamsplitter receives a little less than 3 percent of the telescope's light. Only 60 percent of that remaining light is reflected up toward the polarotor and the depolarization channel's detectors. Further details regarding the depolarization channel and its installation are described in Chapter 4.

The lidar is designed to run during both day and night, so some channels have one set of filters for nighttime, and narrowband filters for daytime observation. The filters are switched in spring and fall. Seven of the eight PMTs are model Hamamatsu R7400-03. The other (607.5 nm) requires the extended response Hamamatsu R7400-20.

Counting Electronics

The Raman channels require pure photon counting modules. As these channels are not required for depolarization analysis, they will be discussed no further here.

In the Elastic channels, Licel combined analogue and photon counting transient recorders (model TR20-160) are used for data acquisition. The transient recorder sampling rate of 20 MHz gives a vertical measurement resolution of 7.5 m. The simultaneous photon counting and analogue measurements for each photomultiplier tube extend the dynamic range over which the PMT responds linearly.

Photon counting (PC): The photon counting method is very sensitive, counts individual photons as they hit the PMT, and is accurate and responds linearly for low signal levels such as those from high altitudes. At higher signal levels, common from clouds and from

low altitudes, it responds nonlinearly and becomes saturated.

Analogue (ANA): The analogue method is valid at low signal levels, but is less sensitive and more uncertain than the photon counting method is at these signal levels. It responds linearly at higher signal levels than the photon counting mode is able to reach.

To make a full profile of lidar returns with altitude, post-processing of the data is required to “glue” or “merge” these two types of data together. This procedure is critical for depolarization measurements at the CRL, and is discussed in Section 5.7.

3.4 Measurement “channels” used in this thesis

The word “channel” is used to mean several somewhat different things. Depending on context, it could mean: a) a hardware channel [numbers i and ii in the figure and detailed list of channels below], b) a raw measurement channel [iii through viii], or c) a glued measurement profile channel [ix through xi]. As a result, there are either two, three, or six “channels” involved in depolarization calculations depending on how one counts. These are specified in Figure 3.4 and further details are provided below.

Hardware channels

There are two hardware channels. Each specifies a particular beam path through the lidar receiver to a specific PMT. Each hardware channel makes measurements for more than one raw measurement channel.

[i] Visible Rayleigh Elastic channel (measures [iii and iv])

[ii] Depolarization channel (measures [v, vi, vii, and viii])

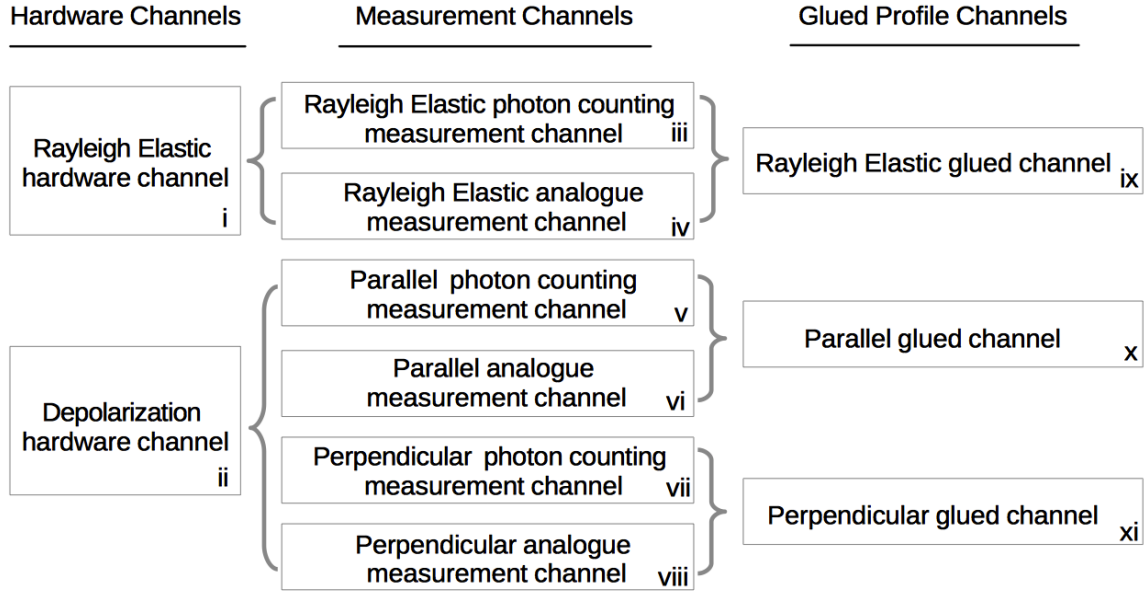


Figure 3.4: Visual representation of the manner in which all lidar channels involved in depolarization parameter calculations relate to one another. Each hardware channel makes measurements in several measurement channels. Pairs of measurement channels are combined to create the glued profile channels.

Raw measurement channels

There are six raw measurement channels. There is a single data profile of either photon counts or analogue signal as a function of altitude bin for each of these six measurement channels, every minute. Two or more raw measurement channels' data are collected by a single PMT in one hardware channel.

[iii] Visible Rayleigh Elastic photon counting measurements

(measured by [i], glued into [ix])

[iv] Visible Rayleigh Elastic analogue measurements

(measured by [i], glued into [ix])

[v] Parallel depolarization photon counting measurements

(measured by [ii], glued into [x])

[vi] Parallel depolarization analogue measurements

(measured by [ii], glued into [x])

[vii] Perpendicular depolarization photon counting measurements

(measured by [ii], glued into [xi])

[viii] Perpendicular depolarization analogue measurements

(measured by [ii], glued into [xi])

Pairs of measurement channels' data are used to create glued measurement profile channels (described below).

Glued channels

There are three glued measurement profile channels. Pairs of raw measurement channel measurements are glued together to create the three glued profiles of backscatter signal as functions of altitude. These glued profiles are those used to calculate interpreted data products (depolarization parameter, in the case of this thesis) from the lowest to the highest altitudes for CRL.

[ix] Visible Rayleigh Elastic glued profiles (combining [iii and iv])

[x] Parallel glued profiles (combining [v and vi])

[xi] Perpendicular glued profiles (combining [vii and viii])

Specifications will be made in situations for which the intended meaning of “channel” is not clear. It is hoped that this small summary will help sort out any ambiguities later in the document.

3.5 CRL operations

The CRL is able to operate nearly continuously at all hours of the day, throughout the year. Remote operators can operate the CRL instrument from anywhere with an internet connection, provided that there is at least one instrument safety person onsite at Eureka. There are safety overrides available to the on-site safety person, so that the lidar may be

shut down locally if required. The on-site personnel is usually provided by CANDAC, and divides their time supporting research groups who are operating in excess of 30 atmospheric remote sensing instruments at Eureka.

The lidar may be operated semi-autonomously. The remote operator must check the weather, start up the lasers and receiver systems, and begin data collection. If a sky alignment is required, the operator must do this as well, which requires less than one hour. Once the lidar is operating, there are automatic computerized checks in place to ensure that measurements are being duly acquired and to ensure that the weather has not worsened to the point that the lidar must close. If the lidar operations software determines that there is a problem, the remote operator is notified. The remote operator can then rectify the problem by closing the lidar, restarting the data acquisition, etc, as required. If there is no response from the remote operator (perhaps due to a dropped internet connection) within a predetermined time, the operations software carries out an automatic shutdown procedure, notifying the remote operator that this is taking place. The remote operator can, at any time, check on any of the procedures taking place at the lidar.

Twice per day the remote operator manages the saved measurement files. Handover procedures from one remote operator to another are smooth and allow the lidar to continue operations throughout.

The lidar may of course also be operated locally from within the CRL's container. More recently during the work of this thesis, techniques were developed to operate the CRL "remotely" from locations elsewhere in Eureka. This requires use of the CANDAC network within Eureka, and thus a few modifications were required for it to work correctly. It allows lidar personnel to operate and supervise CRL operations via computer while physically being in another laboratory on site, helping with other CANDAC projects. This is a great help to personnel resource management.

In order for major hardware upgrades or detailed hardware-intensive calibrations to be made at the lidar, a CRL-specific operator travels to Eureka to carry out the work. Fre-

quently, upgrades are made in tandem between one on-site CRL person at Eureka, and a second (or more) CRL person working remotely in a support capacity from a university in Southern Canada. Recently, the remote personnel have been located at Dalhousie University (Halifax, NS) and at the University of Western Ontario (London, ON).

The installation and calibration of the depolarization detection systems at Eureka required several trips. Many tasks needed only to be completed once. Others can be repeated remotely now that they are set up, and others still, such as certain calibrations (e.g. one-metre-diameter optics being placed above the telescope), will need to be repeated when personnel are available at Eureka.

With appropriate personnel support, extensive use of the CRL for all types of measurement will continue in upcoming years.

Chapter 4

Installation of the CRL lidar depolarization channel

The work of this thesis includes the installation, testing, calibration, and characterization of the CRL lidar depolarization channel. For this reason, the description of its installation is located in its own chapter here rather than being included in Chapter 3.

The depolarization channel of CANDAC Rayleigh-Mie-Raman Lidar (CRL) allows measurements of cloud particle phase. The lidar was built without this capability in 2008, but the plans to add it existed from the beginning. The original idea was to install the depolarization channel on a separate telescope. Instead, in 2010, the depolarization channel hardware was installed within the polychromator with all of the other lidar channels.

The depolarization channel is slightly different from all the others. It uses a Licel polarotor (blue anodized unit on the top of the polychromator, seen in Figure 4.1.) to permit lidar returns in two orthogonal polarization planes to be measured by a single detector.

During installation, the main goal was not to impact any of the well-calibrated measurements in the other pre-existing lidar channels. No optics for the other channels were changed or removed during the installation of the depolarization channel. Although this would have been helpful for depolarization measurements, it might have compromised

other channels. It should be understood that getting the depolarization channel running at all was of lower priority than keeping existing channels operating nominally.

4.1 Situation of depolarization channel within the CRL

During manufacture, the polychromator had several spare 2" holes included in the top for potential expansion of the lidar by the addition of new lidar channels. The depolarization channel takes advantage of one of these spare locations between the Visible Rayleigh Elastic channel and the red 607 nm Nitrogen channel. A diagram illustrates the location of the pickoff pellicle optic for the depolarization channel in relation to these two other channels (Figure 4.1).

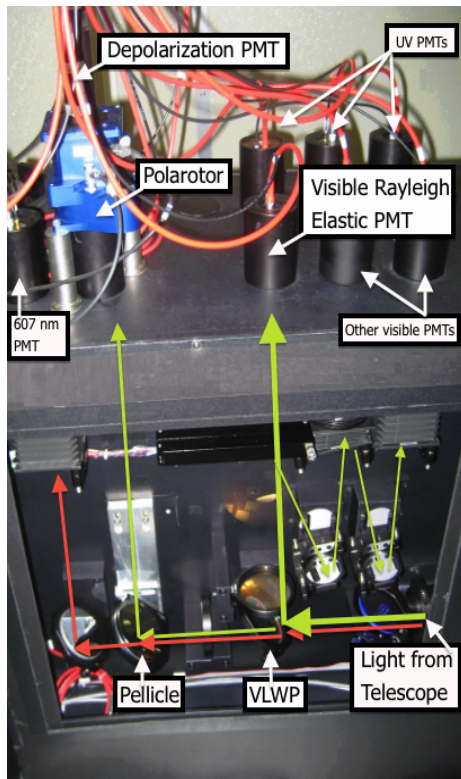


Figure 4.1: The 50/50 pellicle beamsplitter is visible below the blue anodized polarotor in the depolarization channel. It lies between the visible long wave pass (VLWP) filter leading to the Rayleigh Elastic channel (on the right), and the mirror leading to the 607 nm Nitrogen channel (on the left). The other visible wavelength channels are also seen at the right of the photograph. The optics for the ultraviolet channels are located on the other side of the back wall in this photograph, and are not seen in this image.

While the spare location chosen for the depolarization channel is good as it is on the visible-light side of the polychromator, it suffers from being “downstream” of many optics. The Chroma 580DCLP visible Long Wave Pass (VLWP) filter was chosen specifically to

reflect as much 532 nm light upward into the Visible Rayleigh Elastic channel as possible. Part of this light is used in two subsequent visible channels, the 531.2 nm and the 528.7 nm. This was achieved with a VLWP surface reflectivity at 532 nm of approximately 97 percent. The depolarization channel located farther downstream to the left of the VLWP makes do with the small amount of residual green light which is transmitted through the long wave pass filter on its way to the 607 nm channel.

The residual green light has to be directed upward into the depolarization channel using a partially reflective optic between the VLWP and the 607 nm channel. The 607 nm channel optics were already well-aligned and characterized at the time of depolarization installation. Therefore, a regular plate beamsplitter or dichroic mirror could not be used to pick off the green light for the depolarization channel; this would have translated the transmitted 607 nm light too much, and the downstream channel would have had to be realigned. A pellicle beamsplitter was selected to reflect light into the depolarization channel, as this provides the smallest amount of translation possible to the transmitted beam.

From the pellicle beamsplitter, the light travels upward and into the polarotor. The polarotor is mounted atop the polychromator. It sits on a 2" diameter 3" high beamtube and is bolted to support posts. On top of the polarotor, there is a 1" diameter 1" tall beamtube containing an interference filter (Section 4.5), then a 1" diameter 2" tall beamtube containing a 75 mm focusing planoconvex lens. Next, there is an adjustable focusing tube in which the PMT is seated, which allows the active area photomultiplier tube to be positioned at an appropriate distance from the focusing lens. See Figure 4.2 for a photograph of the polarotor in place in the lab.

The reason for placing the polarotor at such height above the polychromator has to do with the geometry of the light beam leading into it. The diameter of the light beam traversing the polychromator is slightly larger than 2" and, thanks to a collimating lens just upstream of the pellicle, is slightly converging. The polarotor has an acceptance diameter of only 20 mm, and an acceptance angle of 15° . Were the polarotor placed directly above the

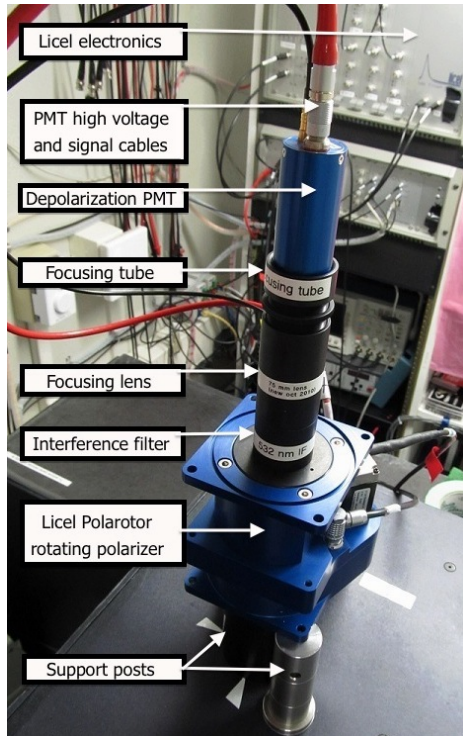


Figure 4.2: Polarotor (large blue anodized object at the bottom of the stack) and its associated beamtube optics and photomultiplier tube (small blue cylinder at the top) installed in its current position on top of the polychromator. The electronics rack is visible in the background.

pellicle beamsplitter, most of the light would be missed. A set of focusing and collimating optics could be used to narrow the light beam, but this is not necessary. By placing the polarotor a sufficient distance from the pellicle, the entire beam is accepted by the polarotor without the need for extra optics in between. It is also convenient to have the cables from the polarotor to the electronics rack be accessible without the need to open the polychromator.

4.2 The Polarotor

The Licel Polarotor rotating polarizer was designed specifically for multispectral detection systems such as the CRL lidar [87]. It is controlled by the lidar computer. The polarotor acts as the master trigger for the entire lidar system, forcing the laser to fire and the detectors to record every time the prism rotates through 450° . This is accomplished by spinning the polarizer steadily at high speed and using a synch pulse from the built in timing disk to photoelectrically trigger the lidar system at 10 Hz.

Every 450 degree rotation of the prism rotates the polarization acceptance plane by 90° .

The polarotor's α -BBO Glan-Thompson prism thus lets through light which is polarized parallel to, and perpendicular to, the lidar laser light, on alternate laser shots. The extinction of the polarizer is better than 5×10^{-5} . Two recording buffers are used in the Licel Transient Recorder, one for parallel and one for perpendicular photocounts profiles. The polarotor triggers each in turn. Calibrations to find where the "parallel" and "perpendicular" planes lie in relation to the lab and to the polarotor itself give the reference planes from which all analysis is based. The polarotor delays can be set to trigger from any polarizer angle. It is also possible, using the stepper motor, to step the polarizer slowly through a series of angles. The repeatability of these angles is not perfect, so orientation calibrations were done at CRL by varying the trigger delay rather than attempting to get an absolute orientation in steps.

The polarotor is available from Licel GmbH, Berlin, Germany. The polarotor's control module is easily integrated with other Licel components such as the transient recorder. Software is available in LabView, but was rewritten (primarily by M. Coffin and G. Nott) in Python for use at CRL. Further specifications for the polarotor are given in [88].

4.3 Advantages to a rotating polarizer design

This design reduces the number of differences between hardware characteristics of both depolarization channels because the backscattered light traverses identical optics and impinges on the same photomultiplier tube. Given that the basic depolarization calculation is a ratio of the signals in the perpendicular channel to those in the parallel, having identical components means that many calibration parameters cancel out of the calculation.

4.4 The pellicle beamsplitter

The beamsplitter to pick off the light for the depolarization channel was chosen solely for its minimal amount of translation of transmitted light. Numerous options for pellicle

beamsplitters are available. Some polarize more than others. In a polarization experiment, it is helpful to choose a nonpolarizing beamsplitter.

The pellicle beamsplitter used at present is a 3" CVI-Melles Griot 633nm 50/50 pellicle beamsplitter. This pellicle is the most non-polarizing option available at 532 nm in reflectance, which still allows as much 607 nm light through as possible. A photograph of the polychromator, including the pellicle, is available in Figure 4.1.

4.5 Interference Filter Specifications

The interference filter chosen for the depolarization channel has a bandwidth of 1 ± 0.2 nm centered at 532.0 ± 0.2 nm, and is a 25 mm diameter optic. Its transmission is greater than 45 %, and it has 1×10^{-4} average blocking from X-ray to far infrared wavelengths. This filter is Andover Corporation Part Number 532FS02-25. Specifications are available in [89].

For comparison, the interference filter for the Visible Rayleigh Elastic channel has a bandwidth of $0.35 \text{ nm} \pm 0.07 \text{ nm}$ centered at $532.08 \pm 0.06 \text{ nm}$. Its reflectance is greater than 80% from 526nm to 531.8nm (Design goal).

In an ideally-designed lidar, these filters would be identical. Modelling of the Raman temperature spectrum of the atmosphere was done in relation to the bandwidths of the two filters, in case atmospheric or laboratory temperature was to have some effect on the depolarization products calculated in this thesis. This was found to have no effect on the results in this thesis, so the plots are not included here.

4.6 Calibration Equipment

To do various calibrations of the depolarization channel in the lidar, some specialized equipment is required. This includes lamps (e.g. white light sources), optics (polarizers and depolarizers), and some custom mounting hardware for these items. Such items are

inventoried in this section, to be referenced later. Testing and development of calibration techniques was required during the work of this thesis because the CRL had not needed polarization/depolarization calibration tests before this time.

4.6.1 Calibration light sources

For calibrations, current-controlled light sources are required. These must be bright enough at the 532 nm wavelength of depolarization measurements to make calibrations in appropriate amounts of time. They must be able to be mounted in the lidar safely, and must be able to be run on the power supplies available at Eureka.

- **Ocean Optics Lamp**

There is one dedicated calibration lamp installed permanently in the CRL. It is an Ocean Optics calibration quartz-tungsten lamp. Its intended use is calibration of the lidar's water vapour measurements, and it was hoped that it would be of use for the depolarization calibrations as well. Unfortunately, though it is ideal for use in UV channels and works fine too for the Visible Rayleigh Elastic channel which receives most of the visible light, other visible channels do not receive sufficient light for timely calibrations.

As this lamp is mounted in the shadow of the secondary telescope mirror, between the tertiary mirror and the focus stage, any calibrations made using this lamp necessarily skip the first four optics of the system (including the roof window).

No calibrations in this thesis use this lamp, although attempts were made to do so.

- **Tractor Headlight**

The best calibration lamp that was used for calibrations in this thesis is usually employed as a headlight on tractors and other large machinery.

It is relatively affordable, easily bolted onto various locations in the lidar, can be operated on a precision current-controlled power supply (and thus have its intensity well controlled), is weather sealed, and is one of the few lamps bright enough to illuminate the

perpendicular depolarization channel sufficiently for the tests. The lamp is model “A18759 Light Assy.” produced by CNH (Case) Original Parts, and was purchased from J.R. Brisson Equipment Ltee, Ottawa ON.

A B&K Precision 1760 ADC Power Supply is used to power the lamp, running at up to 24 Volts, 1.1 Amps. It was calibrated in January 2013. This current-stable power supply ensures that the lamp’s output power remains constant throughout the lidar tests.

A photograph of this lamp in operation in the lidar is given in Figure 8.2 in Chapter 9. When a “calibration lamp” or a “lamp” is mentioned in this document, the tractor headlight is what was used.

4.6.2 Depolarizing calibration optics

When calibrating the depolarization ratios, it is necessary to have light of a known depolarization ratio enter the system. The easiest way to do this is to put completely unpolarized light in and measure the results in both channels. Numerous methods of obtaining completely unpolarized calibration light have been attempted at CRL:

- Waiting for some multiply scattering clouds, and hoping that the light is completely unpolarized light during the entire calibration
- Calibration lamp with a depolarizing diffuser in front of it in the shadow of the secondary mirror of the telescope
- Calibration lamp with a depolarizing diffuser in front of it in front of the entrance aperture to the whole system
- Using laser backscatter returns, but interrupting them with a depolarizing diffuser at some point in the receiver

The cloudy sky method proved unreliable for CRL. It was not possible to ensure that the sky was providing uniformly unpolarized light to the detector. Therefore, none of these tests are included in this thesis, although they were attempted.

All other methods require some form of material which depolarizes light into a completely unpolarized beam. There are optics available for that purpose, but they tend to be small and expensive. The smallest optic that CRL could employ is approximately 2.5 cm in diameter, and an optic this small necessarily is located well within the receiver, forcing the calibration to skip most early optics.

Ideally, the CRL would have a depolarizing optic in excess of 1-m diameter which could be placed above the window of the roof hatch. This depolarizer would need to be sufficiently lightweight not to damage the window. It would need to be able to withstand temperatures below -50°C , and some blowing snow and wind. It would also need to be transportable to Eureka, which is nontrivial for large and/or fragile objects.

The depolarizing optics tried at CRL include:

- 2.5 cm (1") diameter ground glass optic. These were already available at CRL. However, they attenuated the light too much to be of use. Further, calibrations made with this optic did not include effects of the roof window, telescope, or focus stage.
- Kitchen parchment paper. This proved to be an insufficient depolarizer for the CRL's purposes, and therefore did not work.
- Home-grade kitchen waxed paper. This is widely available in large quantities. It is inexpensive, and can be taped together into large sheets, and cut to shape. It is easy to transport to Eureka. Some brands of grocery store waxed paper depolarize quite well with one layer. Others require multiple sheets, which then attenuate the light too much. Results were inconsistent with this material, but promising enough to search for other similar materials. It is not unheard of to use waxed paper as a depolarizer, or as a depolarizing calibration material in scientific experiments. Some interesting references to its use in this capacity are the biology research papers [90] on the subject of polarization contrast in octopus vision, and [91] which examines polarization sensitivity in brittle stars, which have no eyes.
- Industrial-grade kitchen waxed paper. The thicker waxed paper intended for use in food

service establishments was a better depolarizer than the home-grade waxed paper. For approximately one year it was the best depolarizer option available to CRL. It was used in one of the calibration tests made during that time, and is included in this thesis in Section 8.2.3.

- **Glassine.** This is archival-quality waxed paper, tried at the suggestion of a CANDAC mentor. It is the thin material that one might generally see protecting colour plates in books, or used between layers of art or documents. This material is a fantastic depolarizer, particularly when two sheets are layered in orthogonal directions. The brand used at CRL is Archivalware "Acid Free Glassine" produced by Lineco (Item number 448-1626). This is available in sheets (ours were 16" x 20") quite inexpensively. The sheets are folded when packaged, and are easily transported to Eureka. In this thesis, when the word "depolarizer" is used without a qualifier, it is glassine waxed paper which is being employed. It was without question the best depolarizing optic option available to the CRL laboratory at the time of the calibrations. Tests were made to calibrate the glassine itself, and to verify its optical properties. They are detailed below (Section 4.6.2.1).

4.6.2.1 Calibration tests of the optical qualities of glassine waxed paper

To use glassine waxed paper as a depolarizing optic, it was important to test its depolarizing qualities in advance. Through the following measurements, it was determined that one layer is sufficiently effective for use as a depolarizer, and that two layers placed in orthogonal directions with respect to each other is ideal.

This test was done using an incandescent lamp, two Polaroid linear polarizers, and a photodiode with a voltmeter, all held within a darkened tube. The path the light took, as in Figure 4.3 was: 1. Lamp, 2. Linear sheet polarizer (fixed), 3. Glassine sheet(s), 4. Linear sheet polarizer (rotated through various angles θ), 5. Photodiode read out by voltmeter in units of mV. The photodiode voltage is directly related to the intensity of the light measured.

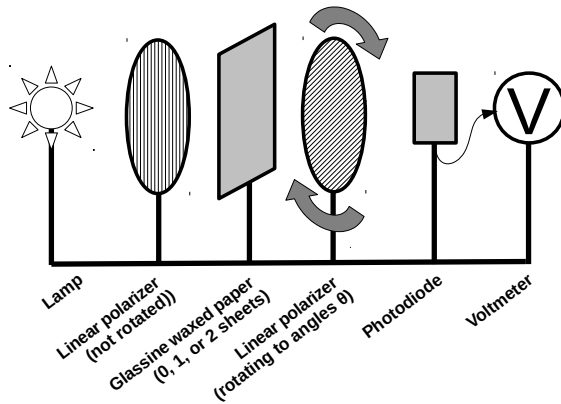


Figure 4.3: Diagram of the test used to verify that Glassine waxed paper is an effective depolarizing optic. The lamp and first linear polarizer are held fixed. Zero, one or two sheets of glassine are held fixed (depending on the test). The second polarizer is rotated through various angles θ . The light through these optics is measured using a photodiode, which is read out on a voltmeter. The voltage is directly related to the intensity of the light measured by the photodiode.

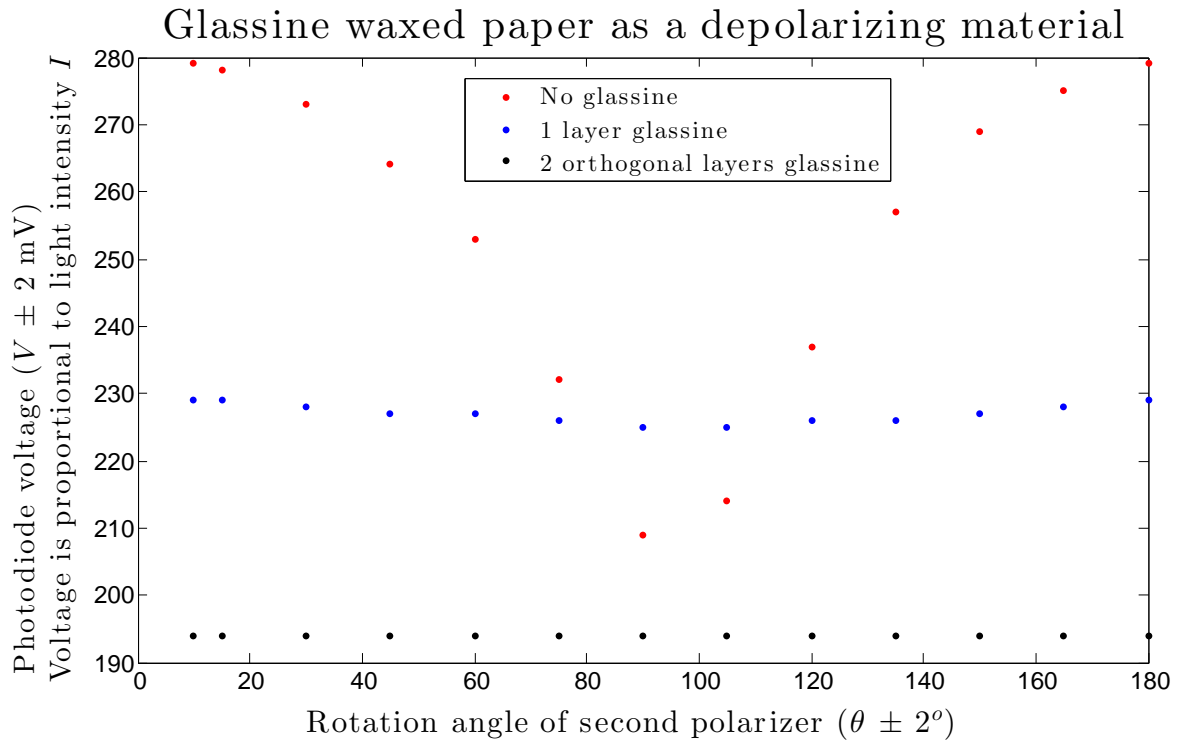


Figure 4.4: Results of the calibration test to verify that glassine does depolarize light, set up according to Figure 4.3. The red data points do not include glassine. The shape of Malus' law for two polarizers is evident. The dark blue data points demonstrate the considerable depolarizing effect of one glassine sheet placed between the polarizers. The black points demonstrate the complete depolarization possible when two glassine sheets are layered orthogonally to one another.

The plot in Figure 4.4 shows the photodiode measurements (in mV) of the light which is transmitted through all three optics for various rotation angles of the analyzing (2nd) polarizer. The polarizers are perpendicular to each other at the 100 degree mark on the plot.

The red points show the result with no glassine between the polarizers. Here, the shape is the cosine-squared relationship expected from Malus's Law:

$$I = I_o \cos^2(\theta) \quad (4.1)$$

in which I is measured intensity, I_o is initial intensity, and θ is the rotation angle of the analyzing polarizer.

The dark blue points show the result with one layer of glassine between the polarizers. Here the curve has mostly flattened out with rotation angle of the analyzing polarizer. It is not quite perfectly constant, but gives less than 1% variation from a constant (± 2 mV on a scale of 230 mV).

The black points show the result with two layers of glassine, oriented orthogonally to each other (crossed). This is perfectly constant to within the measurement precision of the test in terms of damping out polarization, but also attenuates the light more than is done by one layer alone.

It is concluded that glassine is a valuable optic to be used for depolarization in either single or double sheet configurations, with a preference for using two crossed sheets where the attenuation from doing so is acceptable.

4.6.2.2 Practical considerations when using glassine

Calibrations with the CRL were carried out with scenarios of both 1 and 2 layers of glassine. It was found that in practice, it was usually not possible to get bright enough calibration light (or lidar returns, even from bright clouds) to make a 2-sheet glassine calibration possible given its attenuation. Thus, the 1% error on the one-sheet calibration is accepted. A possibility for improvement would be to rotate the glassine periodically and measure with

various angles, then average the results, but this was not done in any of the calibration tests in this thesis.

The glassine waxed paper turned out to be a fantastic solution to the problem of obtaining a large depolarizing calibration optic. Some techniques which made it work well in Eureka include:

- Having light-blocking sheet material (such as opaque plastic sheeting used in film photography) available to cover any cracks in the glassine material (especially “on the fly”, once everything has been installed, and a quick modification is necessary);
- Having opaque tape, such as light-tight black masking tape, for connecting multiple sheets together. Scotch tape and other clear tapes are well-known *polarizers*, so avoiding their use in the construction of a depolarizing optic is necessary;
- Placing a line of opaque tape lengthwise on both sides of the glassine anywhere that a cut is wished, and then cutting along the taped area. This prevents the glassine from tearing at the edges. Small tears tend to widen quickly, particularly in the cold;
- Where possible, placing the glassine gently taught within a rigid frame. This allows it to be easily wielded within the lidar, and gently held in place in a repeatable manner. CRL’s frame was constructed from two layers of foam core, and is used in the photograph of Figure 8.2.
- Having plenty of glassine available;
- Having foam, or similar materials to hand, to construct wedges to keep the glassine in the intended location. For example, it was paramount that the glassine be prevented from blowing into the lidar’s laser beam during tests in which the glassine was on the roof;
- Having available some blocking material of approximately the same dimensions as the glassine. This was useful for double-checking dark counts and for leakage around the glassine in some calibrations.

4.6.3 Polarizing calibration optics

Polarizing optics are also required for calibrations at CRL. Only some of the calibration constants for depolarization parameter calculations may be made using depolarized light. Several polarizers have been used, including linear sheet polarizers and cube polarizing beamsplitters.

- Sheet polarizer: PF006 "Linear Polarizer by the Foot". This large sheet polarizer from Aflash Photonics (Polarization.com) comes on a 1' wide roll. Four linear feet were purchased for use in the CRL.

Efforts were made to use very large (200 cm x 222 cm) sheet polarizers at the entrance to a) the hatch window and b) the primary mirror of the telescope. This includes more optics in the calibration. This polarizer is student grade, rather than lab quality, but is inexpensive and able to cover a large area. Tests attempting to install this type of polarizer above the entire primary mirror of the telescope did not prove fruitful. Large sheet polarizers are very difficult to control. It is very difficult to make the polarizer lie flat, as it comes in a roll. It tended to warp and droop, even when held in a rigid frame, bringing its uniform polarization capabilities into question. Small cracks form at the edges when flattening the material and extend quickly inward. Great care must be taken with the material in cold, dry conditions. Rotating the large polarizer in any uniform manner proved impractical.

- Sheet polarizer: PFH DU "High-Temperature linear polarizer". This polarizer is sold in flat sheets from Aflash Photonics (Polarization.com) and has adhesive on one side. Size AD SM 25×15 cm (10×6 in) was purchased for the CRL.

This polarizer is designed to tolerate temperature swings down to -40°C, which is useful in the Arctic. This polarizer is also high-temperature-tolerant, so it was able to be placed directly onto a very warm calibration lamp. Tests in which the polarizer was adhered to the calibration lamp were successful, except that without the ability to rotate the calibration

lamp itself, the polarization plane of the light cannot be rotated, either. Further, the lamp had to be placed relatively close to the polychromator entrance in order to get sufficient photons into the PMTs to measure a signal. Attempts were made to have the lamp directed into the telescope primary mirror, but signal rates were too low in this configuration. With a more intense lamp, perhaps this kind of polarizer would be more convenient to use. When not adhered directly to the lamp, it must be used with a frame to keep it rigid, and the adhesive attracts lots of dust particles.

- 45-668 "8.5 x 15" Linear Polarizing Laminated Film". This lab-quality sheet polarizer was purchased from a known source: Edmund Optics.

This sheet polarizer was placed into a round cardboard frame of approximately 25 cm diameter. It was fairly rigid, so was easy to keep flat and to rotate reliably once placed in the frame. To use this polarizer, the majority of the entrance aperture to the telescope was blocked off by opaque plastic sheeting. A small hole was left to admit the round polarizer. This polarizer in the small aperture was then rotated above the primary telescope mirror during lidar observations for one evening. The results of this calibration are potentially useful in the long run, but are not included in this thesis for several reasons: a) As a result of the other optical effects in sheet polarizers (not just polarization, but also reorientation of the outgoing light), the analysis of this calibration data was unexpectedly complicated, and b) results from other lidar groups ([92]) have indicated that measurements made using only one part of the primary mirror are liable to be very different from those made using another portion. For these reasons, detailed interpretation of measurements from this calibration test were foregone in favour of calibration tests using a linear cube polarizing beamsplitter and calibration lamp.

- Linear cube polarizing beamsplitter: Newport 10BC16PC.3 Pol Cube Beamsplitter, 532 nm, $T_p/T_s > 1000:1$, 25.4 mm diameter. Part number PK18302.

This linear cube polarizing beamsplitter was the highest optical quality polarizer available to CRL, and was used in the calibration tests described later in this thesis. This polarizer has a diameter many times smaller than that available for the sheet polarizers detailed above. Therefore, it cannot be used effectively above the primary mirror of the telescope. Instead, the cube beamsplitter was mounted in a rotating Newport mount on the 2" beam-tube at the entrance to the polychromator. It was rotated by hand to the desired orientation. The downside to using this polarizer is that all such calibrations miss the effects of the first eight optics in the lidar: The window, the telescope, and the focus stage. Despite these drawbacks, the quality of calibrations made using this high quality polarizer exceeded the quality of calibrations made using the sheet polarizers by a large margin.

Future polarization generators

In future, perhaps CRL can obtain a direct source of polarized light, such as an LCD, rather than relying on passing unpolarized light through a polarizer. If a large-area polarized light source becomes available, it would be preferable to use this above the primary mirror of the telescope so that the polarization effects of the majority of CRL receiver optics may be included in the calibration test.

Chapter 5

Low-level data processing for depolarization channels

5.1 Introduction to low level data analysis

CANDAC Rayleigh-Mie-Raman lidar (CRL) measurements are integrated in the Licel Transient Recorders for one minute at a time (600 laser shots) at 7.5 metre resolution before being written out to disk.

Some channels have only photon counting capability (“PC” or “digital”) while others have dual analogue (“ANA”) and photon counting simultaneous capability. The latter is the case for all channels used in depolarization analyses. In all cases, the data is read into software, overflow flagged bits are removed, photon counting values are dead-time corrected, analogue values are dark profile subtracted, measurements are coadded together in space and time to the desired resolution, and backgrounds are subtracted. Analogue signals are converted to virtual counts units to match the unit of the photon counting signals. Finally, where appropriate, corresponding high-count-rate sections of analogue and low-count-rate sections photon counting profiles are merged or glued together to produce a single profile of the atmosphere. Together, these processes make up the low level data

analysis at CRL.

The resulting glued, corrected, photocount profiles are then ready to be used for higher analysis into useful data products such as depolarization ratio, depolarization parameter, water vapour mixing ratio, etc. Such further analyses for depolarization measurements are discussed in Chapter 6 and beyond.

5.2 Analysis software and languages

5.2.1 Python programming at Dalhousie University

5.2.1.1 Python Data Acquisition

From the beginning of the CRL's operations, Dalhousie University's Atmospheric Optics Laboratory, led by Prof. T. Duck, has developed code written in Python to acquire and save the lidar measurements. Authors of this code include T. Duck, M. Coffin and G. Nott. Functionality was built in from the beginning to handle the eventual depolarization channel data, should such hardware ever be installed. With the installation of the depolarization channel during the work of this thesis, little writing was done to upgrade the data acquisition codes.

The CRL data acquisition system records one Hierarchical Data Format 5 (HDF5) file each minute which includes all measurement channels' profiles [93]. This method allows each minute of data to be saved separately; if the acquisition fails mid-measurement, none of the data up until the minute of the failure should be affected. This results in little danger of corruption in large quantities of measurements. Calibration measurements and alignment measurements are also saved as HDF5 files; these are stored separately from the routinely measured data.

Included in each raw data file are: 12 photocount profiles (one for each PC and analogue channel), number of laser shots, analogue range settings, discriminator thresholds, etc. The files are saved in a binary format, and this must be taken into account when reading the

data into analysis programs.

5.2.1.2 Python Data Analysis

Measurement analysis codes were developed for the initial lidar hardware channels, also in Python, by the Dalhousie group. For the first several years of CRL operation, only photon counting measurements were used. Analogue measurements were recorded, but were not brought into the analysis at that time. Since the development of analogue data analysis algorithms in MATLAB during the work of this thesis for depolarization channels (Section 5.2.2), similar algorithms have been included in the Python codes at Dalhousie.

Quicklook software was written to display raw depolarization channel data, and a preliminary depolarization ratio product was developed, but more sophisticated interpretation and manipulation of the results has not been carried out in Python to date.

5.2.2 MATLAB at the University of Western Ontario

The University of Western Ontario joined the CRL project with the installation of the depolarization channels, and developed software for the detailed analysis of depolarization measurements.

The “home lab” for Western is the Purple Crow Lidar (PCL) in London, Ontario. PCL has run MATLAB data analysis software for many years. Thus, depolarization analysis codes written for this thesis were made in such a way as to integrate fully with existing Picon version 11d code, which is used to analyze the PCL data. In retrospect, it would have been more sensible to add to Dalhousie’s Python code rather than to Western’s Matlab code, but now that many of the intricacies of combining the depolarization data have been worked out in MATLAB, discussed be a relatively quick process to port these lessons and the algorithm over to Python.

In the MATLAB CRL data analysis code, the ability to read in and produce useable photocount profiles was carried out for all channels. Photon counting and analogue mea-

surements for all channels work in the same manner. Despite being written specifically to handle the depolarization analysis, nothing in this chapter is restricted to the depolarization channels. The MATLAB code can produce corrected photocount profiles for any CRL channel.

This thesis will discuss only the MATLAB code which I wrote, developed for the depolarization analyses.

5.3 Reading in data files

First, the HDF5 files are easily loaded into MATLAB with one command, turning the binary data into decimal format automatically.

The CRL data from the Licel counters is recorded as multi-bit words; The photon counting channels are 16-bit words while the analogue channels are 25-bit words formed from a 16-bit least significant word and a 9-bit most significant word [94]. In each case, the most significant bit is a flag bit which indicates that the counter has either underflowed or overflowed on at least one laser scan. In this case, one or more of the 600 scans recorded that minute has oversaturated the detector, or has recorded exactly a value of zero. In both cases, the transient recorder indicates that the value is not to be trusted. This is because the true value could have been exactly the maximum value measured, or it could have been far in excess of this number, as only the maximum measurable value will be reported.

A complicating factor for the manner in which MATLAB reads HDF5 files is that it makes no distinction between this flag bit and the bits recording the actual value of photon counts or analogue voltage in the channel. To be useable, the MATLAB values must each be turned back into binary, the most significant bit must be trimmed from the binary word, and the remains must be turned back into a decimal value.

The procedure for dealing with the flagged bits was necessarily different for photon counting and analogue channel data because of the different ways in which MATLAB's

loading function interprets the flags. The effect of the flag bit being “flagged” in PC is that MATLAB interprets the entire value as a negative number. Conversely, the effect of the flag bit being “flagged” in ANA is that MATLAB interprets the entire value as being much, much larger than the actual stored value. This difference results in different code being written to trim the flag bit from each kind of data.

5.3.1 Handling Analogue channel overflow flags

For analogue channels, MATLAB interprets the flagged bit to be a regular bit in the number; that is to say, setting this bit to ‘1’ results in a value which is orders of magnitude larger than the same value would be with the ‘0’ of an unflagged bit.

There are two options for dealing with this. The first, and the option used for CRL, is to use the `dec2bin` command to convert the decimal number into binary. Then make a new variable which takes all binary bit values except for the most significant bit. Use `bin2dec` to take this new binary value, and turn it back into a decimal number, which is the measured value according to the transient recorder. To keep track of which data points have had a flagged bit in the first place, the difference between the original and new decimal numbers may be examined. If the difference is zero, then the most significant bit was zero also, as chopping it off has not had any influence. If the difference is non-zero, then one of the scans going into that value must have been overflowed.

An alternate method for identifying the flagged bit is simply to determine the maximum decimal value to which the Licel is able to measure. In the case of the analogue channel, which has a 25-bit value including the flagged bit, and thus contains 24-bits of true information, the maximum decimal value the counter can achieve is $2^{24} = 8388608$. Any values higher than that must have occurred by setting the most significant (flag) bit to ‘1’, reaching a maximum decimal value of $2^{25} = 33554432$. If the flag bit is set, but otherwise the counts are zero, then the value in binary will be `10000000000000000000000000`. That is a ‘1’ followed by 24 zeros. The decimal representation of this number is 16777216. There is

evidently a huge difference between the largest decimal value to which a non-overflowed count can reach and the smallest overflowed count which will be recorded.

It should be possible to simply remove any analogue data points which have been flagged, but in practice it is instructive to simply convert them to their “as measured” values, and note that they have in fact been flagged. Any rejection of data based on such flags may be done at a later stage if so required. This is discussed further in Section 5.3.3.

5.3.2 Handling Photon Counting channel overflow flags

For the photon counting channels, the method used for analogue channels does not work. This is because, in the case of photon counting channels, MATLAB interprets flag bits as indicative of a negative number rather than a very large one, and `dec2bin` only works on nonnegative integer inputs.

Instead, photon counting raw count values lower than zero in decimal notation, indicating overflowed large numbers, are identified on the basis of their sign, and are excluded in that manner from further analysis.

5.3.3 Removal (or not) of the flagged values

Recall that the PC channel is best for low count rates, and saturates easily. The ANA channel is better for high count rates. It does not saturate until much higher count rates than the PC channel, although its uncertainties exceed those for the PC channel in regions where both are valid.

The decision to remove flagged photon counting values is simple. If the PC channel is saturated to the point of flagging the most significant bit, then it has also begun to respond nonlinearly at count rates even below this point. For the depolarization glued channels, anywhere the photon counting has saturated may be filled in using information from the analogue channels during a gluing procedure. As will be shown in the procedures about merging/gluing, the best transition region in terms of count rate from PC to ANA data

happens at a count rate much lower than the PC's saturation threshold, in a region where the PC counts are still responding linearly to input signals.

Decisions for the analogue channels require more consideration. It is clear that one should not just blindly ignore the flagged bits. The consequence of doing this would be a profile with sudden jumps to orders-of-magnitude higher values than those actually measured. At the very least, the flagged bit itself must be removed from the measured value according to the procedure in Section 5.3.1. This leaves a profile with the values the data acquisition system reports as having measured.

It is then up to the scientist to determine whether the values measured by the transient recorder, and reported as flagged, are trustworthy or not. An examination of a general selection of lidar data will reveal whether the lidar's analogue channel is consistently operating at the top of its dynamic range. If this is the case, and there is an overflow bin flagged, then chances are that it is truly an overflow, and that measurements from many of the 600 laser shots contributing to each minute of data have overflowed. One should not use the bin's data because it is, on the whole, underreporting the number of photons incident on the detector for bits which are flagged. Consistently high numbers of overflowed bins suggest that the analogue range settings should be reconsidered to allow for higher count rates, or perhaps a neutral density filter can be placed in front of the detector to reduce the incoming signal.

A flagged bit is a different situation entirely if it is found practically in isolation of other flagged bits, which happens if the analogue channel operates comfortably within its dynamic range most of the time. This is the case for CRL; most often, the analogue channels are operated at reasonable signal levels. A flagged bit in these conditions is less likely to indicate an overflow in many of the 600 contributing laser shots. It is more likely to indicate a "fluke" spike from an oriented ice crystal or similar for only one of the 600 shots in a minute of data. Even a sizeable overflow in one of 600 shots is not going to make a huge difference when you add them all up and take the average. If the signal were to, in

an extreme case, actually double for a single one of the laser shots, this would only be an increase in overall signal for that minute of $(1/600) \times 100\% = 0.1167\%$.

The case is further solidified if the values, once the flagged bit has been trimmed off, lie within the realm of neighbouring values. If the value still appears to be an outlier, then potentially it should be excluded. More likely, if the value fits in with its neighbours, the number remains meaningful.

For further encouragement of this practice (remove flagged PC; keep flagged bit-trimmed ANA but note that they are flagged in case it matters later), an examination was done of derived data products for the CRL. If the flagged analogue bits were truly meaningless, then odd effects would be expected. These have not been seen in several years worth of data, in any of the derived data products produced by the CRL.

5.4 Turning altitude bins into metres

The transient recorder maximum sample rate is 20 MHz, which corresponds to 7.5 metre range resolution for lidar measurements. Because of the manner in which the triggering works in the lidar, the first altitude bin of the measurements does not correspond with 0 metres altitude. Rather, the recorder begins measuring slightly in advance of the laser shot being transmitted to the sky.

There is always a several bin offset in Licel transient recorders between the photon counting and the analogue channel data. This has to do with the manner in which the data is read out to disk [95]. The channels are compared to each other and diagnostic spikes in the photocount profiles are used to match one channel up with another in terms of altitude. The first bin with any returns is designated as the bin halfway between 0 and 7.5 metres altitude. Later bins follow upward from there every 7.5 metres. For parallel and perpendicular photon counting channels, the first true signal comes at bin number 407, while for analogue it is bin 416. For Visible Rayleigh Elastic, PC begins at bin 404

and analogue at bin 413. Care must be taken when determining these bins. Atmospheric features with very sharp gradients in height can be useful as checks that the measurements are coordinated properly in altitude.

These first number of bins in advance of the lidar backscatter signal are generally ignored in CRL analyses. However, it is possible for them to be used as a pre-firing measurement of the background levels in the lidar. Comparisons with background levels measured after the laser fires, as is usually done for CRL, can indicate problems with fluorescence in the system if the background values are not similar. Although CRL routinely ignores these data, there is information in there that could be useful under some circumstances. Therefore, rather than removing the data from the analysis programs entirely, it is retained during most stages of data processing assigned to negative altitude bin values which are explicitly rejected from the latest stages of processing.

5.4.1 Removing counts outside of appropriate altitude range

All counts assigned to altitudes below 0 m (when the PMTs record before the laser fires) are routinely rejected from analyses, and so are any counts below about 500 metres. The reason for the latter threshold is that the photomultipliers have a tendency to electronically ‘ring’ in the analogue measurements, and the largest effects of the geometric overlap of the lidar are present below 500 m.

5.5 Photon counting signals, uncertainties, and corrections

The photon counting channels’ corrections and uncertainty analysis are detailed one by one, in the order in which they are carried out.

5.5.1 Photon Counting raw signals and uncertainty

The photocount profiles are given as $N(z)$, in which N is the number of photocounts as a function of altitude z for a particular one-minute profile.

Photon counting carries poisson statistics. The uncertainty σ_N is given as:

$$\sigma_N = \sqrt{N}, \quad (5.1)$$

where N is the number of photon counts in the sample. As the size of the signal N increases, so too does the size of the uncertainty, but more slowly at \sqrt{N} . What shrinks (advantageously) with increased signal is the relative error, $\frac{\sqrt{N}}{N}$. Figure 5.1 displays the signal, absolute uncertainty, and relative uncertainty using poisson statistics for a variety of count values. The shot noise uncertainty σ_N is propagated through equations in the next sections.

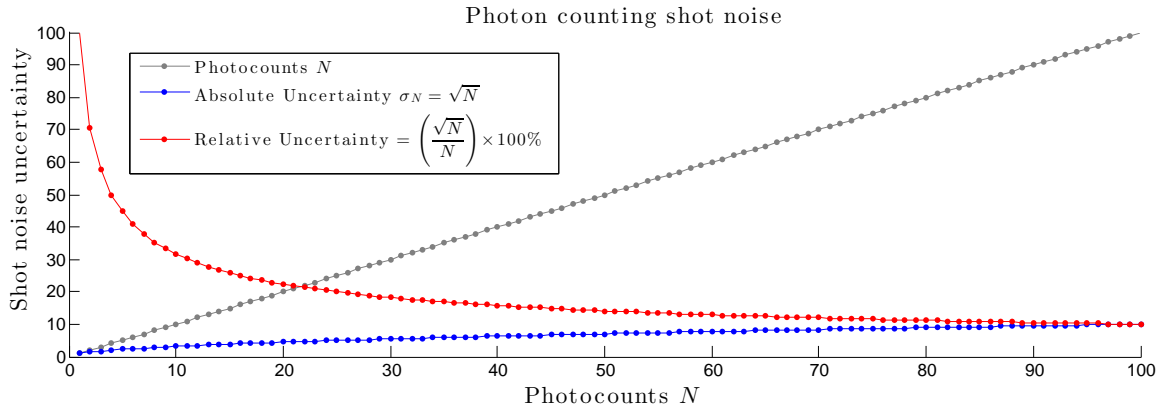


Figure 5.1: Demonstration of the effect of increased photon count numbers on absolute and relative uncertainty due to shot noise. Absolute uncertainty (blue) is small at low count rates N , but it is of the order of the same size as the count rate itself (grey), and equal to it for $N=1$ photon. Therefore the relative uncertainty (red) is high: 100%. At high count rates N , the absolute uncertainty is larger, but it has not grown at the same rate as the signal. The relative uncertainty is therefore smaller: 10%. Relative uncertainty continues to decline with increased count rate. The decrease in relative uncertainty is the reason that longer integration times and coadding, or binning, of photon counts is advantageous for lidar measurements.

5.5.2 Turning photon count rates into MHz

Lidar photon counting measurements are made in units of “number of photons per two-way altitude bin per integration time”. Of course, because altitude itself is inferred from a time measurement, using the speed of light c , the “two-way altitude bin” may be expressed as the time required for light to traverse one altitude bin and return. Thus, lidar measurements are in the odd-sounding unit of “photons per time per time”.

It is sometimes desirable to convert the data to units of MHz. Expressed in this manner, lidars of differing power-aperture products, repetition rates, laser powers, etc, may be “fairly” compared. For example, a lidar with twice the laser power will have a profile showing twice the frequency of photon counts for each altitude when expressed in MHz.

The following equation is given by the manufacturer of the transient recorder, for the conversion of photon counts to MHz [94]:

$$MHzData = norm * \frac{bins}{\mu s}, \quad (5.2)$$

in which *norm* is the mean number of counts per bin per shot, and $bins/\mu s$ is the number of bins per microsecond. Some further explanation is in order.

The MHz unit has to do with, specifically, the rate at which photons are hitting the photomultiplier tube at any given time. In a sense, when we turn our photon counts into MHz, it’s the “spatial” vertical time from each one laser shot we care about, and not the “time” time over which several shots are integrated. MHz is equivalent to “counts per shot per microsecond”.

The procedure to convert from raw counts to MHz begins with the “time” time (the measurement integration time), which must be converted into units of number of laser shots. The CRL’s native integration time t_{maxres} is one minute, or 60 seconds. Sometimes measurements are coadded n_{tbins} times to give longer time bins of, in units of seconds:

$$\Delta t_t = t_{maxres} n_{tbins}. \quad (5.3)$$

The repetition rate of the system in units of shots per second, may be used to convert the time bins from seconds to shots:

$$\Delta t_t = t_{maxres} n_{tbins} Rep, \quad (5.4)$$

in which:

Δt_t is the measurement integration time, expressed as the number of *recorded* laser shots.

t_{maxres} is the maximum time resolution of the lidar in units of seconds.

$Rep = Lf$ is the number of laser shots *recorded* per second in the relevant measurement channel (the repetition rate of the recorder), in which:

L is the laser repetition rate

f is the fraction of laser shots recorded in the measurement channel (for example, if the measurement channel records data on every second laser shot, f would have a value of 0.5. If it records on every laser shot, f would have a value of 1).

Next, the “spatial” time is dealt with. The two-way altitude bin is converted to time units:

$$\Delta t_z = \frac{2z_{res} 10^6}{c} \quad (5.5)$$

$$\Delta t_z = \frac{2z_{maxres} n_{zbins} * 10^6}{c}, \quad (5.6)$$

in which:

Δt_z is the two-way altitude bin time in microseconds

c is the speed of light in metres per second

10^6 is the number of microseconds per second

$z_{res} = z_{maxres} * n_{zbins}$ is the altitude resolution of the lidar in metres, in which:

z_{maxres} is the maximum native altitude resolution of the lidar in metres

n_{zbins} is the number of altitude bins which have been coadded in the measurement.

All together, this allows conversion of the raw photon counts measurement from units of “counts per altitude bin per time bin” to units of “counts per recorded shot per microsecond”. Because “shot” is not really a unit (it’s just a number of recorded laser shots), this is equivalent to “counts per microsecond” (understood that it is for one shot equivalent), or simply “MHz count rate”. The final conversion looks like this:

$$CtsMHz = \frac{Rawcounts}{(\Delta t_z)(\Delta t_t)} \quad (5.7)$$

$$CtsMHz = \frac{Rawcounts}{\left(\frac{2z_{maxres}n_{zbins}10^6}{c}\right)(t_{maxres}n_{tbins}Rep)} \quad (5.8)$$

$$CtsMHz = \frac{Rawcounts}{\left(\frac{2z_{maxres}n_{zbins}10^6}{c}\right)(t_{maxres}n_{tbins}Lf)} \quad (5.9)$$

$$CtsMHz = \frac{Rawcounts}{(c^{-1})(z_{maxres} \cdot t_{maxres} \cdot L \cdot f \cdot 2 \times 10^6)(n_{zbins} \cdot n_{tbins})} \quad (5.10)$$

$$CtsMHz = \frac{Rawcounts}{MHz_{ConversionFactor}(n_{zbins} \cdot n_{tbins})}. \quad (5.11)$$

For the CRL lidar:

$Rawcounts$ is the value read from the data file

$c = 299792458 \approx 3 \times 10^8$ is the speed of light in metres per second

10^6 is the number of microseconds per second

$z_{maxres} = 7.5$ is the maximum altitude resolution of the lidar in metres.

$T_{maxres} = 60$ is the maximum time resolution of the lidar in seconds.

$L = 10$ is the repetition rate of the laser in shots per second.

$f = 0.5$ is the fraction of laser shots recorded by the parallel and perpendicular measurement channels. $f = 1$ is the fraction of laser shots recorded by the Rayleigh Elastic measurement channel. (Thus making the repetition rate of the recorder, Rep , either 5 Hz or 10 Hz, depending on the channel).

$n_{zbins} = 1$ is the number of altitude bins which have been coadded in the measurement. For raw count measurements, this value is 1.

$n_{tbins} = 1$ is the number of time bins which have been coadded in the measurement. For raw count measurements, this value is 1.

To collect the common terms, the conversion factor from raw counts units to MHz is defined as:

$$MHz_{ConversionFactor} = (c^{-1})(z_{maxres} \cdot t_{maxres} \cdot L \cdot f \cdot 2 \times 10^6). \quad (5.12)$$

To get a general understanding of the conversion between raw counts and MHz for each channel, estimates are given here using the approximate value for the speed of light for each channel.

For the Rayleigh Elastic channel, the conversion is approximately:

$$MHz_{ConversionFactor \ Ray} = (3 \times 10^8)^{-1}(7.5 \cdot 60 \cdot 10 \cdot 1 \cdot 2 \times 10^6) = 30 \quad (5.13)$$

For the Parallel and Perpendicular channels, the conversion is approximately:

$$MHz_{ConversionFactor \ ParaPerp} = (3 \times 10^8)^{-1}(7.5 \cdot 60 \cdot 10 \cdot 0.5 \cdot 2 \times 10^6) = 15 \quad (5.14)$$

So if no coadding has taken place ($n_{tbins} = 1$ and $n_{zbins} = 1$), then to change raw photon counts to MHz it suffices (approximately) to divide the signal by 30 for the Rayleigh Elastic

channel, or by 15 for the Parallel and Perpendicular channels:

$$CtsMHz_{Rayleigh} = \frac{Rawcounts_{Rayleigh}}{30} \quad (5.15)$$

$$CtsMHz_{ParaPerp} = \frac{Rawcounts_{ParaPerp}}{15}. \quad (5.16)$$

There are some corrections which are best done in units of MHz. For example, correcting for PMT dead time can be done most sensibly in terms of the frequency with which photons are hitting the PMT. This correction does not care that the CRL repeated the measurement 600 times to accumulate a one-minute integrated profile; it needs to know the behaviour on the photomultiplier tube at a particular time.

5.5.3 Dead time correction for photon counting channels

Photon counting channels can only measure one photon at a time. Any voltage from the photomultiplier tube (PMT) which exceeds a certain discriminator threshold is counted as ‘one count’ in the summation, and then the logic is reset to prepare for the next photon arrival. The time it takes for the reset is called “dead time”, τ . In the case in which two or more photons arrive at the PMT in such quick succession that the first photon is still being counted when the second arrives, the second will not be counted as there is no second event of the voltage passing the discriminator threshold. Higher overall signal rates increase the probability of having the photon pulses ‘pile up’, resulting in saturation of the detector; fewer photons are counted than have arrived (Figure 5.2). The nature of the dead time relations for PMTs are understood, so a dead time correction may be performed to recover the true signal rate.

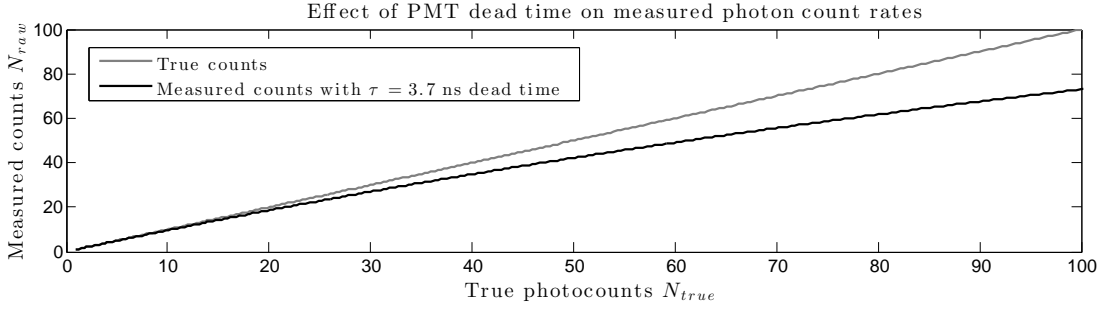


Figure 5.2: Effect of dead time on measured signal rate. As more photons per unit time arrive at the PMT, a corresponding number more photons should be measured by the PMT (grey line). Dead time effects cause fewer photons to be counted (black line) than have arrived at the PMT. Dead time effects are important for CRL above true count rates of approximately 20 MHz.

In terms of dead time, there are two types of PMTs: paralyzable and non-paralyzable. Every additional photon arriving during the dead time of a paralyzable PMT itself extends the dead time. In a non-paralyzable PMT, the dead time remains the same whether one or two or more photons fall on the detector in quick succession. The Hamamatsu PMTs with the Licel recorders can be best described as a non-paralyzable PMT setup [96], [97].

As described in [96], the dead time correction is performed as follows for CRL photon counting data:

$$CountRate_{deadtimecorrected} = \frac{CountRate_{uncorrected}}{1 - CountRate_{uncorrected}\tau}. \quad (5.17)$$

It is possible to perform a dead time correction in terms of either MHz or raw data signals in units of photons per altitude bin per minute. Either way, the dead time units must be the inverse of the units used for the count rate. Both methods are demonstrated here.

If the count rate is in MHz, then the dead time must be in microseconds.

$$CountRate_{dtc,MHz} = \frac{CountRate_{raw,MHz}}{1 - CountRate_{raw,MHz}\tau_{\mu s}}. \quad (5.18)$$

Using the relations in Equation 5.16 from the previous section, each instance of *CountRate* in MHz is replaced by raw counts and the MHz cnversion factor. As the current goal is dead

time correction, there is no coadding of data, and so n_{zbins} and n_{tbins} are both 1. A dead time correction in the units of raw counts, is:

$$\left(\frac{CountRate_{dtc, RawCountUnits}}{MHzConversionFactor} \right) = \frac{\left(\frac{CountRate_{Raw, RawCountUnits}}{MHzConversionFactor} \right)}{1 - \left(\frac{CountRate_{Raw, RawCountUnits}}{MHzConversionFactor} \right) \tau_{\mu s}} \quad (5.19)$$

$$CountRate_{dtc, RawCountUnits} = \frac{CountRate_{Raw, RawCountUnits}}{1 - CountRate_{Raw, RawCountUnits} \left(\frac{\tau_{\mu s}}{MHzConversionFactor} \right)}. \quad (5.20)$$

Because there is not a perfectly known value for CRL dead time, we select $0.0037 \mu s$, (3.7 ns) given in [98], and use a range of uncertainty for it of about 8%. This allows dead times between 3.4 ns and 4 ns, which is a reasonable range for PMTs such as those in the CRL.

To see how much of an effect the uncertainty in the dead time correction will have on the count rates, a test was made to calculate dead time corrected counts for some example “measured” count rates between 0 and 100 MHz per altitude bin per shot. The dead time used in the test is 3.7 ns, as well as 3.7 ns plus and minus 5%. Figure 5.3 gives the corrected counts as a function of input counts, and the percent differences between the corrected and uncorrected counts.

Even by 30 MHz, the correction is no more than 12% of the raw counts value. Furthermore, any uncertainty in the dead time correction makes an even smaller difference, much smaller than 1%. Given that through gluing and merging activities of PC and ANA signals (Section 5.7) any photon-counting data over 20 MHz will be discarded in any case, the propagated uncertainty induced from dead time uncertainty ends up not being of great importance to the final results. Anywhere that there is a count rate high enough in PC for the dead time correction to make a difference, the analogue signals will have already taken over. The maximum correction for data that is used in derived measurement products (such as depolarization parameter) is 8% of the raw count rate (7.5% of the corrected rate), and the error introduced by a 5% error in the dead time value contributes only a 0.3% overall difference in corrected count rate.

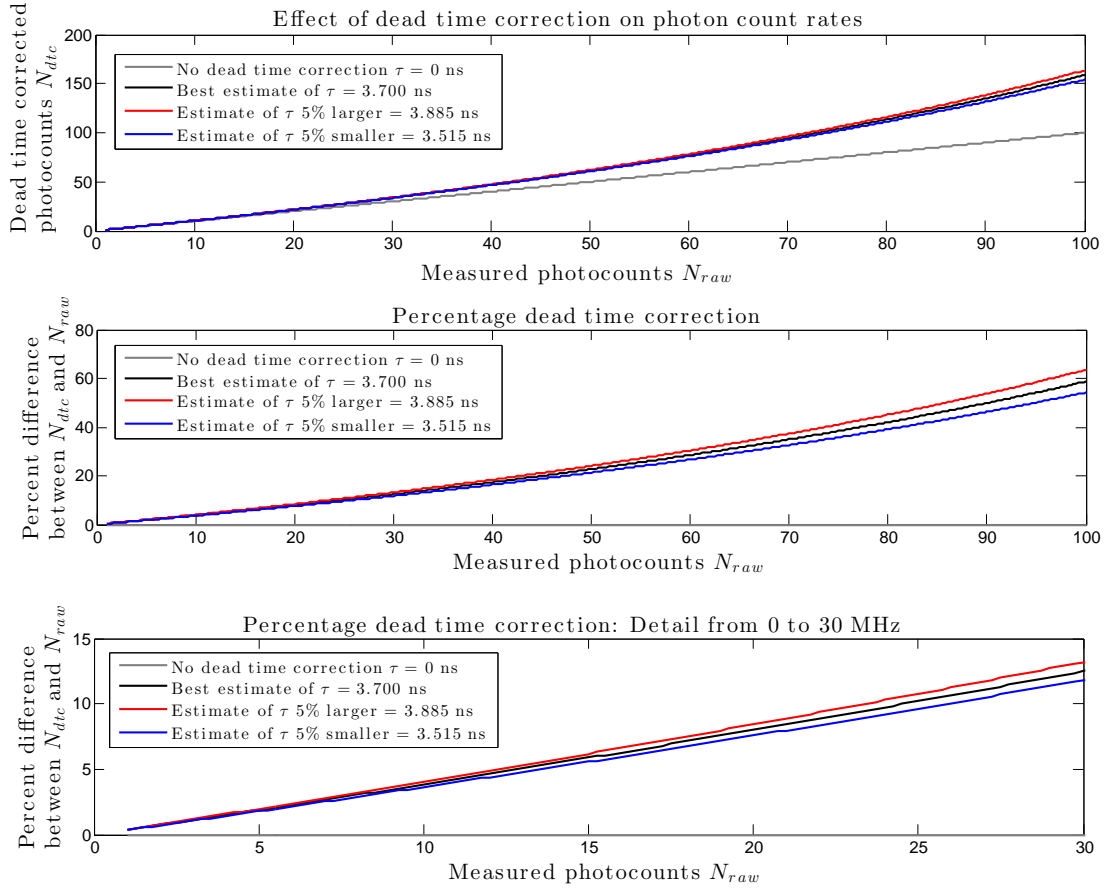


Figure 5.3: Dead time correction demonstration. Example measured count rates from 0 to 100 MHz were dead time corrected. Upper panel: The 1:1 line for the plot (light grey) corresponds to the uncorrected values. Corrected values using the best known dead time value of 3.7 ns ($0.0037 \mu\text{s}$) are plotted in black. Corrected values using best known dead time value, plus 5% (red), and minus 5% (blue) show that the uncertainty in the dead time estimate is inconsequential on the scale of the correction itself. Centre panel: Percent difference between the corrected and uncorrected count rates. Lower panel: Detail of the centre panel, for measured count rates between 0 and 30 MHz. CRL never uses photon counting measurements above 20 MHz count rate. The correction there is less than 8%, with dead time uncertainty contributing less than 0.3%.

The significantly dead time corrected photon counting data is mostly discarded in the merging procedure. Nevertheless, these values can aid in determining the merging coefficients during calibrations. The dead time corrections demonstrated here extend the range over which the PC channel's measurements are linear, and helps give more data points

(and better statistics) for comparing analogue to photon counting signals. Without this, the “gluing region” is smaller, but the procedure will still work.

Note that dead time corrections must be done for both Counts and Background Counts, and must precede any background subtraction. The PMT does not care about the reason that a photon fell on it; it just cares that it is a photon. And if it gets any kind of photon too close to another photon in time, then it needs a dead time correction. This is the reason that dead time correction must be done as early as possible in the data processing procedures.

5.5.4 PC deadtime uncertainty

The shot noise uncertainty must be propagated through the dead time equation. The dead time equation is, based on Equation 5.20,

$$N_{\text{dte}} = \frac{N_{\text{raw}}}{1 - N_{\text{raw}} \cdot \tau}, \quad (5.21)$$

in which:

N_{raw} is the raw count rate, with uncertainty $\sigma_N = \sqrt{N}$

τ is the dead time of 3.7 ns, with uncertainty $\sigma_\tau = 0.3$, or approximately 8% uncertainty.

N_{dte} is the dead time corrected count rate, with uncertainty $\sigma_{N_{\text{dte}}}$, which will be determined shortly.

Uncorrelated uncertainties are assumed, and standard error propagation for multiplication and division of arbitrary quantities with uncertainties is used. In general, for a function $f = AB$ or $f = \frac{A}{B}$, with uncertainties σ_A and σ_B , the uncertainty in function f takes the form of:

$$\sigma_f = |f| \sqrt{\left(\frac{\sigma_A}{A}\right)^2 + \left(\frac{\sigma_B}{B}\right)^2}. \quad (5.22)$$

Using this rule twice for the dead time correction equation reveals the uncertainty in the dead time corrected photon count profile:

$$\sigma_{N_{\text{dte}}} = \left| \frac{N}{1 - N\tau} \right| \sqrt{\left(\frac{\sqrt{N}}{N} \right)^2 + \left(\frac{|N\tau| \sqrt{\left(\frac{\sqrt{N}}{N} \right)^2 + \left(\frac{\sigma_\tau}{\tau} \right)^2}}{1 - N\tau} \right)^2}. \quad (5.23)$$

The equation looks identical for the dead time corrected background profiles BG_{dte} as well, as these are physically the same things at this stage of calculations. Having separate variables allows clearer explanations in the next section.

$$\sigma_{BG_{\text{dte}}} = \left| \frac{N}{1 - N\tau} \right| \sqrt{\left(\frac{\sqrt{N}}{N} \right)^2 + \left(\frac{|N\tau| \sqrt{\left(\frac{\sqrt{N}}{N} \right)^2 + \left(\frac{\sigma_\tau}{\tau} \right)^2}}{1 - N\tau} \right)^2}. \quad (5.24)$$

N and τ must always have inverse units compared to each other.

5.5.5 Coadding to improve signal to noise

A common low-level data processing technique for lidar is coadding or binning of signals. This involves summing together the measurements from more than one minute and/or altitude bin.

Coadding improves signal to noise ratios (SNR). Most lidar background photons are white noise (see section 5.5.7) which averages to zero when summed together. Summing lots of white noise photons does not increase its level; there as many low values as there are high values, so they cancel out in general. Summing of signal photons, on the other hand, does increase its level. Therefore, as long as most of the background is white noise, summing the raw measurements improves the signal to noise ratio. The penalty for this choice is a reduction in resolution of the final data products.

Depending on the features in which researchers are interested, either altitude binning, or time binning, or both, may be selected. Looking for thin cloud layers, one frequently

wishes to retain vertical resolution, and so the time resolution is allowed to decrease in favour of improved signal to noise. For quick changes in the weather, high time resolution is necessary, but the vertical resolution may matter less.

Processing for CRL is done at as high resolution as possible while keeping SNR above some useable threshold for the application (frequently above $SNR = 1$ or 2).

There are some calibrations made in later chapters of the thesis demonstrating the utility of making calibration measurements at extremely low time resolution, but using the result to calibrate high-resolution data.

Coadding is performed before background subtraction, which is discussed in Section 5.5.5.

Coadding is a simple sum of all counts N in the n time and/or altitude bins which are being combined:

$$N_{dtc,coadded} = \sum_{i=1}^n N_{dtc,i}. \quad (5.25)$$

Therefore, when coadding is done in units of photocounts, the number of photocounts in the combined bin is the sum of the contributing bins. The units there are still photocounts per altitude bin per time bin, but the altitude and/or time bins are now larger. This sounds trivial, but is pointed out because in the case that coadding is done in MHz units, the number of MHz in the combined bin does *not* increase. The result is the mean, instead, because the units here remain in photon counts per microsecond, and the microsecond does not change in size.

5.5.6 PC uncertainty in coadding

Coadding reduces each of the contributing uncertainties by a factor of the square root of the number of bins being coadded together.

The coaddition procedure is a sum. For a function $f = A + B + C + \dots$, the uncertainty will be:

$$\sigma_f = \sqrt{(\sigma_A)^2 + (\sigma_B)^2 + (\sigma_C)^2 + \dots} \quad (5.26)$$

Thus,

$$\sigma_{N_{dtc,coadded}} = \sqrt{\sum_{i=1}^n (\sigma_{N_{dtc,i}})^2}, \quad (5.27)$$

which is the square root of the sum of the squares of all the contributing uncertainties.

5.5.7 Background subtraction from the sky

Background photocounts come from many sources. Some backgrounds are electronic. Others are optical. Sunlight is one of the largest sources of non-lidar-backscatter photons which are introduced into the photomultipliers during daytime measurements. Moonlight likewise enters the system. Any light leaks in the detectors will also contribute. The vast majority of these sources are both white sources and are independent of altitude in the lidar measurements. Therefore, background levels are inferred by examining the lidar data from altitudes above which the last truly backscattered lidar signals have arrived. For a tropospheric system such as CRL, 80 km and above are typically used.

To isolate the background counts and remove them from the raw lidar signals, several options are possible. All are done after coadding procedures. The modes available in the MATLAB Picon program are:

1. None (No background removal at all)
2. Constant (Calculate the mean rate above a cutoff altitude beyond which no backscattered laser photons are expected; subtract this rate from each value in the profile)
3. Linear (Fit a linear slope and offset to bins above some cutoff altitude beyond which no backscattered laser photons are expected; extrapolate this line and subtract its rate from each value in the profile)

4. Auto (Calculate the line the Linear method would remove if that had been the chosen method. Compare that to the value determined using the Constant method. Use whichever result has the lower uncertainty.)

One would hope that a Constant background removal would work perfectly all the time. Running in “Auto” mode reveals that linear is sometimes helpful too. CRL analyses do not change much as a result, and so are generally run in Constant background removal mode.

The “None” option is very useful for white light calibration measurements in which there is not a sloping profile going down into a constant noise floor; in essence, the entire desired measured profile in these cases is a constant which looks the same as a background signal. If it were to be subtracted out in a background removal procedure, all calibration data would be lost.

5.5.8 Determining the PC background value

The Constant background removal method is used. The signals from high altitudes, known as the background signal, are combined to form one background estimate to be subtracted from the whole altitude range later.

$$BG_{\text{mean}} = \frac{\sum_{i=1}^n BG_{\text{dtc,coadded},i}}{n}, \quad (5.28)$$

in which:

BG_{mean} is the mean background value. There is one value for each (coadded) profile, and this value is used for all altitudes in that profile.

n is the number of altitude bins which are summed for the background determination (number of already-coadded bins above 80 km, usually, for CRL).

$BG_{\text{dtc,coadded},i}$ is the individual dead time corrected, coadded photocount value from bin number i of the background determination.

5.5.9 PC background uncertainty

A mean is used to calculate this representative value, as in Equation 5.28, so standard error propagation assuming uncorrelated errors again is employed.

As a mean involves a sum with uncertainty divided by a constant with no uncertainty (the number of bins summed together is known), the following general relation for uncertainties of sums is required. For a function $f = A + B + C + \dots$, the uncertainty will be:

$$\sigma_f = \sqrt{(\sigma_A)^2 + (\sigma_B)^2 + (\sigma_C)^2 + \dots} \quad (5.29)$$

Thus, the uncertainty in the sum of the background counts is:

$$\sigma_{\Sigma_{BG}} = \sqrt{\sum_{i=1}^n (\sigma_{BG_{dte,coadded,i}}^2)}. \quad (5.30)$$

To calculate the uncertainty in the mean background value, then, with the sum of all background counts in the range given as Σ_{BG} with uncertainty $\sigma_{\Sigma_{BG}}$, and the number of bins added together in this sum as n with uncertainty 0,

$$\sigma_{\text{meanbg}} = \left| \frac{\Sigma_{BG}}{n} \right| \sqrt{\left(\frac{\sigma_{\Sigma_{BG}}}{\Sigma_{BG}} \right)^2 + \left(\frac{\sigma_n}{n} \right)^2} \quad (5.31)$$

$$= \left| \frac{\Sigma_{BG}}{n} \right| \sqrt{\left(\frac{\sigma_{\Sigma_{BG}}}{\Sigma_{BG}} \right)^2 + 0} \quad (5.32)$$

$$= \left| \frac{\Sigma_{BG}}{n} \right| \left(\frac{\sigma_{\Sigma_{BG}}}{\Sigma_{BG}} \right) \quad (5.33)$$

$$= \frac{\sigma_{\Sigma_{BG}}}{n} \quad (5.34)$$

$$= \frac{\sqrt{\sum_{i=1}^n (\sigma_{BG_{dte,coadded,i}}^2)}}{n}. \quad (5.35)$$

The background is expected to be relatively constant. Therefore, the uncertainty for each background element $\sigma_{BG_{dte,i}}$ is approximately the same, and the mean of the individual

uncertainty values can be used instead: $\sigma_{BGdtc_{mean}}$ identically for each element which goes into the mean. This means that the uncertainty in the sum of the background counts is:

$$\sum_{i=1}^n (\sigma_{BGdtc_i}^2) = n (\sigma_{BGdtc_{mean}}^2) \quad (5.36)$$

and the uncertainty in the mean of the background counts is:

$$\sigma_{meanbg} = \frac{\sqrt{\sum_{i=1}^n (\sigma_{BGdtc,coadded,i}^2)}}{n} \quad (5.37)$$

$$= \frac{\sqrt{n (\sigma_{BGdtc,coadded,mean}^2)}}{n} \quad (5.38)$$

$$= \frac{\sigma_{BGdtc,coadded,i_{mean}}}{\sqrt{n}} \quad (5.39)$$

$$= \frac{mean(\sigma_{BGdtc,coadded,i})}{\sqrt{n}} \quad (5.40)$$

5.5.10 Subtracting background from PC profiles

For each (coadded) time bin of data, there is one profile in altitude. Each profile has its own mean background value, BG_{mean} . BG_{mean} is subtracted as a constant from all values in the profile. For each value of dead time corrected, coadded photocounts,

$$N_{dtc,coadded,BGcorr} = N_{dtc,coadded} - BG_{mean}. \quad (5.41)$$

This will from now on be referred to as the “Corrected Counts” signal, as all PC corrections have been finished.

$$N_{corrected} = N_{dtc,coadded,BGcorr}. \quad (5.42)$$

5.5.11 Uncertainty in background-subtracted PC profiles

Once both the photon counting profile uncertainty and the mean background uncertainty are available, they may be combined when creating a background-subtracted photon count profile. As it is a subtraction, the uncertainties add in quadrature, like before:

$$\sigma_{N_{\text{corrected}}} = \sqrt{(\sigma_{N_{\text{dtc,coadded}}})^2 + (\sigma_{\text{meanbg}})^2} \quad (5.43)$$

This is the uncertainty for dead time corrected, coadded, background subtracted, photon counting signals.

5.5.12 Photon counting uncertainty: Relative sizes of contribution from all sources

Most of the uncertainty in the photon counting channel is derived from shot noise. This uncertainty is then propagated through the equations of the low level data processing in the following order:

1. Begin with photon shot noise. This is applicable for both raw counts and raw background counts. This is a statistical uncertainty.
2. Propagate this uncertainty through the dead time equation, in which the dead time uncertainty is a systematic uncertainty (cannot improve by coadding or longer integration).
3. Propagate the uncertainty through the coadding equations. This generally reduces the overall size of the relative uncertainty in the measurement.
4. Determine the uncertainty in the background constant determined from the dead time corrected background values at high altitudes. This is a statistical uncertainty, because it includes the shot noise uncertainty.

5. Add the dead-time corrected, coadded, shot uncertainty and the dead-time corrected, coadded, background uncertainty in quadrature to get a total PC uncertainty for each unbinned data point.

An example of the various contributions for one minute profile on the 12th March, 2013, are given in Figure 5.4. Shot noise is by far the largest contributor at this resolution, but with coadding it can improve. Dead time uncertainty cannot improve without a better estimate of dead time.

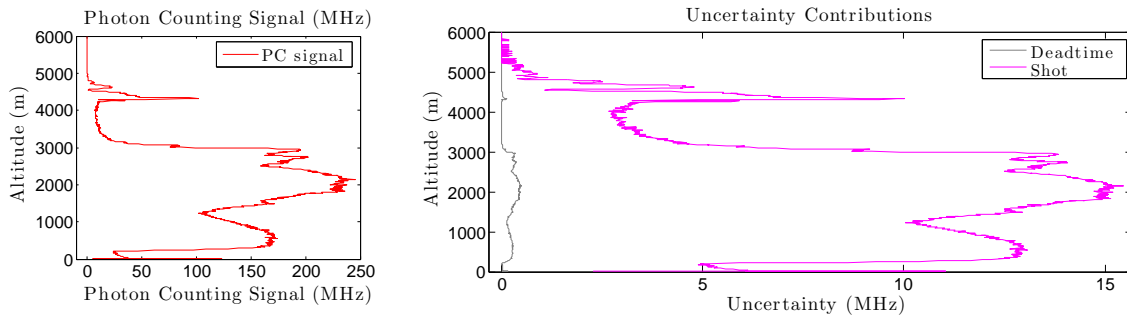


Figure 5.4: One minute profile from 12 March 2013 to illustrate the relative contributions of various uncertainty terms to the photon counting data. Left: Photon counting signal in MHz units. Right: Dead time correction (grey) and Shot noise uncertainty. Shot noise is by far the largest contributor to the overall analogue uncertainty when integrating for a single minute.

5.6 Analogue signals, uncertainties, and corrections

The analogue channels' corrections and uncertainty analysis is slightly more involved than that for the photon counting channels.

There is no dead time correction required, because analogue measurements work by integrating the charge produced by PMT photons rather than by counting individual photons. There is no dead time. There is also no gradual saturation of the detector. There is a maximum analogue rate, which is the maximum binary number which the detector can reach, but the analogue measurement responds linearly to the number of incident photons

up to that point. Uncertainties are larger for analogue measurements at low count rates, however.

A dark count profile is relevant for analogue channels. Even shot noise is not as simple to understand for analogue signals as it is for photon counting signals. These, too, are detailed in this section.

5.6.1 Raw analogue signals

Analogue signals are recorded using an analogue-to-digital converter (ADC) in binary “codes”, with each of the bits (2^{24} in CRL’s case) corresponding to a specific voltage. The maximum bit value can be made to correspond to either 20 mV, 100 mV, or 500 mV, as the user desires. Each interval from one code to the next, then, corresponds to a certain interval in voltage. These intervals are commonly called “steps”. Ideally, each of these steps would be precisely equal in size to each other, and each have a value of 1 least significant bit (LSB). Also ideally, a plot of voltage input to the ADC versus the output codes would yield a linear function over the whole range of the ADC.

Several uncertainties are associated with the raw binary analogue values, from shot noise and from Analogue to Digital Converter (ADC) errors.

5.6.2 ADC error for CRL

Two sources of error are possible during the analogue to digital conversion process: Differential Nonlinearity (DNL) is the difference, in units of LSB, between the actual width of each step and the ideal value of 1 least significant bit. Integral Nonlinearity (INL) is the deviation, in units of LSB, of the transfer function from a straight line. A good summary of the development of these errors is available in [99], produced by Maxim Integrated.

Estimates for the maximum values of the DNL and INL errors for the CRL’s ADC are provided in the specification sheet for the Licel transient recorder: 1.25 LSB for DNL, and

1.0 LSB for INL [100]. These uncertainties may be combined by addition in quadrature to give one overall uncertainty from the ADC in units of least significant bits:

$$\sigma_{\text{ADC}} = \sqrt{(\sigma_{\text{DNL}})^2 + (\sigma_{\text{INL}})^2} \quad (5.44)$$

$$= \sqrt{(1.25 \text{ LSB})^2 + (1.0 \text{ LSB})^2} \quad (5.45)$$

$$= \sqrt{2.25 \text{ LSB}^2} \quad (5.46)$$

$$= 1.6 \text{ LSB}. \quad (5.47)$$

Recall that the value of the least significant bit depends on the range setting of the lidar. This uncertainty may be translated into whichever units are used for analogue data. For raw analogue data, the units are unitary as one LSB in LSB units is just 1. For analogue data converted to mV as suggested by Licel, $\sigma_{\text{ADC}_{\text{mV}}} = 1.6(\text{range}/2^{\text{bits}-1})$ would be the ADC uncertainty mV units using the same conversion formula as for regular data (see Section 5.6.4). For CRL, the lower level data processing range-scales the data, but has not divided by the number of digital steps (Section 5.6.4). Thus, $\sigma_{\text{ADC}_{\text{range scaled}}} = 1.6(\text{range})$ in the range scaled units of the analogue “counts” as they are going through the low level processing and into the gluing procedures which will turn them into virtual counts, or MHz.

5.6.3 Analogue shot noise uncertainty

The second source of analogue uncertainty is shot noise. The shot noise in the analogue (ANA) channel originates from the same Poisson statistics as it does in the photon counting channel, as in Section 5.5.1. However, there are some differences in how it manifests in the analogue data: The noise factor, F , in the ANA channel is larger than that in the PC channel for the same PMT ($F = 1.3$ for ANA, rather than 1 for PC), and only the PC channel has a discriminator to reduce fluctuations in the pulse heights. For more detail, please refer to reference [101] by Hamamatsu, which gives a detailed explanation of the PC and ANA measurement methods in terms of the numbers of electrons, charge, noise factors, etc, in the

PMT. The larger noise factor makes the uncertainty in the ANA channel larger than that in the PC channel by a corresponding factor of $\sqrt{1.3} = 1.14$ for CRL's photomultipliers [101]. Recall that the PC shot noise is equal to the square root of all photons which hit the PMT (including all signal and background photons) and *which are measured*. Correspondingly, for ANA,

$$\sigma_{\text{shot}_{\text{ANA}}} = \sqrt{1.3} \sqrt{N_{\text{ANAm eas}}} \quad (5.48)$$

$$= 1.14 \sqrt{N_{\text{ANAm eas}}}, \quad (5.49)$$

in units of counts or units of MHz, neither of which are directly recorded by the analogue channel.

For the PC channel, this value is very accessible, as the raw photon counting value, $\sqrt{N_{\text{PC raw}}}$. As the analogue data is in analogue units, and not in photon counts nor MHz, taking the square root of the raw measurements has no sense. If we can figure out which true photon count rate corresponds with each analogue measurement, it will be possible to take the square root of that number ($N_{\text{ANAm eas}}$ in units of photons per time bin per altitude bin) to use for the uncertainty calculation.

Help comes from the photon counting measurements which are simultaneous with the analogue measurements. The same photons hit the PMT in both cases, so the true count rates should be identical. As with PC shot noise, the uncertainty in ANA comes from all photons *measured*, and since ANA does not saturate, it is the dead time corrected PC value which is applicable. If one knows the dead time corrected photon counting value which is associated with it (and we do, for CRL), one can find the shot noise for that minute and altitude bin of analogue channel data: $1.14 \sqrt{N_{\text{PC, dtc}}}$.

The complication comes from determining the photon counting shot noise in the absence of photon counting measurements, for instance at high count rates where the PC channel saturates. The solution is to fit a function for each day relating dead time corrected photon counting measurements to the corresponding background corrected analogue count

rates in virtual count units, or MHz. Then it is possible to extend this function to the higher count rates applicable to the analogue data, and infer what the shot noise would have been for count rates of that level.

As laid out in this section, the shot noise determination may seem somewhat recursive. In practice, the corrections and MHz conversions of the analogue signals are carried out first, without regard to uncertainties. Then the shot noise and other uncertainties are determined and are propagated through standard uncertainty equations after the fact, with the original calculated products fed into the equations where necessary.

5.6.4 Turning analogue count rates range-scaled units

The recorder can be set to any of three range options, with the maximum bit value corresponding to either 20 mV, 100 mV, or 500 mV. The measurements must therefore be range-scaled before they may be used. It is possible to turn these binary measurements into physical units (mV), and eventually into units of virtual photon counts (photons per time bin per altitude bin) or virtual photon count rates (MHz).

To turn analogue channel values into physical units, Licel documentation gives the following equation, resulting in units of mV [94]:

$$phys = norm * \frac{analogRange}{2^{ADCbits} - 1}, \quad (5.50)$$

in which *phys* is the analogue signal in mV, *norm* is the mean ADC bit values normalized with the shot number, $2^{ADCbits} - 1$ is the maximum ADC bit value, and *analogRange* is the analogue range setting on the transient recorder. Written in more detail, this is equivalent to:

$$mVdata = \frac{\frac{RawAnalogue}{minute}}{\frac{shots}{minute}} \frac{range}{2^{bits} - 1}, \quad (5.51)$$

in which:

RawAnalogue is the value read from the data file, converted to decimal from binary.

range is the analogue range setting on the transient recorder. This can be set to 20 mV, 50 mV or 100 mV depending on the sensitivity desired for the measurement channel.

bits is the number of bits in the analogue word written to file (25 in this case).

mVdata is the resulting measurement values in units of millivolts.

shots is the number of laser shots included in the one-minute measurement. For CRL, some channels do not measure on each laser shot.

Therefore:

$Rep = Lf$ is the number of laser shots *recorded* per second in the relevant measurement channel (the repetition rate of the recorder), where:

L is the laser repetition rate in units of shots per second

f is the fraction of laser shots recorded in the measurement channel (for example, if the measurement channel records data on every second laser shot, f would have a value of 0.5. If it records on every laser shot, f would have a value of 1).

And thus, in the equation:

$$\frac{\text{shots}}{\text{minute}} = 60 \frac{\text{seconds}}{\text{minute}} \cdot Rep, \text{ which is 600 for the Rayleigh Elastic channel, and 300 for both the parallel and perpendicular channels.}$$

To avoid unnecessary computation with very large and very small numbers, it was determined that for CRL analysis, part of this equation is not necessary to do. Knowing that the end goal with the analogue measurements is to merge them with the photon counting measurements, it is only necessary to find some values that may be scaled to the number of photons measured in the PC channel. The actual mV measurement on the phototube is not required for any reason.

It was decided that range-scaling the measurements was necessary as the range setting on the analogue device was changed between measurement campaigns in order to change the sensitivity of the detector (the detector was made less sensitive; the photon counting channel captures the low count rates well, and even the analogue detector was being saturated at high count rates at the lower range setting), and because the range setting differs between the depolarization PMT and the Rayleigh Elastic PMT. This range-scaling will make values comparable between years with fewer exceptions and “special cases” in the analysis software.

The equation used is:

$$ANAdat a = \frac{\frac{RawAnalogue}{minute}}{\frac{shots}{minute}} range. \quad (5.52)$$

These values are the analogue measurements used to scale into equivalent photon count rates in virtual count rate or MHz units via gluing procedures.

It is acceptable to leave the $2^{bits} - 1$ out of the above equation, as it would just be divided out, and then multiplied back in again. This maximum binary value is the same for all three measurement channels, for all years of measurements. It is simpler to let that be accounted for in the gluing coefficients if needed. The range might change from measurement to measurement, but as the Licel unit does not change, the number of bits will not change.

5.6.5 Uncertainty in turning analogue count rates into range-scaled values

Neither the number of shots per minute, nor the range value, has any uncertainty.

It is possible to convert σ_{ADC} to range-scaled values (using Equation 5.6.4, with the uncertainty in place of the signal), but it is not possible (or not easily possible, in any case) to convert the shot noise into range-scaled units.

It is much better to leave these calculations until later. It is not sensible to figure out the other uncertainties here, but if it was,

$$\sigma_{ANAdat} = \frac{\frac{\sigma_{RawAnalogue}}{\text{minute}}}{\frac{\text{shots}}{\text{minute}}} \text{range}, \quad (5.53)$$

in which

$$\sigma_{RawAnalogue} = \sqrt{\sigma_{\text{shotANA}}^2 + \sigma_{\text{ADC}}^2}. \quad (5.54)$$

5.6.6 Dark Counts

When measuring with a licel and a PMT, there is the possibility of signal being recorded in the absence of incident photons. This is referred to as the “dark counts” signal. As these are noise, and do not make up the desired part of the lidar signal, it is helpful to mitigate as many components of the dark counts as possible. The measurement and removal of some of these dark count contributions is discussed for the CRL in this chapter.

Dark counts in the photon counting channels will be examined first, briefly, in Section 5.6.8. They were not discussed before, in the PC section, because they are small and do not need a correction. The tests confirming this assertion are given in the present section for completeness. The analogue dark counts discussion is more involved, in Section 5.6.9.

5.6.7 Types of dark counts

There are two sources of what are called “dark counts” in this thesis:

1. Photons from infrared emissions which could be avoided or reduced by cooling the detectors. The CRL’s detectors are not cooled, so these photons are free to affect both PC and analogue channels. There is no evidence that this is contributing heavily to the dark count signal, and they will not be discussed further.
2. Any electronic signal that is not caused by photons. This includes spurious signal-induced noise and stray background electrical noise (applicable to both photon counting

and analogue channels), and the much larger floating voltage unique to the analogue channels.

5.6.8 Measuring the dark count profiles in PC channels

The photon counting channels are fine with no dark count subtraction, but for completeness, the results in photon counting channels for Parallel, Perpendicular and Rayleigh Elastic are presented here.

Measurements were made with the lidar's flashlamps on, but with the laser not firing, and with all apertures blocked to prevent stray light from entering the detectors. Results are given in Figure 5.5.

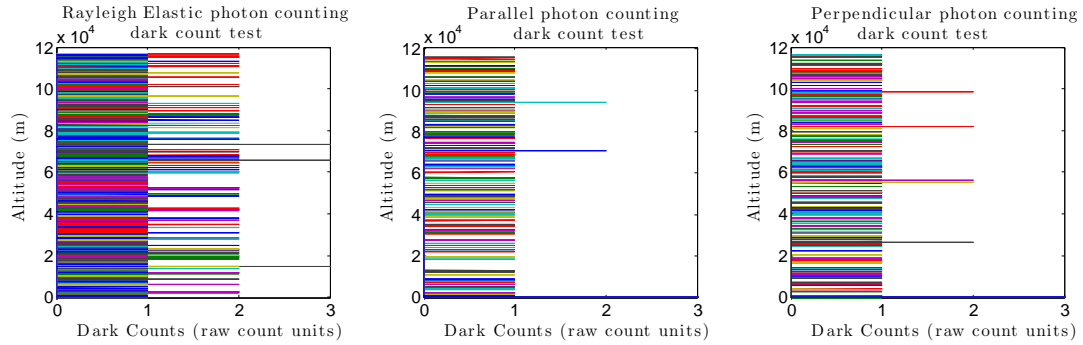


Figure 5.5: Photon counting channel dark count profiles for Rayleigh Elastic (left), Parallel (centre), Perpendicular (right). These are all given in units of raw photon counts, and all have on average fewer than one photon per altitude bin per minute. Therefore, no correction is made for dark counts in photon counting channels.

Values Figure 5.5 in are in units of raw photon counts. To obtain the values in MHz, Rayleigh Elastic counts must be divided by 30, and Parallel and Perpendicular counts must be divided by 15 each. These photon counting dark profiles all come out to constant values of 0 to 1 photons. Therefore, no correction is required. Calculations are considerably more complicated in the analogue channels.

5.6.9 Measuring the dark count profiles in Analogue channels

In the analogue channels there is an intentionally introduced “floating voltage”. This is a baseline number, or zero offset, upon which measurements are made so that any spurious backlash below zero in signal will not require the lidar to measure negative counts in the analogue system [98], [95]. Allowing the transient recorder to deal only with positive values avoids the need for an overly complicated hardware system. This voltage floor is fairly constant with time but can drift with lab temperature, and has no requirement to be constant with altitude bin, either. M. Walker [102] has noted that the profile varies considerably during the first half hour of the licel being turned on, as the instrument warms up (20 minutes is the estimated warm-up time according to the instrument manual, [95]).

Electronic noise is also present. The CRL is able to be run in a variety of configurations, including with a couple of triggering options: The lasers may be triggered internally, or they may be triggered by the rotating polarotor. It is possible that these options have different effects on the dark count profiles. The profiles are expected to be different for each channel, so several tests were carried out to determine what profiles exist under various laboratory conditions.

Tests were carried out on 4 November 2013. Table 5.1 lists, for each test, whether the polarotor was rotating, whether the laser was triggered by the polarotor or the internal Laser 1 trigger (L1), whether the laser was flashing, and whether the laser was firing (it never was). In all cases, the roof hatch was closed and the room lights were turned off. The lab was made as dark as possible to isolate the effects of electronic noise from the effects of stray photons leaking into the detectors. Each setting was run for a minimum of 5 minutes.

Table 5.1: Dark count profile test conditions

Test number	Polarotor Rotating?	Trigger	Flashing?	Firing?	Measurements
1	No	L1 internal	No	No	R
2	Yes	Polarotor	No	No	R, \parallel , \perp
3	Yes	L1 internal	No	No	R, \parallel , \perp
4	Yes	L1 internal	Yes	No	R, \parallel , \perp
5	Yes	Polarotor	Yes	No	R, \parallel , \perp

Measurements were made in the three channels of interest for this thesis: Visible Rayleigh Elastic (Figure 5.6), Parallel (Figure 5.7), and Perpendicular (Figure 5.8). Each plot gives the profiles from the tests in Table 5.1, differentiated by colour, and offset from each other by 100 counts, for better visibility. Test 1 was only measured with the Rayleigh Elastic channel. The parallel and perpendicular channels cannot make measurements without modifications to the lidar without the polarotor rotating. Consequently, they are not in operation in Test 1.

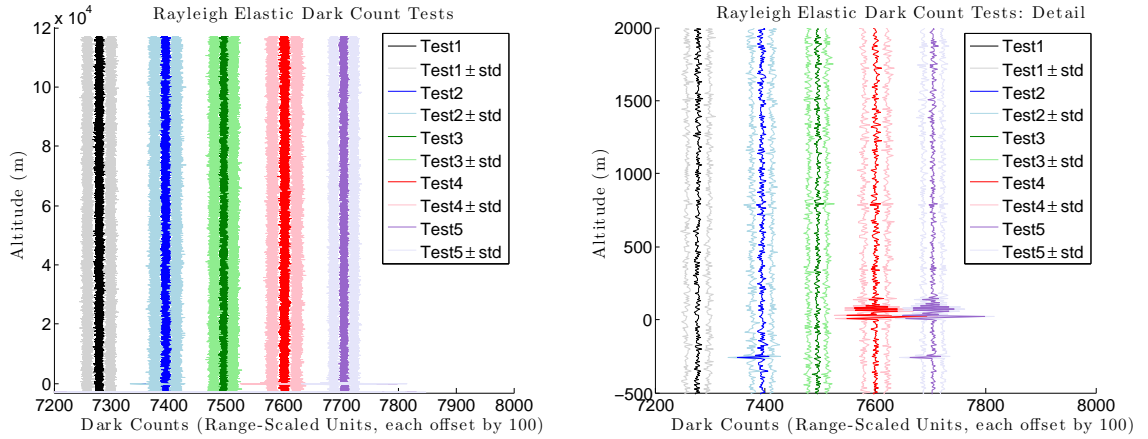


Figure 5.6: Left: Dark counts in the Rayleigh Elastic analogue channel. Right: Detail of low altitude region. All profiles offset by 100 counts from one another for better visibility.

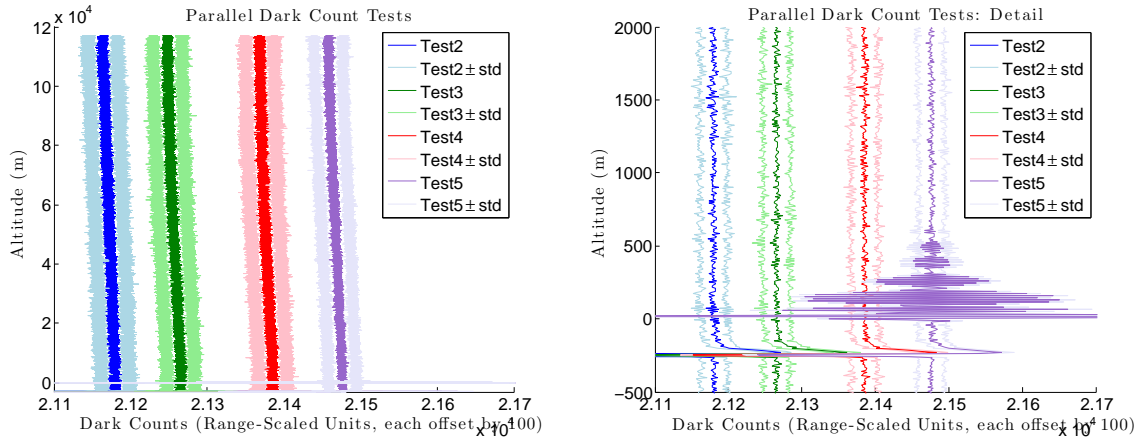


Figure 5.7: Left: Dark counts in the Parallel analogue channel. Right: Detail of low altitude region. All profiles offset by 100 counts from one another for better visibility. Test 1 not included because the polarotor is required to rotate for Parallel measurements (without lidar modifications).

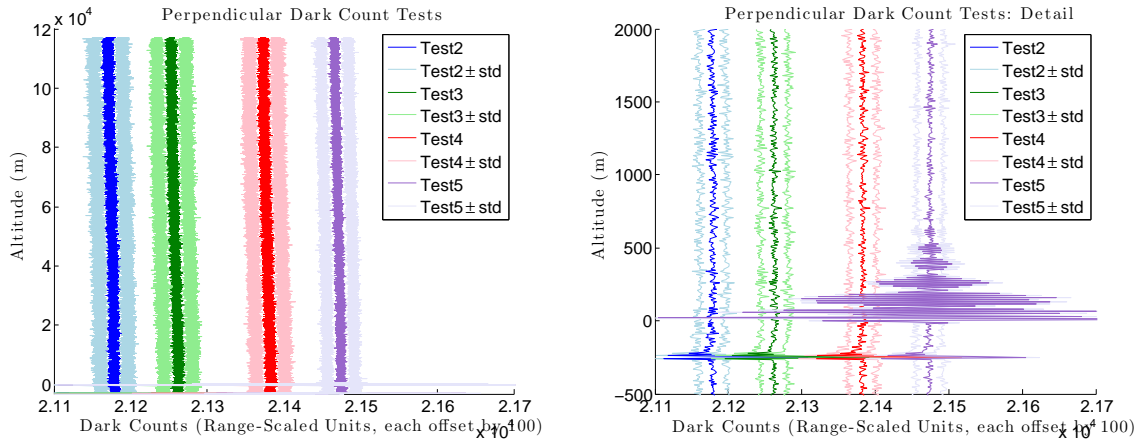


Figure 5.8: Left: Dark counts in the Perpendicular analogue channel. Right: Detail of low altitude region. All profiles offset by 100 counts from one another for better visibility. Test 1 not included because the polarotor is required to rotate for Perpendicular measurements (without lidar modifications).

There are several observations to make comparing the profiles within each plot, and comparing the plots to each other.

5.6.9.1 Effect of flashlamps on dark counts

During tests 4 and 5 in which the laser is flashing, there are visible increases in signals at low altitudes in every channel compared to the tests in which the laser is not flashing (1, 2, 3). See the right hand panels of Figures 5.7, 5.8, and 5.6 for details. Dark signals contribute strongly in the Rayleigh Elastic channel from about 0 m altitude up to about 100 m altitude. It contributes in the Perpendicular and Parallel channels to a greater extent; from about 0 m altitude up to about 500 m altitude. This is the reason that measurements below 500 m are discarded from data processing at later stages. Particularly striking in the parallel channel's data is the ringing shape in the Test 5 profile.

The flashlamps must leak signal into the detectors, either by photons or by noise. Since it is impossible to measure the lidar returns from the sky without the flashlamps being on, this contribution to the signal will always be present when the lidar is in routine operation. It is therefore important to ascertain whether the shape of this noise is the same all the time for any particular channel, and whether the trigger mode has any effect on the shape.

5.6.9.2 Effect of laser trigger on dark counts

Examining the Rayleigh Elastic channel plot first in Figure 5.9, it is evident that the signal present in both flashlamp tests (Test 4 and Test 5) match, although Test 4 was triggered with the laser's internal trigger, and Test 5 was triggered by the polarotor. A more detailed view is given in Figure 5.9, with altitudes between 0 and 150 metres. The profiles in this section have not been offset from each other as they were in previous plots.

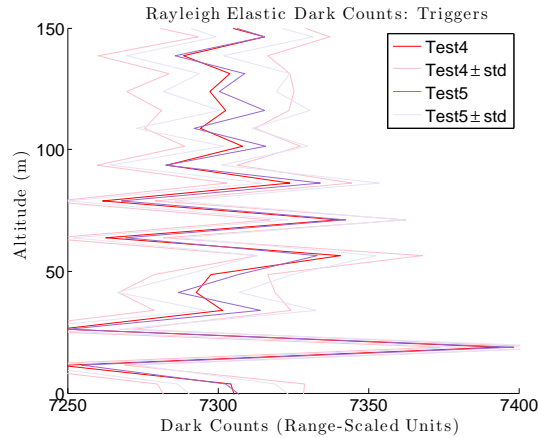


Figure 5.9: Comparison of Rayleigh Elastic channel dark count profiles from tests with two different triggers: Test 4 used the laser’s internal trigger. Test 5 used the polarotor as the laser trigger. The oscillations of the profile in altitude attributed to the flashlamps are identical for both triggering setups.

Not only is the ringing present to the same extent during tests with either trigger, the specific shape of the ringing is consistent, as well.

The results from the same test for the other two channels does not give the same result. In the case of parallel (Figure 5.10, left) and perpendicular (Figure 5.10, right) profiles, the ringing in the dark profiles looks different (and much worse) when using the polarotor as a trigger as in Test 5 than it does with the internal laser trigger of Test 4. Something consistent here is the envelope of the ringing shape in Test 5 in both channels. It peaks around 250 m, again around 400 m, and again at 500 m in both Parallel and Perpendicular measurement channels.

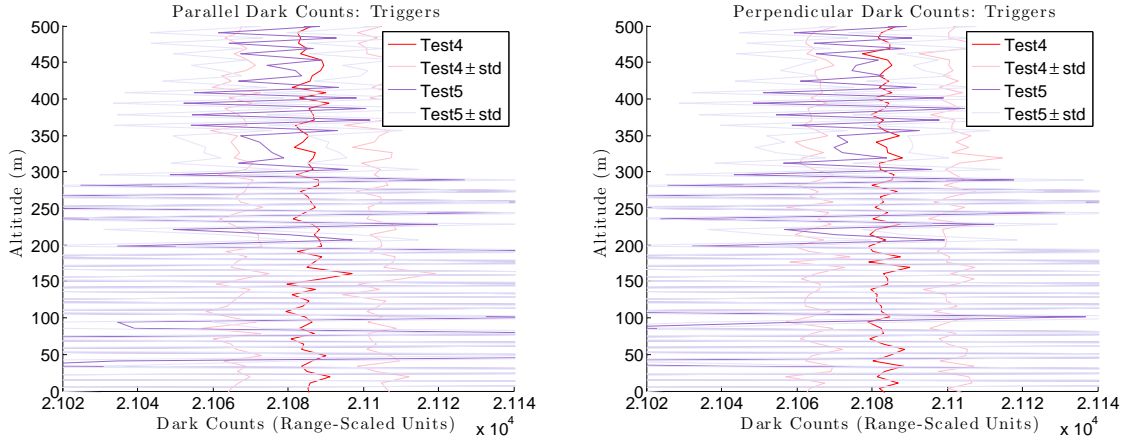


Figure 5.10: Comparing the effect of triggering on Parallel (Left) and Perpendicular (Right) dark count profiles. The ringing is worse with the polarotor acting as trigger (Test 5) than it is with the internal laser acting as trigger (Test 4).

There is unfortunately little to be done to mitigate this for the depolarization channels. The polarotor must remain in operation in order to make the measurements in those channels. It would be impractical to reliably remove the effects of the flashlamps from the dark profiles.

5.6.9.3 Overall trend of the dark count profiles

Ignoring the effect of the flashlamps, the overall trend of the floating analogue voltage may be compared. This is done by removing the mean value from each individual test's profiles (not just the mean profile for each test), and plotting them on top of one another in Figure 5.11.

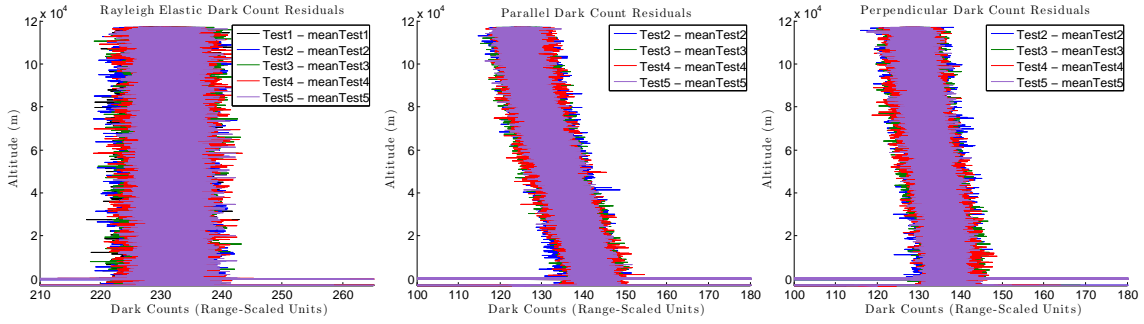


Figure 5.11: Examining the overall shape of the dark count profiles for Rayleigh Elastic (Left), Parallel (Middle), Perpendicular (Right). The Rayleigh Elastic profiles appear linear. The Parallel and Perpendicular profiles appear to curve, and are larger at low altitudes than at high altitudes. The shape of the Parallel and Perpendicular profiles does not appear to be the same.

Comparing the individual profiles within each plot, it is evident that the shape of the profile remains approximately constant over the several hours taken to do all five tests. A linear polynomial fits the Rayleigh Elastic channel well. Different third order polynomials fit the Parallel and Perpendicular profiles best. These two depolarization channels share the same PMT, but they do *not* share the same Licel counter memory, so it is not unreasonable that they be slightly different in this regard.

5.6.10 Choosing a dark count profile to remove for each analogue channel

One dark counts profile needs to be chosen for each channel so that it can be routinely subtracted out of measurement data. As all measurements are generally made with the polarotor as a trigger, and with flashlamps on, the data from those dark count tests (Test 5) are used with additional measurements from November 4th and 11th 2013 to determine the profile. The mean profile was calculated for each channel. The standard deviation of all the dark count measurements from the dark counts test gives the uncertainty estimate. These are illustrated in Figure 5.12. The overall mean dark count value for each channel and its

uncertainty is given in Table 5.2 in units of range-scaled analogue counts for each channel.

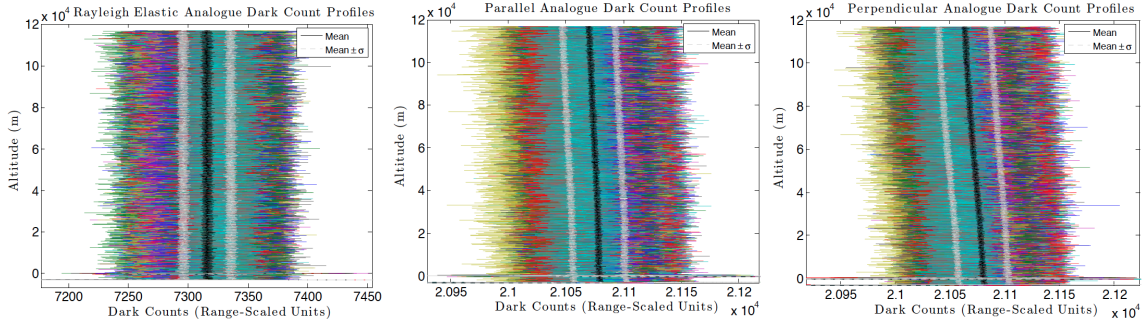


Figure 5.12: Dark count profiles for each analogue channel. Each coloured line is a single profile. Black lines are means; grey lines are the mean \pm the standard deviation. The Rayleigh Elastic mean profile is nearly constant. Neither the Parallel nor the Perpendicular mean profiles are constant.

Channel	Mean Dark Value	Mean Standard Dev.
Parallel	21071	24
Perpendicular	21074	23
Rayleigh Elastic	7315	20

Table 5.2: Mean dark count values for each analogue channel with their associated standard deviations.

Anywhere that the analogue signals are used in data analyses, count rates exceed 20 MHz. At that minimum cutoff for use of the analogue data, these uncertainties correspond to less than 0.3% for the Parallel and Perpendicular channels. Rayleigh Elastic signals are more generally on the order of 80 MHz, making the dark count removal uncertainty an effect on the order of 0.4%. These uncertainties are propagated later in this chapter, and their effects are negligible.

Having a mean value for each profile is instructive regarding the overall magnitude of the correction to be made, and the dark count profiles for Rayleigh Elastic do appear to suggest straight lines. Still, the other two are not linear, and none of the channels is truly constant in altitude. The detrimental effect of removing only a constant dark count profile

is amplified when signals are coadded; the dark count profiles are not white noise, and therefore necessarily add as the signal does. It is necessary to remove the shape of the profiles.

5.6.10.1 Mean profiles for other years

The procedure to find the mean profiles above was tested on the 2013 dark count data. This method was repeated for 2014 dark count measurements. Only the Rayleigh Elastic channel 74 changed noticeably. Current best CRL practices include measuring dark count profiles routinely so that mean dark count profiles may be determined at minimum every time the lidar is opened for a new campaign (once to twice per year).

5.6.11 Removing the dark counts profile

The first approach is:

$$ANA_{\text{Dark Corrected}} = ANA_{\text{Raw}} - \text{DarkProfile}(z). \quad (5.55)$$

If the entire mean dark counts profile as a function of altitude, z , for each channel is subtracted from every measurement scan, some of the resulting dark count corrected scans end up entirely below zero. Although the profiles going into the mean dark profile had the same shape to within small uncertainty, they were offset from one another by a sufficient amount to cause problems. This variation is likely due to the temperature of the transient recorder as it varied with warmup time and lab temperature, and appears only to affect the constant portion of the dark count profiles. This seemed to happen especially for 2014 measurement data when using 2013 dark count profiles. With the new 2014 dark count profiles for use with 2014 data this is less of a problem, but there is a simple solution to the entire difficulty.

It is not necessary to subtract the entire dark count profile from the raw measurement signals all at once. It suffices to remove the *shape* of the profile here, and to leave any

remaining constant-with-height profile to be removed during the subtraction of the constant sky background in a later step.

This is done by:

$$ANA_{\text{Dark Corrected}} = ANA_{\text{Raw}} - \text{DarkProfile}(z) + Q. \quad (5.56)$$

In this manner, raw analogue counts have the entire dark profile subtracted, and then have some constant offset value Q added back in (which is different for each channel). This prevents the dark count corrected analogue signals from being artificially forced below zero, while correctly removing the *shape* of the dark counts profile. The offset values chosen are 21000 for Parallel, 21000 for Perpendicular, and 7325 for Rayleigh Elastic. These values are typical mean values of the dark counts profiles at high altitude (where counts are lowest and the danger of dropping artificially below zero is highest). Using the offset is simpler than attempting to remove some of the mean from each dark counts profile, and calculating this value each time.

In the later background subtraction procedure (Section 5.5.7), a constant or linear background is removed from each dark count corrected analogue profile. This will take care of the offset which has been added in, only insofar as it must to bring the mean values at very high altitudes back to zero. The background subtraction procedure does not differentiate between a constant background from photons from the sky or a constant background from dark count noise, it will treat all sources in the same manner, and eliminate it.

5.6.12 Uncertainty in ANA dark count removal

This uncertainty calculation will be given later, in units of virtual counts and MHz, but it is indicated here in any case.

Because the dark count removal is a subtraction, the uncertainties add in quadrature (Q has no uncertainty, because it was chosen as a specific value):

$$\sigma_{ANADark\ Corrected} = \sqrt{\sigma_{ANASignal}^2 + \sigma_{DarkProfile(z)}^2}. \quad (5.57)$$

5.6.13 Demonstration of dark count removal on example data

An example day's data is presented here to demonstrate the effects of dark count removal on real measurement data from 3 March 2014. In the plots of Figure 5.13, Equation 5.56 is applied to raw analogue measurements. The large signal below 2 km is the actual atmospheric signal. The rest of the profile is the background from both dark counts and the sky. Following the dark count profile correction, the overall amplitude of the resulting profile is not important (other than that it is above zero); rather, note the improvement in shape of the background; it becomes more constant in altitude.

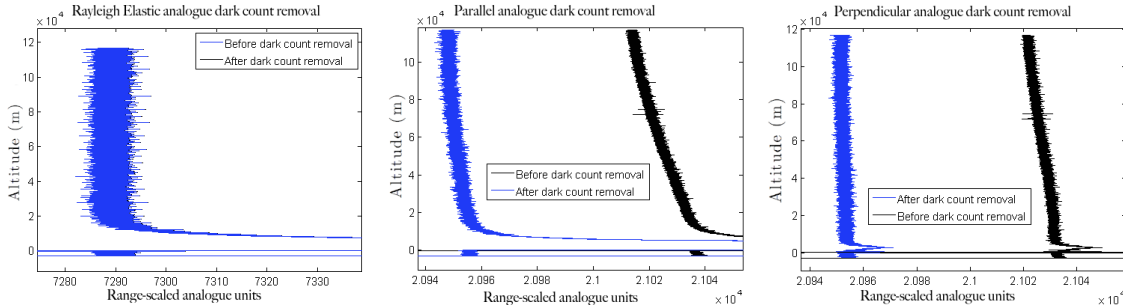


Figure 5.13: Before and after removal of dark counts profiles from 3 March 2013 in the Rayleigh Elastic channel (left), Parallel channel (centre) and Perpendicular channel (right). Note that in the case of the Rayleigh Elastic channel, the dark count correction is so small that the uncorrected black profile is completely hidden behind the corrected blue profile.

Parallel and Perpendicular profiles have straightened out, and are largely constant in height, especially at high altitudes. The Rayleigh Elastic corrected measurements lie practically atop the uncorrected measurements, as only a very shallow slope was removed.

To give some numerical indication of straightness in the resulting profile, the counts were fit with a linear function of altitude. For the Perpendicular channel, for example, the results are:

Fit above 20 km:

$$ANA_{\text{Before Dark Removal}} = -0.0001053z + 21033 ; \text{Norm of residuals} = 108.09 \quad (5.58)$$

$$ANA_{\text{After Dark Removal}} = -0.000017953z + 20953 ; \text{Norm of residuals} = 143.57 \quad (5.59)$$

Fit above 100 km:

$$ANA_{\text{Before Dark Removal}} = -0.000075825z + 21030 ; \text{Norm of residuals} = 43.199 \quad (5.60)$$

$$ANA_{\text{After Dark Removal}} = -0.0000064879z + 20951 ; \text{Norm of residuals} = 59.603 \quad (5.61)$$

The slope coefficients are sufficiently small that the profiles may be considered constant. Thus, the dark count correction procedure appears to be effective.

5.6.14 Discussion regarding prevention of analogue dark signals

Stray background electrical noise is induced by several factors for the CRL, some of which will likely never be specifically measured given the feasibility of doing these studies.

Some of the dark signal is reasonably well understood, and can be measured more specifically for the CRL in future. The floating voltage intentionally used in the transient recorder, for instance, could be measured as a function of time that the recorder has been on, lab temperature, etc. as in [102].

Other lidar groups (e.g. R. Neely, Colorado and Leeds) have reported electronic noise in their signals with every flashlamp trigger. As this noise happens below an equivalent of 500 m in the CRL's data, this is something that could attempt to be somewhat shielded, but likely will not be. The measurements from 500 m and below are removed from analyses routinely.

It is possible that the polarotor itself is inducing noise in the PMTs. If this is the case, perhaps the cables can be better shielded. Further tests with and without the polarotor as a trigger can be carried out at CRL when time permits.

E. Eloranta (University of Wisconsin) has reported seeing ground spike flashes from the laser reflecting off of the roof window in some lidars [103]. The CRL's slow decrease with altitude back to a constant level suggests that this is not a heavily contributing factor to CRL's dark profiles, as such a long lifetime for this type of effect is not expected.

The photomultiplier tubes may be aging and getting more noisy as they do so. Replacement of the PMTs is one option. Lowering the high voltage on some of the photomultiplier tubes has also been suggested as a possible method by which the dark profiles might be mitigated.

Other dark count influences are typically discussed for high signal levels (e.g. during PMT saturation, etc). These do not apply during the CRL's dedicated dark profile tests as the photon signals in these tests were minimal.

For the present, based on the information gleaned from the tests presented in this chapter, CRL's protocols include measuring the dark count profiles regularly so that they may be reliably subtracted from the measurements.

5.6.15 Determining ANA background values

This is done in precisely the same manner as it is for photon counting. The mean signal above some altitude (usually 80 km for CRL) is calculated for each time bin of data, and is subtracted from each value in altitude in the profile. Again, this is done after coadding procedures have been completed.

5.6.16 Analogue background uncertainties

Calculations in much the same manner as those for regular signal are made for background profile uncertainty to begin with, including the same systematic σ_{ADC} and shot

noise $\sigma_{\text{shot}_{\text{ANA BG}}} = \sigma_{\text{shot}_{\text{ANA}}}$ in accordance with the level of the background signal.

From this point, as with the photon counting backgrounds, the uncertainty of the analogue backgrounds is reduced by taking the mean of the n background region measurements.

$$\sigma_{\text{ANAmeanbg}} = \frac{\sqrt{\sum_{i=1}^n (\sigma_{\text{ANABG}_i}^2)}}{n} \quad (5.62)$$

$$= \frac{\sqrt{n (\sigma_{\text{ANABGmean}}^2)}}{n} \quad (5.63)$$

$$= \frac{\sigma_{\text{ANABGmean}}}{\sqrt{n}} \quad (5.64)$$

$$= \frac{\text{mean}(\sigma_{\text{ANABG}})}{\sqrt{n}}. \quad (5.65)$$

Again, the uncertainty of the overall background measurement is the mean of the uncertainties of all background measurements which went into the calculation, divided by the square root of the number of measurements included.

To find the σ_{ANABG} in the first place, the same procedure is used as that for finding the shot noise.

5.6.17 Uncertainty in removing the background from ANA profiles

This procedure is the same as that used in the PC process.

$$\sigma_{\text{ANA,coadded,bgCorr}} = \sqrt{\sigma_{\text{ANA,coadded}}^2 + \sigma_{\text{ANAmeanbg}}^2}. \quad (5.66)$$

These uncertainties are determined specifically following all conversions to virtual counts units.

5.6.18 Conversion of ANA to the same units as PC

To merge the analogue and photon counting profiles into a single profile of photon counts as a function of altitude, both contributing profiles must be in the same units. Photon counting profiles are natively in the units of photon counts per (possibly coadded) altitude bin per (possibly coadded) time bin. The process for converting photon counting profiles to MHz units is given in the previous chapter. The analogue channel's signals must be converted into one of these units in order for the combination of the profiles to be possible. Information from the photon counting channel is required in order to accomplish this.

The method to convert ANA signals into virtual photon counts depends on the following: In principle, if the photomultiplier is recording a count rate at which both analogue and photon counting channels are responding linearly, and without too much noise, both channels' measurements should eventually report the same number of counts for the signal. They are measuring the same photons, after all. If measurements are made at several such count rates, a linear function can be discovered to reliably transform analogue signals to virtual counts which match the photon counting signals. This takes the form [96]:

$$ANA_{VC} = a * ANA_{raw} + b, \quad (5.67)$$

in which:

ANA_{VC} is the analogue count rate in virtual counts units

ANA_{raw} is the range-scaled, dark count subtracted analogue signal

a and b are the “gluing coefficients” required to transform analogue signals into MHz.

Because, where linear, $ANA_{VC} = PC_{counts\ units}$, the above equation is equivalent to:

$$PC_{counts\ units} = a * ANA_{raw} + b, \quad (5.68)$$

and a line may be fit to a plot of $x = ANA_{raw}$, $y = PC_{counts\ units}$, to determine the slope, a , and the offset, b .

This procedure can be done equally well in terms of MHz units, in which $PC_{counts\ units}$ is everywhere replaced with PC_{MHz} , and the a and b coefficients will have different values. For CRL, the procedure was done using photon counts units.

The processing which *must* be done to the analogue signal before this calculation includes range scaling and dark count correction. The floating voltage which the raw analogue signals carry is not from photons, and therefore does not contribute to the virtual photon rate which is sought here.

The processing to be done to the photon counting signal may or may not include a dead time correction. If a dead time correction is included, this extends the range over which the PC signal is said to be responding linearly. It therefore extends the range of count rates which can be used to find a and b . If it is not done, the top limit for photocount rates which may be included in finding the gluing coefficients will be lower. CRL chooses to dead time correct the PC data before determining gluing coefficients, but both ways have been tested and give the same result.

In neither case is the sky background subtraction required, but it is allowable, and if done for one channel, must be done for the other channel as well. A photon is a photon, whether background or signal, as long as it is not electronic noise. For background subtraction, each profile has had the same number of photons subtracted from the total, although in the analogue profile's case, it was done in other units. The advantage to doing the background subtraction for CRL is that the dark count removal routine may be carried out as usual, with the background subtraction routine taking out all residual constant dark noise (the “ Q ” value added in Section 5.6.11). The gluing coefficients determined in each method will be different, and must be applied later to routine measurements at the same stage of processing. If opting to subtract the background before determining gluing coefficients, as the CRL does, care must be taken to determine the eligibility of all counts in the coefficient

test using their non-background subtracted counterparts (see Section 5.6.18.1).

Note about terminology: Note that the term “gluing coefficients” is common in the literature, despite their true use as unit conversion coefficients to turn the analogue signals into counts or MHz. This is because many lidars include the processes in this section as part of the “merging” or “gluing” procedure. At CRL, it is felt that it makes more sense to look at the processing up to this point as a means to unit conversion for the analogue signals only, for the following reason: The end result of this piece of the procedure is *not* a glued profile; rather, it is two profiles of the same quantity, in the same units. The gluing procedure (Section 5.7) will then take these two profiles (PC and ANA, both in identical units), choose the best pieces of each, and combine these best pieces into one merged, or glued, profile.

5.6.18.1 Linearity limits used for determining gluing coefficients

To choose a subset of lidar data which is eligible to be used for determining gluing coefficients, a check must be made to determine where each channel is responding linearly. That is to say, over what range of input photon count rates does the measurement accurately report the presence each additional photon?

Measurements on a clear sky night can provide the answer. Consider that the PMT must be responding linearly if it is measuring the number of photons it is supposed to for a given bin. How many are correct? A clear sky should have raw photocount profiles which, when scaled for altitude, are proportional to the density of the atmosphere. As the density profile of the atmosphere with altitude is an exponential, it suffices to plot the range-scaled profile on a log scale, and expect that a straight line will result. Where the profile deviates drastically from the straight line, there is an indication that the channel is not responding linearly. That is to say, photons are arriving at the detector which are not being counted. These are then some indication of the limiting count rates which can be used for gluing. An example plot of such measurements from 28 February 2013 is given in Figure 5.14

for the Rayleigh Elastic channel. Both profiles are given using non-background-corrected photocounts. Saturation limits for the PC channel especially depend on the *raw* photon count rates, as measured. If photons from signal plus background were arriving at rates too high for linearity, subtracting a mean background rate in post-processing doesn't undo this saturation.

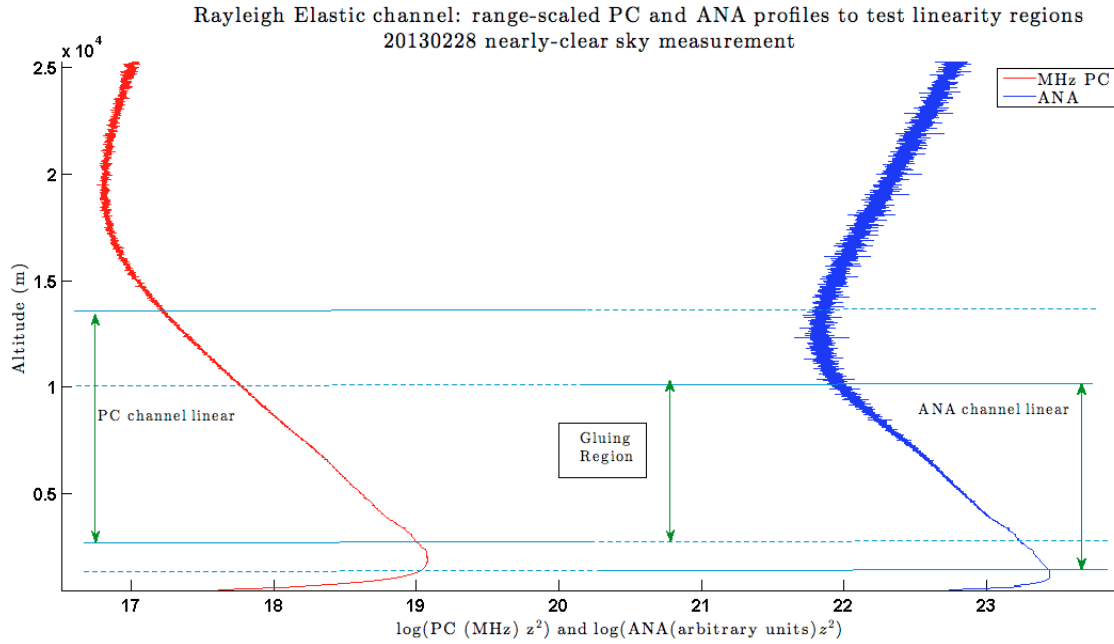


Figure 5.14: Gluing regions for the Rayleigh Elastic channel. Regions of linearity for photon counting (red profile) and for analogue (blue profile) are indicated. The linear region in common for both channels is the gluing region. The PC values are given here in MHz units as the specification sheets provided by Licel indicate gluing cutoffs in these units.

This plot includes one small region of cloud at low altitudes, but indicates that the photon counting channel behaves linearly between count rates of 7.24×10^{-6} MHz (or approximately 0 photons per 7.5 metre altitude bin per 1-minute time bin, which is at 13600 m altitude in this particular profile) and 23.8 MHz (714 counts/bin/min; here at 2738 m altitude). The analogue channel behaves linearly between 35.35 analogue range-scaled units (here at 10007 m altitude) and 7076 analogue range-scaled units (here at 1455 m altitude). The upper limit is not because the ANA channel has saturated; rather, it is low enough in the atmosphere that the exponential dropoff of signal with altitude is no longer a good

assumption. The gluing region, the range of linearly-responding signals in common with both channels, lies between 0.514 MHz and 23.8 MHz. This happens to correspond to 2738 metres to 10007 metres altitude in this plot, for this day, for this minute of measurement.

There is no need for the gluing region to remain constant *in altitude* from day to day, or indeed from minute to minute; rather, the region remains reasonably constant in time *in terms of count rate limits*.

5.6.18.2 Linear fits to determine gluing coefficients

The coefficients were calculated for 5 nights in 2013 using only data with photon count rates between 0.514 MHz and 23.8 MHz (15.42 to 714 counts/bin/minute; Figure 5.15; Table 5.3). The variation between days is much smaller than the uncertainty in the regression and in the measurements. The coefficients are different between each PMT. The values for Parallel and Perpendicular which use the same PMT are very similar to each other, but are different from the Rayleigh Elastic, which uses a different PMT, set at a different analogue maximum range setting.

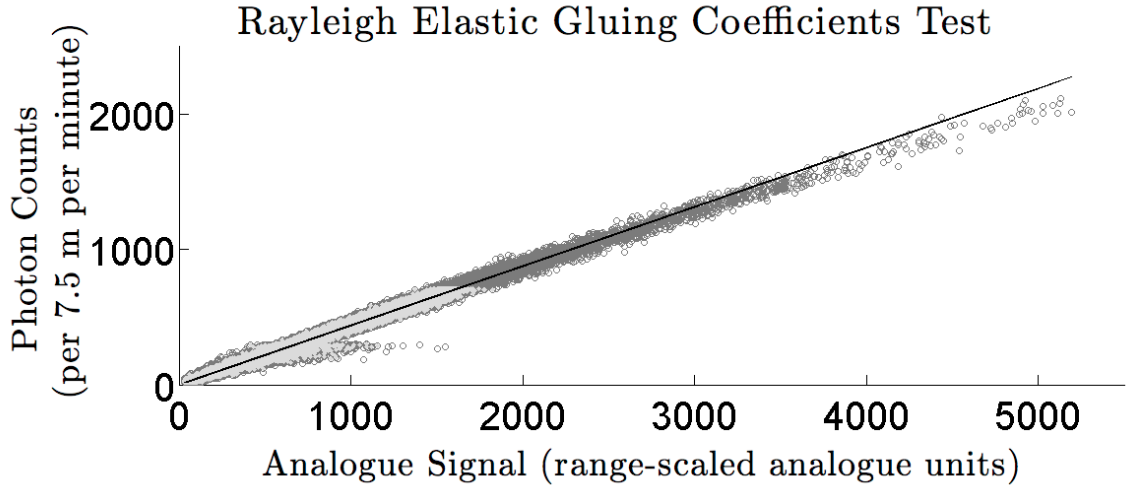


Figure 5.15: Test for the Rayleigh Elastic channel to determine its gluing coefficients. Dark grey circles are all 5 gluing coefficient days' PC measurement plotted as a function of their ANA counterparts. The light grey dots clustered at lower left indicate which of these data points are in the gluing region determined in Section 5.6.18.1. The light grey points are used to create a linear regression, which is plotted as the line. The slope and offset of this line give the gluing coefficients a and b . In actuality, there are three lines plotted: The fit, and the fit plus and minus its uncertainty. Although there is a decently large spread in the measurements, the uncertainty in the fit itself is very small; all three lines are indistinguishable from each other at the scale of this plot.

Channel	a (bg subtracted)	b (bg subtracted)
Rayleigh Elastic	0.43854 ± 0.00005	0.53 ± 0.02
Parallel	0.08614 ± 0.00004	-0.243 ± 0.004
Perpendicular	0.0865 ± 0.0001	-0.254 ± 0.008

Table 5.3: Gluing coefficient results from 5 nights of measurement in 2013. The coefficients are similar for the Parallel and Perpendicular channels which share a PMT, and are different for the Rayleigh Elastic channel. These are for background subtracted measurements, and were calculated in units of photon counts per bin per minute. They can be used to convert ANA signals into units of virtual count rates; not MHz.

To give an idea regarding the effect of uncertainty in the a fitting coefficient on the final retrieved depolarization parameter using the Option 2 method (with Rayleigh Elastic and Parallel channel data; Chapter 9): Using $a + \sigma_a$ for the Rayleigh Elastic channel as quoted here (0.00005), and comparing to a alone, for a cloud which has moderate depolarization parameter of value 0.55 at 1000 m altitude above the ground, and which begins with a

Rayleigh Elastic analogue signal of 5000, the result is a net change in d of only ± 0.00012 (or 0.03% relative change). If σ_a is determined instead only to the ± 0.001 level, d changes by ± 0.003 (0.6% relative change). If σ_a is determined only to the ± 0.01 level, d changes by ± 0.03 (6% relative change). As other uncertainties (many much larger; see Figure 5.16 for some examples) also enter into the calculation for d , those due to each gluing coefficient should be made as small as is reasonably possible during calibration in an effort to keep total uncertainty in d less than ± 0.1 .

Data from 19 November 2013 was used to test the effect of leaving the background in or removing it during the coefficient calculations (Table 5.4). The values for slope (a) did not change much, but those for the offset (b) did. This makes sense. The a slope factor describes “For each additional quantity of analogue signal, how many additional photons must have fallen on the PMT?”, while the b takes into account all offset terms (such as Q which was added into ANA but not to PC, etc).

Channel	a (bg subtr.)	b (bg subtr.)	a (no bg subtr.)	b (no bg subtr.)
Rayleigh Elastic	0.44	1.9	0.44	-25
Parallel	0.082	3.4	0.081	7.8
Perpendicular	0.086	0.39	0.085	3.5

Table 5.4: Gluing coefficient results from 19 November 2013. The values of a do not change between the background-subtracted and the non-background-subtracted cases. The offsets b do change. These are in units of photon counts per bin per minute, and not MHz.

Once the gluing coefficients are determined for each channel, the analogue counts may be converted to equivalent virtual count rates through the use of Equation 5.67.

5.6.18.3 Conversion of ANA signals to MHz

Once the analogue signals are known in units of virtual photon counts per unit time per unit altitude, they may be converted to MHz units through the same procedure that was used to convert PC photon counts to MHz in Section 5.5.2. Equation 5.11 is given again, here:

$$CtsMHz = \frac{Rawcounts}{MHz_{ConversionFactor}(n_{zbins} \cdot n_{tbins})}, \quad (5.69)$$

in which, for the CRL's analogue channel:

Rawcounts is the dark count corrected, background subtracted, coadded analogue signal in units of virtual photon counts per altitude bin per time bin

MHz_{ConversionFactor} is the conversion factor to apply, which is approximately:

MHz_{ConversionFactor} ≈ 30 for Rayleigh Elastic

MHz_{ConversionFactor} ≈ 15 for parallel and perpendicular.

n_{zbins} = 1 is the number of 7.5 metre altitude bins which have been coadded.

n_{tbins} = 1 is the number of 1 minute time bins which have been coadded.

The uncertainties must also be converted to these units.

5.6.18.4 Conversion of ADC error to virtual counts and MHz

All analogue measurements N_{ANA} are converted into “virtual counts” units through one linear equation which includes a gluing slope coefficient (a) and a gluing intercept coefficient (b) found during the gluing procedure. The analogue ADC range settings are included explicitly here as R_{ADC} .

$$N_{ANAVirtual\ Counts} = a * N_{ANA}R_{ADC} + b. \quad (5.70)$$

The uncertainty term behaves in the same manner:

$$\sigma_{ADC\ Virtual\ Counts} = a * \sigma_{ADC}R_{ADC} + b. \quad (5.71)$$

These virtual counts may be converted to virtual MHz through the same conversion factor used on photon counting conversion to MHz, X_{MHz} . This results in:

$$N_{ANA_{MHz}} = \frac{a * N_{ANA} R_{ADC} + b}{X_{MHz}}. \quad (5.72)$$

The uncertainty term behaves in the same manner:

$$\sigma_{ADC_{MHz}} = \frac{a * \sigma_{ADC} R_{ADC} + b}{X_{MHz}}. \quad (5.73)$$

5.6.18.5 Analogue dark count uncertainties in MHz

Calculations given in Section 5.6.10 have already indicated the dark count uncertainties, in units of range-scaled analogue signals, and are presented here now converted into MHz:

$$\sigma_{\text{dark}_{ANA \perp}} = 24 \text{ Range-scaled units} = 0.122 \text{ MHz} \quad (5.74)$$

$$\sigma_{\text{dark}_{ANA \parallel}} = 23 \text{ Range-scaled units} = 0.122 \text{ MHz} \quad (5.75)$$

$$\sigma_{\text{dark}_{ANA R}} = 20 \text{ Range-scaled units} = 0.310 \text{ MHz} \quad (5.76)$$

To see the effect of the dark count uncertainty on the overall uncertainty, the measurements from 11 March 2013 were checked in detail. At the lowest analogue MHz rate ever employed for CRL data, the inclusion of the dark count uncertainties in the overall uncertainty calculations (Section 5.6.19) results only in a tiny increase: less than 0.015 MHz for Rayleigh Elastic at 80 MHz count rates, less than 0.0019 MHz for Parallel at 20 MHz count rates (the lowest used), and less than 0.06 MHz at the location of maximal effect in the perpendicular channel - but the perpendicular channel's count rates were all below 20 MHz and thus the analogue would not be used at all in that data set. Therefore, it makes almost no difference whether or not the dark count uncertainties are included in the budget.

5.6.19 Uncertainty contributions: Relative sizes from all the sources, ANA

To see the relative sizes of various analogue uncertainty terms, refer to Figure 5.16. Shot noise is by far the largest contributor. However, since shot noise is statistical, this can be improved with coadding, while some of the other terms cannot.

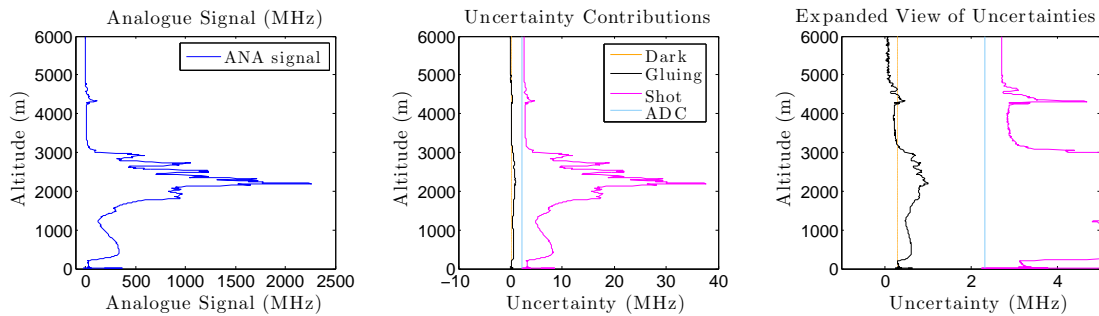


Figure 5.16: One minute profile from 12 March 2013 to illustrate the relative contributions of various uncertainty terms to the analogue data. Left: Analogue signal in MHz units. Centre: Dark count (orange), Gluing uncertainty (black), Shot noise (magenta) and ADC least significant bit error (light blue) are plotted. Right: Expanded view of centre plot to see detail in the smaller quantities. Shot noise is by far the largest contributor to the overall analogue uncertainty when integrating for only one minute.

5.7 Gluing: Combining the ANA and PC channels

The Licel transient recorder creates two measurements for each photomultiplier tube: one photon counting (PC) and the other analogue (ANA). The photon counting measurements are good only for low count rates; they can count single photons, but begin to saturate fairly quickly at higher rates. The analogue channels are noisy at low count rates, but are able to integrate photons together into a current, and thus measure high count rates effectively until the upper bit limit of the detector is reached. In order to use these signals, it is helpful to merge them together into a single profile extending from very low to very high count rates.

At this stage of processing, both ANA and PC data are in units of virtual counts (or MHz, if that is preferred). Being in the same units as each other, their profiles should be identical where they are both valid, and it should be possible to construct the best composite profile using the information from the two profiles where each is performing optimally.

5.7.1 Choice of profile to use at each point

The uncertainty in photon counting measurements is necessarily smaller than the uncertainty in analogue measurements expressed in virtual counts or MHz. Therefore, the photon counting channel is preferred in locations where it is correct to use it.

Because the PMT channel linearity depends strictly on how many photons hit the photocathode, and nothing else, any decisions about whether the PC profile is trusted to be linear at a certain altitude have to be made based on how many photons were incident on the phototube during that minute, within the time for that altitude bin. This means that the dead time corrected, but not background subtracted, photon counting values should be used for assessing the cutoffs. Saturation and nonlinearity, again, does not care whether the photons that hit the cathode of the PMT are part of the background or the signal; it only counts them linearly, if there are sufficiently few, or does not, if there are too many.

With the high count rate limit for photon counting being 23.8 MHz for CRL, the decision was made to code the gluing procedures using a 20 MHz cutoff. This allows a small buffer between the desired upper limit and the true upper limit of the detector.

In CRL measurements, the count rates in the perpendicular channel rarely exceed 20 MHz. It happens most often in the parallel channel, and happens regularly in the Rayleigh elastic channel. Thus, the algorithm is slightly different programmatically for each channel, but always amounts to using PC for raw PC count rates under 20 MHz, and analogue otherwise. Details for each channel are given here:

- The perpendicular channel hardly ever saturates the photon counting channel. It does not get many photons, both because the sky will only return a maximum count rate in

perpendicular which is half of the maximum parallel count rate because of scattering physics in the atmosphere and CRL's polarized laser beam, and because the CRL's upstream optics suppress the transmission of perpendicularly polarized light. Thus, it rarely needs to dip into its analogue signal, except in rare cases where there is a huge unpolarized sky background already contributing some large number of photons, and then there is a thick depolarizing cloud which adds even more photons to that channel. Thus, by default, the dead time and background corrected photon counting channel is used. If the raw photon counting channel indicates that the upper limit in this channel has been reached (20 MHz), then the background corrected analogue profile is examined to see whether that is eligible. If so, it is used for the PC-saturated data point.

- The parallel photon counting channel frequently oversaturates. It is only at very high altitudes that the photon counting profile is usually useable for this channel. It makes sense to use analogue measurements by default, and then look at the raw photon counting profile to identify any regions which are under the 20 MHz upper limit for photon counting, and use the corrected photon counting data there. The difference in algorithm compared to that used for perpendicular has only to do with saving computational time when processing the data.
- The Rayleigh elastic channel is quite well-balanced. Its photon counting channel saturates some of the time, but not all. Like for the parallel channel, the analogue signal is used by default, with photon counting measurements filling in where appropriate.

In all three channels, exceptions are made for any photon counting locations marked as underflow or which have been flagged for some other reason; if analogue measurements are eligible in those locations, they are used despite their usually larger uncertainty.

5.7.2 An example night of gluing: 12 March 2013

For an example night, it is instructive to show 12 March 2013. This night has clear periods and cloudy periods. The 10th Rayleigh Elastic channel profiles from this night show a reasonably sharp cloud in which photon counting profiles clearly oversaturate, going back to linear count rates above the cloud.

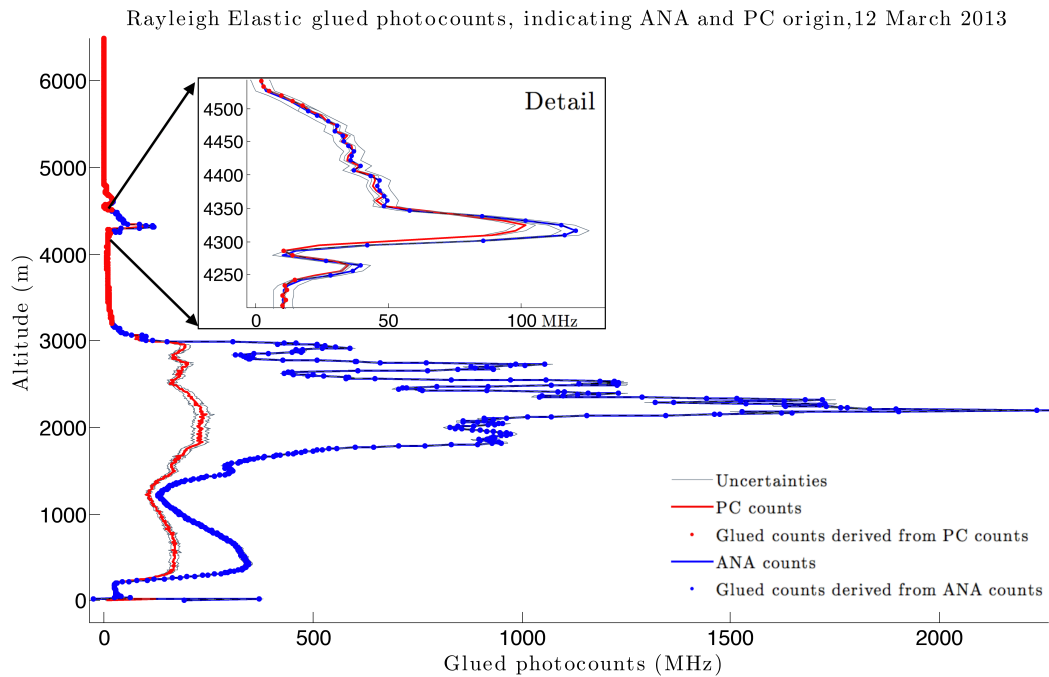


Figure 5.17: One minute glued profile of data from the Rayleigh Elastic channel. The origins of each of the glued data points, from PC (red) and from ANA (blue), are indicated. Uncertainties are also plotted, but they are so small at these scales as to be difficult to see in the plot. A detailed section of the small peak at 4350 m is also provided. Here, the glued profile (dots) begins using the PC profile, switches to the ANA, and then goes back to the PC. The peak at 4350 m is saturated for the photon counting channel, but is still responding well for analogue.

In Figure 5.17, it is clear that the photon counting and analogue measurements, when both in MHz units, give identical results at low count rates (albeit with lower PC uncertainty); the profiles lie on top of one another. For higher count rates, large differences are seen. The PC rates there have reasonable uncertainties indicated, but we must recall that

these describe how certain we are that those values are what the PC channel measured; they are not an indication of how correctly the PC channel is measuring the photons incident on the PMT. The values are, in fact, completely invalid at count rates much above 20 MHz. The analogue profile, at these count rates, continues to provide accurate measurements of the photon rate on the PMT.

The glued profile, including the best contributions of both channels, is indicated in the plot. It looks acceptably smooth in its transitions from PC to ANA and back again. This is typical of most CRL data in the Rayleigh Elastic, parallel, and perpendicular channels.

On days where the gluing coefficients are perhaps not ideal (say, the calibration was done many months apart from the measurement and something changed slightly in the system during that time), and on days in which the count rate is jumping back and forth above and below 20 MHz along the profile, there can be some artifacts introduced to the glued profile. It is helpful to have both original profiles available for checking in cases that high frequency oscillations in derived products are found.

This plot is a helpful reminder that choosing to use PC above a certain fixed altitude, and ANA below, is a terrible idea for tropospheric measurements. If that had been attempted for the case of 12 March, the derived products would be either more uncertain than necessary (in the best case, if the analogue measurements “cut in” at too high an altitude), or would be completely wrong (in the worst case, in which the PC measurements are assumed to be linear above a certain, poorly chosen altitude). In the absence of a cloud, perhaps the PC count rate would usually be below 20 MHz at 2000 or 3000 m altitude. That certainly is not the case with the cloud indicated in the profile of Figure 5.17. Going back to the raw count rates for *each data point* is the safest way to ensure the best possible measurements are contributing to the glued profile.

5.7.3 Glued profile uncertainties

These are the easiest uncertainty estimates to find. For data points which were contributed by the photon counting channel, then the uncertainty of the photon counting measurement is applied. For those from the analogue, the analogue uncertainty is applied.

This sometimes makes the uncertainty envelope around the glued profile have some discontinuous jumps when the contribution changes from PC to ANA, but this is not a problem; it is just something to be aware of if interpreting lots of data right around these regions.

5.7.4 Other gluing options not used by CRL

Merging or gluing together analogue and photon counting data is a common practice in order to get more orders of magnitude of lidar signal. There are lots of different ideas about how to find the coefficients, and how to apply them. The CRL group agrees with some of these, but has not implemented these procedures as of yet. Other methods are not appropriate to use. Some methods to glue profiles together are explored here, but as this is a whole field of study in and of itself, a more detailed survey of gluing and merging options for analogue (ANA) and photon counting (PC) profiles is beyond the scope of this thesis. CRL used the first method which worked well enough to continue calibration of the depolarization measurements, although improvements may be made in future.

Making a cutoff based on altitude to switch from PC to ANA in the glued profile

Arguments are made here instead for keeping the cutoff criteria for switching between PC and ANA based on raw photon counting rates rather than altitude. The altitude-cutoff method works well for lidars which have no clouds in their data. One example of such a lidar is the Purple Crow Lidar in London, Ontario, which glues its profiles primarily for use in making stratospheric temperature profiles. There are no clouds included in any of the

useable data. Their profiles always have approximately the same count rates at the same altitudes from day to day. That means that if they have a large enough range for which both ANA and PC profiles are linear, then the little bit of variation in the ideal cutoff value for altitude from one to the other can vary and still be in that linear range, even on days where there is more moon background, sun background, or lower laser power.

This does not work at all for CRL, which is primarily a tropospheric instrument designed for studying clouds. More often than not, a cloud appears in the data brighter than 20 MHz (requiring analogue signals), surrounded by regions above and below with count rates smaller than 20 MHz (where PC would be better). Clearly for CRL, making the switch between analogue signals at low altitudes, and photon counting signals at high altitudes, cannot be done with a single constant cutoff in altitude.

Doing a linear regression on each profile of data to find gluing coefficients for each minute

CRL uses carefully curated measurements from a clear sky date, combining the entire night's data together, when determining gluing coefficients.

Checking gluing coefficients for every lidar profile can be computationally intensive, and is not necessarily instructive unless all profiles contain a variety of count rates within the linearly-responding region of the PC channel, coming mostly from regions of clear air. In the case of clouds, this makes no sense. Petty and Turner 2006 [104] derive gluing coefficients profile-by-profile (in the same manner as CRL, but only with a single profile's data at a time), but recognize that fits cannot be attempted when there are clouds, or when the sky background is greater than the 50 MHz maximum of the linear region of their PC channel. They suggest instead calculating an *a priori* slope and offset, and adjusting these every couple of hours, whenever a suitable situation presents itself.

One advantage to calculating glue coefficients minute-by-minute is that there are statistical fluctuations in the glue coefficients, according to [104], which cannot be removed by

statistical screening. It is possible that CRL gets around this issue by removing the constant background signal with every shot before gluing. So long as the statistical fluctuations discussed in [104] are constant in altitude (i.e. the shape of the dark counts profile remains the same, and just migrates to larger or smaller values, as we seem to find with CRL), then the CRL's background removal procedure removes these statistical fluctuations for each scan. This bears further investigation for CRL. In any event, CRL measurements are more often cloudy than not. The times for suitable gluing coefficient measurements may be few and far between as a result.

It has been found by Newsom et al. 2009 [105] that the glue coefficients change with time of day, due to the solar background. This effect may be smaller for CRL than it is for other lidars. The field of view of the CRL is smaller than the field of view for many other lidars. Also, the CRL's depolarization measurements are made in the green, and not in the UV, where most sunlight photons lie. A recent study by Zhang et al. 2014 [106] has followed the work of Newsom et al. and has attempted to use their method, but with more stringent restrictions on the quality of data going into each profile's fit to find the glue coefficients. They have found that when lots of daytime low-correlation data was included, more variation in slope from daytime to nighttime was produced. When this low-correlation data was not used, there were fewer data points in the daytime fits, but the overall trend of the slope was constant over 24 hours. This is encouraging for CRL which calculates its slopes but once in a while.

There is at least one paper on this subject whose language implies a gluing procedure which does not make sense at all. In this paper, gluing coefficients are derived profile by profile, and it is stated that the calibration values a and b change depending on the weather, but this is not strictly-speaking true; the values calculated in a cloudy day are not different gluing coefficients at all – in fact, the data are ineligible to be used for calculating the gluing coefficients in the first place. Yes, values calculated using the same regression method will be different from clear sky days to days with a thick cloud (and therefore saturated PC count

profiles), but that's because the cloudy PC values are in effect "wrong" for this purpose. Analogue count rates are compared there with oversaturated photon counting rates.

CRL uses a single set of gluing coefficients for as long as possible, just checking periodically to ensure that they are still valid.

One possible benefit to calculating the gluing coefficients for a clear portion of each night, or a portion of each night with good linear ranges in both channels is that this makes a good check that the gluing values are not changing too much day to day, and thus checking that the system itself (hardware especially) is not changing too much, either. This is the sort of calibration measurements done not so that an effect may be corrected, but to have a record of changes in the system over time. The gluing values should be consistent with time, within a reasonable range. If the hardware does not change, neither should the gluing coefficients. If one is worried about long-term drift in the analogue floating voltage shape, perhaps it would be better to track these changes directly with dark count measurements.

Standard operating procedure for CRL is to use one single set of carefully curated gluing coefficients for as long as they are viable. Checks are made regularly when clear sky measurements are available. If the lidar is not changing, then neither should the gluing coefficients.

Newsom et al. [105] merge their measurements in a similar manner to that used for CRL, but do not remove the sky backgrounds, first. They find that the gluing coefficients drift with time of day as the sunlit background increases. They report that D. Whiteman has communicated to them (2008) that this diurnal variation is less when backgrounds are removed, as in [107].

CRL removes the backgrounds, in general, before gluing. This is likely to continue as standard procedure, as it may also get around the problem of fluctuating analogue electronic noise profiles (see above).

Using a lamp mapping technique

Walker et al. [102] use light from a halogen lamp, rather than from the sky, to calculate gluing coefficients. The lamp may be positioned at various locations above the telescope by means of a precisely-controlled kinematic stage, thus controlling the amount of signal entering the detector. As CRL does not have such a scanning lamp available, it cannot make use of this method.

Using a maximum-likelihood reconstruction of photon count using the data from both channels to influence the resulting profile

Veberič et al. 2012 [108] model the behaviour of the PC and the ANA channel, with backgrounds still in, and minimize the errors when using a variety of input count profiles.

This is a great idea which may be instituted at CRL in the future. It uses all the information contained within the two profiles. This paper also points out many of the drawbacks to the usual gluing methods in use, and addresses some of these. The reference itself is quite clear, and so the information within it will not be repeated here.

5.8 Statistical vs. systematic uncertainties

There are both systematic and statistical uncertainties in the corrected photocount profiles. Systematic uncertainties, though they may have been derived themselves from measurements with random (statistical) uncertainties, do not change regardless of how long the measurement is integrated. For example, in $\delta = kS_{Para}/S_{Perp}$, the k has an associated uncertainty. Parallel and perpendicular signals may be measured as long as desired, and their own random uncertainties decrease, but the uncertainty of k is systematic and remains whatever it was when the calibration constant k was originally determined.

These uncertainties include: Calibration constant k , Gluing coefficients, Dark count correction value uncertainty, and Dead time correction uncertainty.

If these are all summed together, a minimum total uncertainty results, even if integration (coadding) has gone on so long as to make relative uncertainty from random uncertainties in the measurement approximately zero. That is to say, the total uncertainty cannot ever be less than the systematic uncertainties, unless these systematic uncertainties are reduced through further calibrations.

5.9 Conclusion of low level data processing chapter

The glued photocount profile for each of the channels (one for parallel, one for perpendicular, and one for Rayleigh Elastic), with their associated uncertainties, are the end goal for this chapter. These profiles are used in all subsequent chapters of this thesis when a “counts profile” is indicated.

For this thesis, the glued profiles are used in the calculation of two main derived data products: Depolarization Ratio and Depolarization Parameter.

Chapter 6

Traditional Depolarization Method

The purpose of the CANDAC Rayleigh-Mie-Raman lidar (CRL)'s new depolarization channel is to provide measurements of linear depolarization parameter in tropospheric Arctic clouds, to help differentiate ice particles from water particles in the backscattered lidar data.

With the new hardware installed at CRL (see chapter 4), the first task was to carry out depolarization calibration and calculations based on the data, using the traditional methods already in use in the community.

6.1 Traditional Depolarization Method Theory

Chapter 2 detailed several expressions for the depolarization of the lidar's laser beam as a result of the microphysical properties of the particles in the cloud. Three equations were given:

Equation 2.23 for the depolarization ratio in terms of measured signals was:

$$\delta = k \frac{S_{\perp}}{S_{\parallel}}, \quad (6.1)$$

Equation 2.25 for the depolarization parameter in terms of the depolarization ratio was:

$$d_{G1} = \frac{2\delta}{1 + \delta}, \quad (6.2)$$

and Equation 2.27 for the depolarization parameter in terms of measured signals was:

$$d_{G1} = \frac{2k \frac{S_{\perp}}{S_{\parallel}}}{1 + k \frac{S_{\perp}}{S_{\parallel}}}, \quad (6.3)$$

in which:

S_{\perp} is the signal measured by the perpendicular channel

S_{\parallel} is the signal measured by the parallel channel

$k = \frac{G_{\parallel}}{G_{\perp}}$ is the depolarization calibration constant, in which:

G_{\parallel} is the gain (attenuation) of the parallel channel

G_{\perp} is the gain (attenuation) of the perpendicular channel

A different pair of expressions for d is discussed in the following section, so the d from Equations 6.2 and 6.3 has been labelled d_{G1} here to differentiate these expressions from the others. Calculations of d are the primary quantity of interest in this thesis.

6.1.1 Lower uncertainty expression for depolarization parameter d

Lower uncertainty (σ_d) results for the depolarization parameter are possible if d_{G1} is recast by dividing numerator and denominator by $\delta = k \frac{S_{\perp}}{S_{\parallel}}$. The new expressions for d are labelled d_{G2} .

Equation 6.2 becomes:

$$d_{G2} = \frac{2}{\frac{1}{\delta} + 1}, \quad (6.4)$$

and Equation 6.3 becomes:

$$d_{G2} = \frac{2}{\frac{1}{k} \frac{S_{\parallel}}{S_{\perp}} + 1}. \quad (6.5)$$

The newly expressed d in Equations 6.5 and 6.4 are labelled d_{G2} in this chapter to differentiate them from d_{G1} . d_{G2} is not mathematically different from d_{G1} . In the case that all signal and calibration coefficient uncertainties are zero, the uncertainties associated with

d_{G1} and d_{G2} will also be identical. However, in the real-world case in which these signal and calibration uncertainties are greater than zero, the uncertainties associated with d_{G1} and d_{G2} will be different.

In both the d_{G1} and d_{G2} cases, d and its uncertainty σ_d can be calculated starting from depolarization ratio δ and its uncertainty σ_δ . To determine the best expression to use, the one with the final lower uncertainty is selected. Unsurprisingly, the expression which includes an uncertainty term only once (d_{G2} , Equation 6.4) was usually more desirable than that which included the uncertainty term in both numerator and denominator (d_{G1} , Equation 6.2).

To determine quantitatively which would be the superior expression, each type of depolarization parameter with its associated uncertainty was calculated for many combinations of depolarization ratio and depolarization ratio uncertainty, each ranging from 0.01 to 1. This simple model allows us to see the circumstances for which each expression is better. To demonstrate the advantage of the second expression, Figure 6.1 shows the difference between the uncertainties for each expression of d . The uncertainties from d_{G2} have been subtracted from those from the expression given directly in Gimmestad (2008), d_{G1} ; Difference = $\sigma_{dG1} - \sigma_{dG2}$. Hence, red (positive) values indicate d_{G2} being the better choice, and blue (negative) values indicate d_{G1} being the better choice.

At very low depolarization ratio values (below 0.1) with high uncertainty (greater than 0.5, in the units of depolarization ratio), d_{G1} fares better, with lower overall uncertainty than d_{G2} . Everywhere else, d_{G2} has the lower uncertainty. As most of the interesting clouds take place with depolarization ratio values higher than 0.1, it is advantageous to use the d_{G2} expression.

Recall that the depolarization parameter values calculated for both expressions are identical; only the final uncertainty differs. If the expressions using signals and k calibration factor are used, the result is the same; d_{G2} still outperforms d_{G1} . That test is just harder to visualize, so is not plotted here.

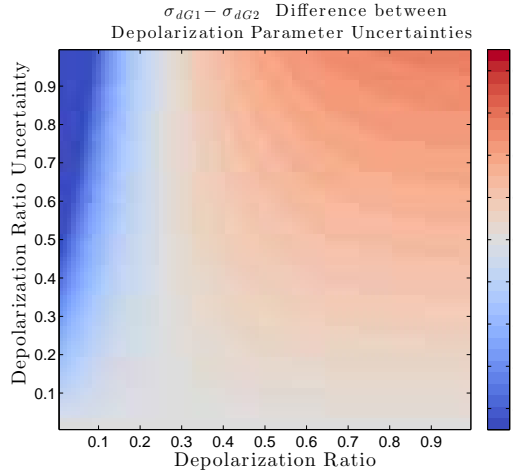


Figure 6.1: Plot in units of depolarization parameter which compares the absolute uncertainty propagated through both expressions for depolarization parameter d . The x-axis gives the depolarization ratio test input values, δ . The y-axis gives the depolarization ratio uncertainty test input values, σ_δ . For each combination, uncertainties were propagated through the equations 6.2 and 6.4 for d . The colourbar indicates the difference between these two uncertainties: $\sigma_{dG1} - \sigma_{dG2}$. The many positive (red) values indicate that uncertainties for d_{G2} are most often smaller than those for d_{G1} . Therefore, d_{G2} is the preferable expression for the traditional calculation method of d .

From this point on, any references to d or to “the traditional method depolarization parameter” refer to calculations made using the d_{G2} expression, Equation 6.5.

6.2 Traditional Method Calibration

The traditional method’s calibration constant is relatively simple to calculate. Recalling that $d = \frac{2}{\frac{1}{k} \frac{S_{\parallel}}{S_{\perp}} + 1}$ (from equation 6.5) and $\delta = k \frac{S_{\perp}}{S_{\parallel}}$ (from equation 6.1), and that at zero depolarization (where all light remains linearly polarized), $d = \delta = 0$ and that at maximum depolarization (all light has become unpolarized), $d = \delta = 1$. If we perform a calibration run forcing the light going into the detector to be completely unpolarized ($d = \delta = 1$ in the equations), we can solve for k most easily:

$$k = \frac{S_{\parallel, d=1}}{S_{\perp, d=1}}. \quad (6.6)$$

The calibration is carried out by putting white light into the detector, forcing $d = 1$, measuring the signal in each channel, and taking a ratio of these white light signals.

6.2.1 The contents of k : Making gains realistic for CRL

According to Gimmestad 2008 [60], the k value includes only a ratio of the PMT gains for each channel. The signals S_{\parallel} and S_{\perp} are supposed to be “calibrated” to begin with in an absolute sense – in essence, a pre-calibration by normalization to some value. For CRL, there is a problem: Neither channel is “calibrated”, to begin with in any absolute sense, so k must include all gains; not just PMT gains.

Were only PMT gains to be included in the calibration for CRL, $G_{PMT\parallel} = G_{PMT\perp} = G_{PMT\parallel\perp}$ (because the PMT is physically the same object in each channel) would indicate that the calibration constant k should always be 1, and we should not have to calibrate our lidar at all! This is clearly not the case.

There are additional gain terms which differ for each channel in the CRL, resulting from optics upstream of the polarizer, and these must be taken into account. There is no operational difference in the calibration. The same white light approach works; it is just that the contributions of k are different for CRL than for pre-calibrated lidars.

A summary of the gains used in this thesis:

- $G_{PMT\parallel\perp} = G_{PMT\parallel} = G_{PMT\perp}$ is the photomultiplier tube gain of the parallel and perpendicular channels’ PMT.
- $G_{upstream\parallel}$ is the gain contribution of all optics and devices upstream of the polarotor which contribute to the parallel channel’s signal.
- $G_{upstream\perp}$ is the gain contribution of all optics and devices upstream of the polarotor which contribute to the perpendicular channel’s signal.
- $G_{\parallel} = G_{PMT\parallel\perp} G_{upstream\parallel}$ is the total overall gain of all optics and devices contributing to the parallel channel’s signal.
- $G_{\perp} = G_{PMT\parallel\perp} G_{upstream\perp}$ is the total overall gain of all optics and devices contributing to the parallel channel’s signal.

6.2.2 Are gains sufficient? Is k a constant for CRL?

Are gain terms sufficient to describe the interactions of upstream optics with the light on its way to the parallel and perpendicular channels? Considering that k includes the gain contributions from all optics upstream of the PMTs, in addition to the PMT gains (which cancel), it is reasonable to ask whether the upstream optics add any other modifications to the received signals: Retardance, rotation, etc. Perhaps k is not a sufficient calibration to make. If k is not sufficient, then the “ d ” which is calculated by the CRL using the traditional method and the equations from this chapter is not truly the depolarization parameter; it is some other quantity, and not that which we desire. If k is sufficient, then the quantity d calculated here is indeed a fair representation of the depolarization parameter as measured by the CRL.

In following chapters, we explore whether this k as a function of gains is truly sufficient for the CRL, or whether improvements can be made by following a more complete matrix derivation of the depolarization parameter which accounts for more than simple attenuation. (The answers: 1. Yes, just using the gains is fine. We get depolarization ratios and parameters which make sense; 2. Yes, we can improve our analyses by eliminating the perpendicular channel altogether in favour of another channel which gets more photons, and so the matrix derivation turns out to be useful anyways).

It is at least possible, with the geometry of the CRL, to have all the optical elements contribute to gain only, and nothing else: One can imagine, for example, a partial-polarizer-like effect from the combined efforts of all upstream optics. This would result in a reduction in signal for one plane of polarization more than the reduction in signal for the orthogonal plane of polarization. For the remainder of the current chapter, we’ll proceed assuming that the traditional method works, and that we can use it for the CRL. This allows a demonstration of the CRL’s depolarization capabilities in a manner accepted by the community.

For the equations in this chapter to make sense, we require the channel gains to include

more than only the PMT gains $G_{PMT\parallel\perp}$, and to include the gain effects of all optics upstream of the polarotor, in the following manner:

6.2.3 Method for k calibration

A $d = \delta = 1$ setup may be arranged by shining a lamp at the detector through a depolarizing sheet of glassine waxed paper, or by letting the backscattered lidar light go through a sheet of glassine. See section 4.6.3 earlier in this thesis for information about glassine and other (un)polarization generating optics. The basic process to follow with the calibration is:

1. Low-level data processing (see Chapter 5) of Parallel and Perpendicular channel measurements to obtain corrected photocount profiles for each. Background is only subtracted in the case of a laser calibration.
2. Select time-altitude region of interest. For example, this might include a region with a bright cloud which scatters many photons into the detector.
3. Reject any data points under the minimum signal-to-noise ratio (SNR) and minimum counts thresholds (typically SNR greater than 0 and photon counts greater than 1).
4. Using remaining data points, calculate a representative value for the fraction $k = \frac{S_{\parallel}}{S_{\perp}}$. This may be done either by calculating k individually for each time-altitude bin and then taking a mean of these k values, or by summing all parallel and all perpendicular signals, and taking the ratio of these summed values.
5. Use standard uncertainty propagation methods to determine the uncertainty in this value k , appropriate to the method for calculating k chosen above.

This process is illustrated in the following subsection using an example calibration measurement from November 2013.

6.2.4 Sample Detailed Calibration Test from 1 November 2013 (laser; glassine above window)

This first calibration example uses the depolarizing glassine sheet as the first optic in the detection system; it precedes even the roof window (See figure 6.2). Thus, the k value from this test encompasses the polarizing gain effects of all elements upstream of the depolarization channel's polarization analyzer (the polarotor).

To reduce the attenuation from the glassine, and to keep the photon count rates as high as possible during the test, only a single layer of glassine waxed paper was used. As the Calibration Equipment section shows, two crossed pages of glassine would be better for ensuring full depolarization.

In the figure, we see that the sealed-beam headlight calibration lamp is mounted above the glassine-covered window. For the current calibration, however, the headlight was removed, and the lidar's backscattered laser light was used for illumination.

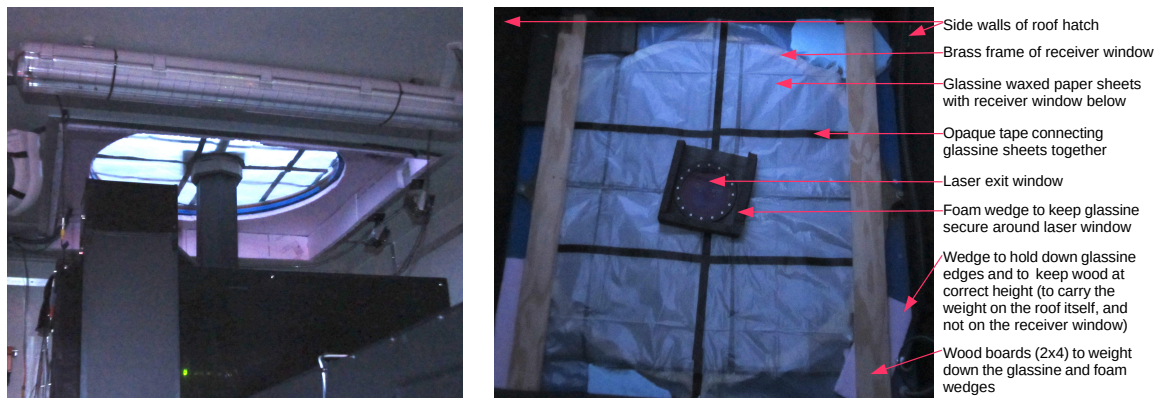


Figure 6.2: Photographs of the glassine-covered lidar window. Left: Looking upward from inside the lab, sunlight is visible coming through the glassine-covered receiver window. Right: Looking down into the lidar hatch with the glassine securely installed for calibration tests.

This test was carried out for over 22.8 hours, between 22:40 on 1 November 2013 and 21:00 on 2 November 2013. During this time, a large cloud was present between 1 to 3 km altitude, which lasted several hours. The first task was to carry out the low-level data

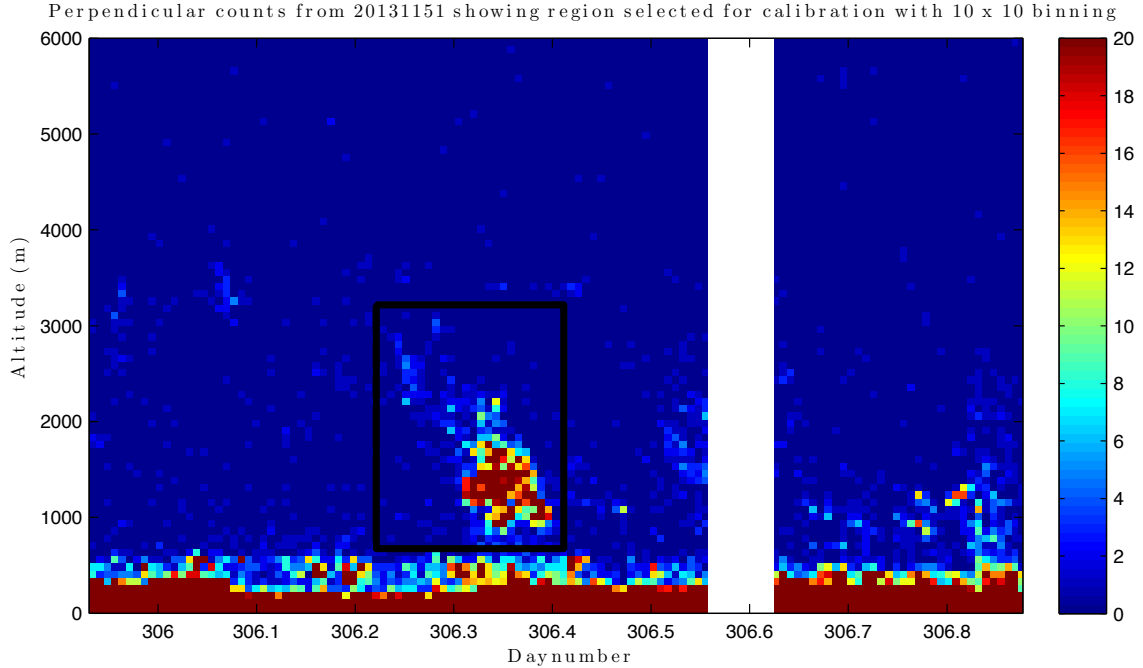


Figure 6.3: Colour plot of perpendicular channel coadded and corrected photocounts. Black box indicates region of interest to be used in the calibration analysis.

processing (see Chapter 5) of Parallel and Perpendicular channel measurements to obtain background-corrected photocount profiles for each channel. Second, an appropriate time-altitude region of interest must be selected for the calibration. Regions with clouds or other high-backscatter features are desirable. In Figure 6.3, we see an image plot of the Perpendicular channel background-corrected photocount profiles for the entire calibration measurement. Because of the high attenuation from the polarization-scrambling glassine, many areas have zero counts in the Perpendicular channel, even at low altitudes.

We see higher count rates in two places: 1. In the cloud, and 2. Below 500 m altitude. Analysis for calibration was attempted on the whole data set and on just the area of the cloud. It was repeated for a variety of coadding times and altitude resolutions. All resolutions provided similar results, but tests using altitudes below 500 m gave different results. As measurements under 500 m altitude are in general rejected for the lidar, it is acceptable that the calibrations include only measurements from above this altitude. The black box in Figure 6.3 shows the region of measurement selected for the calibration calculations.

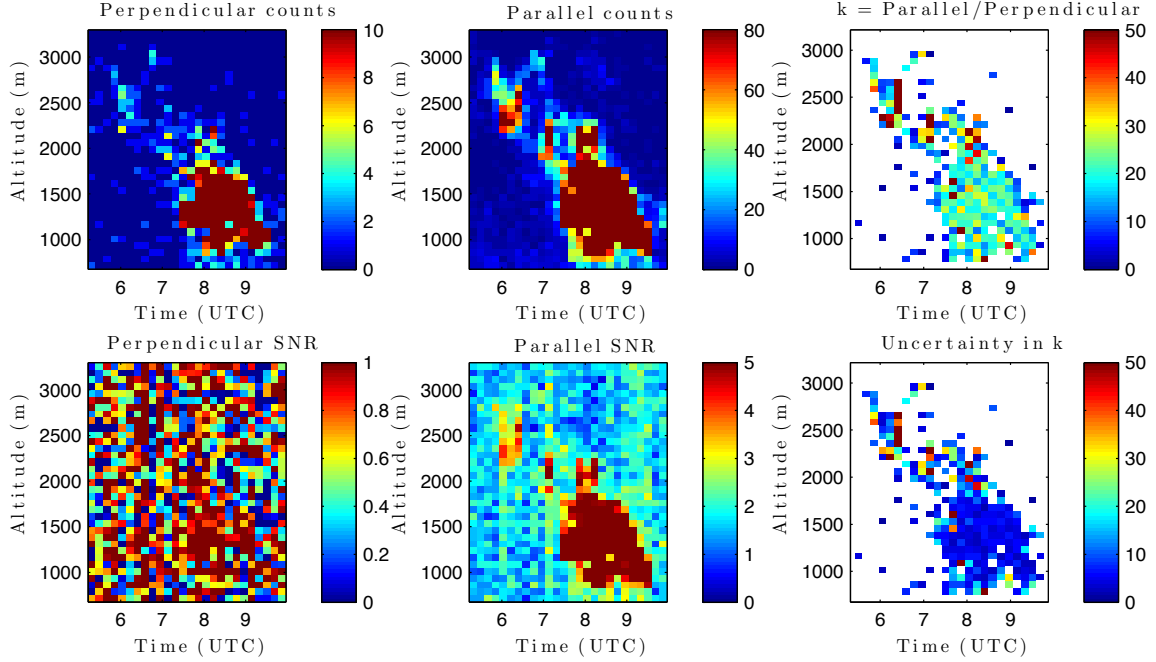


Figure 6.4: Parallel and perpendicular channel corrected photocounts within the calibration region of interest, with their associated signal-to-noise ratios plotted beneath. Top right panel shows the ratio of the counts for each time-altitude point (k), with the associated uncertainties in k shown at bottom right.

Next, any unsatisfactory data must be rejected from the calibration. Such regions include those with too few photon counts, or too low signal-to-noise ratio. In Figure 6.4, a 10 x 10 binned example (37.5 m altitude resolution, 5 minute time resolution) plots the photon counts for both Parallel and Perpendicular channels and the corresponding SNR plots. The rightmost top panel shows the ratio of Parallel to Perpendicular counts for each data point, which is the value k . The lower right panel shows the uncertainty for k calculated in this way.

Once the data has been quality controlled, there are several approaches for determining k . Two of these are:

1. Calculate a summed or mean count value for the whole calibration altitude-time space in each of the two channels, and then take the ratio of these to calculate one k representative of the whole region. The result using this method of dividing summed count

values is $k = 20.71 \pm 0.43$.

2. Calculate a k value individually for each altitude-time bin, and then combine k values into an overall constant using the mean of these k values. The result using this method is $k = 21.67 \pm 1.4$ (see Figure 6.4 above).

We note that in this particular case, we get similar results from the two methods, but the uncertainty is smaller if summing and taking the mean. Both results, where possible, are given in Table 6.1 later in the chapter.

6.2.4.1 Calibration tests with various resolutions

To ensure that the calibration constant k is not biased in any way by the time and altitude resolution chosen for the calibration, a comparison is made between 7 time and altitude co-adding combinations (Table 6.1, plotted in Figure 6.5). All trials use the same three-hour-long calibration measurement between 1 and 2.5 km on November 11, 2013. Values of photon counts are only kept in the case that, for each coadded time-altitude bin: Parallel Count SNR > 1.5 , Perpendicular Count SNR > 0 for Perpendicular, Number of Photon Counts > 0.1 in each channel. A constant background was removed from each coadded profile.

Table 6.1: Calibration constant values of k from various time and altitude coadding trials

Test ID	Number of 1-min time bins coadded	Number of 7.5-m altitude bins coadded	k value from summed parallel and perpendicular counts	Uncertainty in k from summed values	Mean of individual k values	Uncertainty in mean of individual k values
Trial a	20	20	21.25	0.47	20.70	1.67
Trial b	20	10	20.97	0.43	21.30	1.44
Trial c	20	5	20.99	0.44	21.17	1.20
Trial d	10	10	20.91	0.44	21.91	1.43
Trial e	10	5	21.11	0.46	24.09	1.29
Trial f	10	2	21.17	0.53	25.75	1.22
Trial g	5	2	20.58	0.60	27.29	1.55

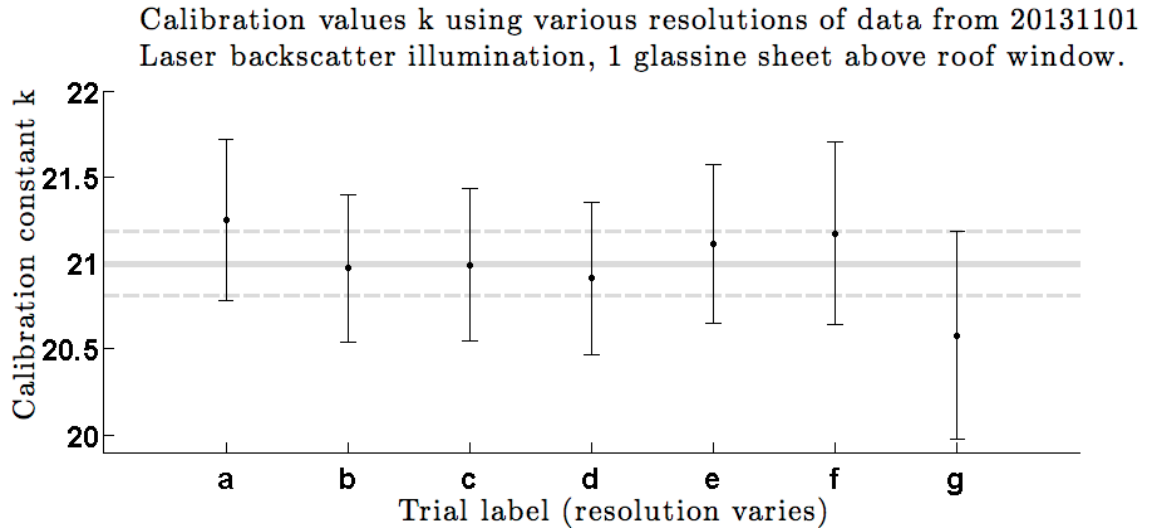


Figure 6.5: Calibration constant values of k from various time and altitude coadding trials detailed in Table 6.1 from 20131101. The mean of the values is indicated by the solid grey line, with uncertainty in the mean indicated by dashed lines. Visually, the results when using the summed values are equal to within their errorbars. The mean value is $k = 21.0 \pm 0.2$.

There is no trend with either time or with altitude in the value of k (plots not shown for this). Combining the results from the trials of the various resolutions, and using standard error propagation (assuming no correlated errors, which is not completely true), gives a mean value of:

$k = 21.0 \pm 0.2$. This value will be used in the following section to calibrate the depolarization ratio and depolarization parameter measurements for the night of March 12, 2013.

6.3 Which optics contribute most to the k value? Testing depolarizing material at various locations

In the calibrations in the previous section, the polarization generator (in this case, one sheet of glassine to unpolarize completely the light entering the system) was placed above the roof window; this is the optimal position as the known-polarization light generated by the glassine then passes through all detector optics; the k determined in this way is therefore

representational of the effects of all detector optics on the signals.

Many lidar groups choose instead to use calibration lamps part way through their system, rather than using a lamp which scans or is projected over the whole entrance aperture at the first optic of the system. One notable exception is the lidar group at Howard University led by Prof. Venable. See, for example [92], applied to a water vapour lidar. Tests become easier to do as one moves the optic downstream in the detector for several reasons:

- Any optic placed at the beginning of the detector chain must be as large as the first optic itself. In the case of CRL, this means a circle with diameter 1-metre. Optics of this size are expensive and unwieldy, and are sometimes impossible to obtain.
- Any optic placed at the beginning of the detector chain will necessarily be outdoors, and be exposed to the elements. In Eureka this includes temperatures colder than -50°C , significant wind, blowing snow, and working on a roof. These conditions are difficult for optics, and are difficult for people. If a lamp is used for illumination, power is also needed on the roof, which is inconvenient.
- Going downstream brings the optic and the person inside, and makes the required optics smaller. Any optics placed between the telescope and the focus stage must be about 25 cm^2 . Optics after the focus stage may be as small as 25 mm^2 .
- Smaller optics are easier to rotate in a controlled manner (e.g. for polarizer calibrations discussed in subsequent chapters).

The first question is: At what cost to the calibration and science do these practical advantages come? Various tests were made to determine how the calibration constant k changed depending on the location of the calibration materials during the test. The results of placing the depolarizing optic at different locations in the system are demonstrated in the following subsection.

A second benefit of this test is that: We discover which optics are contributing most to the CRL's very high value of calibration constant k .

6.3.1 Setup for testing k at various locations in the detector

These tests were carried out over a 2-hour period on April 1, 2013. A white light calibration lamp source was turned on just upstream of the focus stage. Note that this skips the first 4 optics of the system (window and three telescope mirrors). Therefore, the contributions of these optics to the overall k value of the lidar is not evaluated in this test except in the context of comparison with the overall value for the calibration constant from the tests in previous sections.

A waxed-paper depolarizing sheet was temporarily installed at various locations in the detector chain to ensure that all light proceeding from that point was completely unpolarized. The choice to use industrial kitchen grade waxed paper (from Eureka kitchens) rather than glassine was because this test preceded our discovery and tests of glassine; we later found glassine to be a superior material).

Starting from as close to the photomultiplier tube detector as we could get, we worked backwards placing the depolarizer between any two optics where there was room to safely insert it (Figure 6.6). Measurements were made with the polarotor in operation as usual, with the lidar measuring both parallel and perpendicular channel photons. The signals in each channel were compared as in the test for k described in the previous chapter. These are expressed as k values in Table 6.2, and graphically as percentages of the total parallel plus perpendicular signal.

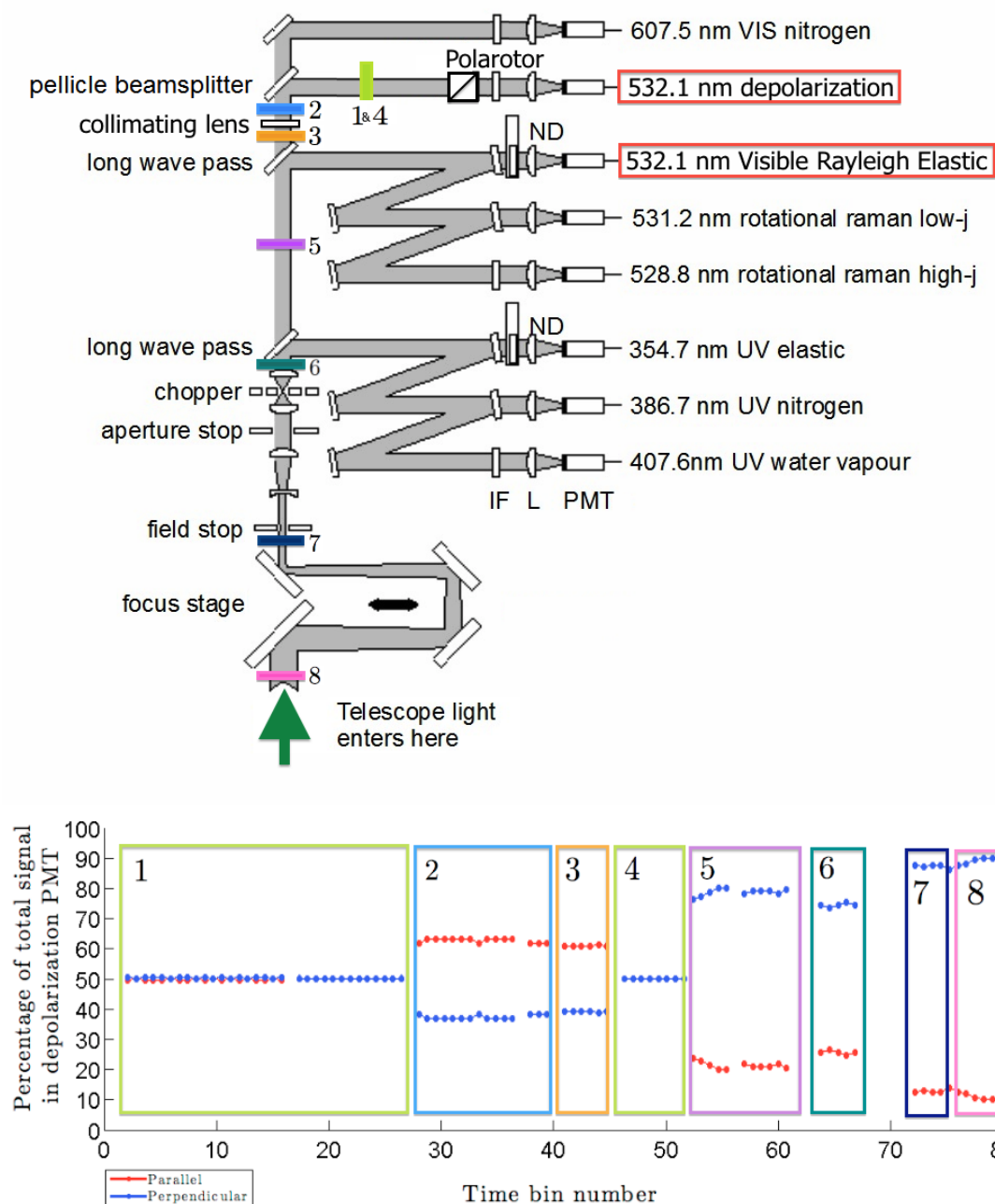


Figure 6.6: The waxed paper sheet was placed at various locations within the CRL's detector system, and count rates were measured in the parallel and perpendicular channels. Test locations, numbered 1 through 8, are indicated in the schematic (top) by coloured lines, which correspond to the coloured boxes in the plot of the measurements (below). Tests 1 and 4 are at the same location (green). The test numbers correspond to those in Table 6.2, which includes some discussion of the results.

Test	Box Colour	Depolarizer Location	$k \pm \Delta k$	Comments
1	Light Green	Directly upstream of polarotor	0.99 ± 0.01	We expect $k = 1$ here, and it is. Parallel: No change. Perpendicular: No change. Contribution to k : None.
2	Sky Blue	Upstream of pellicle	0.61 ± 0.02	Parallel: Decreases. Perpendicular: Increases. Contribution to k : Moderate.
3	Orange	Upstream of collimation optic	0.67 ± 0.01	Parallel: Decreases. Perpendicular: Increases. Contribution to k : Minimal.
4	Light Green	Just before polarotor	0.99 ± 0.01	Check: Same result as Test 1 with identical setup.
5	Purple	Just upstream of the Visible Long Wave Pass dichroic (LWP)	3.5 ± 0.3	Parallel: Increases. Perpendicular: Decreases. Contribution to k : Very large, $> 40\%$.
6	Dark Green	Just upstream of the UV LWP dichroic	2.8 ± 0.1	Parallel: Decreases. Perpendicular: Increases. Contribution to k : Small compared to the VIS LWP's contribution.
7	Navy Blue	At the entrance of the polychromator (downstream of focus stage, upstream of apertures)	6.1 ± 0.4	Parallel: Increases. Perpendicular: Decreases. Contribution to k : Large, $> 12\%$.
8	Pink	Right after the lamp, upstream of the focus stage	7 ± 1	Parallel: Increases. Perpendicular: Decreases. Contribution to k : Small.

Table 6.2: Measuring calibration constant k using a depolarizer at various locations in the polychromator. The VIS LWP filter and collimating optics contribute most. Comparison with the overall $k = 21$ value for whole system indicates that calibration tests must include all optics. The (un)polarization generating calibration optic must precede the roof window.

6.3.2 Results for k from various positions

The first test location (Test 1; repeated for Test 4 as a check) is indicated in Figure 6.6 in light green, directly downstream of the pellicle beamsplitter. Because all subsequent optics (interference filter, focus lens, etc) are in a closed beamtube, it is not sensible to try and insert a depolarizer inside there. As indicated in Figure 6.6 and Table 6.2, the measurements here showed approximately equal amounts of light in the parallel and perpendicular channels. This indicates that the collection of optics downstream are not contributing to the value of k we originally measured for the whole lidar. This immediately tells us that we must indeed take into account the gains of other optics in the system, rather than only the gains of the PMTS, when calibrating for depolarization.

Subsequent tests moving upstream each time indicated that most of the optics in the polychromator are indeed partially polarizing the returned lidar beam, some favouring attenuation of parallel-polarized light, and others attenuation of perpendicular-polarized light. Particularly large contributors to the overall k value include the VIS LWP dichroic, and the collimating lenses at the start of the polychromator.

The large difference in k value measured from upstream of the first system optic (above the roof window; $k = 21$) and measured from downstream of the telescope ($k = 7$) demonstrates that the window and telescope also contribute considerable amounts to the overall calibration constant required for depolarization analyses with the CRL.

6.3.3 Impact on future CRL design and calibration decisions

The tests in Section 6.3 are important for CRL future planning.

First, they indicate that we *must* calibrate for k by placing the depolarizing optic at the beginning of the optical chain. Choosing a convenient location within the lidar will not suffice.

Second, they indicate which of our optics are contributing most to the large overall

calibration factor of the system. This allows us to see which optics would be most advantageous to remove or upgrade the next time we change optics in the lidar.

One of the largest problems arising from a large calibration factor which suppresses the perpendicular channel compared to the parallel channel is that we end up with quite low count rates in the perpendicular channel. The maximum amount of light received by the telescope in the perpendicular polarization direction ($\frac{1}{2}I_{unpol}$; maximum in the situation in which the lidar beam is fully depolarized with $I_{pol} = 0$ and $I_{total} = I_{unpol}$) will only ever be approximately half the maximum intensity of that in the parallel direction ($\frac{1}{2}I_{unpol} + I_{pol}$; maximum in the situation in which the lidar beam is not depolarized at all with $I_{unpol} = 0$ and $I_{total} = I_{pol}$). The current CRL setup, unfortunately, suppresses by a factor of 21 the already-low perpendicular channel.

This would not be such a huge problem if separate depolarization PMTs were used for each channel. In that case, it would suffice to change the sensitivities of the Licels to make the Perpendicular channel more sensitive, and the Parallel channel less so. Since they *are* physically the same PMT, compromise is required. This means remaining on a setting that really is not sensitive enough for the perpendicular because putting the gain setting any higher to correct this would constantly saturate the parallel signals.

For optimal measurement using a single PMT (which of course has a single gain setting, a single photon-counting threshold, etc) the most desirable calibration value would be $k < 1$ (rather than $k = 1$ which would be an intuitive desire, perhaps). This would suppress the already-large parallel signal while allowing the already-small perpendicular signal through, providing more comparable count rates.

Things which could be attempted in future:

- Rotate the laser's polarization by 90 degrees (that way, the collection of optics in the polychromator will suppress the large parallel signal instead, and enhance the small perpendicular by comparison);
- Put a quarter wave plate at the entrance to the polychromator for the same reason;

- Replace the visible long wave pass filter with one which is less polarizing, or less polarizing in the perpendicular-suppressing direction;
- Look into the collimating lenses in the polychromator for the same reason;
- Use two depolarization PMTs and a beamsplitter which spatially separates the light;
- Move depolarization detector further upstream in the detector, perhaps with a pick-off beamsplitter at the beginning of the optical chain.

The whole-detector calibration result of $k = 21.0 \pm 0.2$ stands as the most appropriate value for the CRL. This will be used for calculations in subsequent sections and chapters.

6.4 Traditional Method Sample Calibrated

Measurements from 20130312

Using the best value of calibration constant $k = 21.0 \pm 0.2$ found in Section 6.2.4.1, we can apply this value to our calculations of δ and d for a sample day's measurements; for example, those from 12 March 2013. Figure 6.7 shows the depolarization ratio, depolarization parameter, and the uncertainties and relative errors for each.

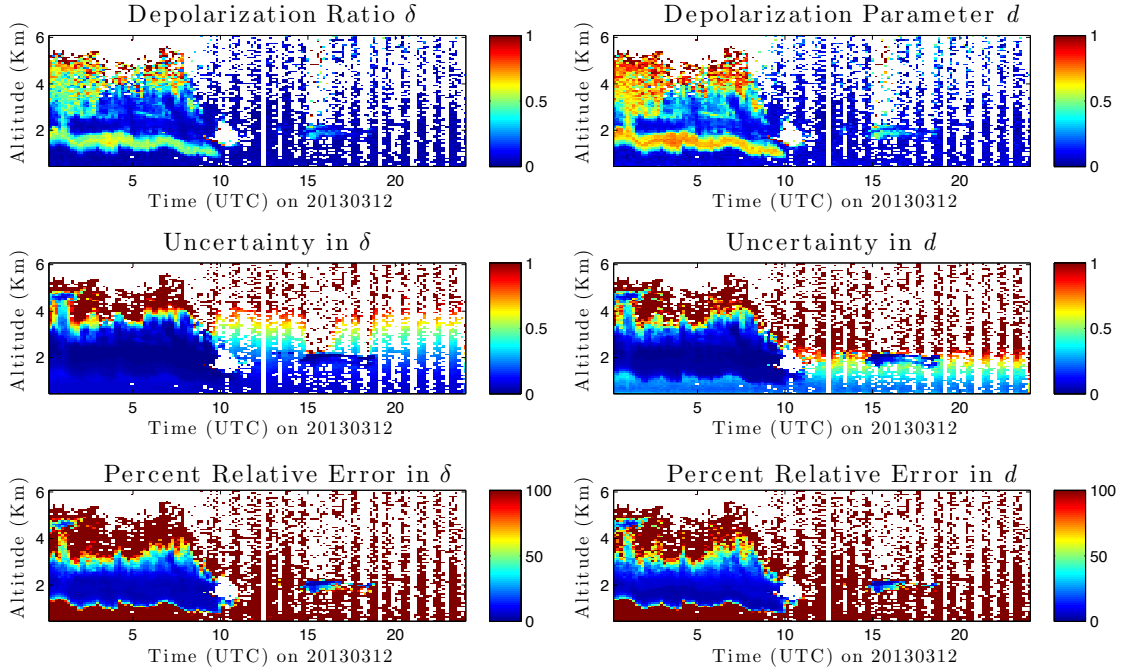


Figure 6.7: Contour plot of traditional depolarization results. Left plots show the depolarization ratio, its associated absolute uncertainty, and its relative error. The right plots show the same for the depolarization parameter.

Just below 2 km altitude, a region of high depolarization is evident with low uncertainty. This implies that this region of the cloud is icy rather than made of liquid droplets. As altitude increases in the cloud, the depolarization drops. Is this because the cloud has suddenly turned into liquid droplets? Perhaps, but notice a few other factors: 1. The uncertainty is higher in these regions, 2. The applicability of the assumption that we have no multiple scattering is decreasingly trustworthy, and 3. The two channels may have differing amounts of extinction. By high in the cloud, photons have to pass through the thick cloud below, *twice*, on their way upward and then back to the lidar. The most trustworthy depolarization values are those for which we have both low uncertainty *and* reasonable confidence that we have a low extinction single-scattering situation for every photon involved in the data for that altitude-time bin.

Producing plots for use in analyses, it may be desirable to cut out regions which are not providing trustworthy depolarization values. The values could be cut based either on

relative error or on absolute error. The latter is chosen in this situation because a measurement of a depolarization parameter $d = 0.01 \pm 0.01$ is still meaningful, despite having 100% relative error. Interpretations deal with cutoffs between different values of d and the measurements need to be sensitive enough to discern this cutoff, without going overboard and eliminating all of the data. The difference is shown in Figure 6.8 below:

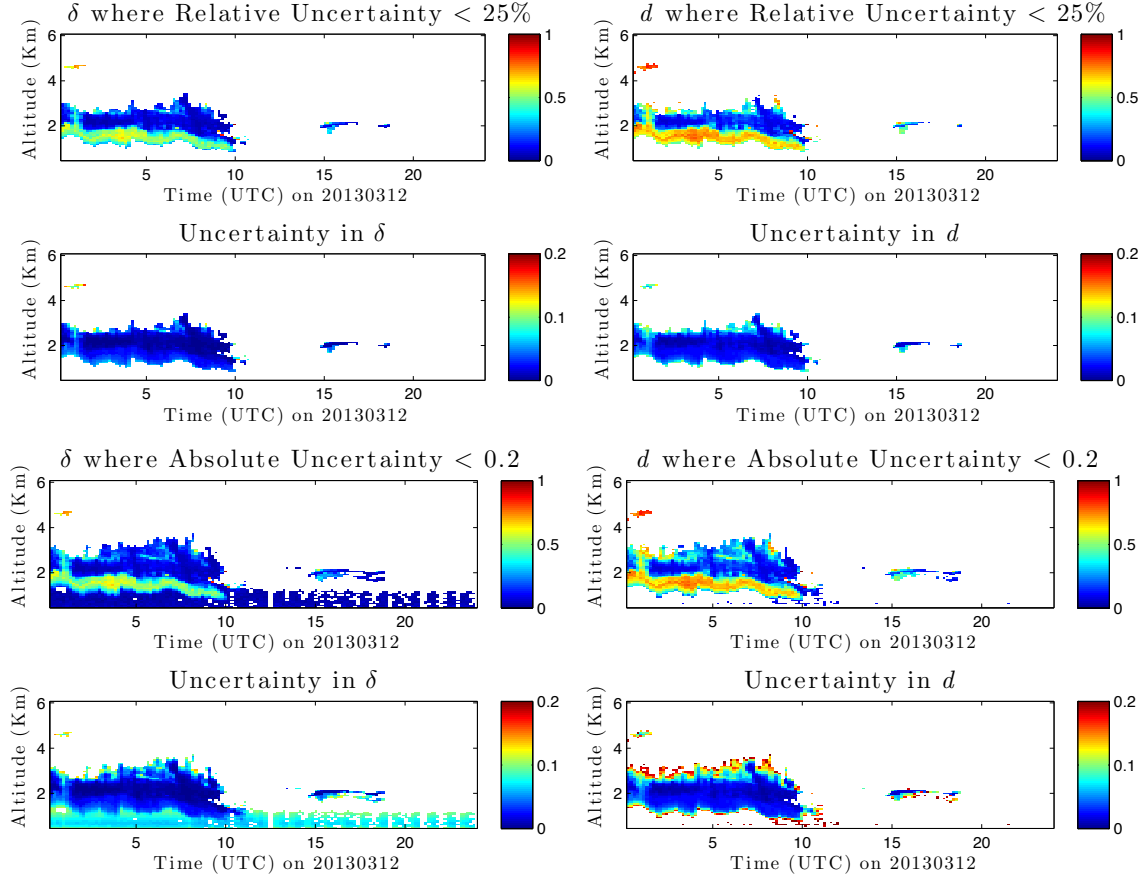


Figure 6.8: Plots from 20130312 demonstrating the depolarization parameter and ratio with associated uncertainties. The top four panels have eliminated any points with relative uncertainty greater than 25%. The bottom four panels have instead eliminated any points with absolute uncertainty greater than 0.2. The difference between the top panels and the bottom panels shows the difference in confidence expressed for depolarization values based on the interpretation and use made of the calculated uncertainty. This is discussed in further detail in the current section.

Far more low-depolarization-parameter values are kept by cutting off on the absolute uncertainty rather than the relative uncertainty, without losing any interpretation confi-

dence. When cutting based on absolute error, the depolarization ratio fares better than the depolarization parameter does. Still, it all comes from the same data, and a superior method to each of these is explored later in the thesis.

It is worthwhile to make the point here that very few publications of depolarization ratio and depolarization parameter in the literature include any discussion whatsoever with regards to uncertainty, and none to the author's knowledge routinely publish these values alongside the measurements. Any increased discussion of lidar depolarization uncertainty is an improvement in this regard.

6.5 Caveats on Traditional Method and motivation for other methods

The traditional methods of calculating depolarization quantities for the atmosphere *appear* to work fine for the CRL, but there remains a major concern: they make the assumption that calibrating only for gains is appropriate and sufficient. In a lidar designed specifically for depolarization measurements, there are no extraneous optics between the sky and the polarizers. A telescope is necessary, as well as some focusing and collimating optics perhaps, but these would be selected on the basis of them not adding any additional instrument polarization to the system. This situation does not match with the reality of the CRL design, in which the depolarization channel was added to a pre-existing lidar.

Chapter 7 resolves this issue. There, the signals are derived for each lidar channel for a non-ideal lidar in which the optics upstream of the polarizer may exist and have any optical qualities in addition to attenuation. A more complete optical matrix algebra derivation of d is carried out using 4×4 Mueller matrices, rather than a constant gain term, for each set of optics. Results are compared to those from the traditional calibration and calculation methods to demonstrate that the original analysis method is, indeed, acceptable.

Chapter 7

More Complete Depolarization

Parameter Method: Mathematical Description

In the previous chapter, some assumptions were made regarding the nature of the signals recorded in the Parallel and Perpendicular channels used in calculations of depolarization parameter d . Perhaps these are too simplistic, and it would do well to evaluate these assumptions by examining a more complete matrix derivation of the problem.

The opportunity is also taken to add a Rayleigh Elastic channel to the discussion. This is one of the fundamental lidar channels at the CRL, used for Visible Rayleigh Backscatter measurements. It measures at the same wavelength (532 nm) as the depolarization channels do, but is intended to be polarization-independent. In following chapters, it will be shown how the three channels under consideration may be combined in various ways to solve for d . It should not be a surprise that a polarization-independent channel could be used in this manner (e.g. [52], [109], [68]), but a detailed practical development in this context has not been carried out to date to the author's knowledge.

Note that the goals in this chapter differ from those of Hayman et al. [84], which uses

similar Mueller matrix algebra to more fully explore the optical properties of the atmosphere. Here, the matrix algebra aims to more fully diagnose the optical properties of the CRL lidar itself.

As many depolarization lidars carry a polarization-independent Rayleigh Elastic channel, it is hoped that this explicit development of its properties in terms of depolarization calculations may be of use to others in the community.

7.1 Matrix description of signals in each channel

The full Mueller matrix derivation of the depolarization parameter d is given, making as few assumptions as possible regarding the optical properties of optics upstream of the photomultiplier tubes. These equations are used to demonstrate the precise circumstances under which the simplified versions (Traditional Method from Chapter 6 included) often seen in the literature may be used .

In the Gimmestad treatment of the depolarization problem, only two-polarized-channel methods are examined; one method for linear and one method for circular polarization. Therein, all matrices are normalized, and the signals in the receivers, S_x , are “assumed to be calibrated” [60]. Implicitly, we are to understand that this calibration is a single different constant for each channel. In other words, the combination of all optics upstream of the photomultiplier tubes (PMTs), and the gain differences of the PMTs, act together in the role of a partial polarizer in the system. Here instead, we will explicitly include the gain G_x of each channel in the matrix calculations to demonstrate its role in the problem.

Included in this section is a full matrix description for the upstream optics, and indeed for the whole system. Perhaps through measurements of the calibration constants we will arrive back at the expressions given by Gimmestad, but due diligence requires that this be checked for the CRL.

7.1.1 Describing the behaviour of the lidar as matrix equations

In the case of atmospheric lidar operation, the original laser light is described as a Stokes vector which will be operated on by several things, each of which can be described by a 4×4 matrix. If we use these to operate on our laser Stokes vector in the right order, then we can determine the Stokes vector of the light which hits the PMTs, and predict the signal which will be measured in each of our channels: S_{\parallel} (parallel channel measurement), S_{\perp} (perpendicular channel measurement), and S_R (Rayleigh Elastic (hopefully)-polarization-independent channel).

Hans Mueller was the first to develop the field of Mueller Matrix Algebra in the early 1940s. His early original works on the topic are nigh on impossible to obtain as they take the form of conference proceedings and lectures (e.g. [110], [111] and [112]), some of which were classified during World War II. Despite considerable effort to find a copy, [113] and [114] remain unavailable, as they are unclassified but still restricted to all but the U.S. Government and their contractors. The reference [115] has been unclassified and is available, and describes the design and use of the [113], including some mathematics, but not the matrix algebra. Mueller's student Nathan Grier Parke III's Ph.D. thesis [116] is accessible, describes all of the Mueller matrix algebra in considerable detail, and is cited in this work.

Why use Mueller matrix algebra rather than Jones Algebra as is done in many optics texts? Parke states this well himself: "The fundamental point of [Mueller's] theory is the recognition of the fact that the quantities of his algebra are observables and that those of Jones algebra are not" ([116], page 4).

In its most basic format, Mueller algebra functions as: $L' = ML$, in which L and L' are the Stokes vectors of incident and emerging radiation, respectively, and M is the 4×4 real matrix effect of the instrument [116]. Mueller algebra also indicates that Stokes vectors add incoherently, and therefore the effect of any two instruments in series is equal to the

product of their matrices (and for those in parallel is equal to their sum, but this is not relevant to this thesis).

Stated in terms of a matrix equation, the effect of these optical components on the incoming backscattered light is:

$$\begin{pmatrix} \text{Detected light} \\ \text{Stokes vector} \end{pmatrix} = \begin{pmatrix} \text{Channel – specific} \\ \text{instrument} \\ \text{matrix (or matrices)} \end{pmatrix} \begin{pmatrix} \text{Atmospheric} \\ \text{scattering} \\ \text{matrix} \end{pmatrix} \begin{pmatrix} \text{Laser light} \\ \text{transmitted} \\ \text{Stokes vector} \end{pmatrix} \quad (7.1)$$

Descriptively,

1. Start with a vector for light transmitted by the laser to sky
2. Include a matrix to describe how the atmosphere changes the properties of the laser light as it backscatters it (including depolarization parameter d which we want to find)
3. Choose instrument matrices to describe how this light is changed by the receiver optics before it hits the detectors
4. Calculate the resulting vector for the light received by the PMTs.
5. The signal S that can be detected by a PMT for any of these is equal to the first element in the Stokes vector. The PMT measures a value proportional to the total intensity of the light which impinges on it, with no inherent regard to the polarization state of this vector.

The following subsections show how the matrices are selected for the CRL.

7.1.2 Choice of laser light transmitted Stokes vector

In general, light can be described as a Stokes vector with I = total intensity, Q = intensity in the x (+) or y (-) axis, U = intensity in the $+45^\circ$ or -45° axis, and V = intensity for left hand and right hand circular polarization [50].

$$I_{\text{Arbitrary Stokes Vector}} = \begin{pmatrix} I \\ Q \\ U \\ V \end{pmatrix} \quad (7.2)$$

In this format, completely unpolarized light is given by the vector:

$$I_{\text{unpolarized}} = \begin{pmatrix} 1 \\ 0 \\ 0 \\ 0 \end{pmatrix} \quad (7.3)$$

Light linearly polarized in the x -direction is given as:

$$I_{\text{polarized},x\text{-direction}} = \begin{pmatrix} 1 \\ 1 \\ 0 \\ 0 \end{pmatrix} \quad (7.4)$$

Light linearly polarized in the y -direction is given as:

$$I_{\text{polarized},y\text{-direction}} = \begin{pmatrix} 1 \\ -1 \\ 0 \\ 0 \end{pmatrix} \quad (7.5)$$

The CRL lidar emits horizontally linearly polarized light, with laser intensity I_{laser} :

$$I_{\text{laser}} = \begin{pmatrix} 1 \\ 1 \\ 0 \\ 0 \end{pmatrix} \quad (7.6)$$

I_{laser} is the laser intensity to the sky. This is not constant as it varies from laser shot to laser shot, with flashlamp use, with laser voltage, and so on, but for any given integrated minute of data, it will be constant in the equations in this thesis for all three channels.

7.1.3 Choice of atmospheric scattering matrix

A matrix is required to describe the effects of the atmosphere on the light that is scattered back toward a receiver. Backscatter by a sphere, or an ensemble of spheres, is given by the operating matrix (here normalized):

$$\begin{pmatrix} 1 & 0 & 0 & 0 \\ 0 & 1 & 0 & 0 \\ 0 & 0 & -1 & 0 \\ 0 & 0 & 0 & -1 \end{pmatrix} \quad (7.7)$$

but to use something more general instead, as not all atmospheric scatterers are perfect spheres, the full normalized backscattering matrix for any shape of particle (after [117]) is:

$$\begin{pmatrix} a_1 & 0 & 0 & 0 \\ 0 & a_2 & 0 & 0 \\ 0 & 0 & -a_2 & 0 \\ 0 & 0 & 0 & a_1 - a_2 \end{pmatrix}. \quad (7.8)$$

Van de Hulst [52], page 55, provides a similar matrix specifically for backscattering of a cloud of asymmetrical particles with rotational symmetry, for which each particle has a mirror particle in equal numbers, and where there is no preferred orientation. In that expression, the last element in reference is not specified in reference to the other three, but is given rather as a_4 .

Particularly interesting are changes in polarization during the scattering events. Introducing a variable d such that the matrix is normalized to have an intensity of 1 ($a_1 = 1$), and allowing $a_2 = a_1 - d$, (i.e. $a_2 = 1 - d$), Gimmestad's version of the Muller matrix for scatterers in the atmosphere is produced:

$$M_{atm} = \begin{pmatrix} 1 & 0 & 0 & 0 \\ 0 & 1-d & 0 & 0 \\ 0 & 0 & d-1 & 0 \\ 0 & 0 & 0 & 2d-1 \end{pmatrix} \quad (7.9)$$

To make things clearer later on, this matrix is un-normalized with a constant factor out front, b . The “constant” term b is not constant forever, or even over several-minute timescales. Still, for any given minute of data, it will be constant in the equations for all three channels.

$$M_{atm} = b \begin{pmatrix} 1 & 0 & 0 & 0 \\ 0 & 1-d & 0 & 0 \\ 0 & 0 & d-1 & 0 \\ 0 & 0 & 0 & 2d-1 \end{pmatrix} \quad (7.10)$$

The value d is the depolarization parameter for the atmosphere above the lidar, as described in Equation 6.5, and describes the extent to which the transmitted light has been depolarized by the atmosphere. It varies between 0 (no depolarization) and 1 (complete depolarization). Our goal is to use the lidar’s detected light to determine d .

7.1.4 Choice of instrument matrices

The backscattered light (already acted upon by M_{atm}) is acted on by various analyzing polarizers: either a) a parallel polarizer, b) a perpendicular polarizer, or c) no polarizer at all. These analyzers act as 4×4 matrices. There are also optics both upstream (telescope, focus stage, beamsplitters, long-wave-pass filters, etc), and downstream (focusing lenses, neutral density filters, all optics in the PMT tube) of the polarizers for each channel.

Each channel has its own instrument matrix which takes the form:

$$\begin{pmatrix} \text{Instrument} \\ \text{matrix} \end{pmatrix} = \begin{pmatrix} \text{Optics} \\ \text{downstream} \\ \text{of polarizer} \end{pmatrix} \begin{pmatrix} \text{Polarizer} \end{pmatrix} \begin{pmatrix} \text{Optics} \\ \text{upstream} \\ \text{of polarizer} \end{pmatrix} \quad (7.11)$$

7.1.4.1 Matrices for optics upstream of the analyzing polarizers

If designing a lidar specifically for depolarization measurements, there would be no extraneous optics between the sky and the polarizers, and certainly none which rotate any of the polarization or otherwise complicate matters. Care would be taken to choose a telescope with the least polarizing effects possible. Given that the depolarization hardware was added to the CRL after all of the other channels had been operating for several years, this was not an option. Instead, CRL's depolarization hardware must make do being downstream of a whole host of interfering optics. In so general a system such as the CRL, which was not designed for depolarization, perhaps there *may be* polarizing, retarding, etc, optics upstream of the analyzers.

We account for these possible upstream optics as a 4×4 matrix for each channel, but we make no assumptions as to the values of the matrix elements.

There is the possibility of some as yet unaccounted for constant which varies with altitude. Geometric overlap is such a term which is constant in time, but varying in altitude. The CRL's constant includes more than only geometric overlap, but for the purposes of this thesis it is not important to know them all separately, so this term will be named for its familiar component. Consequently, this constant will be called the “overlap function” $O(z)$.

The depolarization channels Parallel and Perpendicular share an identical optical path, so they share an identical matrix as well, which takes into account the combined effects of all upstream receiver optics which the parallel and perpendicular channels have in common. The overlap function will also be the same for parallel and perpendicular, $O_{\parallel\perp}(z)$.

$$M_{\parallel\perp upstream} = \begin{pmatrix} M_{00} & M_{01} & M_{02} & M_{03} \\ M_{10} & M_{11} & M_{12} & M_{13} \\ M_{20} & M_{21} & M_{22} & M_{23} \\ M_{30} & M_{31} & M_{32} & M_{33} \end{pmatrix} O_{\parallel\perp}(z) \quad (7.12)$$

Similarly, a second matrix takes into account the combined effects of all optics upstream of the Rayleigh Elastic channel receiver. Some of these are the same as in $M_{\parallel\perp upstream}$, above, but some are different, so we make an entirely new matrix, with its own overlap function $O_R(z)$ because of its different travel path for light within the detector.

$$T_{Rupstream} = \begin{pmatrix} T_{00} & T_{01} & T_{02} & T_{03} \\ T_{10} & T_{11} & T_{12} & T_{13} \\ T_{20} & T_{21} & T_{22} & T_{23} \\ T_{30} & T_{31} & T_{32} & T_{33} \end{pmatrix} O_R(z) \quad (7.13)$$

7.1.4.2 Matrices for optics upstream of the analyzing polarizers: Simplified case

In a hypothetical case for which the only instrument effect is a constant difference in total gains $G_{\parallel total}$, $G_{\perp total}$, and G_{Rtotal} between the channels, the instrument matrices must each be constant. Also, the overlap functions must be identical so that they are able to cancel when a ratio of the signals is made. In this case, the upstream instrument matrices are:

$$M_{\parallel \text{ upstream simple}} = G_{\text{upstream}\parallel} \begin{pmatrix} 1 & 0 & 0 & 0 \\ 0 & 1 & 0 & 0 \\ 0 & 0 & 1 & 0 \\ 0 & 0 & 0 & 1 \end{pmatrix} O_{\parallel\perp}(z) = G_{\text{upstream}\parallel} \quad (7.14)$$

$$M_{\perp \text{ upstream simple}} = G_{\text{upstream}\perp} \begin{pmatrix} 1 & 0 & 0 & 0 \\ 0 & 1 & 0 & 0 \\ 0 & 0 & 1 & 0 \\ 0 & 0 & 0 & 1 \end{pmatrix} O_{\parallel\perp}(z) = G_{\text{upstream}\perp} \quad (7.15)$$

$$T_{R \text{ upstream simple}} = G_{\text{upstream}R} \begin{pmatrix} 1 & 0 & 0 & 0 \\ 0 & 1 & 0 & 0 \\ 0 & 0 & 1 & 0 \\ 0 & 0 & 0 & 1 \end{pmatrix} O_R(z) = G_{\text{upstream}R} \quad (7.16)$$

These equations are identified here as this is the simplification made implicitly when carrying out the traditional depolarization method (Chapter 6) with calibrations as given in Gimmetstad [60].

7.1.4.3 Polarizer matrices

The Mueller matrices for linear polarizers are well-known (See, for example, [118]). The laser beam has linear polarization in the horizontal direction. Because arrangements were made for the “parallel” analyzer to be parallel to the unchanged, returned lidar beam, the parallel channel’s polarizer is a horizontal polarizer, too.

The Muller matrix for a horizontal linear polarizer (parallel channel):

$$M_{\parallel} = \frac{1}{2} \begin{pmatrix} 1 & 1 & 0 & 0 \\ 1 & 1 & 0 & 0 \\ 0 & 0 & 0 & 0 \\ 0 & 0 & 0 & 0 \end{pmatrix} \quad (7.17)$$

The Muller matrix for a vertical polarizer (perpendicular channel):

$$M_{\perp} = \frac{1}{2} \begin{pmatrix} 1 & -1 & 0 & 0 \\ -1 & 1 & 0 & 0 \\ 0 & 0 & 0 & 0 \\ 0 & 0 & 0 & 0 \end{pmatrix} \quad (7.18)$$

The Muller matrix for no polarizer, such as in the total Rayleigh Elastic channel is:

$$M_R = \begin{pmatrix} 1 & 0 & 0 & 0 \\ 0 & 1 & 0 & 0 \\ 0 & 0 & 1 & 0 \\ 0 & 0 & 0 & 1 \end{pmatrix} \quad (7.19)$$

The latter is the same form as a constant attenuator, so it is not necessary to use the full matrix in the CRL equations. This entire matrix is just like a scalar “1” and does not affect the calculations.

7.1.4.4 Matrices for optics downstream of the analyzing polarizers

Each channel has a few optics after the analyzing polarizer such as a focusing lens, and an interference filter. The photomultiplier tubes (PMTs) each have their own gain, as well. The only combined effect of these optics is to reduce the amplitude of the signal measured by the lidar. They are well-described as constant scalar factors:

- $G_{PMT\parallel}$ gives the gain of the parallel channel PMT and associated optics.
- $G_{PMT\perp}$ gives the gain of the perpendicular channel PMT and associated optics.
- $G_{PMT R}$ gives the gain of the Rayleigh Elastic channel PMT and associated optics.

In the case of the CRL, where the parallel and perpendicular channels are physically on the same PMT, going through the same optics, the gains for these channels are equal. We

define a constant $G_{PMT\parallel\perp}$ to be equal to these for ease of writing out calculations later:

$$G_{PMT\parallel\perp} = G_{PMT\parallel} = G_{PMT\perp}. \quad (7.20)$$

This assertion can be verified by the calibration tests made in Section 6.3 in which unpolarized light was shone directly into the receiver at the polarotor, and the measured signals in the Parallel and Perpendicular channels was identical. Note that this need not be the case for all lidars. In lidars with two separate PMTs for parallel and perpendicular, the gains need not be the same.

7.1.4.5 A note about gains

Gains are used in various ways in this thesis. They may represent either a true gain (increase in amplitude, if Gain > 1) or an attenuation (reduction in amplitude, if Gain < 1). Some of the expressions for gain include the other, more specific, gains. This convention is written out for the parallel channel here, and the other channels are treated in the same manner:

- $G_{PMT\parallel}$ is the gain of the photomultiplier tube only
- $G_{upstream\parallel}$ is the gain of the upstream optics only (occasionally abbreviated as $G_{up\parallel}$)
- $G_{\parallel} = G_{PMT\parallel}G_{upstream\parallel}$ is the overall gain of the channel including all contributions.

7.1.5 Signals available in each detector

To determine an expression for the signals available in each detector, the following matrix equations are used. They, are, as usual multiplied from right to left.

$$\begin{pmatrix} \text{Detected} \\ \text{light} \\ \text{Stokes} \\ \text{vector} \end{pmatrix} = \begin{pmatrix} \text{Optics} \\ \text{downstream} \\ \text{of polarizer} \end{pmatrix} \begin{pmatrix} \text{Polarizer} \end{pmatrix} \begin{pmatrix} \text{Optics} \\ \text{upstream} \\ \text{of polarizer} \end{pmatrix} \begin{pmatrix} \text{Atmospheric} \\ \text{scattering} \\ \text{matrix} \end{pmatrix} \begin{pmatrix} \text{Laser light} \\ \text{transmitted} \\ \text{Stokes} \\ \text{vector} \end{pmatrix} \quad (7.21)$$

Each channel begins with the laser output Stokes vector, multiplied by each optical element in turn (including that of the atmosphere), resulting in a final Stokes vector for the light received at that channel's detector. The signal in each channel is just the first term in the appropriate returned Stokes vector.

7.1.5.1 Signals in Parallel channel

I_{\parallel} is the Stokes vector for light that should make it to the PMT which can be measured in the parallel channel.

$$I_{\parallel} = \frac{G_{PMT\parallel}}{2} \begin{pmatrix} 1 & 1 & 0 & 0 \\ 1 & 1 & 0 & 0 \\ 0 & 0 & 0 & 0 \\ 0 & 0 & 0 & 0 \end{pmatrix} \begin{pmatrix} M_{00} & M_{01} & M_{02} & M_{03} \\ M_{10} & M_{11} & M_{12} & M_{13} \\ M_{20} & M_{21} & M_{22} & M_{23} \\ M_{30} & M_{31} & M_{32} & M_{33} \end{pmatrix} bO_{\parallel\perp}(z) \begin{pmatrix} 1 & 0 & 0 & 0 \\ 0 & 1-d & 0 & 0 \\ 0 & 0 & d-1 & 0 \\ 0 & 0 & 0 & 2d-1 \end{pmatrix} I_{laser} \begin{pmatrix} 1 \\ 1 \\ 0 \\ 0 \end{pmatrix} \quad (7.22)$$

$$= \frac{G_{PMT\parallel} bO_{\parallel\perp}(z) I_{laser}}{2} \begin{pmatrix} 1 & 1 & 0 & 0 \\ 1 & 1 & 0 & 0 \\ 0 & 0 & 0 & 0 \\ 0 & 0 & 0 & 0 \end{pmatrix} \begin{pmatrix} M_{00} & M_{01} & M_{02} & M_{03} \\ M_{10} & M_{11} & M_{12} & M_{13} \\ M_{20} & M_{21} & M_{22} & M_{23} \\ M_{30} & M_{31} & M_{32} & M_{33} \end{pmatrix} \begin{pmatrix} 1 \\ 1-d \\ 0 \\ 0 \end{pmatrix} \quad (7.23)$$

$$= \frac{G_{PMT\parallel} bO_{\parallel\perp}(z) I_{laser}}{2} \begin{pmatrix} 1 & 1 & 0 & 0 \\ 1 & 1 & 0 & 0 \\ 0 & 0 & 0 & 0 \\ 0 & 0 & 0 & 0 \end{pmatrix} \begin{pmatrix} M_{00} + M_{01}(1-d) \\ M_{10} + M_{11}(1-d) \\ M_{20} + M_{21}(1-d) \\ M_{30} + M_{31}(1-d) \end{pmatrix} \quad (7.24)$$

$$= \frac{G_{PMT\parallel} bO_{\parallel\perp}(z) I_{laser}}{2} \begin{pmatrix} M_{00} + M_{01}(1-d) + M_{10} + M_{11}(1-d) \\ M_{00} + M_{01}(1-d) + M_{10} + M_{11}(1-d) \\ 0 \\ 0 \end{pmatrix}.$$

The quantity of photons that the PMT actually measures is the signal rate S_{\parallel} . This is just the intensity element of the Stokes vector I_{\parallel} :

$$S_{\parallel} = \frac{G_{PMT\parallel} b O_{\parallel\perp}(z) I_{laser}}{2} (M_{00} + M_{10} + (M_{01} + M_{11})(1 - d)). \quad (7.25)$$

Recall that the polarized fraction of the backscattered light is $(1-d)$, and the unpolarized fraction is (d) . These are fractions and are therefore not in units of intensity. Equivalently, this equation may be described in terms of the intensities of polarized and unpolarized light received from the sky:

$$S_{\parallel} = \frac{G_{PMT\parallel} b O_{\parallel\perp}(z) I_{laser}}{2} \left(M_{00} + M_{10} + (M_{01} + M_{11}) \left(\frac{I_{polarized}}{I_{unpolarized} + I_{polarized}} \right) \right). \quad (7.26)$$

7.1.5.2 Signals in Perpendicular channel

The same calculations may be made with the Perpendicular detection chain. The only difference is that the polarizer matrix has elements (0,1) and (1,0) equal to -1 rather than the +1 which was needed for the Parallel position. The factors b and I_{laser} and $O_{\parallel\perp}(z)$ remain the same in both cases.

$$I_{\perp} = \frac{G_{PMT\perp} b O_{\parallel\perp}(z) I_{laser}}{2} \begin{pmatrix} M_{00} - M_{01}(1 - d) + M_{10} - M_{11}(1 - d) \\ M_{00} - M_{01}(1 - d) + M_{10} - M_{11}(1 - d) \\ 0 \\ 0 \end{pmatrix} \quad (7.27)$$

The quantity of photons that the PMT actually measures is, as before, the signal rate S_{\perp} . This is the intensity element of the Stokes vector I_{\perp} :

$$S_{\perp} = \frac{G_{PMT\perp} b O_{\parallel\perp}(z) I_{laser}}{2} (M_{00} - M_{10} + (M_{01} - M_{11})(1 - d)). \quad (7.28)$$

Equivalently:

$$S_{\perp} = \frac{G_{PMT\perp} b O_{\parallel\perp}(z) I_{laser}}{2} \left(M_{00} - M_{10} + (M_{01} - M_{11}) \left(\frac{I_{polarized}}{I_{unpolarized} + I_{polarized}} \right) \right). \quad (7.29)$$

7.1.5.3 Signals in Rayleigh Elastic channel

The same procedure is followed for the Rayleigh Elastic channel.

$$I_R = G_{PMTR} \begin{pmatrix} 1 & 0 & 0 & 0 \\ 0 & 1 & 0 & 0 \\ 0 & 0 & 1 & 0 \\ 0 & 0 & 0 & 1 \end{pmatrix} \begin{pmatrix} T_{00} & T_{01} & T_{02} & T_{03} \\ T_{10} & T_{11} & T_{12} & T_{13} \\ T_{20} & T_{21} & T_{22} & T_{23} \\ T_{30} & T_{31} & T_{32} & T_{33} \end{pmatrix} bO_R(z) \begin{pmatrix} 1 & 0 & 0 & 0 \\ 0 & 1-d & 0 & 0 \\ 0 & 0 & d-1 & 0 \\ 0 & 0 & 0 & 2d-1 \end{pmatrix} I_{laser} \begin{pmatrix} 1 \\ 1 \\ 0 \\ 0 \end{pmatrix} \quad (7.30)$$

$$= G_{PMTR} bO_R(z) I_{laser} \begin{pmatrix} 1 & 0 & 0 & 0 \\ 0 & 1 & 0 & 0 \\ 0 & 0 & 1 & 0 \\ 0 & 0 & 0 & 1 \end{pmatrix} \begin{pmatrix} T_{00} & T_{01} & T_{02} & T_{03} \\ T_{10} & T_{11} & T_{12} & T_{13} \\ T_{20} & T_{21} & T_{22} & T_{23} \\ T_{30} & T_{31} & T_{32} & T_{33} \end{pmatrix} \begin{pmatrix} 1 \\ 1-d \\ 0 \\ 0 \end{pmatrix} \quad (7.31)$$

$$= G_{PMTR} bO_R(z) I_{laser} \begin{pmatrix} 1 & 0 & 0 & 0 \\ 0 & 1 & 0 & 0 \\ 0 & 0 & 1 & 0 \\ 0 & 0 & 0 & 1 \end{pmatrix} \begin{pmatrix} T_{00} + T_{01}(1-d) \\ T_{10} + T_{11}(1-d) \\ T_{20} + T_{21}(1-d) \\ T_{30} + T_{31}(1-d) \end{pmatrix} \quad (7.32)$$

$$= G_{PMTR} bO_R(z) I_{laser} \begin{pmatrix} T_{00} + T_{01}(1-d) \\ T_{10} + T_{11}(1-d) \\ T_{20} + T_{21}(1-d) \\ T_{30} + T_{31}(1-d) \end{pmatrix} \quad (7.33)$$

The quantity of photons that the PMT actually measures is, as before, the signal rate S_R . This is the intensity element of the Stokes vector I_R :

$$S_R = G_{PMTR} bI_{laser} (T_{00} + T_{01}(1-d)). \quad (7.34)$$

Equivalently:

$$S_R = G_{PMT R} b O_R(z) I_{laser} \left(T_{00} + T_{01} \left(\frac{I_{polarized}}{I_{unpolarized} + I_{polarized}} \right) \right). \quad (7.35)$$

Notice that if the instrument matrix element $T_{01} = 0$, then the Rayleigh Elastic channel will truly be independent of polarization. If this is not the case, its signal will depend on the depolarization effects of the atmosphere. As the Rayleigh Elastic channel is intended to be independent of polarization, we hope that the verification tests in the following chapter confirm this. (Answer: Detailed calibrations show that if there is any sensitivity to polarization, this effect is orders of magnitude smaller than the uncertainty in routine lidar measurements and does not affect analyses).

7.1.6 Signals if a simplified lidar is assumed

Many lidars account for all optics upstream of the analyzing polarizer as a single gain term, potentially different for each channel. This can happen physically in a few ways which are detailed here.

7.1.6.1 Physical description of a simplified lidar

1. Physically separate perpendicular and parallel channels, with neutrally attenuating optics (can be different optics for each channel);
2. Partial polarizers in each channel, (can be different optics for each channel);
3. Parallel and Perpendicular channels sharing an optical path and all optical components in which the components act together as a single partial linear polarizer.

The third manner is the only one applicable to the CRL which could allow the traditional maths to work, by allowing the gain to be different for each channel, but still acting just as *only* a gain (and not a retarder, or rotator, etc.) for each. To show that this is optically equivalent to having two separate channels, each with their own simple attenuator, consider the following example.

Each case starts with arbitrarily-polarized light with a Stokes vector $[a, b, c, d]$. These variables in this section are simply arbitrary alphabetical choices for the purposes of demonstration within the current subsection (Subsection 7.1.6.1). None of these letters means anything, and we are not talking about depolarization parameter at all right here.

Situation 1: Physically separate channels, non-polarizing attenuators in each

In this situation, the optic in each channel is acting as a simple attenuator. It is followed by the analyzing polarizer appropriate to each channel.

Parallel:

$$I_{\parallel} = \frac{1}{2} \begin{pmatrix} 1 & 1 & 0 & 0 \\ 1 & 1 & 0 & 0 \\ 0 & 0 & 0 & 0 \\ 0 & 0 & 0 & 0 \end{pmatrix} \begin{pmatrix} G_{up\parallel} & 0 & 0 & 0 \\ 0 & G_{up\parallel} & 0 & 0 \\ 0 & 0 & G_{up\parallel} & 0 \\ 0 & 0 & 0 & G_{up\parallel} \end{pmatrix} \begin{pmatrix} a \\ b \\ c \\ d \end{pmatrix} \quad (7.36)$$

$$= \frac{G_{up\parallel}}{2} \begin{pmatrix} a + b \\ a + b \\ 0 \\ 0 \end{pmatrix} \quad (7.37)$$

Perpendicular:

$$I_{\perp} = \frac{1}{2} \begin{pmatrix} 1 & -1 & 0 & 0 \\ -1 & 1 & 0 & 0 \\ 0 & 0 & 0 & 0 \\ 0 & 0 & 0 & 0 \end{pmatrix} \begin{pmatrix} G_{\perp up} & 0 & 0 & 0 \\ 0 & G_{up\parallel} & 0 & 0 \\ 0 & 0 & G_{up\parallel} & 0 \\ 0 & 0 & 0 & G_{up\parallel} \end{pmatrix} \begin{pmatrix} a \\ b \\ c \\ d \end{pmatrix} \quad (7.38)$$

$$= \frac{G_{\perp up}}{2} \begin{pmatrix} a - b \\ -(a - b) \\ 0 \\ 0 \end{pmatrix} \quad (7.39)$$

Situation 2: Physically separate channels, partial linear polarizer in each

Partial polarizers take the form

$$\begin{pmatrix} A & B & 0 & 0 \\ B & A & 0 & 0 \\ 0 & 0 & C & 0 \\ 0 & 0 & 0 & C \end{pmatrix} \quad (7.40)$$

in which it does not particularly matter what A, B, C are, other than that they are constants for that particular partial polarizer. This format comes from [119]. For completeness, the detailed matrix is:

$$\frac{1}{2} \begin{pmatrix} p_x^2 + p_y^2 & p_x^2 - p_y^2 & 0 & 0 \\ p_x^2 - p_y^2 & p_x^2 + p_y^2 & 0 & 0 \\ 0 & 0 & 2p_x p_y & 0 \\ 0 & 0 & 0 & 2p_x p_y \end{pmatrix} \quad (7.41)$$

in which p_x and p_y are the transmittances of the electric field in orthogonal directions. In the case that $p_x = 1$ and $p_y = 0$, it is a full linear polarizer in the $+Q$ direction. In the case that $p_x = 0$ and $p_y = 1$ it is a full linear polarizer in the $-Q$ direction, and in the case that $p_x = p_y$ it is a neutral density filter. These details are immaterial to the discussion presented here. We require only the former, clearer, expression.

Again, arbitrarily-polarized light is introduced, to find:

Parallel:

$$I_{\parallel} = \frac{1}{2} \begin{pmatrix} 1 & 1 & 0 & 0 \\ 1 & 1 & 0 & 0 \\ 0 & 0 & 0 & 0 \\ 0 & 0 & 0 & 0 \end{pmatrix} \begin{pmatrix} A & B & 0 & 0 \\ B & A & 0 & 0 \\ 0 & 0 & C & 0 \\ 0 & 0 & 0 & C \end{pmatrix} \begin{pmatrix} a \\ b \\ c \\ d \end{pmatrix} \quad (7.42)$$

$$= \frac{1}{2} \begin{pmatrix} 1 & 1 & 0 & 0 \\ 1 & 1 & 0 & 0 \\ 0 & 0 & 0 & 0 \\ 0 & 0 & 0 & 0 \end{pmatrix} \begin{pmatrix} aA + bB \\ aB + bA \\ cC \\ dD \end{pmatrix} \quad (7.43)$$

$$= \frac{1}{2} \begin{pmatrix} aA + bB + aB + bA \\ aA + bB + aB + bA \\ 0 \\ 0 \end{pmatrix} \quad (7.44)$$

$$= \frac{1}{2} (A + B)(a + b) \begin{pmatrix} 1 \\ 1 \\ 0 \\ 0 \end{pmatrix} \quad (7.45)$$

And since $(A + B)$ is a constant which can be given any label, it is called $G_{up\parallel}$ in this thesis.

This gives:

$$I_{\parallel} = \frac{1}{2} G_{up\parallel} \begin{pmatrix} a + b \\ a + b \\ 0 \\ 0 \end{pmatrix} \quad (7.46)$$

which is exactly equal to the expression from the separate-channels neutral density filter example above.

Perpendicular:

$$I_{\perp} = \frac{1}{2} \begin{pmatrix} 1 & -1 & 0 & 0 \\ -1 & 1 & 0 & 0 \\ 0 & 0 & 0 & 0 \\ 0 & 0 & 0 & 0 \end{pmatrix} \begin{pmatrix} A & B & 0 & 0 \\ B & A & 0 & 0 \\ 0 & 0 & C & 0 \\ 0 & 0 & 0 & C \end{pmatrix} \begin{pmatrix} a \\ b \\ c \\ d \end{pmatrix} \quad (7.47)$$

$$= \frac{1}{2} \begin{pmatrix} 1 & -1 & 0 & 0 \\ -1 & 1 & 0 & 0 \\ 0 & 0 & 0 & 0 \\ 0 & 0 & 0 & 0 \end{pmatrix} \begin{pmatrix} aA + bB \\ aB + bA \\ cC \\ dD \end{pmatrix} \quad (7.48)$$

$$= \frac{1}{2} \begin{pmatrix} aA + bB - aB - bA \\ -aA - bB + aB + bA \\ 0 \\ 0 \end{pmatrix} \quad (7.49)$$

$$= \frac{1}{2}(A - B)(a - b) \begin{pmatrix} 1 \\ -1 \\ 0 \\ 0 \end{pmatrix} \quad (7.50)$$

And since $(A - B)$ is a constant which we can label anything we want, we call it $G_{\perp \text{ up}}$. This gives:

$$I_{\perp} = \frac{1}{2} G_{\perp \text{ up}} \begin{pmatrix} a - b \\ -(a - b) \\ 0 \\ 0 \end{pmatrix} \quad (7.51)$$

which is exactly equal to the expression for the separate-channels neutral density filter example above. Of course, if these are separate optics there would be no need for $(A + B)$ or $(A - B)$ to be equal for each, but they could be.

Situation 3: Physically the same optical path including a partial linear polarizer used for both channels; analyzing polarizer alternates between parallel and perpendicular

Next, the upstream optics can be conceptualized as the same physical object. Thus, A and B must be equal for each channel. The math for this is identical to Situation 2 just presented. Additionally, because the A and B are now identical, the gains are related for each channel:

$$G_{up\parallel} = (G_{\perp up} + B) + B = G_{\perp up} + 2B. \quad (7.52)$$

This is not really material to the problem at hand. The point is, *if* the CRL has a partial polarizer upstream (or several optics whose Mueller matrices multiply out to a partial polarizer) with no other features, an assumption of a simple and separate gain term for parallel and perpendicular channels may be appropriate. This gain term will be entered into the equations which follow as $G_{up\parallel}$ and $G_{\perp up}$.

Determining whether simple form is allowed

In order to decide whether the general or idealized simple form is required, it is helpful to investigate the circumstances under which their calibrated values of d work out to be the same. They will only *exactly* work out the same if there is exactly the same format between:

$$\begin{pmatrix} M_{00} & M_{01} & M_{02} & M_{03} \\ M_{10} & M_{11} & M_{12} & M_{13} \\ M_{20} & M_{21} & M_{22} & M_{23} \\ M_{30} & M_{31} & M_{32} & M_{33} \end{pmatrix} = \begin{pmatrix} A & B & 0 & 0 \\ B & A & 0 & 0 \\ 0 & 0 & C & 0 \\ 0 & 0 & 0 & C \end{pmatrix} \quad (7.53)$$

Thus, we would require $M_{00} = M_{11}$ and $M_{10} = M_{01}$. This would also mean that $G_{up\parallel} = A + B = M_{00} + M_{01}$ and $G_{\perp up} = A - B = M_{00} - M_{01}$. Therefore,

$$\frac{G_{up\parallel}}{G_{\perp up}} = \frac{M_{00} - M_{01}}{M_{00} + M_{01}} \quad (7.54)$$

$$= \frac{1 - \frac{M_{01}}{M_{00}}}{1 + \frac{M_{01}}{M_{00}}}, \quad (7.55)$$

and this can be compared with the Chapter 6 traditional method calibration constant k :

$$\frac{G_{up\parallel}}{G_{\perp up}} = k = \frac{1 - \frac{M_{01}}{M_{00}}}{1 + \frac{M_{01}}{M_{00}}}. \quad (7.56)$$

This can be tested with calibrations. The matrix equations to determine the signals available in each detector are carried out much like those for the general signals earlier in this chapter, and are included here in case they turn out to be applicable to the CRL (Answer: They are fine).

If the calibrations reveal small differences, subjective decisions can also be made about whether these simplifications are a good enough approximation for the task at hand, even if they are not strictly speaking quite true.

7.1.6.2 Signals in Parallel channel: simplified lidar

Note: Now back to our usual meanings of b as a constant, d as depolarization parameter.

The signals in each channel are calculated for a simplified lidar using the same matrix multiplication procedures as were used before. This time, the upstream optics are all included as a constant gain term.

$I_{\parallel simple}$ is the Stokes vector for the light which enters and is counted by the parallel PMT.

$$I_{\parallel \text{ simple}} = \frac{G_{PMT\parallel}}{2} \begin{pmatrix} 1 & 1 & 0 & 0 \\ 1 & 1 & 0 & 0 \\ 0 & 0 & 0 & 0 \\ 0 & 0 & 0 & 0 \end{pmatrix} G_{upstream\parallel} bO_{\parallel\perp}(z) \begin{pmatrix} 1 & 0 & 0 & 0 \\ 0 & 1-d & 0 & 0 \\ 0 & 0 & d-1 & 0 \\ 0 & 0 & 0 & 2d-1 \end{pmatrix} I_{laser} \begin{pmatrix} 1 \\ 1 \\ 0 \\ 0 \end{pmatrix} \quad (7.57)$$

$$= \frac{G_{PMT\parallel}}{2} \begin{pmatrix} 1 & 1 & 0 & 0 \\ 1 & 1 & 0 & 0 \\ 0 & 0 & 0 & 0 \\ 0 & 0 & 0 & 0 \end{pmatrix} G_{upstream\parallel} bO_{\parallel\perp}(z) I_{laser} \begin{pmatrix} 1 \\ 1-d \\ 0 \\ 0 \end{pmatrix} \quad (7.58)$$

$$= \frac{G_{PMT\parallel} G_{upstream\parallel} bO_{\parallel\perp}(z) I_{laser}}{2} \begin{pmatrix} 2-d \\ 2-d \\ 0 \\ 0 \end{pmatrix} \quad (7.59)$$

$$= G_{PMT\parallel} G_{upstream\parallel} bO_{\parallel\perp}(z) I_{laser} \begin{pmatrix} 1-d/2 \\ 1-d/2 \\ 0 \\ 0 \end{pmatrix}$$

The first (intensity) term of this $I_{\parallel \text{ simple}}$ vector is $S_{\parallel \text{ simple}}$. This is the actual signal rate measured in the parallel channel's PMT. Recall that the polarized fraction of the light is $(1-d)$, and the unpolarized fraction is (d) . These are fractions and are therefore not in units of intensity.

$$S_{\parallel \text{ simple}} = G_{PMT\parallel} G_{upstream\parallel} bO_{\parallel\perp}(z) I_{laser} \left(1 - \frac{d}{2}\right). \quad (7.60)$$

Equivalently,

$$S_{\parallel simple} = G_{PMT\parallel} G_{upstream\parallel} bO_{\parallel\perp}(z) I_{laser} \left((1-d) + \frac{d}{2} \right) \quad (7.61)$$

$$= G_{PMT\parallel} G_{upstream\parallel} bO_{\parallel\perp}(z) I_{laser} \left(\frac{I_{polarized}}{I_{unpolarized} + I_{polarized}} + \frac{1}{2} \frac{I_{unpolarized}}{I_{unpolarized} + I_{polarized}} \right) \quad (7.62)$$

$$= G_{total\parallel} bO_{\parallel\perp}(z) I_{laser} \left(\frac{I_{polarized}}{I_{unpolarized} + I_{polarized}} + \frac{1}{2} \frac{I_{unpolarized}}{I_{unpolarized} + I_{polarized}} \right). \quad (7.63)$$

7.1.6.3 Signals in Perpendicular channel: simplified lidar

$I_{\perp simple}$ is the Stokes vector for the light which enters and is counted by the perpendicular PMT.

$$I_{\perp simple} = \frac{G_{PMT\perp}}{2} \begin{pmatrix} 1 & -1 & 0 & 0 \\ -1 & 1 & 0 & 0 \\ 0 & 0 & 0 & 0 \\ 0 & 0 & 0 & 0 \end{pmatrix} G_{upstream\perp} bO_{\parallel\perp}(z) \begin{pmatrix} 1 & 0 & 0 & 0 \\ 0 & 1-d & 0 & 0 \\ 0 & 0 & d-1 & 0 \\ 0 & 0 & 0 & 2d-1 \end{pmatrix} I_{laser} \begin{pmatrix} 1 \\ 1 \\ 0 \\ 0 \end{pmatrix} \quad (7.64)$$

$$= G_{PMT\perp} G_{upstream\perp} bO_{\parallel\perp}(z) I_{laser} \begin{pmatrix} d/2 \\ -d/2 \\ 0 \\ 0 \end{pmatrix} \quad (7.65)$$

$$= G_{PMT\perp} G_{upstream\perp} bO_{\parallel\perp}(z) I_{laser} \begin{pmatrix} d/2 \\ -d/2 \\ 0 \\ 0 \end{pmatrix} \quad (7.66)$$

The first (intensity) term of this I_{\perp} vector is S_{\perp} . This is the actual signal rate measured in the perp channel's PMT. Recall that the polarized fraction of the light is $(1-d)$, and the unpolarized fraction is (d) . These are fractions and are therefore not in units of intensity.

$$S_{\perp \text{ simple}} = G_{PMT\perp} G_{upstream\perp} bO_{\parallel\perp}(z) I_{laser} \left(\frac{d}{2} \right). \quad (7.67)$$

Equivalently,

$$S_{\perp \text{ simple}} = G_{PMT\perp} G_{upstream\perp} bO_{\parallel\perp}(z) I_{laser} \frac{1}{2} \left(\frac{I_{unpolarized}}{I_{unpolarized} + I_{polarized}} \right) \quad (7.68)$$

$$= G_{total\perp} bO_{\parallel\perp}(z) I_{laser} \frac{1}{2} \left(\frac{I_{unpolarized}}{I_{unpolarized} + I_{polarized}} \right). \quad (7.69)$$

7.1.6.4 Signals in Rayleigh Elastic channel: simplified lidar

$I_{R \text{ simple}}$ is the Stokes vector for the light which enters and is counted by the Rayleigh elastic PMT.

$$I_{R \text{ simple}} = G_{PMT R} G_{upstream R} bO_R(z) \begin{pmatrix} 1 & 0 & 0 & 0 \\ 0 & 1-d & 0 & 0 \\ 0 & 0 & d-1 & 0 \\ 0 & 0 & 0 & 2d-1 \end{pmatrix} I_{laser} \begin{pmatrix} 1 \\ 1 \\ 0 \\ 0 \end{pmatrix} \quad (7.70)$$

$$= G_{PMT R} G_{upstream R} bO_R(z) I_{laser} \begin{pmatrix} 1 \\ 1-d \\ 0 \\ 0 \end{pmatrix} \quad (7.71)$$

$$= G_{total R} bO_R(z) I_{laser} \begin{pmatrix} 1 \\ 1-d \\ 0 \\ 0 \end{pmatrix} \quad (7.72)$$

The first (intensity) term of this I_R vector is S_R . This is the actual signal rate measured in the total channel's PMT. Recall that the polarized fraction of the light is $(1-d)$, and the unpolarized fraction is (d) . These are fractions and are therefore not in units of intensity.

$$S_{R \text{ simple}} = G_{PMT R} G_{upstream R} bO_R(z) I_{laser}(1). \quad (7.73)$$

And if we would like to force d or $I_{polarized}$ and $I_{unpolarized}$ into our equations so that they will look like the others, this is equivalently:

$$S_{R \text{ simple}} = G_{PMT R} G_{upstream R} bO_R(z) I_{laser}(1 - d + d) \quad (7.74)$$

$$= G_{PMT R} G_{upstream R} bO_R(z) I_{laser}((1 - d) + d) \quad (7.75)$$

$$= G_{PMT R} G_{upstream R} bO_R(z) I_{laser} \left(\frac{I_{polarized}}{I_{unpolarized} + I_{polarized}} + \frac{I_{unpolarized}}{I_{unpolarized} + I_{polarized}} \right). \quad (7.76)$$

7.1.7 Summary of signals received in each detector

Summary of all signals in terms of depolarization parameter d , general lidar:

$$S_{\parallel} = \frac{G_{PMT \parallel} bO_{\parallel \perp}(z) I_{laser}}{2} (M_{00} + M_{10} + (M_{01} + M_{11})(1 - d)) \quad (7.77)$$

$$S_{\perp} = \frac{G_{PMT \perp} bO_{\parallel \perp}(z) I_{laser}}{2} (M_{00} - M_{10} + (M_{01} - M_{11})(1 - d)) \quad (7.78)$$

$$S_R = G_{PMT R} bO_R(z) I_{laser} (T_{00} + T_{01}(1 - d)) \quad (7.79)$$

Summary of all signals in terms of depolarization parameter d , simplified lidar:

$$S_{\parallel \text{ simple}} = G_{PMT \parallel} G_{upstream \parallel} bO_{\parallel \perp}(z) I_{laser} \left(1 - \frac{d}{2} \right) \quad (7.80)$$

$$S_{\perp \text{ simple}} = G_{PMT \perp} G_{upstream \perp} bO_{\parallel \perp}(z) I_{laser} \left(\frac{d}{2} \right) \quad (7.81)$$

$$S_{R \text{ simple}} = G_{PMT R} G_{upstream R} bO_R(z) I_{laser} \quad (7.82)$$

During observations,

$S_{\parallel}, S_{\perp}, S_R$ are measurements

M_{xx} and T_{xx} are determined by calibration measurements.

G_x are determined by calibration measurements.

b and I_{laser} are never truly known. We will try to develop equations for routine use which cancel these last parameters out.

$O(z)$ is difficult to determine, as overlap functions for lidars generally are. The overlap function here, recall, includes both geometric overlap as well as any other factors which are constant in time, but not in altitude. It will be canceled out where possible, and available means will be used to determine it as well as possible via calibration when that is not possible.

The upcoming chapters determine through calibration whether the more complete descriptions of signals are required, or whether the simple versions from the Traditional Method will be sufficient.

7.2 Deriving an expression for the depolarization parameter d in terms of observables

Using the summarized S_{\parallel} , S_{\perp} and S_R from above for the general lidar, it is possible to solve for the depolarization parameter d to learn about the atmosphere. The calculations of d for the CRL are slightly more cumbersome than they are for the idealized lidar described in Gimmestad, but are still straightforward.

Instead of only showing one method (Option 1: \parallel, \perp), other methods, which also have advantages, are introduced in this thesis. This is motivated by the CRL having much, much lower perpendicular signal rates than parallel and Rayleigh Elastic during routine observations. Included here are possibilities for calculations using the following combinations: (Option 2: \parallel, R), (Option 3: \perp, R) and (Option 4: \parallel, \perp, R).

7.2.1 Option 1: Use only S_{\parallel} and S_{\perp} measurements

Most depolarization lidars use a combination of a Parallel channel and a Perpendicular channel (\parallel, \perp) to calculate d so the first demonstration is for an option to do the same at the CRL.

The simplest method for combining lidar signals S_{\parallel} and S_{\perp} into an equation to solve for the depolarization parameter comes from creating the following quantity, recalling that $G_{PMT\perp} = G_{PMT\parallel} = G_{PMT\parallel\perp}$ for the CRL:

$$\frac{S_{\parallel} - S_{\perp}}{S_{\parallel} + S_{\perp}} = \frac{\frac{G_{PMT\parallel\perp} b O_{\parallel\perp}(z) I_{laser}}{2} ((M_{00} + M_{10} + (M_{01} + M_{11})(1 - d)) - (M_{00} - M_{10} + (M_{01} - M_{11})(1 - d)))}{\frac{G_{PMT\parallel\perp} b O_{\parallel\perp}(z) I_{laser}}{2} ((M_{00} + M_{10} + (M_{01} + M_{11})(1 - d)) + (M_{00} - M_{10} + (M_{01} - M_{11})(1 - d)))} \quad (7.83)$$

$$= \frac{M_{10} + M_{11}(1 - d)}{M_{00} + M_{01}(1 - d)} \quad (7.84)$$

From there, we can solve for the value d :

$$d = 1 - \frac{\frac{M_{10}}{M_{00}}(S_{\parallel} + S_{\perp}) - (S_{\parallel} - S_{\perp})}{\frac{M_{01}}{M_{00}}(S_{\parallel} - S_{\perp}) - \frac{M_{11}}{M_{00}}(S_{\parallel} + S_{\perp})}, \quad (7.85)$$

or equivalently:

$$d = 1 - \frac{\frac{M_{10}}{M_{00}}(1 + \frac{S_{\perp}}{S_{\parallel}}) - (1 - \frac{S_{\perp}}{S_{\parallel}})}{\frac{M_{01}}{M_{00}}(1 - \frac{S_{\perp}}{S_{\parallel}}) - \frac{M_{11}}{M_{00}}(1 + \frac{S_{\perp}}{S_{\parallel}})}. \quad (7.86)$$

This particular manner of combining the signals is convenient as it allows as many unknown factors to cancel as possible, and condenses to the fewest calibration constants as possible.

Having a variety of mathematically equivalent expressions for d can be useful, as each includes the quantity $\frac{S_{\perp}}{S_{\parallel}}$ and the calibration constants different numbers of times. Depending on what the propagated uncertainties are for a particular lidar, the expression with the smallest total error and uncertainty at the end may be selected. The latter version propagates less uncertainty for the CRL, so is used for the calculations in this thesis.

For calibration, we must determine the instrument constants $\frac{M_{01}}{M_{00}}$, $\frac{M_{10}}{M_{00}}$, and $\frac{M_{11}}{M_{00}}$. Note that we do not require the M_{xx} values individually, nor do we need to know the laser intensity. These calibrations are discussed in Chapter 8.

7.2.2 Option 2: Use only S_{\parallel} and S_R measurements

It is possible to determine the depolarization parameter using exclusively the parallel and Rayleigh Elastic channels (\parallel , R). Because CRL's perpendicular measurements happen to have very low signal rates at all times, this alternative measurement option is a very useful development.

To combine these two signals, the equation is arranged to cancel as many constants as possible. First, the Rayleigh Elastic channel's signal equation is solved for bI_{laser} :

$$bI_{laser} = \frac{S_{R \text{ general}}}{G_{PMT R} O_R(z)} \frac{1}{T_{00} + T_{01}(1 - d)}. \quad (7.87)$$

Substituting this into the Parallel channel's signal equation and solving for d :

$$S_{\parallel} = \frac{G_{PMT\parallel} O_{\parallel\perp}(z)}{2} \frac{S_R}{G_{PMT\perp} O_R(z)} \frac{M_{00} + M_{10} + (M_{01} + M_{11})(1-d)}{T_{00} + T_{01}(1-d)} \quad (7.88)$$

$$d = 1 + \frac{\frac{1}{2} \frac{G_{PMT\parallel} O_{\parallel\perp}(z)}{G_{PMT\perp} O_R(z)} \frac{S_R}{S_{\parallel}} (M_{00} + M_{10}) - T_{00}}{\frac{1}{2} \frac{G_{PMT\parallel} O_{\parallel\perp}(z)}{G_{PMT\perp} O_R(z)} \frac{S_R}{S_{\parallel}} (M_{01} + M_{11}) - T_{01}} \quad (7.89)$$

$$d = 1 + \frac{\frac{1}{2} \frac{S_R}{S_{\parallel}} \left(1 + \frac{M_{10}}{M_{00}}\right) - \left(\frac{G_{PMT\perp} O_R(z)}{G_{PMT\parallel} O_{\parallel\perp}(z)} \frac{T_{00}}{M_{00}}\right)}{\frac{1}{2} \frac{S_R}{S_{\parallel}} \left(\frac{M_{01}}{M_{00}} + \frac{M_{11}}{M_{00}}\right) - \left(\frac{G_{PMT\perp} O_R(z)}{G_{PMT\parallel} O_{\parallel\perp}(z)} \frac{T_{01}}{M_{00}}\right)}. \quad (7.90)$$

From here, it is possible to see that five calibration constants are needed: $\frac{M_{01}}{M_{00}}$; $\frac{M_{10}}{M_{00}}$; $\frac{M_{11}}{M_{00}}$; $\frac{G_{PMT\perp} O_R(z)}{G_{PMT\parallel} O_{\parallel\perp}(z)} \frac{T_{00}}{M_{00}}$; and $\frac{G_{PMT\perp} O_R(z)}{G_{PMT\parallel} O_{\parallel\perp}(z)} \frac{T_{01}}{M_{00}}$. Again, neither M_{xx} nor T_{xx} is needed individually. Nor is any individual overlap function $O(z)$ required, but a ratio of these is included. The ratio of overlap functions is not necessarily stable in time, so when calibrating this must be taken into account. Calibrations for this quantity are likely to be needed more frequently than other calibrations. If there is a clever way to determine this quantity nightly, this should be done.

7.2.3 Option 3: Use only S_R and S_{\perp} measurements

Option 3 will again use the Rayleigh Elastic channel and one polarizer, but the perpendicular channel this time. This method is not so useful for the CRL given CRL's weak perpendicular signal rates, but if the polarotor rotating polarizer were to be stuck in the perpendicular position for an extended period of time, this method provides a better-than-nothing option for measuring d (and this has, in fact, happened at CRL).

Following the same reasoning as in Option 2, the Rayleigh Elastic channel's signal equation is solved for bI_{laser} . Substituting it into the Perpendicular channel's signal equation, and solving for d :

$$d = 1 + \frac{\frac{1}{2} \frac{S_R}{S_{\perp}} \left(1 - \frac{M_{10}}{M_{00}}\right) - \left(\frac{G_{PMT\perp} O_R(z)}{G_{PMT\parallel} O_{\parallel\perp}(z)} \frac{T_{00}}{M_{00}}\right)}{\frac{1}{2} \frac{S_R}{S_{\perp}} \left(\frac{M_{01}}{M_{00}} - \frac{M_{11}}{M_{00}}\right) - \left(\frac{G_{PMT\perp} O_R(z)}{G_{PMT\parallel} O_{\parallel\perp}(z)} \frac{T_{01}}{M_{00}}\right)}. \quad (7.91)$$

Because the gains for parallel and perpendicular are identical ($G_{PMT\perp} = G_{PMT\parallel}$), the calibration constant requirements remain the same as those for Option 2: $\frac{M_{01}}{M_{00}}$; $\frac{M_{10}}{M_{00}}$; $\frac{M_{11}}{M_{00}}$; $\frac{G_{PMTRO_R(z)}}{G_{PMT\parallel\perp}O_{\parallel\perp}(z)} \frac{T_{00}}{M_{00}}$; and $\frac{G_{PMTRO_R(z)}}{G_{PMT\parallel\perp}O_{\parallel\perp}(z)} \frac{T_{01}}{M_{00}}$. Again, M_{xx} and T_{xx} are not needed individually.

7.2.4 Option 4: Use all three S_R , S_{\perp} and S_{\parallel} measurements

If for some reason someone would like to use more measurement data and fewer calibration constants, and the signals in each channel have acceptable signal-to-noise ratios, one can use an equation which takes all three channels' signals into account. This method is much more cumbersome, and is not optimal for the CRL, but is included for completeness.

In this case, one easy path to an equation for d is:

$$\frac{S_{\parallel} + S_{\perp}}{S_R} = \frac{1 + \frac{M_{01}}{M_{00}}(1 - d)}{\frac{G_{PMTRO_R(z)}}{G_{PMT\parallel\perp}O_{\parallel\perp}(z)} \frac{T_{00}}{M_{00}} + \frac{G_{PMTRO_R(z)}}{G_{PMT\parallel\perp}O_{\parallel\perp}(z)} \frac{T_{01}}{M_{00}}(1 - d)} \quad (7.92)$$

$$d = 1 + \frac{\left(\frac{S_{\parallel} + S_{\perp}}{S_R}\right) \frac{G_{PMTRO_R(z)}}{G_{PMT\parallel\perp}O_{\parallel\perp}(z)} \frac{T_{00}}{M_{00}} - 1}{\left(\frac{S_{\parallel} + S_{\perp}}{S_R}\right) \frac{G_{PMTRO_R(z)}}{G_{PMT\parallel\perp}O_{\parallel\perp}(z)} \frac{T_{01}}{M_{00}} - \frac{M_{01}}{M_{00}}} \quad (7.93)$$

Some calibration constants are needed here, but only three of them: $\frac{M_{01}}{M_{00}}$; $\frac{G_{PMTRO_R(z)}}{G_{PMT\parallel\perp}O_{\parallel\perp}(z)} \frac{T_{00}}{M_{00}}$; and $\frac{G_{PMTRO_R(z)}}{G_{PMT\parallel\perp}O_{\parallel\perp}(z)} \frac{T_{01}}{M_{00}}$.

The final equation does appear to be cumbersome, but this format allows the $\frac{M_{01}}{M_{00}}$ term to stand alone for calibration (and this is required in any case for the other methods), while the calibration constants which we do not care particularly for individually are grouped into larger ones all together, including the ratio of the gains and the $\frac{T_{xx}}{M_{00}}$ terms.

Perhaps more interestingly, if slightly off-topic, this equation can be solved for the ratio of the overlap-related functions if one has already calibrated some of the other quantities by other means.

7.3 Summary of the equations for d and calibration constants needed

To differentiate the equations for each option which were created using the detailed calibration, and those made using the simpler calibrations, the following convention is used: Labels such as “Option 1” refer to the complete equation. Labels marked with “b”, as in “Option 1b” refer to the simplified equation.

The following table summarizes the equations for depolarization parameter d and the associated calibration constants for the case in which the full matrix descriptions of signals are used.

Option	Signals	Equation for d and calibration constants needed
1	S_{\parallel}, S_{\perp}	$d = 1 - \frac{\frac{M_{10}}{M_{00}}(1 + \frac{S_{\perp}}{S_{\parallel}}) - (1 - \frac{S_{\perp}}{S_{\parallel}})}{\frac{M_{01}}{M_{00}}(1 - \frac{S_{\perp}}{S_{\parallel}}) - \frac{M_{11}}{M_{00}}(1 + \frac{S_{\perp}}{S_{\parallel}})}$ <p>Calibration constants: $\frac{M_{01}}{M_{00}}, \frac{M_{10}}{M_{00}}, \frac{M_{11}}{M_{00}}$</p>
2	S_R, S_{\parallel}	$d = 1 + \frac{\frac{1}{2} \frac{S_R}{S_{\parallel}} (1 + \frac{M_{10}}{M_{00}}) - (\frac{G_{PMTR} O_R(z)}{G_{PMT\parallel} O_{\parallel\perp}(z)} \frac{T_{00}}{M_{00}})}{\frac{1}{2} \frac{S_R}{S_{\parallel}} (\frac{M_{01}}{M_{00}} + \frac{M_{11}}{M_{00}}) - (\frac{G_{PMTR} O_R(z)}{G_{PMT\parallel} O_{\parallel\perp}(z)} \frac{T_{01}}{M_{00}})}$ <p>Calibration constants: $\frac{M_{01}}{M_{00}}, \frac{M_{10}}{M_{00}}, \frac{M_{11}}{M_{00}}, \frac{G_{PMTR} O_R(z)}{G_{PMT\parallel} O_{\parallel\perp}(z)} \frac{T_{00}}{M_{00}}, \frac{G_{PMTR} O_R(z)}{G_{PMT\parallel} O_{\parallel\perp}(z)} \frac{T_{01}}{M_{00}}$</p>
3	S_R, S_{\perp}	$d = 1 + \frac{\frac{1}{2} \frac{S_R}{S_{\perp}} (1 - \frac{M_{10}}{M_{00}}) - (\frac{G_{PMTR} O_R(z)}{G_{PMT\perp} O_{\parallel\perp}(z)} \frac{T_{00}}{M_{00}})}{\frac{1}{2} \frac{S_R}{S_{\perp}} (\frac{M_{01}}{M_{00}} - \frac{M_{11}}{M_{00}}) - (\frac{G_{PMTR} O_R(z)}{G_{PMT\perp} O_{\parallel\perp}(z)} \frac{T_{01}}{M_{00}})}$ <p>Calibration constants: $\frac{M_{01}}{M_{00}}, \frac{M_{10}}{M_{00}}, \frac{M_{11}}{M_{00}}, \frac{G_{PMTR} O_R(z)}{G_{PMT\parallel\perp} O_{\parallel\perp}(z)} \frac{T_{00}}{M_{00}}, \frac{G_{PMTR} O_R(z)}{G_{PMT\parallel\perp} O_{\parallel\perp}(z)} \frac{T_{01}}{M_{00}}$</p>
4	$S_R, S_{\parallel}, S_{\perp}$	$d = 1 + \frac{(\frac{S_{\parallel} + S_{\perp}}{S_R}) \frac{G_{PMTR} O_R(z)}{G_{PMT\parallel\perp} O_{\parallel\perp}(z)} \frac{T_{00}}{M_{00}} - 1}{(\frac{S_{\parallel} + S_{\perp}}{S_R}) \frac{G_{PMTR} O_R(z)}{G_{PMT\parallel\perp} O_{\parallel\perp}(z)} \frac{T_{01}}{M_{00}} - \frac{M_{01}}{M_{00}}}$ <p>Calibration constants: $\frac{M_{01}}{M_{00}}, \frac{G_{PMTR} O_R(z)}{G_{PMT\parallel\perp} O_{\parallel\perp}(z)} \frac{T_{00}}{M_{00}}, \frac{G_{PMTR} O_R(z)}{G_{PMT\parallel\perp} O_{\parallel\perp}(z)} \frac{T_{01}}{M_{00}}$</p>

Table 7.1: Summary of more complete expressions for depolarization parameter d .

For the case in which the more complete matrix description is not needed (for example in the Traditional Method, Option 1b), and where we can use the simplified lidar expressions from earlier in this chapter, results are given in the table below. We follow the same matrix multiplication procedures as for the more general case, but obtain the simpler equations at the end.

Option	Signals	Equation for d and calibration constants needed
1b	S_{\parallel}, S_{\perp}	$d = \frac{2}{\frac{G_{upstream\perp}}{G_{upstream\parallel}} \frac{S_{\parallel}}{S_{\perp}} + 1} \quad \text{or} \quad d = \frac{2}{\frac{1}{k} \frac{S_{\parallel}}{S_{\perp}} + 1} \quad \text{This is the traditional method.}$ <p>Calibration constants: $\frac{G_{upstream\perp}}{G_{upstream\parallel}}$ (which is $\frac{1}{k}$)</p>
2b	S_R, S_{\parallel}	$d = 1 + \frac{\frac{1}{2} \frac{S_R}{S_{\parallel}} (1 + \frac{M_{10}}{M_{00}}) - (\frac{G_{PMT R} O_R(z)}{G_{PMT \parallel} O_{\parallel\perp}(z)} \frac{T_{00}}{M_{00}})}{\frac{1}{2} \frac{S_R}{S_{\parallel}} (\frac{M_{01}}{M_{00}} + \frac{M_{11}}{M_{00}}) - (\frac{G_{PMT R} O_R(z)}{G_{PMT \parallel} O_{\parallel\perp}(z)} \frac{T_{01}}{M_{00}})}$ <p>Calibration constants: $\frac{G_{PMT R} G_{upstream R} O_R(z)}{G_{PMT \parallel} G_{upstream \parallel} O_{\parallel\perp}(z)}$</p>
3b	S_R, S_{\perp}	$d = 2 \frac{G_{PMT R} G_{upstream R} O_R(z)}{G_{PMT \perp} G_{upstream \perp} O_{\parallel\perp}(z)} \frac{S_{\perp}}{S_R}$ <p>Calibration constants: $\frac{G_{PMT R} G_{upstream R} O_R(z)}{G_{PMT \perp} G_{upstream \perp} O_{\parallel\perp}(z)}$</p>
4b	$S_R, S_{\parallel}, S_{\perp}$	$d = 2 \frac{\left(\frac{S_{\parallel} + S_{\perp}}{S_R}\right) - \frac{G_{PMT \parallel} G_{upstream \parallel}}{G_{PMT R} G_{upstream R} O_R(z)}}{\frac{G_{PMT \perp} G_{upstream \perp} O_{\parallel\perp}(z)}{G_{PMT R} G_{upstream R} O_R(z)} - \frac{G_{PMT \parallel} G_{upstream \parallel} O_{\parallel\perp}(z)}{G_{PMT R} G_{upstream R} O_R(z)}}$ <p>Calibration constants: $\frac{G_{PMT \parallel} G_{upstream \parallel} O_{\parallel\perp}(z)}{G_{PMT R} G_{upstream R} O_R(z)}$; $\frac{G_{PMT \perp} G_{upstream \perp} O_{\parallel\perp}(z)}{G_{PMT R} G_{upstream R} O_R(z)}$</p> <p>or</p> $d = 1 + \left(\frac{\frac{G_{upstream \parallel}}{G_{upstream \perp}} - 1}{\frac{G_{upstream \parallel}}{G_{upstream \perp}} + 1} \right) \left(\left(\frac{S_{\parallel} + S_{\perp}}{S_R} \right) \frac{G_{PMT R} O_R(z)}{G_{PMT \parallel\perp} O_{\parallel\perp}(z)} + 1 \right)$ <p>Calibration constants: $\frac{G_{upstream \parallel}}{G_{upstream \perp}}$ (which is k); $\frac{G_{PMT R} O_R(z)}{G_{PMT \parallel\perp} O_{\parallel\perp}(z)}$</p>

Table 7.2: Summary of simplified expressions for depolarization parameter d .

Comparisons of corresponding equations in the above tables (e.g. Option 1 with Option 1b) indicate which values of calibration constants allow the general and simpler equations to be equivalent. Calibrations to determine whether the values for CRL match the required

values for applicability of the simplified equations are carried out in the following several chapters for Options 1 and 2.

7.4 Choices of methods to pursue

The calibration constants in common between the channels are helpful, as this gives the CRL a redundant channel. The depolarization ratio and/or depolarization parameter can be calculated using *any* two of the channels. The channels with the best signal to noise ratio might be chosen, or comparisons between calculations may be used for cross-calibrations. From this point on, only the two best methods will be used. Chosen by process of elimination:

1. Method 4/4b: This method is unnecessary and cumbersome to use on its own.
2. Method 3/3b: The perpendicular count rates for the CRL are extremely low, so this would not be the preferred way to go, either. Although the CRL has been operated in this mode in the past, it is not optimal. All procedures that will be shown for Method 2/2b are applicable to this method as well, (albeit with far poorer signal to noise and measurement coverage of time and space for Method 3/3b), so to show both would be redundant.
3. Method 2/2b: The parallel and total channels are both good. *If* this method validates well (and it does), it will be our preferred method for routine lidar operations; data coverage is better for these two channels than for the perpendicular channel.
4. Method 1/1b: This is a necessary test to carry out. The entire field of depolarization lidar scientists do this, so it had better work for CRL as well. Data coverage is very low for this method, because the perpendicular channel gets so few counts. It will be verified, but with the hope that Method 2/2b gives the same results where both method 1 and 2 are valid, so that just Method 2/2b can be used for routine analyses. It also turns

out that using Method 1/1b results to calibrate Method 2/2b measurements is quite a useful possibility.

To begin, it is necessary to determine whether Method 2b is sufficient or whether Method 2 will be required. This is done including the uncertainties. Even if Method 2b is “less correct”, error introduced using this method may be overshadowed by some huge uncertainty in Method 2’s results. The “most correct and certain” method will be chosen.

7.5 Caveats regarding these matrix derivations of d

There are many assumptions remaining in this analysis; however fewer than before. The largest assumptions actually come from the atmosphere. The following is not an exhaustive list, but note that we have assumed and/or entirely neglected the following in this derivation:

- Mueller matrices work when working with a single wavelength. We assume that our wavelength band is narrow enough that all our optics act achromatically for the 532 nm returns, yet is wide enough that we can actually make unpolarized light.
- We assume cloud particles to be randomly oriented in the sky
- Complications of sampling two distinct populations of hydrometeors within each scan have not been accounted for.
- Assume that the particles depolarize the same way regardless of the polarization direction of incident light (i.e. if we rotated our entire lidar by some angle, the answer we get out at the end wouldn’t change. This is not always the case, but most lidar people make this assumption whether they claim to or not.)
- Assume that the transmission of the atmosphere does not change depending on polarization of the light either on the way up or on the way down.

- We neglect lab temperature causing drift in filter wavelengths (causing M_{xx} or T_{xx} not to be a constant with temperature)
- We neglect differing filter widths of depolarization versus Rayleigh Elastic.
- The laboratory temperatures are recorded. They are not yet included in any measurement analyses (such as for the analogue dark count profiles).
- Atmospheric temperature changes the amount of Raman scattering signal that squeaks through the wide depolarization channel interference filter, but should not change the amount of Rayleigh signal through either filter. This means that the atmospheric scattering matrix really needs to be two matrices; one for Rayleigh returns (which is what is currently included) and one for Raman returns. Some exploration of our confidence that the existing matrices are sufficient have been carried out, and look promising (though are not included here), so this is a small concern only.

Chapter 8

Calibration for Full-Matrix Expression d , Option 1: Parallel and Perpendicular Signals

The object of this chapter is to verify whether our Traditional Method of determining d and δ are acceptable and appropriate for the CRL. That is to say, can we use the simplified versions of the expressions developed in the previous chapters, or must we use the full matrix expressions?

Recall that the full Mueller-matrix-derived expression for the depolarization parameter using the Option 1 combination of Parallel and Perpendicular channels is:

$$d = 1 - \frac{\frac{M_{10}}{M_{00}}(1 + \frac{S_{\perp}}{S_{\parallel}}) - (1 - \frac{S_{\perp}}{S_{\parallel}})}{\frac{M_{01}}{M_{00}}(1 - \frac{S_{\perp}}{S_{\parallel}}) - \frac{M_{11}}{M_{00}}(1 + \frac{S_{\perp}}{S_{\parallel}})}. \quad (8.1)$$

The calibration constants needed are: $\frac{M_{01}}{M_{00}}$; $\frac{M_{10}}{M_{00}}$; $\frac{M_{11}}{M_{00}}$. Option 1 is the full-matrix counterpart of “Traditional Method” Option 1b. It is important that we do not simply make assumptions about the values of the matrix elements. If we find *through calibration* that $\frac{M_{01}}{M_{00}} = \frac{M_{10}}{M_{00}}$ and that $\frac{M_{11}}{M_{00}} = 1$, then we will know that the traditional method of calibration is acceptable for the CRL. In that instance only, the equation for depolarization parameter re-

duces to $d = \frac{2}{\frac{1}{k} \frac{s_{\parallel}}{s_{\perp}} + 1}$, in which $k = \frac{1 + \frac{M_{10}}{M_{00}}}{1 - \frac{M_{10}}{M_{00}}} = \frac{1 + \frac{M_{01}}{M_{00}}}{1 - \frac{M_{01}}{M_{00}}}$, which is exactly the equation we obtained for the simpler Option 1b, which in turn is equal to the equations used in Chapter 6.

8.1 Calibration setup for Option 1

In each calibration test, we introduce known light to the detector, measure the lidar signals, and calculate the calibration constants. Every combination of light source and polarization generator provides a new matrix equation which we can use to determine the constants. As in the previous chapter, we show the math for the signals we'd expect in our calibration situations, and demonstrate how these signals can be combined to solve for the calibration constants we require.

To avoid repeating nearly identical mathematical descriptions later, the resulting signal in the Rayleigh Elastic lidar channel will be provided along with those for the parallel and perpendicular channels, despite it not being needed for Option 1 calibrations or analysis.

We recall the meanings of each term:

- M_{xx} are terms of the matrix describing the optics in common between the parallel and perpendicular channels, upstream of the polarotor analyzing polarizer;
- T_{xx} are terms of the matrix describing the optics in the Rayleigh Elastic channel, upstream of the PMT;
- $G_{PMT R}$ is the gain of the Rayleigh Elastic PMT;
- $G_{PMT \perp} = G_{PMT \parallel} = G_{PMT \parallel \perp}$ is the gain of the PMT which is shared between the parallel and perpendicular channels.
- $O(z)$ is the overlap function, as a function of altitude z . One works for parallel and perpendicular (same PMT, same optical path), and another for Rayleigh Elastic channel.

We can use either laser backscattered light or lamp light as the calibration light source. The (un)polarizing optics include: 1 m diameter glassine waxed paper; 25 cm diameter industrial kitchen-grade waxed paper; 25 cm diameter sheet polarizers; and 25 mm diameter cube polarizers. As revealed by Section 6.3, the most desirable calibrations are all made with the (un)polarizing test optic placed as far upstream in the detector as possible. While this can be accomplished for depolarizing material (see Section 6.2.4 in Chapter 6 and Section 8.2.2 in this chapter, in which glassine is placed above the roof window), it is decidedly not practically possible for polarizing optics to be placed in such locations. No polarizing optic was obtained which was as large as a 1-m diameter circle, which could be held completely flat, which could survive the harsh outdoor conditions of arctic winter, which could be easily rotated to the appropriate orientation, and which the CRL's budget could afford. Unfortunately, the best that could be done was:

1. To use the sheet polarizer in a small aperture above the primary mirror of the telescope, skipping the roof window.
 - Different optical paths into the primary mirror can result in distinctly differing signals in the detectors [92]. The optic at CRL was not able to be stably mounted, nor rotated with more than about 4 degrees' precision.
 - The Polaroid sheet polarizer linearly polarizes the backscattered laser light re-entering the lidar system, but the light which makes it through the polarizer is not oriented along the same plane on which it was incident on the polarizer. This means that interpreting the measurements are a bit tricky.
 - The lamp is not bright enough to be used for this test. Backscattered laser light is the only option, and the atmosphere can change over the duration of the test.
2. To use the sheet polarizer immediately upstream of the focus stage, with a lamp.

- The optic was not able to be stably mounted, nor rotated with more than about 4 degrees' precision. It was mounted more stably, however, than when it is placed above the primary mirror.
 - The roof window and telescope are both skipped.
 - A current-stabilized constant lamp source was placed, followed by a glassine depolarizing sheet, followed by the rotating sheet polarizer. This ensured that unpolarized light was entering the polarizer, and thus we would begin with equal numbers of photons exiting the polarizer regardless of its orientation.
3. To use the cube polarizer (which is of better optical quality) immediately downstream of the focus stage, skipping the focus stage optics, the telescope, and the roof window.
- Can be rotated with a great deal of precision; is stably mounted on a kinematic rotation mount on a 2" beam tube.
 - Since this skips half of the detector chain, such calibrations investigate the behaviour only of optics downstream of the focus stage.
 - This does not give us even close to a whole-system understanding, although it *does* allow us to say with certainty whether the downstream optics are contributing any non-simple-gain effects to the signals.
 - A current-stabilized constant lamp source was placed, followed by a glassine depolarizing sheet, followed by the rotating sheet polarizer. This ensured that unpolarized light was entering the polarizer, and thus we would begin with equal numbers of photons exiting the polarizer regardless of its orientation.

In future, it behooves us to make further tests of the telescope and roof window. This chapter simply demonstrates the results *to the best of our current technological ability*. It should be pointed out that CRL is not the only lab to place the polarization-generating optic after collimation of the return signal; [120] do this as well.

Since in many cases entire optics of the detector chain are skipped, the M_{xx} factors in each calibration test refer to different numbers of detector optics. Only in the case of the $\frac{M_{10}}{M_{00}}$ test, in which the entire detection chain is examined, does M_{xx} truly refer to the whole system. This is certainly a drawback, but is better than nothing.

In effect, the question answered here is, “If one only considers the lidar detectors beginning after the focus stage, can one use the simplified lidar equations?” and then, “If so, what is the best whole-lidar estimate for the single calibration constant required?”. We answer the second question first.

8.2 Finding $\frac{M_{10}}{M_{00}}$, setting $d = 1$

A single test can give $\frac{M_{10}}{M_{00}}$ by itself for the whole system. For the first way to find $\frac{M_{10}}{M_{00}}$, we introduce known unpolarized light into the lidar detector. This mimics fully-depolarized light returning from the sky, which sets $d = 1$ in our equations.

Chapter 6 previously has used precisely this setup to determine k for the traditional method. Those specific results are useful here; Our full-system value of $k = 21.0 \pm 0.2$ indicates a value of $\frac{M_{10}}{M_{00}} = 0.91 \pm 0.01$, which we will find matches the answer in this section. The matrix derivation of this is given below.

We obtain the “known to be depolarized” light by running the lidar as usual, with the laser transmitted to the sky and scattered back to the lidar, but then we interrupt the optical path of the receiver with an additional depolarizing element: Glassine waxed paper (see the chapter about the CRL lidar and calibration materials for more details) before the backscattered light enters through the roof window of the detector.

8.2.1 Development of the calibration expression for $\frac{M_{10}}{M_{00}}$

As before, we make a matrix equation to calculate the signals expected in the detectors for this setup.

The matrix for a perfect depolarizer is:

$$\frac{1}{2} \begin{pmatrix} 1 & 0 & 0 & 0 \\ 0 & 0 & 0 & 0 \\ 0 & 0 & 0 & 0 \\ 0 & 0 & 0 & 0 \end{pmatrix} \quad (8.2)$$

And with an attenuation parameter G_{gl} which is applicable to a real depolarizing optic (in this case, a sheet of glassine waxed paper), this is:

$$\frac{G_{gl}}{2} \begin{pmatrix} 1 & 0 & 0 & 0 \\ 0 & 0 & 0 & 0 \\ 0 & 0 & 0 & 0 \\ 0 & 0 & 0 & 0 \end{pmatrix} \quad (8.3)$$

For example, the matrix equation for the parallel channel, using the laser as the light source, is:

$$I_{\parallel} = \frac{G_{PMT\parallel\perp}}{2} \begin{pmatrix} 1 & 1 & 0 & 0 \\ 1 & 1 & 0 & 0 \\ 0 & 0 & 0 & 0 \\ 0 & 0 & 0 & 0 \end{pmatrix} \begin{pmatrix} M_{00} & M_{01} & M_{02} & M_{03} \\ M_{10} & M_{11} & M_{12} & M_{13} \\ M_{20} & M_{21} & M_{22} & M_{23} \\ M_{30} & M_{31} & M_{32} & M_{33} \end{pmatrix} \frac{G_{gl}}{2} \begin{pmatrix} 1 & 0 & 0 & 0 \\ 0 & 0 & 0 & 0 \\ 0 & 0 & 0 & 0 \\ 0 & 0 & 0 & 0 \end{pmatrix} bO_{\parallel\perp}(z) \begin{pmatrix} 1 & 0 & 0 & 0 \\ 0 & 1-d & 0 & 0 \\ 0 & 0 & d-1 & 0 \\ 0 & 0 & 0 & 2d-1 \end{pmatrix} I_{laser} \begin{pmatrix} 1 \\ 1 \\ 0 \\ 0 \end{pmatrix} \quad (8.4)$$

$$= \frac{G_{PMT\parallel\perp} G_{gl} b O_{\parallel\perp}(z) I_{laser}}{4} \begin{pmatrix} 1 & 1 & 0 & 0 \\ 1 & 1 & 0 & 0 \\ 0 & 0 & 0 & 0 \\ 0 & 0 & 0 & 0 \end{pmatrix} \begin{pmatrix} M_{00} & M_{01} & M_{02} & M_{03} \\ M_{10} & M_{11} & M_{12} & M_{13} \\ M_{20} & M_{21} & M_{22} & M_{23} \\ M_{30} & M_{31} & M_{32} & M_{33} \end{pmatrix} \begin{pmatrix} 1 & 0 & 0 & 0 \\ 0 & 0 & 0 & 0 \\ 0 & 0 & 0 & 0 \\ 0 & 0 & 0 & 0 \end{pmatrix} \begin{pmatrix} 1 \\ 1-d \\ 0 \\ 0 \end{pmatrix} \quad (8.5)$$

$$= \frac{G_{PMT\parallel\perp} G_{gl} b O_{\parallel\perp}(z) I_{laser}}{4} \begin{pmatrix} 1 & 1 & 0 & 0 \\ 1 & 1 & 0 & 0 \\ 0 & 0 & 0 & 0 \\ 0 & 0 & 0 & 0 \end{pmatrix} \begin{pmatrix} M_{00} \\ M_{10} \\ M_{20} \\ M_{30} \end{pmatrix}$$

$$= \frac{G_{PMT\parallel\perp} G_{gl} b O_{\parallel\perp}(z) I_{laser}}{4} \begin{pmatrix} M_{00} + M_{10} \\ M_{00} + M_{10} \\ 0 \\ 0 \end{pmatrix} \quad (8.6)$$

Thus, the signals in each channel are:

$$S_{\parallel d=1} = \frac{G_{PMT\parallel\perp} G_{gl}}{2} b O_{\parallel\perp}(z) I_{laser} (M_{00} + M_{10}) \quad (8.7)$$

$$S_{\perp d=1} = \frac{G_{PMT\parallel\perp} G_{gl}}{2} b O_{\parallel\perp}(z) I_{laser} (M_{00} - M_{10}) \quad (8.8)$$

$$S_{R d=1} = G_{PMT R} G_{gl} b O_R(z) I_{laser} (T_{00}) \quad (8.9)$$

Recall that I_{laser} does not remain constant from minute to minute nor from test to test, $O(z)$ is not constant with altitude, and is not constant over long time scales. Parameter b is constant between all three channels for any given altitude bin at any given minute, but is not necessarily constant from minute to minute. We can also never be sure that the sky is producing a 100% depolarizing $d = 1$ light, which is why we add the glassine to ensure that it is the situation going into the lidar calibration.

The signals from the parallel and perpendicular channel are combined as follows, so that we can solve for $\frac{M_{10}}{M_{00}}$ with as many of the unknown factors cancelling out as possible:

$$\frac{S_{\parallel d=1} + S_{\perp d=1}}{S_{\parallel d=1}} = \frac{\frac{G_{PMT\parallel\perp}}{2} bO_{\parallel\perp}(z) G_{gl} I_{laser}(M_{00} + M_{10}) + \frac{G_{PMT\parallel\perp}}{2} bO_{\parallel\perp}(z) G_{gl} I_{laser}(M_{00} - M_{10})}{\frac{G_{PMT\parallel\perp}}{2} bO_{\parallel\perp}(z) G_{gl} I_{laser}(M_{00} + M_{10})} \quad (8.10)$$

$$\frac{S_{\parallel d=1} + S_{\perp d=1}}{S_{\parallel d=1}} = \frac{2M_{00}}{M_{00} + M_{10}} \quad (8.11)$$

$$\frac{M_{10}}{M_{00}} = \frac{2S_{\parallel d=1}}{S_{\perp d=1} + S_{\parallel d=1}} - 1 \quad (8.12)$$

$$\frac{M_{10}}{M_{00}} = \frac{2}{\frac{S_{\perp d=1}}{S_{\parallel d=1}} + 1} - 1 \quad (8.13)$$

We use this equation to find $\frac{M_{10}}{M_{00}}$ during several tests, each with the glassine sheet at a different location in the lidar.

Note that this equation works equally well for the case in which we use a lamp to illuminate the lidar as the several differences in the initial matrix equation cancel out in any case: There is no overlap function, no atmospheric matrix, and we use I_{lamp} instead of I_{laser} . We've put in an unpolarized matrix for I_{lamp} , but because of the glassine layer, we could indeed use any stokes vector we liked and end up with the same result:

$$I_{\parallel} = \frac{G_{PMT\parallel\perp}}{2} \begin{pmatrix} 1 & 1 & 0 & 0 \\ 1 & 1 & 0 & 0 \\ 0 & 0 & 0 & 0 \\ 0 & 0 & 0 & 0 \end{pmatrix} \begin{pmatrix} M_{00} & M_{01} & M_{02} & M_{03} \\ M_{10} & M_{11} & M_{12} & M_{13} \\ M_{20} & M_{21} & M_{22} & M_{23} \\ M_{30} & M_{31} & M_{32} & M_{33} \end{pmatrix} \frac{G_{gl}}{2} \begin{pmatrix} 1 & 0 & 0 & 0 \\ 0 & 0 & 0 & 0 \\ 0 & 0 & 0 & 0 \\ 0 & 0 & 0 & 0 \end{pmatrix} I_{lamp} \begin{pmatrix} 1 \\ 0 \\ 0 \\ 0 \end{pmatrix} \quad (8.14)$$

$$(8.15)$$

This gives signals of:

$$S_{\parallel d=1} = \frac{G_{PMT\parallel\perp} G_{gl}}{2} I_{lamp}(M_{00} + M_{10}) \quad (8.16)$$

$$S_{\perp d=1} = \frac{G_{PMT\parallel\perp} G_{gl}}{2} I_{lamp}(M_{00} - M_{10}) \quad (8.17)$$

$$S_{R d=1} = G_{PMT R} G_{gl} I_{lamp}(T_{00}) \quad (8.18)$$

And results again in

$$\frac{M_{10}}{M_{00}} = \frac{2}{\frac{S_{\perp, d=1}}{S_{\parallel, d=1}} + 1} - 1. \quad (8.19)$$

8.2.2 Sample Detailed $\frac{M_{10}}{M_{00}}$ Calibration Test

This test uses the same selection of data from 20131101 as was used for calibrating for k in the Traditional Method, so the context plots are not repeated here. Again, the glassine sheet was placed above the roof window; binning is 10 time bins and 10 altitude bins. The basic analysis process to follow with the calibration is:

1. Low-level data processing (see Chapter 5) of Parallel and Perpendicular channel measurements to obtain corrected photocount profiles for each. Remove background only in the case of a laser calibration.
2. Select time-altitude region of interest to include appropriate data from calibration.
3. Reject any data points under the SNR and minimum counts thresholds (typically SNR greater than 0.1 for perpendicular, greater than 1.5 for parallel, and photon counts greater than 1 in both channels)

Next, perform either first or second procedure:

1. First Procedure:

- a) Using remaining data points, calculate a representative value for the fraction $\frac{S_{\perp}}{S_{\parallel}}$ for each remaining data point
- b) Make a histogram of $\frac{S_{\perp}}{S_{\parallel}}$ values and fit to this a polynomial to determine the most likely overall $\frac{S_{\perp}}{S_{\parallel}}$ value, and a standard deviation
- c) Use this representative $\frac{S_{\perp}}{S_{\parallel}}$ value in the equation above to calculate $\frac{M_{10}}{M_{00}}$ and use standard uncertainty propagation methods to determine the standard deviation.

2. Second Procedure:

- a) Using remaining data points, calculate a representative value for the fraction $\frac{S_{\perp}}{S_{\parallel}}$ for the whole data set by summing all parallel and all perpendicular signals, and taking the ratio of these summed values.
- b) Use this representative $\frac{S_{\perp}}{S_{\parallel}}$ value in the equation above to calculate $\frac{M_{10}}{M_{00}}$ and use standard uncertainty propagation methods to determine the standard deviation.

Using the first procedure with histogram fitting, the measurements of $\frac{S_{\perp}}{S_{\parallel}}$ appear as in Figure 8.1. Using the result of the associated histogram, we find representative values for $\frac{S_{\perp}}{S_{\parallel}}$ which are indicated in the left column of Table 8.1 with their uncertainties. The corresponding calculated $\frac{M_{10}}{M_{00}} = \frac{2}{\frac{S_{\perp}}{S_{\parallel}} + 1} - 1$ are indicated in the right column. Despite the mean and the peak of the polynomial fit indicating vastly different values on the histogram, they produce calibration constants which are identical to within the uncertainty of the measurements.

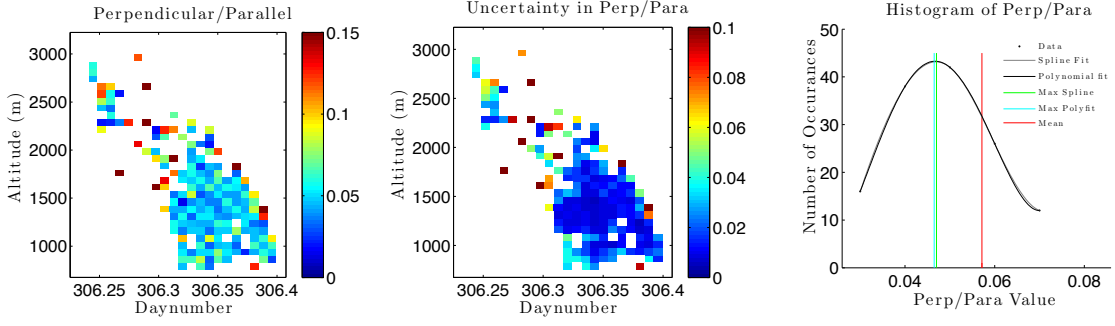


Figure 8.1: Left panel: Calculations of $\frac{S_{\perp}}{S_{\parallel}}$ for each data point. Middle panel: Associated uncertainties in this quantity. Right panel: Histogram illustrating the most probable value of $\frac{S_{\perp}}{S_{\parallel}}$. Spline and 6th order polynomial fits are indicated. Note that the most probable value, in cyan, is not the same as the mean value, in red.

Table 8.1: $\frac{S_{\perp}}{S_{\parallel}}$ and $\frac{M_{10}}{M_{00}}$ values using the first procedure, via histogram fitting.

Method	$\frac{S_{\perp}}{S_{\parallel}} \pm \sigma$	$\frac{M_{10}}{M_{00}} \pm \sigma$
Mean	0.057 ± 0.03	0.892 ± 0.045
Spline	0.047 ± 0.03	0.910 ± 0.046
Polyfit	0.047 ± 0.03	0.911 ± 0.046

Following the second procedure instead, we find that the ratio of the perpendicular and parallel summed counts gives a value of $\frac{S_{\perp}}{S_{\parallel}} = 0.0486 \pm 0.00104$. This leads to $\frac{M_{10}}{M_{00}} = 0.910 \pm 0.002$. These values of course agree with those calculated by first finding k when using the same raw data.

Conclusion: The best value available for the CRL of $\frac{M_{10}}{M_{00}} = 0.91 \pm 0.002$. It is the “best” as it was calculated using a calibration which included all detector optics, and is the expression with the lowest uncertainty. This value will be used throughout the thesis as the actual value of $\frac{M_{10}}{M_{00}}$.

8.2.3 $\frac{M_{10}}{M_{00}}$ values when testing from various locations in the detector

As for k in Chapter 6, $\frac{M_{10}}{M_{00}}$ may be calculated from tests with the depolarizing material at various locations within the detector to see how this value changes depending on where the calibration is carried out.

This is of paramount importance to point out here, because our subsequent tests for the other calibration constants $\frac{M_{01}}{M_{00}}$ and $\frac{M_{11}}{M_{00}}$ are perforce carried out in some of these suboptimal locations. It is helpful to know the corresponding $\frac{M_{10}}{M_{00}}$ when considering results from those locations.

Tests 1 through 8 in Table 8.2 were made using kitchen grade waxed paper, with short duration tests, with a lamp, and all within 2 hours of each other. Tests 9 through 12 were made on different dates using the histogram technique just detailed.

Test	Depolarizer Location	$\frac{M_{10}}{M_{00}} \pm \sigma$
1,4	Directly upstream of polarotor	-0.005 ± 0.005
2	Upstream of pellicle	-0.242 ± 0.013
3	Upstream of collimating lens	-0.198 ± 0.006
5	Just upstream of the Visible Long Wave Pass (LWP) dichroic	0.556 ± 0.076
6	Just upstream of the UV LWP dichroic	0.474 ± 0.029
7	At the entrance of the polychromator (downstream of focus stage, upstream of apertures)	0.718 ± 0.069
8	Right after the lamp, upstream of the focus stage	0.750 ± 0.156
9	Laser, 2 glassine upstream of focus stage	0.88 ± 0.05
10	Laser, 2 glassine above primary telescope mirror, downstream of window	0.87 ± 0.04
11	Laser, 1 glassine above primary telescope mirror, downstream of window	0.88 ± 0.06
12	Laser, 1 glassine above roof window	0.910 ± 0.002

Table 8.2: Measuring calibration constant $\frac{M_{10}}{M_{00}}$ using a depolarizer at various locations in the polychromator. Test numbers correspond with those from Chapter 6. See that chapter also for a diagram.

These tests all give the same result, and all of these match to within uncertainty of $\frac{M_{10}}{M_{00}}$ with our whole system value, with the most robust value of $\frac{M_{10}}{M_{00}} = 0.910$. This corresponds to a value of $k = 21$, so long as we end up in the condition for a simplified lidar (which we will verify in the next few sections of this chapter).

Something interesting to point out: $\frac{M_{10}}{M_{00}}$ tends to be more “forgiving” in terms of accuracy than k does. A small percentage error in $\frac{M_{10}}{M_{00}}$ will yield a larger percent error in k . Thus, one must take care when making a selection of which to use despite the ease with which one may convert between them in the absence of uncertainties.

8.3 Finding $\frac{M_{01}}{M_{00}}$, $\frac{M_{10}}{M_{00}}$, and $\frac{M_{11}}{M_{00}}$ together

A rotating polarizer test can provide a calibration value for all three of these calibration constants at once if we measure as a function of angle at many angles and fit some curves to the signals.

We introduce a polarization-defining optic in the form of a polarizer at some angle θ . Our equations for calibration by illuminating the receiver with light of a known polarization are below. We install a lamp of intensity I_{lamp} (or, equivalently, use backscattered laser light of intensity $bO(z)I_{laser}$), then a depolarizing sheet, then the linear polarizer, and shine this light into the detector. The depolarizing sheet is to ensure that the intensity making it through the polarizer does not change in the test as a function of polarizer angle.

Important note: The CRL's main analyzing polarizer, which is part of the detector, is the rotating cube polarizer in the Licel Polarotor. That optic is located immediately upstream of the parallel/perpendicular PMT beam tube. Though it operates to measure the signals during these calibrations, that optic is NOT the "rotating polarizer" which is discussed in this section. The rotating polarizer here is an *extra* generating polarizer. This test polarizer can be either a second cube polarizer mounted at the entrance to the polychromator, or can be a sheet polarizer at a variety of locations. All angles θ in this section refer to the angle of this test polarizer.

8.3.1 Development of the calibration signals for $\frac{M_{01}}{M_{00}}$, $\frac{M_{10}}{M_{00}}$, and $\frac{M_{11}}{M_{00}}$

For every new calibration hardware situation, we create for ourselves a new matrix equation in the same style introduced in Chapter 7.

In the following equations, we use backscattered laser light as the light source, a sheet of glassine next to unpolarize all of this light, followed by a polarizer oriented at some angle θ with respect to the plane of polarization of the parallel channel.

$$I_{\parallel\theta} = \frac{G_{PMT\parallel}}{2} \begin{pmatrix} 1 & 1 & 0 & 0 \\ 1 & 1 & 0 & 0 \\ 0 & 0 & 0 & 0 \\ 0 & 0 & 0 & 0 \end{pmatrix} \begin{pmatrix} M_{00} & M_{01} & M_{02} & M_{03} \\ M_{10} & M_{11} & M_{12} & M_{13} \\ M_{20} & M_{21} & M_{22} & M_{23} \\ M_{30} & M_{31} & M_{32} & M_{33} \end{pmatrix} \frac{G_{cube}}{2} \begin{pmatrix} 1 & \cos 2\theta & \sin 2\theta & 0 \\ \cos 2\theta & \cos^2 2\theta & \frac{1}{2} \sin 4\theta & 0 \\ \sin 2\theta & \frac{1}{2} \sin 4\theta & \sin^2 2\theta & 0 \\ 0 & 0 & 0 & 0 \end{pmatrix} G_{gl} O_{\parallel\perp}(z) \begin{pmatrix} 1 \\ 0 \\ 0 \\ 0 \end{pmatrix} bI_{laser} \quad (8.20)$$

$$I_{\perp\theta} = \frac{G_{PMT\perp}}{2} \begin{pmatrix} 1 & -1 & 0 & 0 \\ -1 & 1 & 0 & 0 \\ 0 & 0 & 0 & 0 \\ 0 & 0 & 0 & 0 \end{pmatrix} \begin{pmatrix} M_{00} & M_{01} & M_{02} & M_{03} \\ M_{10} & M_{11} & M_{12} & M_{13} \\ M_{20} & M_{21} & M_{22} & M_{23} \\ M_{30} & M_{31} & M_{32} & M_{33} \end{pmatrix} \frac{G_{cube}}{2} \begin{pmatrix} 1 & \cos 2\theta & \sin 2\theta & 0 \\ \cos 2\theta & \cos^2 2\theta & \frac{1}{2} \sin 4\theta & 0 \\ \sin 2\theta & \frac{1}{2} \sin 4\theta & \sin^2 2\theta & 0 \\ 0 & 0 & 0 & 0 \end{pmatrix} G_{gl} O_{\parallel\perp}(z) \begin{pmatrix} 1 \\ 0 \\ 0 \\ 0 \end{pmatrix} bI_{laser} \quad (8.21)$$

$$I_{R\theta} = G_{PMTR} \begin{pmatrix} T_{00} & T_{01} & T_{02} & T_{03} \\ T_{10} & T_{11} & T_{12} & T_{13} \\ T_{20} & T_{21} & T_{22} & T_{23} \\ T_{30} & T_{31} & T_{32} & T_{33} \end{pmatrix} \frac{G_{cube}}{2} \begin{pmatrix} 1 & \cos 2\theta & \sin 2\theta & 0 \\ \cos 2\theta & \cos^2 2\theta & \frac{1}{2} \sin 4\theta & 0 \\ \sin 2\theta & \frac{1}{2} \sin 4\theta & \sin^2 2\theta & 0 \\ 0 & 0 & 0 & 0 \end{pmatrix} G_{gl} O_R(z) \begin{pmatrix} 1 \\ 0 \\ 0 \\ 0 \end{pmatrix} bI_{laser} \quad (8.22)$$

Measurements at many angles θ give several equations for signals:

$$S_{\parallel\theta} = G_{cube} G_{PMT\parallel} G_{gl} \frac{bI_{laser}}{4} (M_{00} + M_{10} + (M_{01} + M_{11}) \cos 2\theta + (M_{02} + M_{12}) \sin 2\theta) \quad (8.23)$$

$$S_{\perp\theta} = G_{cube} G_{PMT\perp} G_{gl} \frac{bI_{laser}}{4} (M_{00} - M_{10} + (M_{01} - M_{11}) \cos 2\theta + (M_{02} - M_{12}) \sin 2\theta) \quad (8.24)$$

$$S_{R\theta} = G_{cube} G_{PMTR} G_{gl} \frac{bI_{laser}}{2} (T_{00} + T_{01} \cos 2\theta + T_{02} \sin 2\theta) \quad (8.25)$$

We obtain very similar equations, but with I_{lamp} instead of bI_{laser} , for the case in which we use a lamp as the light source rather than laser light.

$$S_{\parallel\theta} = G_{cube} G_{PMT\parallel} G_{gl} \frac{I_{lamp}}{4} (M_{00} + M_{10} + (M_{01} + M_{11})\cos 2\theta + (M_{02} + M_{12})\sin 2\theta) \quad (8.26)$$

$$S_{\perp\theta} = G_{cube} G_{PMT\perp} G_{gl} \frac{I_{lamp}}{4} (M_{00} - M_{10} + (M_{01} - M_{11})\cos 2\theta + (M_{02} - M_{12})\sin 2\theta) \quad (8.27)$$

$$S_{R\theta} = G_{cube} G_{PMT_R} G_{gl} \frac{I_{lamp}}{2} (T_{00} + T_{01}\cos 2\theta + T_{02}\sin 2\theta) \quad (8.28)$$

The above equations are valid for any lidar set up similarly to the CRL, with few assumptions. The simplifications which follow must be checked for applicability to the specific lidar for which they are used. For CRL, fortunately, the simplifications do turn out to be applicable (see the following section for an example with some proof of this).

8.3.2 Simplifications of the calibration signal expressions for $\frac{M_{01}}{M_{00}}$, $\frac{M_{10}}{M_{00}}$, and $\frac{M_{11}}{M_{00}}$ when allowed by calibration results

The signal expressions developed in Section 8.3.1 (above) will work for any values of calibration constant that we may find for a given lidar. It is possible that the lidar's calibration constant values are such that some simplifications may be safely made. In this section, we detail the methodical means by which it was determined that the CRL's calibration signal equations could be simplified, and give these simpler equations at the end.

8.3.2.1 First simplification: Symmetry, $M_{02} = 0$ and $M_{12} = 0$

The signal equations Equation 8.26 and Equation 8.27 are simplified a great deal if we find that M_{02} and M_{12} are zero. We can see that that is true if there is symmetry in the curves of the signals with angle (i.e. the values at $\theta = \frac{\pi}{4}$ equal those at $\theta = \frac{3\pi}{4}$ for the parallel and perpendicular).

For the parallel channel,

$$S_{\parallel\theta=\frac{\pi}{4}} = G_{cube}G_{PMT\parallel}G_{gl}\frac{I_{lamp}}{4}\left(M_{00} + M_{10} + (M_{01} + M_{11})\cos\left(2\frac{\pi}{4}\right) + (M_{02} + M_{12})\sin\left(2\frac{\pi}{4}\right)\right) \quad (8.29)$$

$$S_{\parallel\theta=\frac{3\pi}{4}} = G_{cube}G_{PMT\parallel}G_{gl}\frac{I_{lamp}}{4}\left(M_{00} + M_{10} + (M_{01} + M_{11})\cos\left(2\frac{3\pi}{4}\right) + (M_{02} + M_{12})\sin\left(2\frac{3\pi}{4}\right)\right) \quad (8.30)$$

For the perpendicular channel,

$$S_{\perp\theta=\frac{\pi}{4}} = G_{cube}G_{PMT\perp}G_{gl}\frac{I_{lamp}}{4}\left(M_{00} - M_{10} + (M_{01} - M_{11})\cos\left(2\frac{\pi}{4}\right) + (M_{02} - M_{12})\sin\left(2\frac{\pi}{4}\right)\right) \quad (8.31)$$

$$S_{\perp\theta=\frac{3\pi}{4}} = G_{cube}G_{PMT\perp}G_{gl}\frac{I_{lamp}}{4}\left(M_{00} - M_{10} + (M_{01} - M_{11})\cos\left(2\frac{3\pi}{4}\right) + (M_{02} - M_{12})\sin\left(2\frac{3\pi}{4}\right)\right) \quad (8.32)$$

Substitute in the values:

$$\cos\left(2\frac{\pi}{4}\right) = 0 \quad \cos\left(2\frac{3\pi}{4}\right) = 0 \quad \sin\left(2\frac{\pi}{4}\right) = 1 \quad \sin\left(2\frac{3\pi}{4}\right) = -1$$

For the parallel channel,

$$S_{\parallel\theta=\frac{\pi}{4}} = G_{cube}G_{PMT\parallel}G_{gl}\frac{I_{lamp}}{4}(M_{00} + M_{10} + (M_{01} + M_{11})(0) + (M_{02} + M_{12})(1)) \quad (8.33)$$

$$= G_{cube}G_{PMT\parallel}G_{gl}\frac{I_{lamp}}{4}(M_{00} + M_{10} + (M_{02} + M_{12})) \quad (8.34)$$

$$S_{\parallel\theta=\frac{3\pi}{4}} = G_{cube}G_{PMT\parallel}G_{gl}\frac{I_{lamp}}{4}(M_{00} + M_{10} + (M_{01} + M_{11})(0) + (M_{02} + M_{12})(-1)) \quad (8.35)$$

$$= G_{cube}G_{PMT\parallel}G_{gl}\frac{I_{lamp}}{4}(M_{00} + M_{10} - (M_{02} + M_{12})) \quad (8.36)$$

And if our measurements are symmetric, with $S_{\parallel\theta=\frac{\pi}{4}} = S_{\parallel\theta=\frac{3\pi}{4}}$, then we find that

$$G_{cube}G_{PMT\parallel}G_{gl}\frac{I_{lamp}}{4}(M_{00} + M_{10} + (M_{02} + M_{12})) = G_{cube}G_{PMT\parallel}G_{gl}\frac{I_{lamp}}{4}(M_{00} + M_{10} - (M_{02} + M_{12})) \quad (8.37)$$

$$M_{00} + M_{10} + M_{02} + M_{12} = M_{00} + M_{10} - M_{02} - M_{12} \quad (8.38)$$

$$M_{02} = -M_{12}. \quad (8.39)$$

For the perpendicular channel,

$$S_{\perp\theta=\frac{\pi}{4}} = G_{cube}G_{PMT\perp}G_{gl}\frac{I_{lamp}}{4}(M_{00} - M_{10} + (M_{01} - M_{11})(0) + (M_{02} - M_{12})(1)) \quad (8.40)$$

$$= G_{cube}G_{PMT\perp}G_{gl}\frac{I_{lamp}}{4}(M_{00} - M_{10} + (M_{02} - M_{12})) \quad (8.41)$$

$$S_{\perp\theta=\frac{3\pi}{4}} = G_{cube}G_{PMT\perp}G_{gl}\frac{I_{lamp}}{4}(M_{00} - M_{10} + (M_{01} - M_{11})(0) + (M_{02} - M_{12})(-1)) \quad (8.42)$$

$$= G_{cube}G_{PMT\perp}G_{gl}\frac{I_{lamp}}{4}(M_{00} - M_{10} - (M_{02} - M_{12})) \quad (8.43)$$

And if our measurements are symmetric, with $S_{\perp\theta=\frac{\pi}{4}} = S_{\perp\theta=\frac{3\pi}{4}}$, then we find that

$$G_{cube}G_{PMT\perp}G_{gl}\frac{I_{lamp}}{4}(M_{00} - M_{10} + (M_{02} - M_{12})) = \quad (8.44)$$

$$G_{cube}G_{PMT\perp}G_{gl}\frac{I_{lamp}}{4}(M_{00} - M_{10} - (M_{02} - M_{12}))$$

$$M_{00} - M_{10} + M_{02} - M_{12} = M_{00} - M_{10} - M_{02} + M_{12} \quad (8.45)$$

$$M_{02} = M_{12}. \quad (8.46)$$

Because the values for M_{02} and M_{12} must not change and are in common for parallel and perpendicular, then if *both* parallel and perpendicular are symmetric, both $M_{02} = -M_{12}$ and $M_{02} = M_{12}$ must be true simultaneously, so

$$M_{02} = -M_{02} \quad (8.47)$$

$$M_{12} = -M_{12} \quad (8.48)$$

The only way that it can be true to have something equal to its own negative value is if the value is zero. Thus,

$$M_{02} = 0 \quad (8.49)$$

$$M_{12} = 0 \quad (8.50)$$

This simplifies the calibration signal equations to:

$$S_{\parallel\theta} = G_{cube}G_{PMT\parallel}G_{gl}\frac{I_{lamp}}{4}(M_{00} + M_{10} + (M_{01} + M_{11})\cos 2\theta) \quad (8.51)$$

$$S_{\perp\theta} = G_{cube}G_{PMT\perp}G_{gl}\frac{I_{lamp}}{4}(M_{00} - M_{10} + (M_{01} - M_{11})\cos 2\theta) \quad (8.52)$$

And equivalently if a laser is used as the light source:

$$S_{\parallel\theta} = G_{cube}G_{PMT\parallel}G_{gl}\frac{bI_{laser}}{4}(M_{00} + M_{10} + (M_{01} + M_{11})\cos 2\theta) \quad (8.53)$$

$$S_{\perp\theta} = G_{cube}G_{PMT\perp}G_{gl}\frac{bI_{laser}}{4}(M_{00} - M_{10} + (M_{01} - M_{11})\cos 2\theta) \quad (8.54)$$

8.3.2.2 Second simplification: Zero-signals, $M_{10} = M_{01}$ and $M_{00} = M_{11}$

Further simplifications may be made if the parallel and perpendicular channel signals each go to zero at their respective minima. For parallel, this is at integer multiples of $\theta = \frac{\pi}{2}$, where $\cos 2\theta = -1$. For perpendicular, this is at $\theta = 0$ and at integer multiples of $\theta = \pi$, where $\cos 2\theta = 1$. If this is the case, then

$$S_{\parallel\theta} = 0 = G_{cube}G_{PMT\parallel}G_{gl}\frac{I_{lamp}}{4}(M_{00} + M_{10} + (M_{01} + M_{11})(-1)) \quad (8.55)$$

$$0 = M_{00} + M_{10} - M_{01} - M_{11} \quad (8.56)$$

$$S_{\perp\theta} = 0 = G_{cube}G_{PMT\perp}G_{gl}\frac{I_{lamp}}{4}(M_{00} - M_{10} + (M_{01} - M_{11})(1)) \quad (8.57)$$

$$0 = M_{00} - M_{10} + M_{01} - M_{11}. \quad (8.58)$$

We will see in the next sections that the CRL's signals do go to zero in these locations, so we can use the simpler equations. In the case where *both* signals go to zero at their respective locations,

$$0 = M_{00} + M_{10} - M_{01} - M_{11} = M_{00} - M_{10} + M_{01} - M_{11} \quad (8.59)$$

$$M_{10} = M_{01} \quad (8.60)$$

$$M_{00} = M_{11}. \quad (8.61)$$

This leaves the channel signals as:

$$S_{\parallel\theta} = G_{cube} G_{PMT\parallel} G_{gl} \frac{I_{lamp}}{4} (M_{00} + M_{10} + (M_{10} + M_{00}) \cos 2\theta) \quad (8.62)$$

$$S_{\perp\theta} = G_{cube} G_{PMT\perp} G_{gl} \frac{I_{lamp}}{4} (M_{00} - M_{10} + (M_{10} - M_{00}) \cos 2\theta). \quad (8.63)$$

In this mode, we have two constants that we care about (because they're required for calculating depolarization parameter d) and some we do not care about (all the gain terms, lamp intensity, etc). If we prefer, we can cast the equations to reflect this as:

$$S_{\parallel\theta} = G_{cube} G_{PMT\parallel} G_{gl} \frac{I_{lamp}}{4M_{00}} \left(1 + \frac{M_{10}}{M_{00}} + \left(\frac{M_{10}}{M_{00}} + 1 \right) \cos 2\theta \right) \quad (8.64)$$

$$S_{\perp\theta} = G_{cube} G_{PMT\perp} G_{gl} \frac{I_{lamp}}{4M_{00}} \left(1 - \frac{M_{10}}{M_{00}} + \left(\frac{M_{10}}{M_{00}} - 1 \right) \cos 2\theta \right). \quad (8.65)$$

Or equivalently:

$$S_{\parallel\theta} = G_{cube} G_{PMT\parallel} G_{gl} \frac{I_{lamp}}{4M_{00}} \left(\frac{M_{10}}{M_{00}} + 1 \right) (\cos 2\theta + 1) \quad (8.66)$$

$$S_{\perp\theta} = G_{cube} G_{PMT\perp} G_{gl} \frac{I_{lamp}}{4M_{00}} \left(\frac{M_{10}}{M_{00}} - 1 \right) (\cos 2\theta - 1). \quad (8.67)$$

in which $\frac{M_{10}}{M_{00}}$ is the only calibration constant we actually care about, and we have some calibration constants that we do not care about. Note that we do not need to know the value of M_{00} at any point for calculating depolarization parameter d .

8.3.3 Method for determining $\frac{M_{10}}{M_{00}}$ once we have made both simplifications

To determine the correct values for $\frac{M_{10}}{M_{00}}$ from these rotating cube polarizer tests, one option is to least squares fit each of the signals by varying two things: one common constant for all the leading constants that we do not need to know individually, the constant which we do care about.

A perhaps better method is to combine our signal equations. Equations 8.64 and 8.65 both contain the calibration constant we want, but they also include the I_{lamp} term, which

we do not particularly want as we do not know the lamp intensity (and likewise for laser intensity, gains, etc.). If we combine these equations, we can make a third equation which includes only constants that we seek and observables that we measure:

$$\frac{S_{\parallel\theta} - S_{\perp\theta}}{S_{\parallel\theta} + S_{\perp\theta}} = \frac{\frac{M_{10}}{M_{00}} + \cos 2\theta}{1 + \frac{M_{10}}{M_{00}} \cos 2\theta}. \quad (8.68)$$

It is tempting at this point to simply invert this equation and solve for $\frac{M_{10}}{M_{00}}$, as in:

$$\frac{M_{10}}{M_{00}} = \frac{\cos 2\theta - \left(\frac{S_{\parallel\theta} - S_{\perp\theta}}{S_{\parallel\theta} + S_{\perp\theta}} \right)}{\cos 2\theta \left(\frac{S_{\parallel\theta} - S_{\perp\theta}}{S_{\parallel\theta} + S_{\perp\theta}} \right) - 1}. \quad (8.69)$$

This is a correct thing to do, just note that at angles θ where either signal goes to zero, the result for $\frac{M_{10}}{M_{00}}$ is a zero-divided-by-zero fraction. Thus, one must exclude such calibration angles from such a calculation.

8.3.4 Method for determining $\frac{M_{01}}{M_{00}}$, $\frac{M_{10}}{M_{00}}$, and $\frac{M_{11}}{M_{00}}$ if we allow the first assumption, but not the second.

Let's examine the slightly less convenient case in which we allow only the first simplification. We again use the same approach for combining the two channels' signals to eliminate unknown and unwanted constants, but this time we need to keep all three M_{xx} factors in the equation:

$$\frac{S_{\parallel\theta} - S_{\perp\theta}}{S_{\parallel\theta} + S_{\perp\theta}} = \frac{\frac{M_{10}}{M_{00}} + \frac{M_{11}}{M_{00}} \cos 2\theta}{1 + \frac{M_{01}}{M_{00}} \cos 2\theta}. \quad (8.70)$$

As the parallel and perpendicular channels can both only measure positive photons, or zero (never negative photons),

$$-1 \leq \frac{S_{\parallel\theta} - S_{\perp\theta}}{S_{\parallel\theta} + S_{\perp\theta}} \leq 1. \quad (8.71)$$

We would select a range over which to test each constant, and would use a simple model to loop through all combinations of the three in order to best reproduce the measurements. The weighted least squares error is then minimized between the modeled curves and the measured data.

An examination of the signal expressions in this section indicates that we need only the signals from the maximally-parallel and maximally-perpendicular angles in order to determine the calibration constants uniquely. Why rotate the polarization-defining optic rather than put it in the parallel configuration, or at some other 'special case' angles, and leave it there? It is pretty hard to tell at the time of the measurement whether the polarizer is precisely at the right angle or not. Better to measure at lots of angles and fit some functions to be sure of having the most correct answer. We expect the signals in each channel to follow equations 8.26 and 8.27 from the previous section. Once this is done, it is fair to just pick off some points from the curves, but this throws away some potentially valuable data in the process. In practice, estimates made in this manner inform the choices of values over which we loop the model. Since it's hard to get the cube polarizer oriented perfectly in an absolute sense and be sure that they are at that location while doing the test, it is better to just plot the results, and identify the maxima and minima of a well-fit curve after the fact, fitting things from there. Snels et al. [120] do a calibration with a similar setup, and make the similar arguments for measuring at a variety of angles.

We have some indication of valid combinations based on the boundary condition above. From the lower limit of -1 : Our minimum profile occurs at $\theta = \pi/2$, so calculating the quantity there and solving the inequality results in $\frac{M_{10}}{M_{00}} > -1$. From the upper limit of 1 : The maximum profile occurs at $\theta = 0$, so calculating the quantity there and solving the

upper inequality results in $\frac{M_{10}}{M_{00}} - \frac{M_{10}}{M_{00}} + \frac{M_{11}}{M_{00}} - 1 < 0$. We may disregard fits which disobey this boundary condition.

An intermediate situation might exist in which we are sure one of the channels goes to zero, but are not positive about the other. Thus we would be able to determine one M_{xx} if we have the other two (using whichever of Equation 8.55 or 8.57 is appropriate ($0 = M_{10} + \dots$)). We could use this to our advantage when modelling fits to the data. We just loop through many values of $\frac{M_{01}}{M_{00}}$ and $\frac{M_{10}}{M_{00}}$, letting the $\frac{M_{11}}{M_{00}}$ be determined by these two. The weighted least squares error is then minimized between the modeled curves and the measured data as before.

The full method with all three calibration constants as free parameters is carried out in detail in this chapter.

8.3.5 Caveats regarding the calibration signal expressions for $\frac{M_{01}}{M_{00}}$,

$\frac{M_{10}}{M_{00}}$, and $\frac{M_{11}}{M_{00}}$ for CRL

These calibrations have so far been only carried out starting halfway through the detector. As shown in a previous chapter, calibrations done skipping optics are less than perfect, by a considerable margin. Unfortunately, for CRL, at this time, this is all that is available so we make do with what we have, and note that everything we find in terms of values of M_{xx} calibration constants refers only to optics together downstream of the focus stage. Anything at all could be happening upstream in the telescope, as we know indeed that partial polarization effects are occurring.

8.3.6 Sample Detailed Calibration Test from 20140305 with a lamp and cube polarizer rotated downstream of focus stage

The best example of such a $\frac{M_{01}}{M_{00}}$, $\frac{M_{10}}{M_{00}}$, and $\frac{M_{11}}{M_{00}}$ combined calibration for the CRL is made using a lamp and the cube polarizer located after the focus stage. The drawbacks of this

method are detailed earlier in the chapter, but the well-controlled nature of this calibration provides highly certain results regarding at least the latter half of the detector.

As we are beginning after the focus stage, recall that the appropriate k value for this location is 6.1 ± 0.4 and the appropriate corresponding $\frac{M_{10}}{M_{00}}$ value is 0.718 ± 0.156 . Hence, when we do our combined calibration and find that $\frac{M_{10}}{M_{00}} \neq 0.91$, we need not panic; indeed we would expect this to be the case.

8.3.6.1 Physical setup for 20130405 cube rotation calibration test

The generating polarizer is a Newport 10BC16PC.3 Pol Cube Beamsplitter, 532 nm, 25.4mm, $T_p/T_s > 1000 : 1$, a linearly polarizing cubic prism. It is placed immediately downstream of the focus stage and is rotated by hand. The rotating mount has markings in 2 degree steps, and there is about half a step of uncertainty in either direction, hence ± 1 degree uncertainty in the θ axis of all plots shown here.

Directly upstream of the polarizer were the lamp and the glassine sheet (Figure 8.2). The lamp was able to be bolted directly to the telescope frame. To use a calibration lamp as the light source rather than the laser itself allows the more controlled condition whereby a changing sky does not matter over the duration of the test because the sky is not involved at all. As long as the current (and thus output) of the lamp are well controlled (and they are, in this case), this has some advantages.

The Glassine ensures that the light entering the polarizer does not vary during the test (in case calibration lamp is itself partially polarized). The glassine sheet is held in with a frame of foamcore. This frame is placed between the tertiary telescope mirror and the focus stage. The unpolarized light is then sent through the focus stage, then through the extra linear polarizer, and then through the rest of the polychromator. All room lights were darkened during this test.



Figure 8.2: The extra polarizer is a linearly polarizing cubic prism. It is placed immediately downstream of the focus stage and is rotated by hand. The glassine sheet ensures that all light entering the cubic prism is unpolarized. The calibration lamp is securely bolted onto the telescope frame.

8.3.6.2 Measurements during the 5 March 2014 cube rotation calibration

The results of such a test from 5 March 2014 are plotted in Figure 8.3. This plot shows the signal in the parallel channel and in the perpendicular channel as a function of cube polarizer angle θ . Each angle was repeated several times, recorded as a function of the angle value written on the kinematic mount, and the absolute angles were determined in post-processing. The angles were determined such that the maximum in the Parallel channel would be the $\theta = 0\pi$ angle.

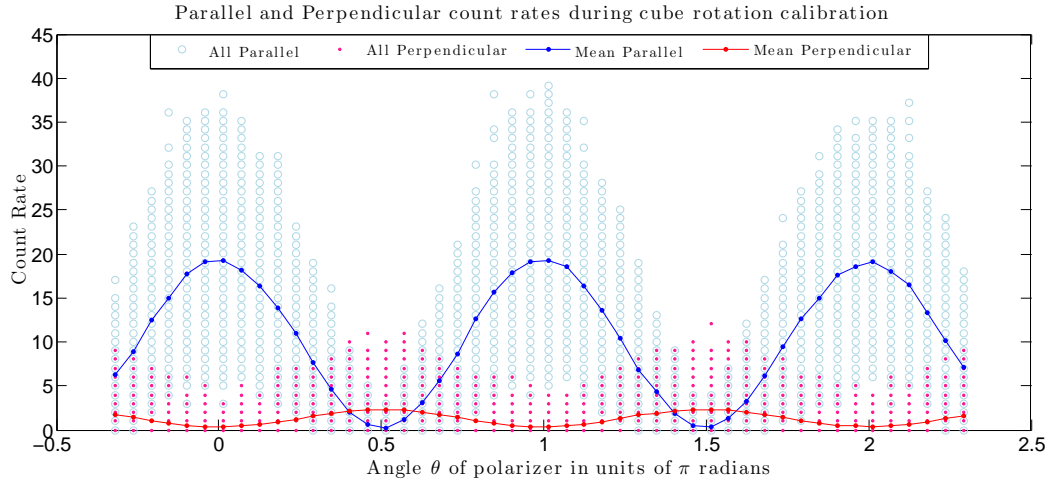


Figure 8.3: Polarized calibration measurements as a function of incident light polarization angle. The cube polarizer was initially placed at an arbitrary angle to ensure that photons were visible in each channel. It was then rotated through a number of steps, spending several minutes at each angle. In total, it was rotated through just more than one full rotation, or 2π radians. All measurements for each angle θ have been combined for this plot. Photocounts are indicated in units of photons per 7.5 metre altitude bin per 1 minute time bin. Parallel measurements are light blue circles. Perpendicular measurements are magenta points. Their respective mean values are indicated by the blue and red points. The curves are not fits, but trace out straight segment to show the path of the mean.

As there are sufficient photons at many angles, a mean value would seem to work for determining the overall signal in either channel at any angle. These are shown with the solid blue and red data points for each curve in the above figure. This does of course work for angles at which there is high signal. But what of the angles at which there are nearly zero photons? The most likely value for that angle might actually be zero, but as the PMTs cannot measure negative photons, a mean value will never be zero.

A helpful method to determine the most likely count rate value at each angle is to examine a histogram for each. An example for the Perpendicular Channel's measurements at a variety of angles is given here:

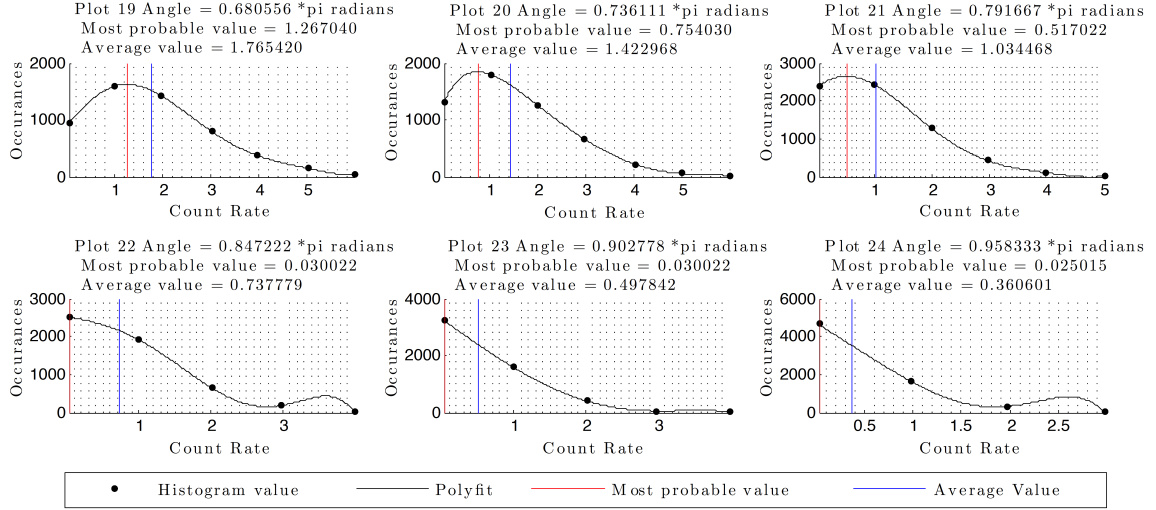


Figure 8.4: Histograms of perpendicular photocount rates for various cube polarizer angles. Note that the most probable value is zero counts at angles surrounding 0 radians, while the average (mean) value reports a value somewhat higher.

Indeed we frequently find that the mean value (labelled “average value” on the plots, indicated with a blue vertical line) is frequently *not* the most probable value (indicated with a red vertical line). This is especially true of low count rate plots. The values in Table 8.3 are informed by these histograms.

8.3.6.3 Verifying first simplification: $M_{02} = 0$ and $M_{12} = 0$

We determined in the previous section that if the calibration measurements at $S_{\perp\theta=\frac{\pi}{4}}$ equal those at $S_{\perp\theta=\frac{3\pi}{4}}$, then we may use the following signal equations:

$$S_{\parallel\theta} = G_{cube} G_{PMT\parallel} G_{gl} \frac{I_{lamp}}{4} (M_{00} + M_{10} + (M_{01} + M_{11}) \cos 2\theta) \quad (8.72)$$

$$S_{\perp\theta} = G_{cube} G_{PMT\perp} G_{gl} \frac{I_{lamp}}{4} (M_{00} - M_{10} + (M_{01} - M_{11}) \cos 2\theta). \quad (8.73)$$

Is our data symmetric in this manner? Yes, it is. This is determined by examining the count rate in each channel at the two diagnostic angles and integer multiples thereof. The values of count rate in each channel at each of the $\theta = \frac{\pi}{4}$ and $\theta = \frac{3\pi}{4}$ angles are given in Table 8.3. Recall that there is approximately a 2° or 0.035 radian uncertainty in the angles when doing this calibration. For the parallel channel, the uncertainty is always 0.5 or more,

and at θ we are examining here, uncertainty is ± 2.5 . For perpendicular, the uncertainties at these angles are ± 1.3 .

Table 8.3: Parallel and perpendicular signals for angles diagnostic of symmetry in the measurements. Each signal is effectively the same at 0.25π and 0.75π radians and integer multiples thereof.

Angle θ (rad)	$S_{\parallel} \pm \sigma_{\parallel}$	$S_{\perp} \pm \sigma_{\perp}$
-0.25π	9.358 ± 2.5	0.666 ± 1.3
0.25π	9.629 ± 2.5	0.693 ± 1.3
0.75π	9.269 ± 2.5	0.701 ± 1.3
1.25π	9.091 ± 2.5	0.834 ± 1.3
1.75π	9.875 ± 2.5	0.789 ± 1.3
2.25π	8.919 ± 2.5	0.830 ± 1.3

It is clear from the table that each channel's signal values at $\theta = \frac{\pi}{4}$ and $\theta = \frac{3\pi}{4}$ are equal to well within their respective uncertainties. Therefore, both channels are symmetric, and the simplified equations may be used. Hence we see that for CRL, $M_{02} = 0$ and $M_{12} = 0$ are valid.

8.3.6.4 Verifying second simplification: $M_{10} = M_{01}$ and $M_{00} = M_{11}$

The next simplification made in the mathematical development section of this chapter has to do with whether the parallel signals and perpendicular signals go to zero at their respective minima. Here we endeavour to verify whether this is the case for the CRL lidar.

The histograms reveal that the most probable value for the perpendicular count rate $S_{\perp\theta=0}$ truly is zero photons per measurement interval. See the bottom row of histograms, right side, at angles of approximately 1π . Similar histograms for the parallel channel reveal that it, too, goes to zero at its minimum (at $\theta = \pi/2$ rad; not shown).

For completeness, and to determine what is the actual cutoff to consider things to be zero, a quick check was carried out: To see how much stray light was getting in through the sides of the cube polarizer, the entrance aperture of the polarizer was temporarily blocked. Count rates equivalent to approximately 0.13 MHz were measured in both channels in this “dark” situation. The majority of this light was determined to be leaking in through the

“wrong” side of the polarizer (the exit side for the rejected polarization of light). Consequently, count rates in the calibration test that are smaller than 0.13 MHz may be considered to be zero to within our ability to measure them.

As the count rates do indeed go to zero at their respective minima, we determine that the second simplification is also appropriate for CRL, and that $M_{10} = M_{01}$ and $M_{00} = M_{11}$. This leaves us finally with only one calibration constant to determine: $\frac{M_{10}}{M_{00}}$.

8.3.6.5 Example calculation of $\frac{M_{10}}{M_{00}}$ with fully-simplified conditions

Recall that we can, in the highly-simplified case, calculate $\frac{M_{10}}{M_{00}}$ directly from our combined lidar signals. This is because we already know that $\frac{M_{10}}{M_{00}} = 1$ and $\frac{M_{01}}{M_{00}} = \frac{M_{10}}{M_{00}}$. Recall also that this calculation method is only valid for angles which are not near the minima of either signal. We could also keep in mind the large relative error adjacent to those locations. In the current example, we have selected to include measurements made within $\pm \frac{\pi}{8}$ of angles which we know to be allowable. That is to say, we used angles from $\theta = \frac{\pi}{8}$ to $\theta = \frac{3\pi}{8}$, from $\theta = \frac{5\pi}{8}$ to $\theta = \frac{7\pi}{8}$, and so on. Once we remove angles outside the appropriate calculation area we may make the calculation. Here is a histogram of the calculated $\frac{M_{10}}{M_{00}}$ values under these circumstances.

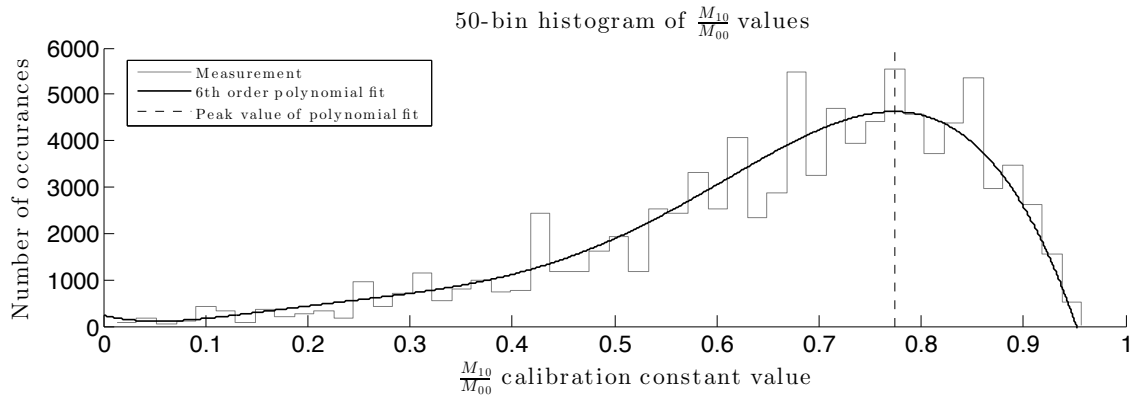


Figure 8.5: Histogram using 50 bins, keeping only the values far from angles where either channel’s signal was near zero. The peak value is 0.77 and the standard deviation in this histogram is 0.18.

It is clear that the peak of the histogram and thus the most probable value of $\frac{M_{10}}{M_{00}}$ is approximately at 0.77. Histograms with between 40 and 200 bins were checked; all peaked between 0.77 and 0.78. As the standard deviation in this histogram is 0.18, these values are equal to the 0.72 ± 0.07 indicated by the glassine depolarization sheet method (Section 8.2.3, Table 8.2) result for calibrations done at the entrance to the polychromator, to within the uncertainty of the measurements.

8.3.6.6 Example model and comparison measurements to determine $\frac{M_{10}}{M_{00}}$, $\frac{M_{01}}{M_{00}}$, and $\frac{M_{11}}{M_{00}}$ with partially-simplified conditions

In the case where one allows the first simplification but not the second, M_{02} and M_{12} go to zero, but the three $\frac{M_{10}}{M_{00}}$, $\frac{M_{01}}{M_{00}}$, and $\frac{M_{11}}{M_{00}}$ remain to be determined by the fit. We use the following to model a combination of our channels' data:

$$\frac{S_{\parallel\theta} - S_{\perp\theta}}{S_{\parallel\theta} + S_{\perp\theta}} = \frac{\frac{M_{10}}{M_{00}} + \frac{M_{11}}{M_{00}} \cos 2\theta}{1 + \frac{M_{01}}{M_{00}} \cos 2\theta}. \quad (8.74)$$

Modelling, we loop through an array of values for each calibration constant in steps of 0.01. The values tested were: 0.7 to 0.9 for $\frac{M_{01}}{M_{00}}$, 0.7 to 0.9 for $\frac{M_{10}}{M_{00}}$, and 0.9 to 1.1 for $\frac{M_{11}}{M_{00}}$. The results are plotted in Figure 8.6. Some of the combinations of values were not valid to be used in the fits (see Section 8.3.4), and are not shown in the plots. The weighted least squares error, shown in Figure 8.7, was minimized between the modeled curves and the measured data to determine the best fit.

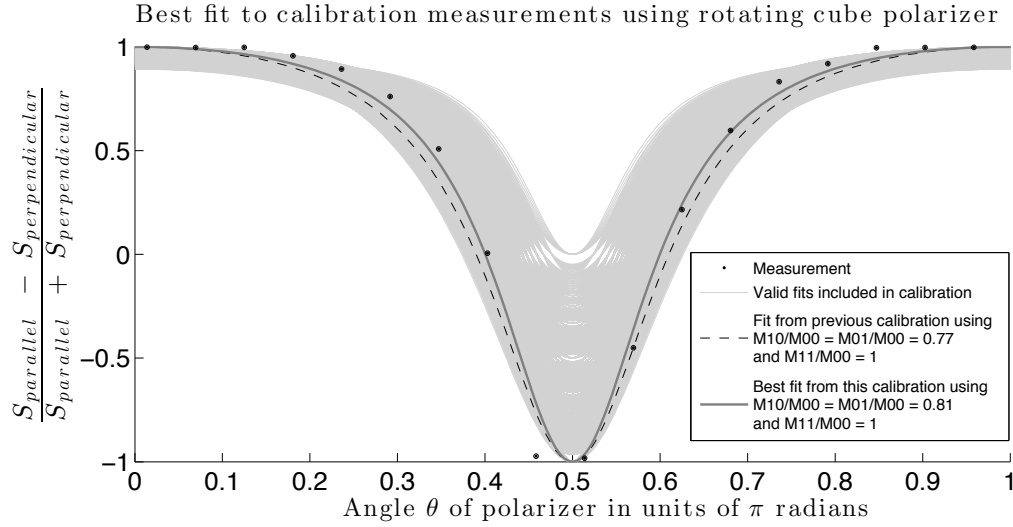
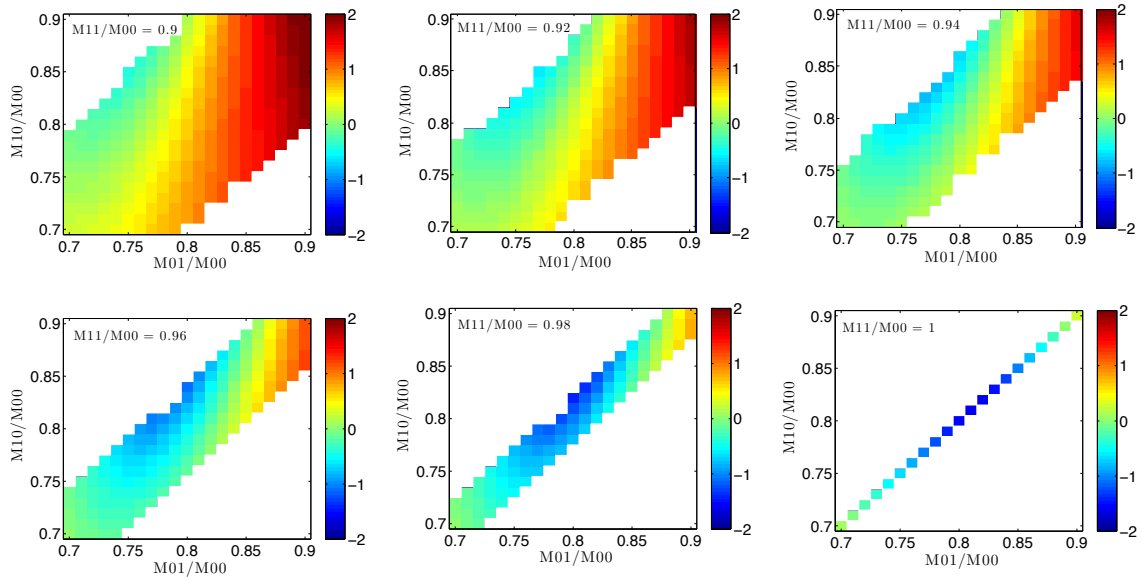


Figure 8.6: Light grey curves are all valid model curves from this test. The solid darker line is the best fit curve based on a weighted least squares comparison between the modeled curves and the measurement data (black circles). The best fit line falls well within $\pm 1\sigma$ of the measurement, and is occurs with values $\frac{M_{01}}{M_{00}} = 0.81$, $\frac{M_{10}}{M_{00}} = 0.81$, $\frac{M_{01}}{M_{00}} = 1$. The dashed line is the curve computed when using the value $\frac{M_{10}}{M_{00}} = 0.77$ calculated in Section 8.3.6.5.

Figure 8.7: Log of weighted least squares error between the measured and modeled data is plotted for various combinations of calibration constants. In each panel, one $\frac{M_{11}}{M_{00}}$ is chosen, and the $\frac{M_{10}}{M_{00}}$ and $\frac{M_{01}}{M_{00}}$ vary within the plot. Any white squares indicate a combination of M_{xx} which is not applicable to the quantity being plotted. At higher values of $\frac{M_{11}}{M_{00}}$, there are fewer valid values of $\frac{M_{01}}{M_{00}}$ and $\frac{M_{10}}{M_{00}}$ to choose from.



The best fit modeled curve indicates that $\frac{M_{01}}{M_{00}} = 0.81$, $\frac{M_{10}}{M_{00}} = 0.81$, $\frac{M_{01}}{M_{00}} = 1$. As a check, the older value $\frac{M_{10}}{M_{00}} = 0.77$ calculated in Section 8.3.6.5, where both simplifications are used, forcing $\frac{M_{11}}{M_{00}} = 1$ and $\frac{M_{01}}{M_{00}} = \frac{M_{10}}{M_{00}}$, was checked against the current test. This fit line, too, reproduces the measurements to within the measurements' error. Thus it is a reasonable choice as well.

Finally, we fit Equations 8.66 and 8.67 using these values to ensure that we *can* get a good fit to our original signal measurements by varying the catch-all constant (includes I_{lamp} , gains, etc, for which we have complete freedom, having no idea what the lamp's intensity actually is). It does in fact work, as shown in Figure 8.8. The value for the initial constant is: $G_{cube}G_{PMT\parallel}G_{gl}\frac{I_{lamp}}{4M_{00}} = 5.2 \pm 0.05$. This value of course changes during measurements. The same calculations carried out with a value of $\frac{M_{10}}{M_{00}} = 0.77$ worked fine, too.

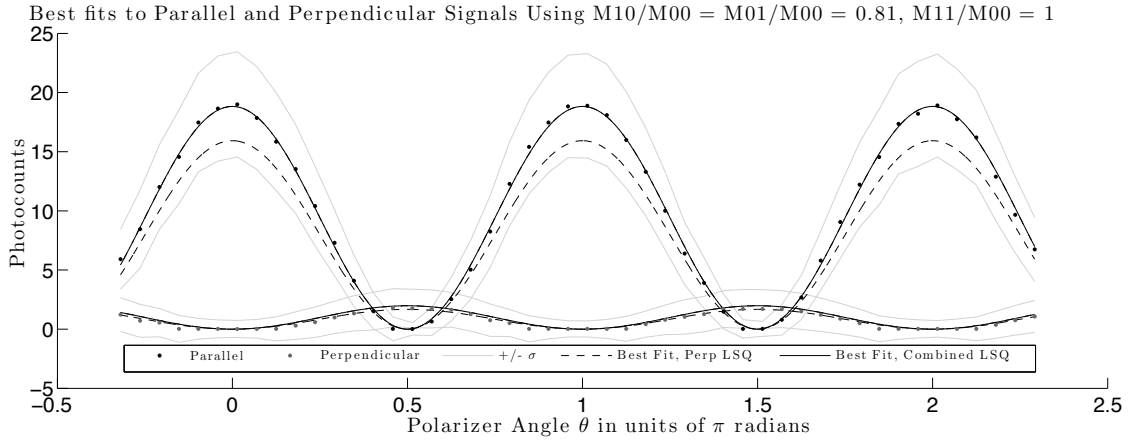


Figure 8.8: Polarized calibration measurements as a function of incident light polarization angle. Angle $\theta = 0\pi$ is completely parallel; $\theta = 0.5\pi$ is completely perpendicular. The best fits to parallel measurements (black dots) and perpendicular measurements (grey dots) are shown for the case in which $\frac{M_{10}}{M_{00}} = \frac{M_{01}}{M_{00}} = 0.81$ and $\frac{M_{11}}{M_{00}} = 1$. The best fit determined by using the Perpendicular signal's least-squares is given by the dashed line. Note that this fit does not fit the Parallel channel at all well. The best fit determined by using the Parallel channel's least-squares fit is given by the solid black line. The best overall fit, using a combination of least squares error from both channels, is indistinguishable from the solid black line as the Parallel channel dominates the fit. The best fit lines fall entirely within $\pm 1\sigma$ of the measurements (light grey).

8.3.7 Other calibration tests attempted

The calibration tests in the preceding sections were not the only ones performed at CRL to verify the $\frac{M_{01}}{M_{00}}, \frac{M_{10}}{M_{00}}, \frac{M_{11}}{M_{00}}$ behaviour of the CRL. These tests used a lamp (rather than a laser like the lidar usually uses) and they skip half of the detector optics, so attempts were made to do better.

Test attempts to use the whole detector didn't work very well and were confusing. It was difficult-to-impossible to install a large sheet polarizer in a stable manner above the telescope. When using laser backscattered light, the sky changed so much that the values from different polarizer orientations were difficult to compare one to another (because the leading “constant” including I_{laser} was constantly changing). When using a lamp in this configuration, too few photons reached the detectors to make meaningful statistical analyses.

8.4 Conclusions regarding Option 1 calibration constants

From the calibrations carried out in this section, it is evident that:

1. $M_{02} = 0$ and $M_{12} = 0$ are valid for the CRL.
2. $\frac{M_{11}}{M_{00}} = 1$ and $\frac{M_{01}}{M_{00}} = \frac{M_{10}}{M_{00}}$ are valid for the CRL.

Therefore, the calibration approach used by others in the community is appropriate for the CRL, despite its many optics between the sky and the analyzing polarizer for the depolarization channel.

Calibrations with the best values are those which are the “most correct” and the “least uncertain”. The calibration tests in which the glassine depolarizer is placed at the beginning of the optical system, above the roof window, are best in both regards. This is due to the availability of many times the amount of raw data going into the calibration, and due to the superiority of a calibration which examines the entire lidar system and not just half.

The values from Section 8.2.2 will be adopted hereafter for the CRL. The calibration constants for Option 1 are:

- $\frac{M_{02}}{M_{00}} = \frac{M_{12}}{M_{00}} = 0$
- $\frac{M_{11}}{M_{00}} = 1$
- $\frac{M_{01}}{M_{00}} = \frac{M_{01}}{M_{00}} = 0.91 \pm 0.01$

These are directly relatable to the traditional method calibration constant from Chapter 6:

- $k = 21.0 \pm 0.2$.

Chapter 9

Calibration for Full-Matrix Expression

d, Option 2: Parallel and Rayleigh

Elastic Signals

The full Mueller-matrix-derived expression for the depolarization parameter using the Option 2 combination of Parallel and Rayleigh Elastic channels (Section 7.3) is :

$$d = 1 + \frac{\frac{1}{2} \frac{S_R}{S_{\parallel}} \left(1 + \frac{M_{10}}{M_{00}}\right) - \left(\frac{G_{PMTRO_R(z)}}{G_{PMT\parallel} O_{\parallel\perp}(z)} \frac{T_{00}}{M_{00}}\right)}{\frac{1}{2} \frac{S_R}{S_{\parallel}} \left(\frac{M_{01}}{M_{00}} + \frac{M_{11}}{M_{00}}\right) - \left(\frac{G_{PMTRO_R(z)}}{G_{PMT\parallel} O_{\parallel\perp}(z)} \frac{T_{01}}{M_{00}}\right)}. \quad (9.1)$$

The calibration constants needed are: $\frac{M_{01}}{M_{00}}$; $\frac{M_{10}}{M_{00}}$; $\frac{M_{11}}{M_{00}}$; $\frac{G_{PMTRO_R(z)}}{G_{PMT\parallel\perp} O_{\parallel\perp}(z)} \frac{T_{00}}{M_{00}}$; $\frac{G_{PMTRO_R(z)}}{G_{PMT\parallel\perp} O_{\parallel\perp}(z)} \frac{T_{01}}{M_{00}}$.

Recall that in Chapter 8 the first three of these calibration constants were determined: $\frac{M_{11}}{M_{00}} = 1$ and $\frac{M_{01}}{M_{00}} = \frac{M_{10}}{M_{00}} = 0.91 \pm 0.01$, which are directly relatable to the traditional method calibration constant from Chapter 6: $k = 21.0 \pm 0.2$. These constants were found using the calibration measurements from a lamp-and-polarizer calibration test carried out on 5 March 2014. In the previous chapter, only the results from the Parallel and Perpendicular channels were presented; however, measurements were also made in the Rayleigh Elastic channel during this calibration. These will be used in Section 9.1 to demonstrate that $T_{01} = 0$, making the whole term $\frac{G_{PMTRO_R(z)}}{G_{PMT\parallel\perp} O_{\parallel\perp}(z)} \frac{T_{01}}{M_{00}} = 0$. Subsequent Section 9.2 will demonstrate the

calibration determination of the term $\frac{G_{PMTRO_R(z)} T_{00}}{G_{PMT\parallel\perp} O_{\parallel\perp}(z) M_{00}}$, which varies as a function of altitude.

9.1 Sample Calibration Test from 5 March 2014 with a lamp and cube polarizer rotated downstream of focus stage: Rayleigh channel

Measurements in all three channels were made on 5 March 2014 during a calibration test in which a cube polarizer was mounted at the entrance to the polychromator, just downstream of the focus stage in the lidar. This polarizer was rotated, and lamp light was shone through with the polarizer at a variety of angles. Including all of the channels' measurements, the data from this calibration is presented in Figure 9.1.

Part of Equation 8.28 is repeated here to show the signal in the Rayleigh Elastic channel as a function of polarizer rotation angle θ . It will be re-numbered for the current chapter:

$$S_{R\theta} = G_{cube} G_{PMTRO_R} G_{gl} \frac{I_{lamp}}{2} (T_{00} + T_{01} \cos 2\theta + T_{02} \sin 2\theta) \quad (9.2)$$

9.1.1 Simplifications of the calibration signal expressions for T_{01} and T_{02} when allowed by calibration results

As before, some simplifications may be made to the calibration equations if the calibration measurements allow it. These, and the calibration results, will be given in the remainder of this chapter. Development of the calibration process for the Rayleigh Elastic channel during this test will be given in far less detail than appeared in Chapter 8 for the Parallel and Perpendicular channels as many of the arguments are the same. If additional explanation is desired, please refer to that chapter.

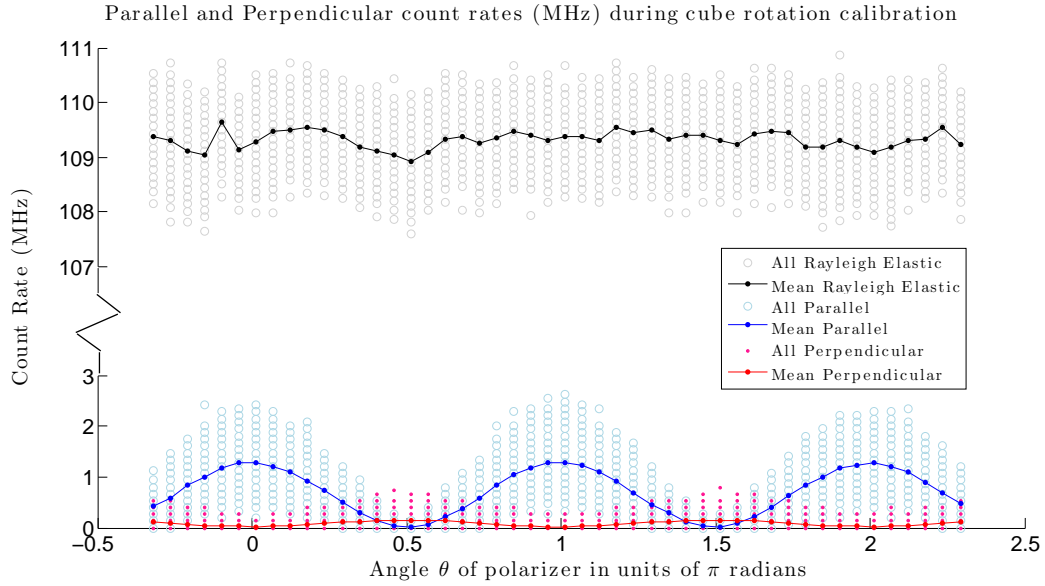


Figure 9.1: Polarized calibration measurements as a function of incident light polarization angle for all channels. Note the broken axis; the Rayleigh Elastic measurements (grey circles and black line) are an order of magnitude larger than the Parallel (light blue circles and blue line) and Perpendicular (pink points and red line) measurements. Here, the measurements are all plotted in MHz, so the difference in measurement repetition rate between the channels has already been accounted for.

9.1.2 First simplification: Symmetry, $T_{02} = 0$

The signal equation 9.2 is simplified a great deal if measurements indicate that T_{02} is zero. This will be the case if there is symmetry in the curve of the signal with angle (i.e. the values at $\theta = \frac{\pi}{4}$ equal those at $\theta = \frac{3\pi}{4}$ for the Rayleigh Elastic channel).

Examining the measurements (which was done mathematically but is not plotted here), it is evident that this simplification is justified; the measurements at $\theta = \frac{\pi}{4}$ equal those at $\theta = \frac{3\pi}{4}$.

Interestingly, T_{02} does not appear in any equations for the depolarization parameter d . It is only because of the calibration setup shown in this chapter that one would need to worry about it at all for the CRL in terms of depolarization measurements.

9.1.3 Second simplification: Constant signal with angle, $T_{01} = 0$

All angle-dependence information in the Rayleigh Elastic channel's signal equation is contained within the term including calibration constant T_{01} . If it is the case that the measurements do not vary with polarizer angle, it may be inferred that $T_{01} = 0$.

An examination of Figure 9.1 demonstrates that this is the case. With such high signal levels in the Rayleigh Elastic channel, there is no need to go to the trouble of histogramming the individual measurements to find the most likely value for each angle; the mean will suffice. The mean at each angle is not statistically significantly different from the mean at any other angle. They are equal to within their uncertainties. Therefore, the CRL (for optics downstream of the focus stage, at least) has the calibration coefficient $T_{01} = 0$.

The resulting signal equation for this channel is:

$$S_{R\theta} = G_{cube} G_{PMT R} G_{gl} \frac{I_{lamp}}{2} (T_{00}). \quad (9.3)$$

All polarization dependence in this channel's equation is gone. As the individual gains of the PMT, the cube polarizer, the glassine, and the intensity of the lamp remain unknown throughout the test, it is not possible to determine T_{00} by rearranging this equation and solving for it. The following section deals with (successful) efforts to determine the final calibration constant required for Option 2: $\frac{G_{PMT R}}{G_{PMT \parallel L}} \frac{T_{00}}{M_{00}}$.

Results indicating that both T_{01} and T_{02} are zero are encouraging for the CRL. Considering that this channel is intended to be polarization-independent, these results are what one would expect. If its measurements indicated a polarization preference, then the CRL's Rayleigh Backscatter Coefficient data products, and all others using this channel, would need to be re-evaluated. Fortunately, the channel performs as intended.

9.1.4 Final equation for Option 2 depolarization parameter d_2

Substitutions of known calibration constants gives the following equation, in which $\frac{M_{10}}{M_{00}}$ has been left for clarity, results in the following equation to be used for depolarization

parameter when using Option 2 with the parallel and Rayleigh Elastic channels.

$$d = 1 + \frac{\frac{1}{2} \frac{S_R}{S_{\parallel}} \left(1 + \frac{M_{10}}{M_{00}}\right) - \left(\frac{G_{PMT R} O_R(z)}{G_{PMT \parallel} O_{\parallel \perp}(z)} \frac{T_{00}}{M_{00}}\right)}{\frac{1}{2} \frac{S_R}{S_{\parallel}} \left(\frac{M_{01}}{M_{00}} + \frac{M_{11}}{M_{00}}\right) - \left(\frac{G_{PMT R} O_R(z)}{G_{PMT \parallel} O_R(z)} \frac{T_{01}}{M_{00}}\right)} \quad (9.4)$$

$$d = 1 + \frac{\frac{1}{2} \frac{S_R}{S_{\parallel}} \left(1 + \frac{M_{10}}{M_{00}}\right) - \left(\frac{G_{PMT R} O_R(z)}{G_{PMT \parallel} O_{\parallel \perp}(z)} \frac{T_{00}}{M_{00}}\right)}{\frac{1}{2} \frac{S_R}{S_{\parallel}} \left(\frac{M_{10}}{M_{00}} + 1\right) - \left(\frac{G_{PMT R} O_R(z)}{G_{PMT \parallel} O_R(z)} \frac{0}{M_{00}}\right)} \quad (9.5)$$

$$d = 1 + \frac{\frac{1}{2} \frac{S_R}{S_{\parallel}} \left(1 + \frac{M_{10}}{M_{00}}\right) - \left(\frac{G_{PMT R} O_R(z)}{G_{PMT \parallel} O_{\parallel \perp}(z)} \frac{T_{00}}{M_{00}}\right)}{\frac{1}{2} \frac{S_R}{S_{\parallel}} \left(1 + \frac{M_{10}}{M_{00}}\right)} \quad (9.6)$$

$$d = 1 + 1 - \frac{\left(\frac{G_{PMT R} O_R(z)}{G_{PMT \parallel} O_{\parallel \perp}(z)} \frac{T_{00}}{M_{00}}\right)}{\frac{1}{2} \frac{S_R}{S_{\parallel}} \left(1 + \frac{M_{10}}{M_{00}}\right)} \quad (9.7)$$

$$d = 2 - \left(\frac{2}{1 + \frac{M_{10}}{M_{00}}}\right) \left(\frac{G_{PMT R} O_R(z)}{G_{PMT \parallel} O_{\parallel \perp}(z)} \frac{T_{00}}{M_{00}}\right) \left(\frac{S_{\parallel}}{S_R}\right) \quad (9.8)$$

$$d_2 = 2 - \left(\frac{2}{1 + \frac{M_{10}}{M_{00}}}\right) \left(\frac{G_{PMT R} O_R(z)}{G_{PMT \parallel} O_{\parallel \perp}(z)} \frac{T_{00}}{M_{00}}\right) \left(\frac{S_{\parallel}}{S_R}\right) \quad (9.9)$$

For the remainder of this chapter, there will be two distinct values of d used together; labelling this one d_2 on occasion (because it is for the Option 2 method) will help keep things clear. The depolarization parameter value from Option 1 will be called d_1 .

9.1.5 Calibration method for determining $\frac{G_{PMT R} O_R(z)}{G_{PMT \parallel \perp} O_{\parallel \perp}(z)} \frac{T_{00}}{M_{00}}$

The final constant $\frac{G_{PMT R} O_R(z)}{G_{PMT \parallel \perp} O_{\parallel \perp}(z)} \frac{T_{00}}{M_{00}}$ remains to be determined through nightly calibration.

Unlike all other calibration terms in the equation for depolarization parameter using the Option 2 setup, the final one may vary with altitude. It contains the overlap functions $O_{\parallel \perp}(z)$ and $O_R(z)$ in a ratio indicating the differential overlap between the Rayleigh Elastic and the Depolarization photomultiplier tube viewing geometries.

Calibrations to determine this calibration “constant” may be carried out during any reasonable night of measurements which contain data from all three channels: Parallel, Perpendicular, and Rayleigh Elastic. In effect, the depolarization parameter determined with Option 1 is used to calibrate the depolarization parameter determined with Option 2.

Equation 9.9 may be solved for the quantity that is desired in the calibration:

$$d = 2 - \left(\frac{2}{1 + \frac{M_{10}}{M_{00}}} \right) \left(\frac{G_{PMT R} O_R(z)}{G_{PMT \parallel} O_{\parallel \perp}(z)} \frac{T_{00}}{M_{00}} \right) \left(\frac{S_{\parallel}}{S_R} \right) \quad (9.10)$$

$$\frac{G_{PMT R} O_R(z)}{G_{PMT \parallel} O_{\parallel \perp}(z)} \frac{T_{00}}{M_{00}} = 0.5 \left(1 + \frac{M_{10}}{M_{00}} \right) \left(\frac{S_R}{S_{\parallel}} \right) (2 - d) \quad (9.11)$$

Since the depolarization parameter d remains physically the same quantity whether it is measured via Option 1 or Option 2, it is possible to solve initially for the depolarization parameter using Option 1, feed it into the calibration equation 9.11, and solve for the calibration term.

9.1.6 Units of $\frac{G_{PMT R} O_R(z)}{G_{PMT \parallel} O_{\parallel \perp}(z)} \frac{T_{00}}{M_{00}}$

It is correct to calculate the calibration constant $\frac{G_{PMT R} O_R(z)}{G_{PMT \parallel} O_{\parallel \perp}(z)} \frac{T_{00}}{M_{00}}$ using the measurements of S_R and S_{\parallel} in either counts per time bin per altitude bin OR in units of MHz, but it should be noted that the constant will be different in either case, and therefore must be applied to measurements in the same units when used for finding depolarization parameter d , later. For CRL, this difference is a factor of two because S_R converts to MHz via division by 30, while S_{\parallel} converts to MHz via division by 15 due to it measuring half as many laser shots per second than the Rayleigh Elastic channel does:

$$\left(\frac{S_R}{S_{\parallel}} \right)_{MHz} = \frac{1}{2} \left(\frac{S_R}{S_{\parallel}} \right)_{countsunits} . \quad (9.12)$$

Therefore,

$$\left(\frac{G_{PMT R} O_R(z)}{G_{PMT \parallel} O_{\parallel \perp}(z)} \frac{T_{00}}{M_{00}} \right)_{MHz} = \frac{1}{2} \left(\frac{G_{PMT R} O_R(z)}{G_{PMT \parallel} O_{\parallel \perp}(z)} \frac{T_{00}}{M_{00}} \right)_{countsunits} . \quad (9.13)$$

All plots which follow are made using counts per altitude bin per time bin.

9.2 Sample Calibration Test from 10 March 2013 to

determine $\frac{G_{PMTRO_R(z)} T_{00}}{G_{PMT\parallel\perp} O_{\parallel\perp}(z) M_{00}}$

All three channels' measurements are required for this calibration:

1. Parallel and Perpendicular to determine the Option 1 version of depolarization parameter d_1 . Many data points will be missing, because perpendicular count rates are low. Coadding is required, so resolution is also low.
2. Then this low resolution d_1 is used with Parallel and Rayleigh Elastic counts which have been coadded to the same resolution to determine the calibration constant once for the night: $\frac{G_{PMTRO_R(z)} T_{00}}{G_{PMT\parallel\perp} O_{\parallel\perp}(z) M_{00}}$.
3. Finally, the single $\frac{G_{PMTRO_R(z)} T_{00}}{G_{PMT\parallel\perp} O_{\parallel\perp}(z) M_{00}}$ for the night is used to calculate d_2 .

Of course it is possible to substitute calibration constant k and the ratio of Parallel to Perpendicular counts into the above equation in the place of d , but it is clearer to solve for d_1 , then calibrate, solve for d_2 and examine the differences in the resulting depolarization parameter plots.

A night of regular-operations measurements (i.e. not a special calibration run) on 10 March 2013 is used for demonstration purposes.

9.2.1 Signals and uncertainties in each channel

This is a typical night, with clear air below several clouds aloft. The clouds are not particularly thick; signal is visible above each of them in the Parallel and Rayleigh Elastic channels. The entire night's measurements and associated uncertainties are given in Figure 9.2.

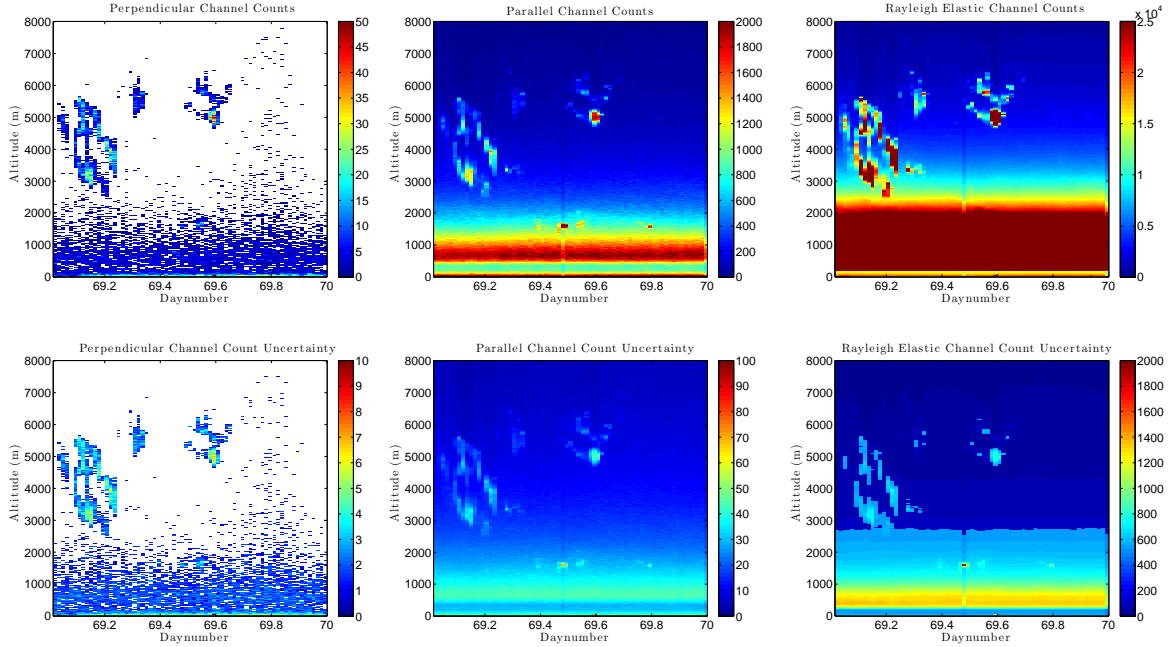


Figure 9.2: These are photocounts from 10 March 2013. The uncertainties are all in units of photon counts. Any locations with signal to noise ratios smaller than 1 have been removed and are coloured white.

The plots here have had low-level data processing performed on them. That is to say, they have been photon counting dead-time corrected, analogue range scaled and dark count correcte, and have been coadded and background subtracted. Coadding resolution was chosen to be 20 time bins (20 minutes) and 1 altitude bin (7.5 metres). Alternate resolutions are given later in the chapter.

9.2.2 Depolarization parameter d as determined by Option 1 procedures

Depolarization parameter d_1 is solved for using the Parallel and Perpendicular channels following the method in Chapter 6.4, resulting in the plots of Figure 9.3.

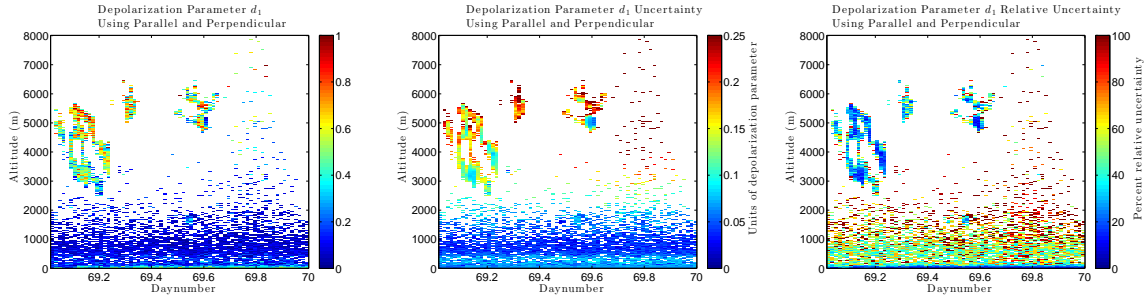


Figure 9.3: Left: The d_1 depolarization values from 10 March 2013. Centre: The uncertainties associated with the d_1 values are all in units of depolarization parameter. Right: The relative uncertainties are in units of percent. Physical interpretation of the measurements: The high depolarization parameter values in the cloud at daynumber 69.2, at 5500 m altitude, indicate that the cloud is composed of particles which are not homogeneous spheres; in context, this means that the cloud is likely composed of ice particles. The uncertainty in this region of the cloud is approximately 12%. For the small cloud at daynumber 69.3, there is less certainty. There, the d_1 values indicate a mix of high and low depolarization varying between 0.4 and 0.8 in a rather noisy fashion. The uncertainty in this small cloud is ± 0.25 or higher, indicating more than 30% relative uncertainty. The edges of all clouds have high uncertainty as well. While a general interpretation of icy clouds in a clear atmosphere is possible, depolarization parameter measurements with higher resolution and/or smaller uncertainty would be better. If there are any clouds at all above 6000 m altitude, d_1 is not sensitive to them because of the low count rates in the perpendicular channel.

Note that the extremely low signal rates in the perpendicular channel lead to many time-altitude points having insufficient signal-to-noise ratios to be considered. Any such points cannot therefore be present in the depolarization parameter plots, either.

9.2.3 Calculations of $\frac{G_{PMT} O_R(z)}{G_{PMT \parallel \perp} O_{\parallel \perp}(z)} \frac{T_{00}}{M_{00}}$ for each data point

Next, the Rayleigh Elastic channel is brought into the evaluation as a ratio with the Parallel channel. Using Equation 9.11 a value of $\frac{G_{PMT} O_R(z)}{G_{PMT \parallel \perp} O_{\parallel \perp}(z)} \frac{T_{00}}{M_{00}}$ is determined for each data point in time and altitude. The results and their uncertainties are given in Figure 9.4. The uncertainties are calculated assuming no correlated errors, using standard error propagation methods.

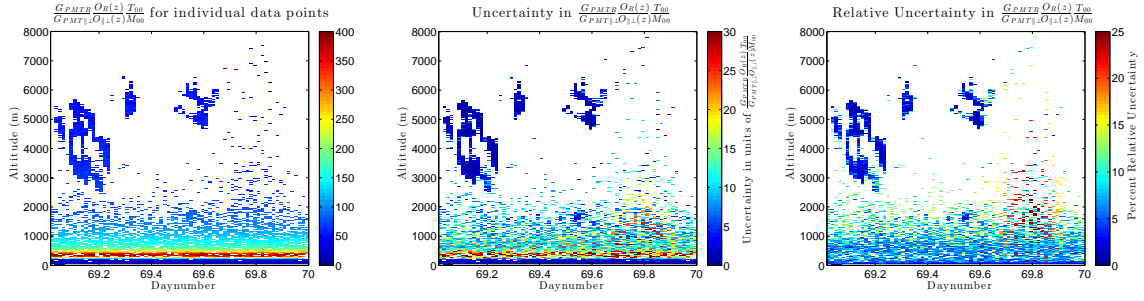


Figure 9.4: Left: The $\frac{G_{PMT_R} O_R(z)}{G_{PMT_{\parallel}} O_{\parallel}(z)} \frac{T_{00}}{M_{00}}$ calibration values from 10 March 2013 individually for each data point. Right: Uncertainties in the calculated individual values of $\frac{G_{PMT_R} O_R(z)}{G_{PMT_{\parallel}} O_{\parallel}(z)} \frac{T_{00}}{M_{00}}$.

Calculating the uncertainties in $\frac{G_{PMT_R} O_R(z)}{G_{PMT_{\parallel}} O_{\parallel}(z)} \frac{T_{00}}{M_{00}}$ is fairly instructive; it indicates the regions in which the quantity may be better or less well trusted, but only insofar as one believes the number of photons hitting the lidar's telescope to be indicative of the state of the atmosphere in the first place. More on what this means appears later in the chapter.

If there was good signal in the perpendicular channel, and thus good calibration quantity measurements for each altitude, it would be possible to calibrate the lidar measurements scan-by-scan. However, there are frequently too few perpendicular measurement to make good statistics in this manner. It is more desirable to determine one single profile for the night (perhaps even persisting longer) to use as a function of $\frac{G_{PMT_R} O_R(z)}{G_{PMT_{\parallel}} O_{\parallel}(z)} \frac{T_{00}}{M_{00}}$ with altitude. We do not expect the quantity to change much in time. Certainly, the $\frac{G_{PMT_R}}{G_{PMT_{\parallel}}}$ and $\frac{T_{00}}{M_{00}}$ portions should be relatively stable in time. It is the differential overlap function which may be changing with such factors as: Temperature of the lab, laser alignment, etc.

9.2.4 Combining individual measurements into a single $\frac{G_{PMT_R} O_R(z)}{G_{PMT_{\parallel}} O_{\parallel}(z)} \frac{T_{00}}{M_{00}}$ for the night

First, a mean profile is taken based on the calculated individual values. The propagated uncertainty reduces drastically as a high number of profiles are combined (just as for any coadding procedure).

A smooth profile was desired so that the profile would not be unduly influenced by small odd clouds, etc. A 10-point moving-average filter was applied to the mean profile to smooth it in altitude.

Deciding on the optimal method to choose the curve of $\frac{G_{PMT\parallel} O_{\parallel}(z)}{G_{PMT\perp} O_{\perp}(z)} \frac{T_{00}}{M_{00}}$ with altitude was a process which involved testing several options:

- Use the smoothed mean profile directly
- Use smoothed mean profile, excluding outlying points (e.g. from signal spikes)
- Use smoothed mean profile up to a certain altitude, and a constant above that (Might make sense if both overlap functions are only affected at low altitudes)
- Use smoothed mean profile up to a certain altitude, and fit a function to use above that altitude which more faithfully represents the trend of the data leading up to that altitude
- Use a fit function for the whole profile

The last option was the most fruitful, and is shown here. A second-order power law of the form $y = ax^b + c$ was found to fit the calibration data (y , the smoothed mean profile) with altitude (x) with goodness-of-fit R-squared of greater than 0.998 in every case studied. Numerous dates, resolutions, etc, were examined. The “fit” function in MATLAB was used to carry out this fit, providing regression coefficients and information regarding goodness of fit. For the example data shown in this section, the coefficients were found to be:

p2 =

General model Power2:

p2(x) = a*x^b+c

Coefficients (with 95% confidence bounds):

a = 1.152e+05 (1.082e+05, 1.223e+05)

b = -1.026 (-1.036, -1.017)

```
c =          31.81  (31.29, 32.34)
>> p2gof
```

```
p2gof =
      sse: 1696.31662259903
    rsquare: 0.998110969218528
      dfe: 731
  adjrsquare: 0.998105800871656
      rmse: 1.52333271985304
```

in which the coefficients to the power law are given by a , b , and c , and for which the goodness of fit was indicated with, in particular, the R^2 value being quite high at 0.998 (of a possible 1.00, indicating a very good fit) and the root mean square error, RMSE, being reasonably low at 1.523 (compared to the values of $\frac{G_{PMT} O_R(z)}{G_{PMT} \parallel O_{\parallel}(z)} \frac{T_{00}}{M_{00}} = 400$ at its largest point, and around 40 to 50 at its smallest).

In the event that measurements in one of the contributing channels do not extend to the full altitude available in the other channels, a fit is still possible, and with the coefficients determined, the calibration constant is able to be determined up to great heights. This is particularly helpful at altitudes for which the perpendicular channel's relative uncertainty is huge, but for which the Rayleigh and parallel channels are still completely fine.

In the following plot of the calibration function with altitude (Figure 9.5), several profiles are plotted: 1. The mean profile, 2. The upper and lower bounds on the mean profile based on the mean profile's uncertainty, 3. The power-law fit function, 4. The upper and lower bounds on the power law fit function based on the root mean square error in the fit itself. Note that the root mean square error in the fit dominates the small error in the mean profile. It was determined that the measurement error in the mean profile could be neglected in the fitting process for this reason. This quantity is quite stable in time.

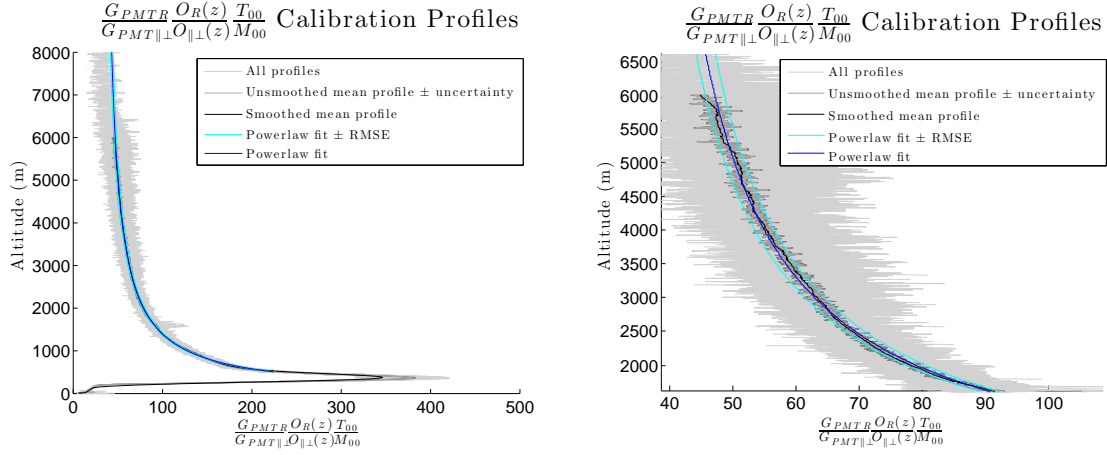


Figure 9.5: Left: The $\frac{G_{PMT\parallel} O_R(z)}{G_{PMT\parallel} O_{\parallel}(z)} \frac{T_{00}}{M_{00}}$ calibration values from 10 March 2013 with the fits to the night's measurements. Right: Zoomed-in portion of the plot on the left to show differences between the lines.

9.2.5 Variation in the profile with changing coadding resolution and with different dates

To check whether the profile of $\frac{G_{PMT\parallel} O_R(z)}{G_{PMT\parallel} O_{\parallel}(z)} \frac{T_{00}}{M_{00}}$ with altitude is drastically different depending on the coadding of the original data (and we hope it is not), the calibration procedure was carried out for the following resolutions of 10 March 2013 data: 1. t10, z1, 2. t20, 71, 3. t10, z5.

To check whether the profile changes very much by date, several more days' data were examined, all at t20, z1 resolution.

Table 9.1: Fitting coefficients and goodness of fit for various days and resolution in March 2013 in the determination of $\frac{G_{PMTRO_R(z)}}{G_{PMT\parallel\perp}O_{\parallel\perp}(z)} \frac{T_{00}}{M_{00}}$. Days marked with “*” used only a portion of the data available for that day: clear sky or thin clouds only.

Test	Day	t	z	a (bounds)	b (bounds)	c (bounds)	R ²	RMSE
i	10	20	1	115200 (108200,122300)	-1.026 (-1.036,-1.017)	31.81 (31.29,32.34)	0.99811	1.52333
ii	10	10	5	48260 (29866,67870)	-0.8896 (-0.9555,-0.8238)	27.36 (22.72,32)	0.98229	4.74997
iii	10*	10	1	92540 (86810,98280)	-0.9876 (-0.9975,-0.9777)	26.04 (25.54,26.62)	0.99803	1.59366
iv	11*	20	1	164900 (154200,175500)	-1.085 (-1.095,-1.075)	35.04 (34.55,35.53)	0.99804	1.54167
v	11	2	2	310200 (230500,390000)	-1.172 (-1.213,-1.131)	26.44 (24.62,28.26)	0.98491	4.75284
vi	14*	20	1	567700 (514400,621000)	-1.304 (-1.318,-1.289)	35.71 (35.29,36.12)	0.99614	1.8601
vii	14*	20	1	407900 (383400,432400)	-1.217 (-1.227,-1.208)	38.6 (38.21,38.98)	0.99838	1.50403

Power law fits to $\frac{G_{PMTRO_R(z)}}{G_{PMT\parallel\perp}O_{\parallel\perp}(z)} \frac{T_{00}}{M_{00}}$ for various days

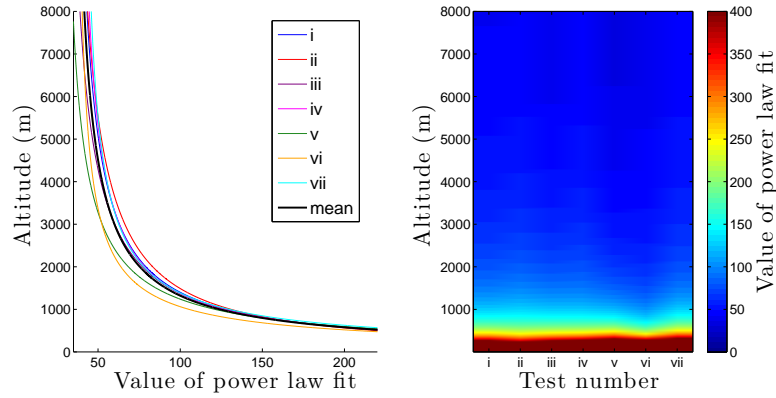


Figure 9.6: Plots of 2nd order power law fits to the calculated profiles of $\frac{G_{PMTRO_R(z)}}{G_{PMT\parallel\perp}O_{\parallel\perp}(z)} \frac{T_{00}}{M_{00}}$ for the test dates and resolutions listed in Table 9.1

The general form of these fits is unchanging for these days in March 2013. This suggests that it is appropriate to use the calibration profile from one day to make d_2 measurements from a nearby day. This could be useful if the perpendicular channel is unavailable for one day for some reason.

9.3 Sample determinations of d using Option 2

The calibration coefficients determined in this chapter were used to calculate depolarization parameters using the Option 2 method and Equation 9.10. The sample from 10 March 2013 is given here; More detailed examination of a selection of dates is examined in Chapter 10.

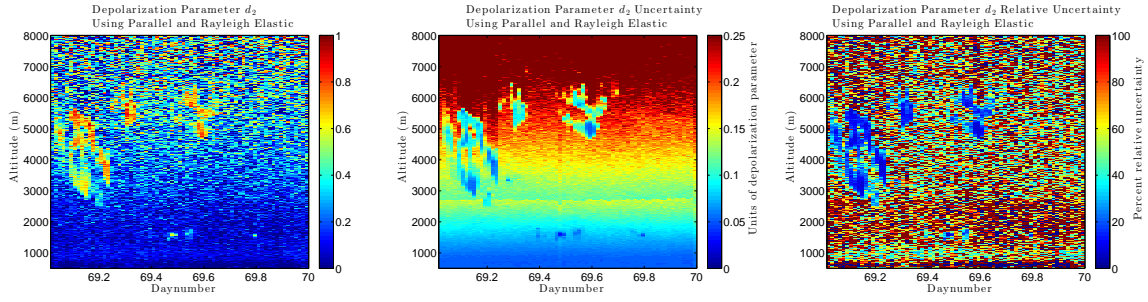


Figure 9.7: Left: The d_2 depolarization values from 10 March 2013. Centre: The uncertainties associated with the d_2 values are all in units of depolarization parameter. Right: The relative uncertainties are in units of percent. Note the better coverage of time and space using this method as compared to using Option 1 for d_1 .

The values retrieved using Option 2 give reasonable results with depolarization parameter values between 0 and 1 as they should be. Regions of high depolarization ratio are visible within the clouds, as they are for the Option 1 results in previous plots. These regions also have low absolute uncertainty, as do the very low altitudes where the density of the atmosphere is large.

A more detailed comparison of the results are given in the following section.

9.4 Comparing the d_1 and d_2 results to verify validity of Option 2

To ensure that the results for d calculated using Option 2 (d_2) are valid, they must be compared with those calculated using Option 1 (d_1) and have the same values to within the uncertainty of the measurements.

The difference between the values is provided in Figure 9.8 for only the data points which are valid for both calculations. Recall that there are many more valid data points for the d_2 , but these have been eliminated in this comparison.

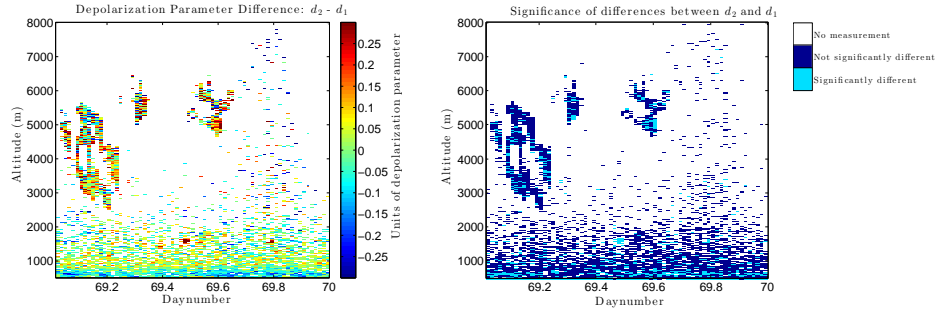


Figure 9.8: Compare depolarization results from both methods. Left: d_2 (from Option 2) - d_1 (from Option 1). Right: Determining whether the differences are significant, taking uncertainties into account. Compare differences in d values to the total combined uncertainty for both methods.

The left panel demonstrates that most values at low altitudes have differences of approximately zero. This is desirable. In the clouds, a variety of differences are visible: Many points are zero, but many points differ by ± 0.25 in the units of depolarization parameter.

The panel on the right takes the uncertainties of the measurements into account, calculating X , the significance. Significant differences in d values are considered true if $X > 0$, and false otherwise.

$$X = \text{abs}(d_2 - d_1) - (\sigma_{d2} + \sigma_{d1}). \quad (9.14)$$

In most altitude and time bins, there is no difference between the depolarization parameters calculated to within the limits of their combined uncertainties. This is encouraging, as it shows that the CRL's Parallel and Rayleigh Elastic method (Option 2) is as valid as its Parallel and Perpendicular method (Option 1).

9.5 Demonstration of calibration and calculation of d_2 for other dates

To demonstrate that the analysis demonstrated in this chapter is valid for dates other than 10 March 2013, and for resolutions other than 20 time bins, 1 altitude bin, the remainder of this chapter presents a selection of the analysis applied to several sorts of measurements. These examples are helpful for illustrating the importance of choosing an appropriate region in time and altitude for the calculation of $\frac{G_{PMTR} O_R(z)}{G_{PMTR} \parallel O_{\parallel}(z)} \frac{T_{00}}{M_{00}}$ for each day.

1. One day has a thick cloud for much of the night (14 March 2013)
2. One day has high clouds as on 10 March early in the day, with a very thick cloud descending to the surface during later hours. (11 March 2013)

9.5.1 Calculation of d_2 for 14 March 2013

This sample date of 14 March 2013 was selected to illustrate the effect of the calibration region chosen on the final d_2 depolarization output for the night.

On this day, there are clouds above 6000 m to begin with, and they descend (or, more likely, clouds at lower altitude move over the lidar) gradually over the day. By 8 hours later, the clouds have become thick enough to extinguish light backscattered above the cloud, and perhaps even from the upper regions of the cloud. The cloud descends to the ground by 1200 UTC and remains there for many hours.

A coadding resolution of 20 time bins (20 minutes) and 1 altitude bin (7.6 metres) was selected for this comparison. This provides sufficient photons in the perpendicular channel to make the calculations.

The depolarization parameters calculated using Option 1 are presented first, with uncertainty and relative uncertainty in Figure 9.9.

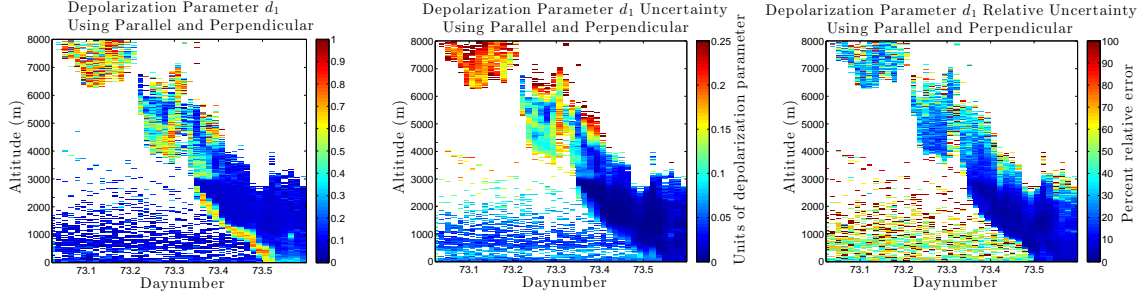


Figure 9.9: Left: The d_1 depolarization values from 14 March 2013. Centre: The uncertainties associated with the d_1 values are all in units of depolarization parameter. Right: The relative uncertainties are in units of percent.

Individual $\frac{G_{PMT R} O_R(z)}{G_{PMT \parallel \perp} O_{\parallel \perp}(z)} \frac{T_{00}}{M_{00}}$ calculations for each time-altitude measurement point for the entire time and altitude range possible to be studied for this day. These are plotted in Figure 9.10. The analysis of determining a single calibration profile for this day, and using it to calculate d_2 , was performed twice: Once including all the data (Figure 9.11; Box A in figure 9.10), and again taking only regions without thick clouds into account (Figure 9.12; Box A in figure 9.10).

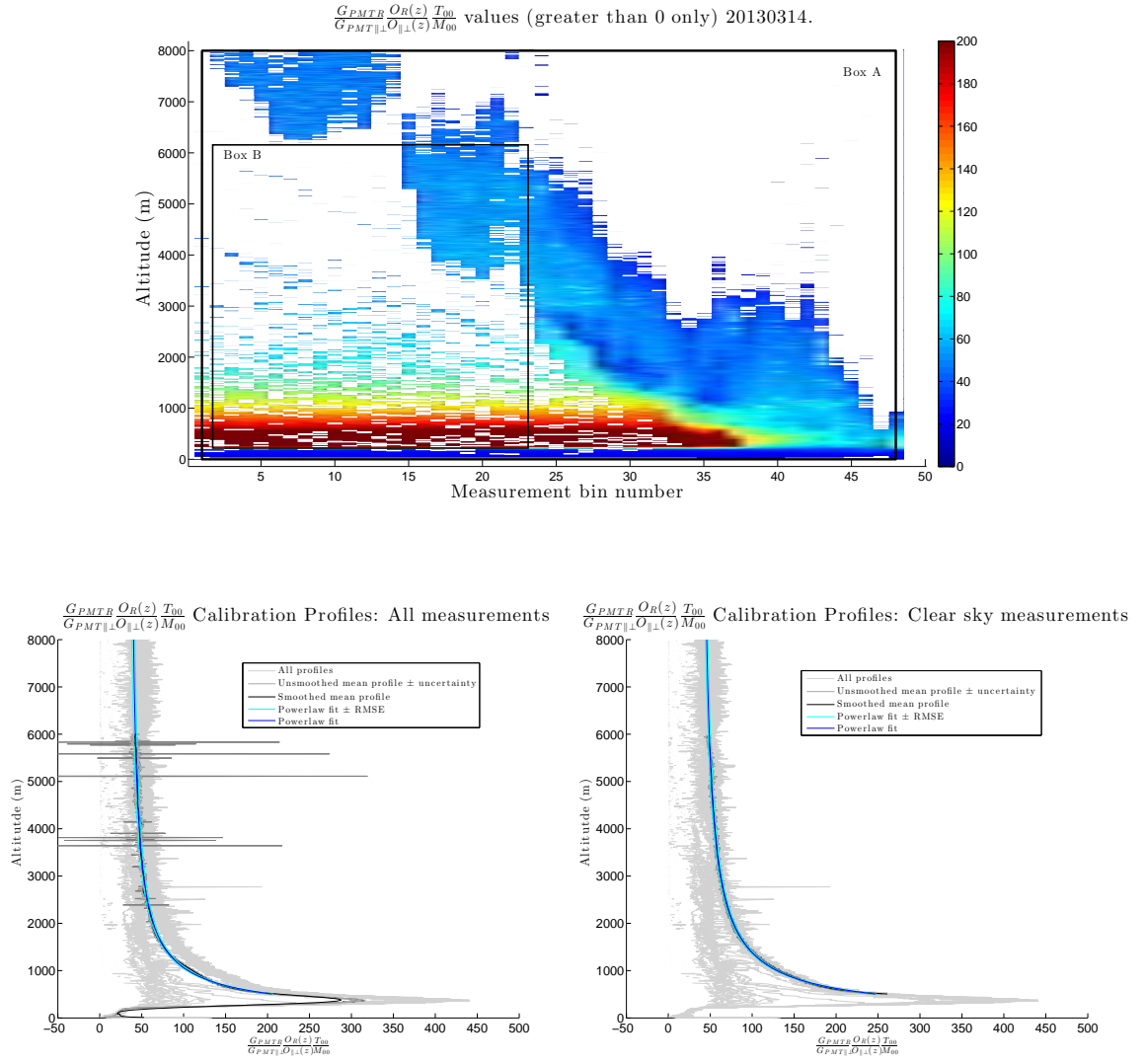


Figure 9.10: Top: Context plot of all individual $\frac{G_{PMTB} O_R(z)}{G_{PMT\perp} O_{\perp}(z)} \frac{T_{00}}{M_{00}}$ values for 14 March 2013. Box A indicates the region included in the nightly profile which includes all measurements (Bottom left). Box B indicates the region included in the nightly profile which excludes any regions with thick clouds (Bottom right).

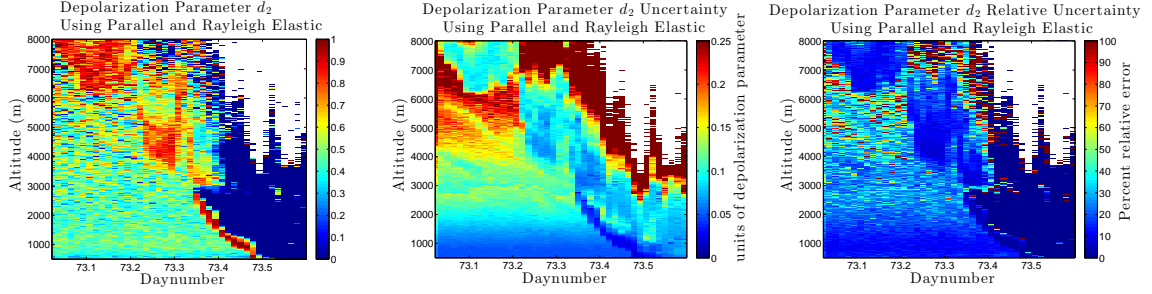


Figure 9.11: Left: The d_2 depolarization values from 14 March 2013, using all data available for that day to influence the calibration profile. Centre: The uncertainties associated with the d_2 values are all in units of depolarization parameter. Right: The relative uncertainties are in units of percent.

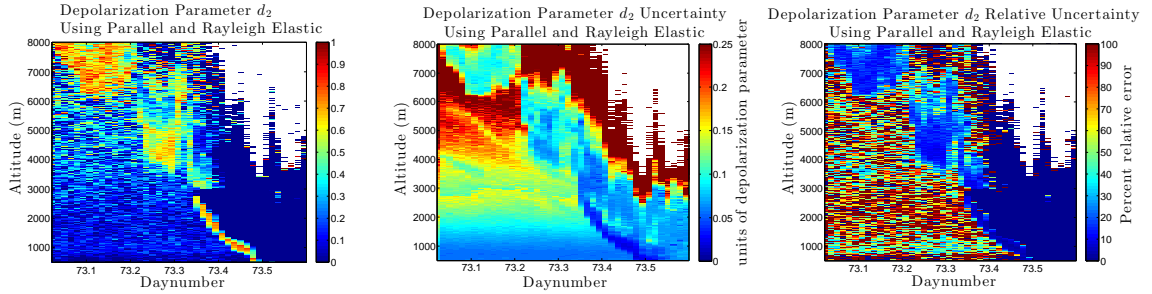


Figure 9.12: Left: The d_2 depolarization values from 14 March 2013, using only clear sky and regular cloud data (thick clouds excluded) to influence the calibration profile. Centre: The uncertainties associated with the d_2 values are all in units of depolarization parameter. Right: The relative uncertainties are in units of percent.

The results for both calculations of d_2 are compared with the d_1 values given in Figure 9.9. Recall that d_1 is calculated using the parallel and perpendicular channels with the traditional method, and is considered to be “correct”, as it is the method currently in use in the lidar community. Whichever new calculation of d_2 has the smallest difference of $d_2 - d_1$ is considered to be the “most correct” version of d_2 .

The differences are plotted for each case: Figure 9.13 when using the whole-region calibration (Box A in Figure 9.10), and Figure 9.14 when using the clear sky calibration (Box B in Figure 9.10).

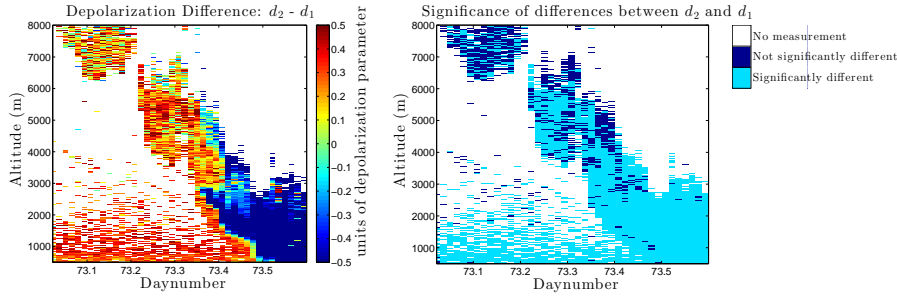


Figure 9.13: Comparisons of the results for $d_2 - d_1$ 14 March 2014 calculated using the default setting of the entire time-altitude range for calibration.

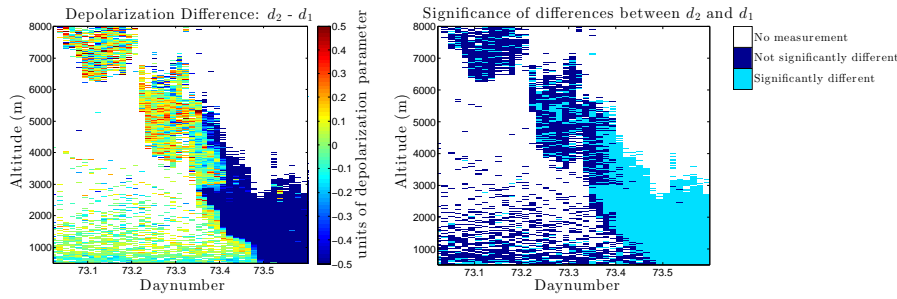


Figure 9.14: Comparisons of the results for $d_2 - d_1$ 14 March 2014 calculated using only clear sky and regular cloud data (thick clouds excluded) to influence the calibration profile.

The plots in Figure 9.13 illustrate the perils of blindly choosing a calibration region of sky. The “default” region, Box B in Figure 9.10 which encompasses the entire data region, does a terrible job of producing d_2 values which mimic those given by d_1 . Most data points for the first half of the time examined are different by depolarization parameter values of more than 0.5 in one direction, and all depolarization ratios within the very thick cloud are different by the same amount in the other direction. That is huge, as d varies only between 0 and 1. The significance plot below is almost entirely light blue, indicating the that the results do not match to within their uncertainties almost anywhere in the plot. The only location with even a tenuous grasp on matching is the cloud at the upper left - a location

which has 30 percent relative error in d_1 to start with. If this had been the test result in the previous section, it would have been concluded that the calibration method did not work. Further examination reveals that the current example just has a bad choice of calibration region.

Consider next the plots on the right of Figure 9.14, in which a more careful calibration region was selected. The entire region with the thick cloud has been excluded from the calculation of the calibration profile. Then this conservative profile has been applied to the entire data space to produce the d_2 plot. An examination of the difference between the d values shows that in almost all cases for the beginning of the measurement, the values are the same to within ± 0.1 (10 percent). The only location which does not match well (though differences are no larger than those in the left plot) is within the thick cloud where the original d_1 measurements are questionable to start with.

The significance plot at lower right reinforces this interpretation. Most of the measurement is good; within the upper regions of the thick cloud, it is not. This should not be a surprise. With only one lidar measurement, the scattering cross section and the extinction cannot be told apart [103], because two things look identical to a lidar: scattering from something small, or scattering from something big after having lost lots of signal already below it.

The conclusion drawn from this sample measurement day is that the calibration constant profile of $\frac{G_{PMTR}O_R(z)}{G_{PMT\parallel\perp}O_{\parallel\perp}(z)} \frac{T_{00}}{M_{00}}$ must be chosen with care. There are several options to deal with this:

- The d_1 values could be curated more carefully before beginning the $\frac{G_{PMTR}O_R(z)}{G_{PMT\parallel\perp}O_{\parallel\perp}(z)} \frac{T_{00}}{M_{00}}$ calibration routine. That is to say, depolarization ratios in clouds in which any of the assumptions about the original analysis are suspect could be excluded. This includes any regions where multiple scattering, too much extinction, etc, dominate.
- The perpendicular count regions could be curated more carefully before beginning. Even

at t20, z1 resolution, photon counts are scarce in the perpendicular channel, and the $\text{SNR} > 1$ criteria was not very strict. Perhaps a longer coadding could be used to create the calibration profile, and then it could be applied to a higher-resolution parallel and Rayleigh data set.

- The procedure can be done same as it was here: The user of the data can simply select an appropriate calibration region for each night of data.
- When both d values are calculated, one may compare both always, and exclude regions which do not match.

Lots of options, but one must not blindly get automatic calibration factors for each night. Some care must be taken to understand which data are trustworthy, which are less so, and the reasons for this.

9.5.2 Calculation of d_2 for 11 March 2013

This example day was selected and was processed in a similar way to previously presented results. Thus, the plots alone will be given here, with the process understood to be that followed before.

1. First, measurements of d_1 (Figure 9.15).
2. Next, measurements of calibration values $\frac{G_{PMTR} O_R(z)}{G_{PMT||\perp} O_{||\perp}(z)} \frac{T_{00}}{M_{00}}$ (Figure 9.16).
3. Then, calculated values of d_2 (Figure 9.17).
4. Finally, the comparison of d_1 and d_2 (Figure 9.18).

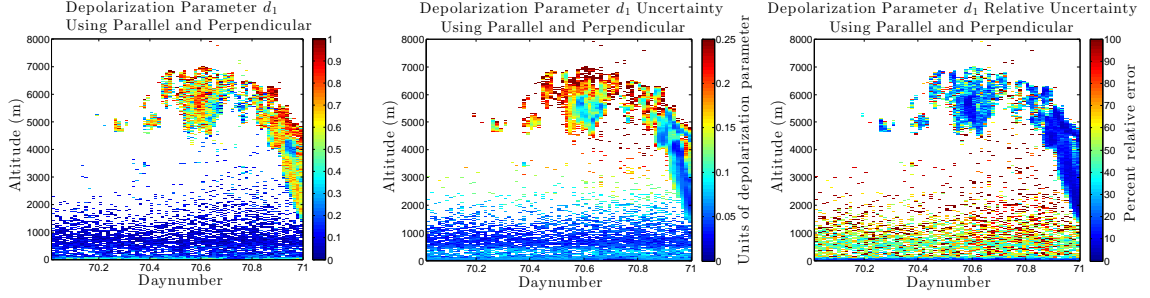


Figure 9.15: Left: The d_1 depolarization values from 11 March 2013. Centre: The uncertainties associated with the d_1 values are all in units of depolarization parameter. Right: The relative uncertainties are in units of percent.

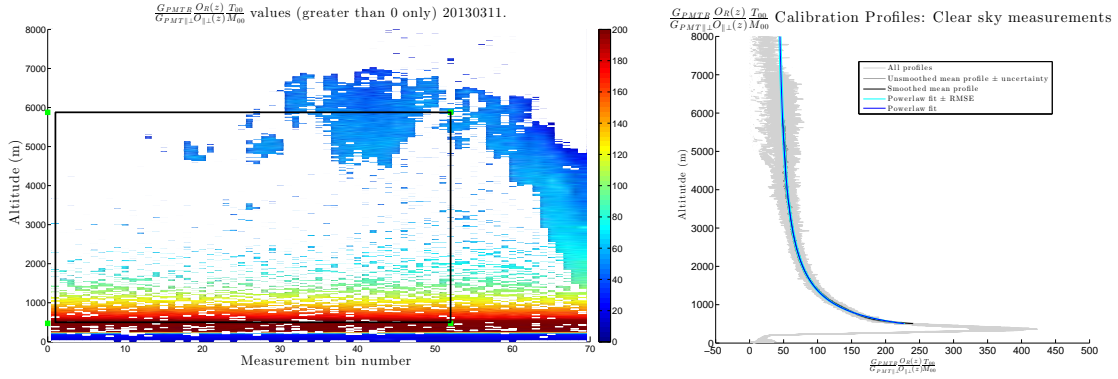


Figure 9.16: Left: Context plot of all individual $\frac{G_{PMTRO}(z) T_{00}}{G_{PMTRO\perp}(z) M_{00}}$ values for 11 March 2013. The black box indicates the region included in the nightly profile (Right); this excludes regions with thick clouds.

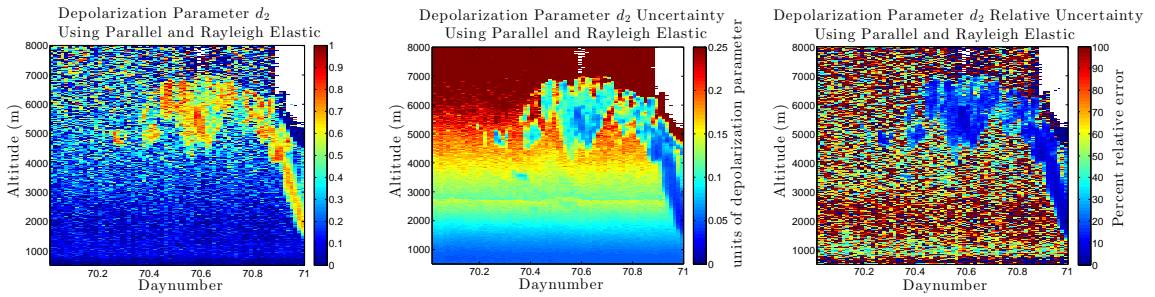


Figure 9.17: Left: The d_2 depolarization values from 11 March 2013, using only clear sky and regular cloud data (thick clouds excluded) to influence the calibration profile. Centre: The uncertainties associated with the d_2 values are all in units of depolarization parameter. Right: The relative uncertainties are in units of percent.

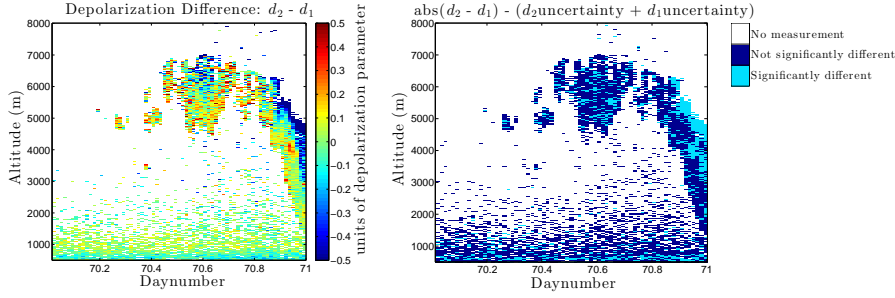


Figure 9.18: Left: Difference between d_1 and d_2 values for 11 March 2013. Right: Significance plot showing regions in which the difference between d_1 and d_2 exceeds the sum of their respective uncertainties. Differences of that magnitude and larger are deemed to be significant.

Similarly to the 14 March example, it is evident that the d_1 and d_2 values are the same to within their uncertainties, with the exception of regions of the plot which lie above thick cloud material (such as after daynumber 70.85). There is a slight (but not deemed significant) difference in the top of the cloud at 70.6; an examination of the d_1 uncertainty in this location encourages the idea that the quality of the well-calibrated d_2 results here exceeds the quality of the d_1 values in this region of the sky.

9.5.3 Conclusions regarding the validity of Option 2

Based on several nights' observations, measurements of the depolarization parameter d made using the Option 2 parallel and Rayleigh elastic method are deemed to be valid and may be used for routine data processing at times when the perpendicular channel is available for the $\frac{G_{PMTR} O_R(z)}{G_{PMT\parallel\perp} O_{\parallel\perp}(z)} \frac{T_{00}}{M_{00}}$ calibration.

Chapter 10

Determining the CRL's optimal depolarization measurement scheme

The previous chapter (Chapter 9) demonstrated the validity of Option 2, the calculation of the depolarization parameter using the parallel and Rayleigh elastic channels. The current chapter seeks to demonstrate a couple of situations in which it has been useful for CRL to use Option 2 rather than the traditional method.

In general, d_2 (from Option 2) is able to retain more useful measurements with lower uncertainties than are possible with d_1 (from the traditional method). It can give depolarization parameter information to much higher altitudes (frequently twice as high), and loses fewer data points to noise. Additionally, d_2 may be used up to much higher resolutions, thus resolving fine scale structure to which d_1 is not sensitive.

Given that depolarization parameter measurements are used in a wide variety of applications in the context of global atmospheric science, improvements to the quality of d measurements help in several ways. First, for comparison measurements with other instruments having high temporal and/or spatial resolution, an increase in lidar d resolution will be important. Comparisons with Eureka's starphotometer measurements and other lidar measurements of fine aerosol layers, or very thin clouds, will be possible if the lidar de-

polarization parameter measurements are available for such fine structures as they are with d_2 , but not with the d_1 data product. Further, many microphysical processes (e.g. evaporation, sublimation, deposition, ice crystal growth, etc.) happen in thin layers or small regions within a cloud; it is desirable that depolarization parameter measurements be sensitive at these spatial scales. Low uncertainty is vital if one is to examine small differences in the depolarization parameter within specific clouds. The increased altitude range of the d_2 measurements has different advantages. There are instruments at Eureka which measure whole-column quantities (having no altitude resolution). The d_2 measurements to higher altitudes, capturing more of the relevant clouds and aerosols in its data (including those missed by d_1 , but which are certainly captured by the whole-column instruments), will allow a more reasonable comparison with these range-integrated data products. Finally, once sufficient depolarization measurements have been made, survey-type investigations may be done to examine the relative frequency and coverage of various types of clouds; this can only be done well if the lidar can see the clouds. This is bound to be a more thorough survey when done using the d_2 product than it is using the d_1 product which misses data from many regions of the atmosphere.

The first example showing the advantages of using d_2 rather than d_1 is 10 March 2013, a date that has been used elsewhere in this thesis, and which should be somewhat familiar to the reader. One cloud near the start of the day extends between 3000 and 5000 m altitude. There are several smaller clouds between 5000 and 6000 m a few hours later. The d_2 measurements are required to identify fine scale cloud structure in high resolution plots. They are also required to make claims with any certainty about the depolarization parameter at low altitudes.

The second example showing the advantages of using d_2 rather than d_1 is 29 March 2013, a date new to this thesis. This date was selected for its different meteorology. This day has no clouds as thick as those on 10 March. Instead, there is one medium cloud between 4000 and 8000 m during the middle of the day. The rest of the time, there were

thin, wispy features visible in plots of the photocounts. The d_2 measurements begin to discern these, while the traditional d_1 has insufficiently low uncertainty at the high resolutions required to see them. Even at (t20, z1) resolution, d_1 cannot see high enough in the atmosphere to make out the single sizeable cloud, while d_2 has no difficulty in doing so.

10.1 Example day 1 showing the advantages of d_2 : 10

March 2013

The procedure for producing the plots in this section is as follows: First, the measurements from 10 March 2013 are used at a resolution of 20 time bins, 1 altitude bin, (t20, z1) to calculate the depolarization parameter in the traditional manner, creating d_1 . With 1-minute profiles and 7.5 metre altitude bins, this resolution works out to be 20 minutes, and 7.5 metres. These data, excluding anywhere with uncertainty greater than 0.2 in depolarization parameter units, are plotted in Figure 10.1.

Second, these measurements are combined with the ratio of Parallel and Rayleigh Elastic counts as in Chapter 9 to determine the calibration function $\frac{G_{PMTR}O_R(z)}{G_{PMT\parallel\perp}O_{\parallel\perp}(z)} \frac{T_{00}}{M_{00}}$ as a function of altitude for the night. The polynomial fit results for this function have already been given in Section .

The polynomial function for $\frac{G_{PMTR}O_R(z)}{G_{PMT\parallel\perp}O_{\parallel\perp}(z)} \frac{T_{00}}{M_{00}}$ from the t20, z1 resolution test are used to determine d_2 , the depolarization parameter using the parallel and Rayleigh elastic channel data. These data, excluding anywhere with uncertainty greater than 0.2 in depolarization parameter units, are plotted in Figure 10.2.

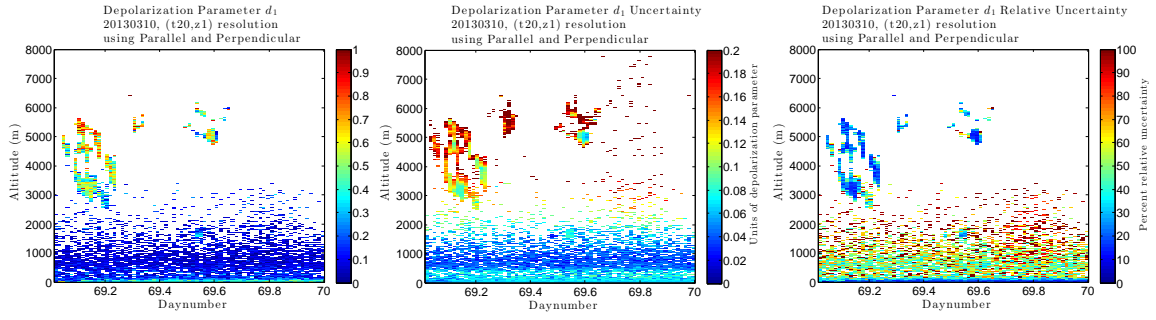


Figure 10.1: The d_1 depolarization values from 10 March 2013, with (t20,z1) resolution, excluding anywhere with more than 0.2 uncertainty in depolarization parameter units. Left: d_1 values. Centre: The uncertainties associated with the d_1 values in units of depolarization parameter. Right: The relative uncertainties are in units of percent.

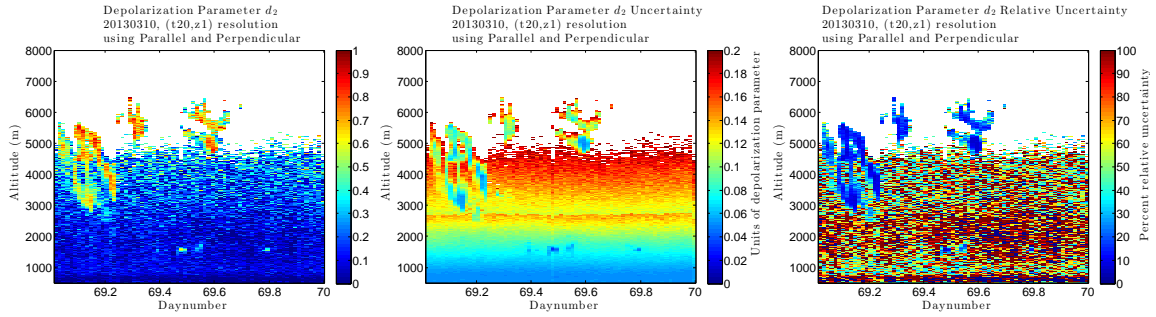


Figure 10.2: The d_2 depolarization values from 10 March 2013, with (t20,z1) resolution, excluding anywhere with more than 0.2 uncertainty in depolarization parameter units. Left: d_2 values. Centre: The uncertainties associated with the d_2 values in units of depolarization parameter. Right: The relative uncertainties are in units of percent. The calibration profile is based on (t20,z1) resolution calculations.

Already, it is possible to see that the d_2 measurements are available for more data points within the time and space region of this test than those for which the d_1 measurements are available. While data for d_1 ends at 4000 m altitude, except in the cloud, data for d_2 extends to above 5000 m. The cloud features are better delineated with d_2 data, and have lower uncertainty as well.

The one location that d_1 appears to exceed d_2 's capability is the horizontal strip along 1000 m altitude. Examining the uncertainty plots, d_1 has less than 0.04 absolute uncertainty in this location, while d_2 's is closer to 0.06, both in units of depolarization parameter. The reason for this is the use of the analogue counting channel in the parallel and Rayleigh elastic counts which go into creating d_2 . As the gluing routine switches over from photon counting to analogue detection, the larger analogue uncertainty is visible for some kilometres above. Further refinement of the gluing routines may help in this regard.

Next, d_1 and d_2 are calculated at twice the resolution, (t10, z1 ; 10 minutes, 7.5 metres), to examine any fine details which may be present. The d_2 calculations still take advantage of the calibration polynomial profile for $\frac{G_{PMT}OR(z)}{G_{PMT}\parallel O_{\perp}(z)} \frac{T_{00}}{M_{00}}$ calculated during the t20, z1 resolution test. Were it to use a profile calculated during the (t10, z1) test itself, the uncertainties on the profile would be much larger. The plots of d_1 and d_2 are given for points with less than 0.2 absolute uncertainty in Figures 10.3 and 10.4.

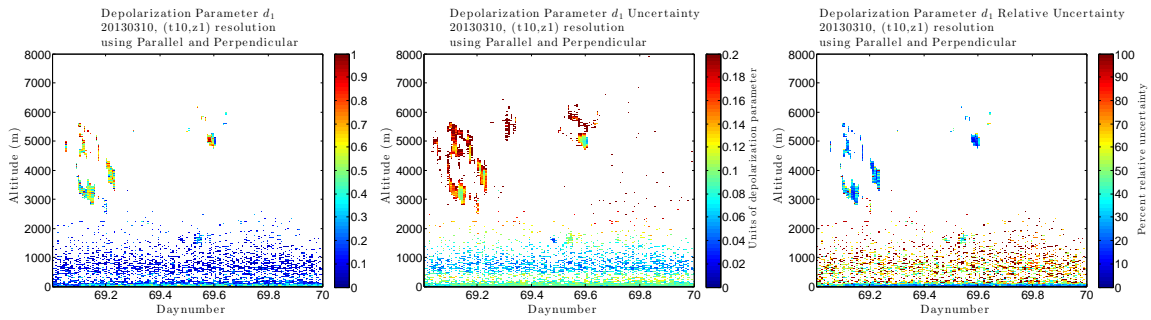


Figure 10.3: The d_1 depolarization values from 10 March 2013, with (t10,z1) resolution, excluding anywhere with more than 0.2 uncertainty in units of depolarization parameter. Left: d_1 values. Centre: The uncertainties associated with the d_1 values in units of depolarization parameter. Right: The relative uncertainties are in units of percent.

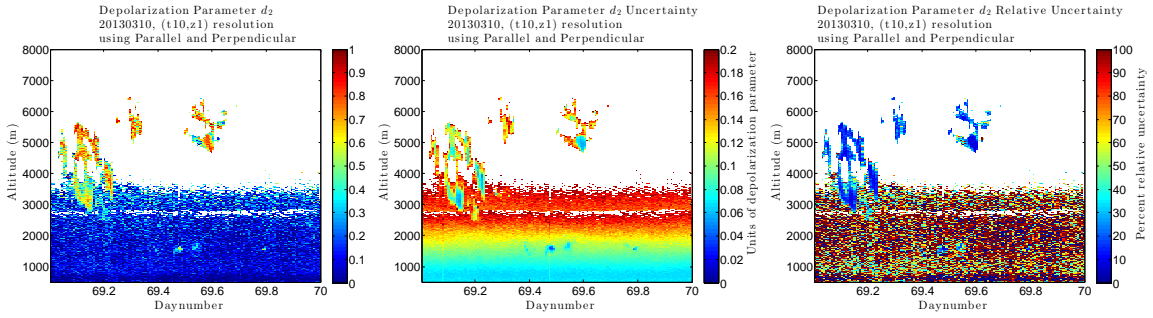


Figure 10.4: The d_2 depolarization values from 10 March 2013, with (t10,z1) resolution, excluding anywhere with more than 0.2 uncertainty in depolarization parameter units. Left: d_2 values. Centre: The uncertainties associated with the d_2 values in units of depolarization parameter. Right: The relative uncertainties are in units of percent. The calibration profile is based on (t20,z1) resolution calculations.

The differences in data coverage at this higher resolution are yet more apparent. d_1 can barely discern that there is a cloud at all at daynumber 69.5, while d_2 still clearly gives the cloud's shape.

The test is repeated again the highest resolution for which any d_1 values at all are left with uncertainty less than 0.2: (t2, z1 ; 2 minute, 7.5 metres) resolution. Again, the (t20,z1) resolution calibration profile is employed in the calculation of d_2 at this highest resolution. Figures 10.5 and 10.6 give these results anywhere uncertainties are less than 0.2.

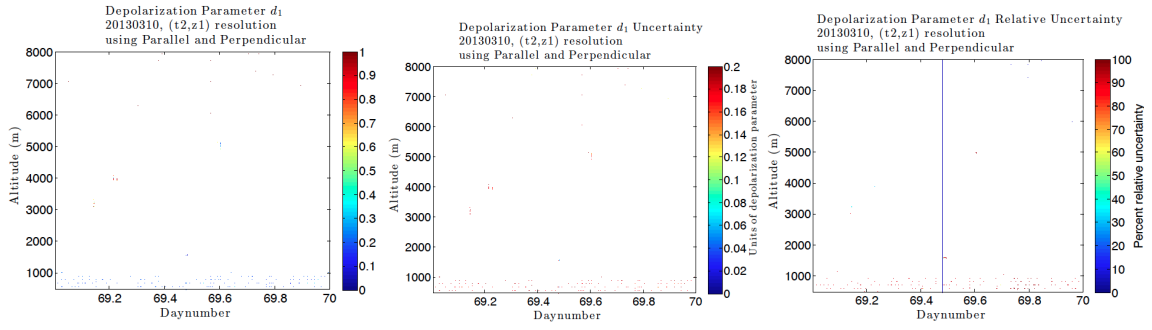


Figure 10.5: The d_1 depolarization values from 10 March 2013, with (t2,z1) resolution, excluding anywhere with more than 0.2 uncertainty in depolarization parameter units. Left: d_1 values. Centre: The uncertainties associated with the d_1 values in units of depolarization parameter. Right: The relative uncertainties are in units of percent. These plots look empty because almost none of the perpendicular measurement bins have enough counts to make it above the SNR thresholds required.

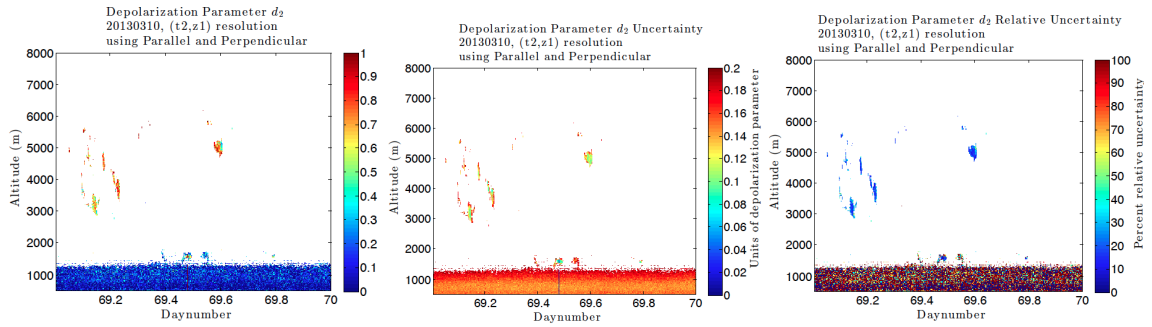


Figure 10.6: The d_2 depolarization values from 10 March 2013, with (t2,z1) resolution, excluding anywhere with more than 0.2 uncertainty in depolarization parameter units. Left: d_2 values. Centre: The uncertainties associated with the d_2 values in units of depolarization parameter. Right: The relative uncertainties are in units of percent. The calibration profile is based on (t20,z1) resolution calculations.

With the final plots in this series, it is evident that the Option 2 parallel/Rayleigh elastic method for calculating depolarization parameter excels at high resolution. There is virtually nothing visible in the d_1 plots. However, using the d_2 plots it is possible to see more detail

regarding the extent of the thickest parts of the clouds aloft. More importantly, d_2 is the only high resolution depolarization information available below 1500 m altitude. With it, it is possible to be sure that there are no high depolarization features at these altitudes on this date. Information gleaned from d_2 measurements is simply not available using the traditional method.

10.2 Example day 2 showing the advantages of d_2 : 29 March 2013

The corrected counts measurements from 29 March 2013 show a medium size cloud surrounded by fine scale features. This makes a good test case for the depolarization channel, to see which features can be picked up by the depolarization parameters of each method.

A resolution of (t20, z1 ; 20 minutes, 7.5 metres) is again examined first in Figures 10.7 and 10.8.

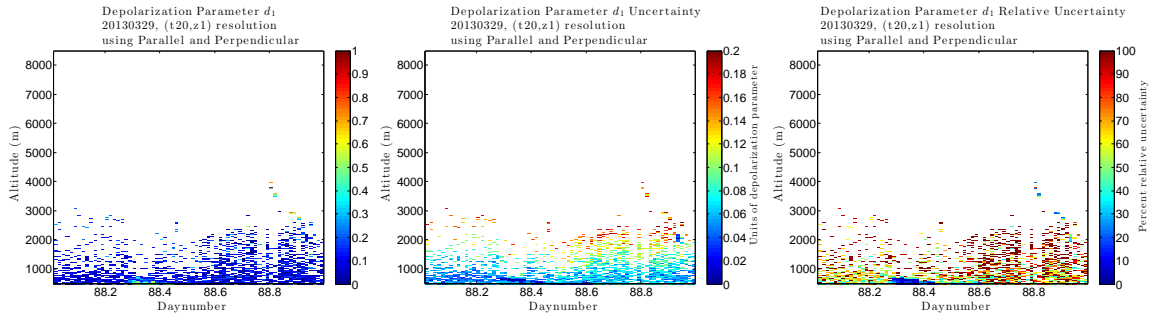


Figure 10.7: The d_1 depolarization values from 29 March 2013, with (t20,z1) resolution, excluding anywhere with more than 0.2 uncertainty in depolarization parameter units. Left: d_1 values. Centre: The uncertainties associated with the d_1 values in units of depolarization parameter. Right: The relative uncertainties are in units of percent.

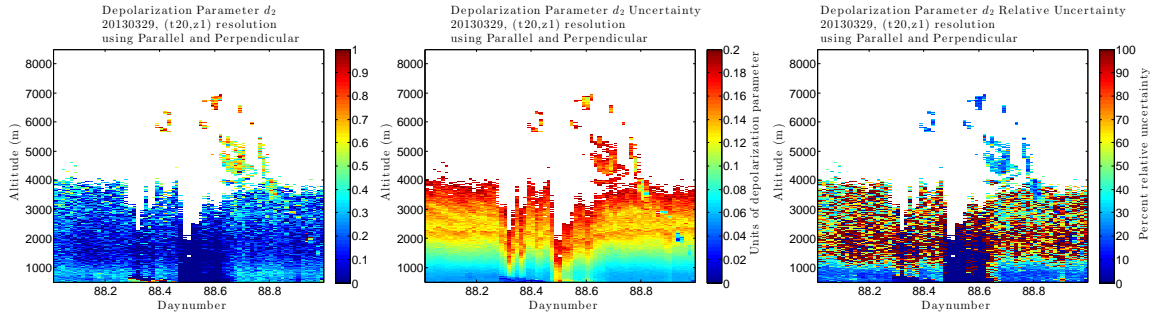


Figure 10.8: The d_2 depolarization values from 29 March 2013, with (t20,z1) resolution, excluding anywhere with more than 0.2 uncertainty in depolarization parameter units. Left: d_2 values. Centre: The uncertainties associated with the d_2 values in units of depolarization parameter. Right: The relative uncertainties are in units of percent. The calibration profile is based on (t20,z1) resolution calculations.

Clouds which are clearly visible in d_2 plots do not show up, except as isolated points, in d_1 plots for the same resolution. Already the resolution of the measurements are too high for the d_1 method to be of particular use. Rather than examining an even higher resolution plot, a lower resolution was selected to see whether it is at all possible for d_1 to pick out the properties of the larger cloud. Resolution of (t20, z5) was used. With 1-minute profiles and 7.5 metre altitude bins, this resolution works out to be 20 minutes, and 35.5 metres in Figures 10.9 and 10.10.

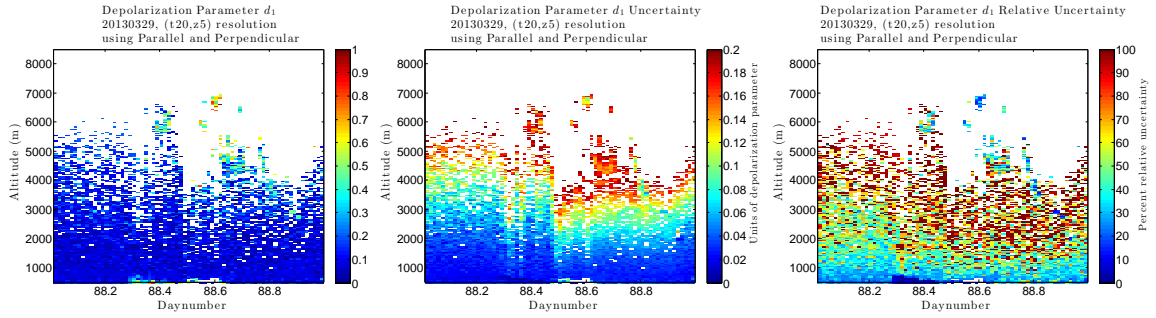


Figure 10.9: The d_1 depolarization values from 29 March 2013, with (t20,z5) resolution, excluding anywhere with more than 0.2 uncertainty in depolarization parameter units. Left: d_1 values. Centre: The uncertainties associated with the d_1 values in units of depolarization parameter. Right: The relative uncertainties are in units of percent.

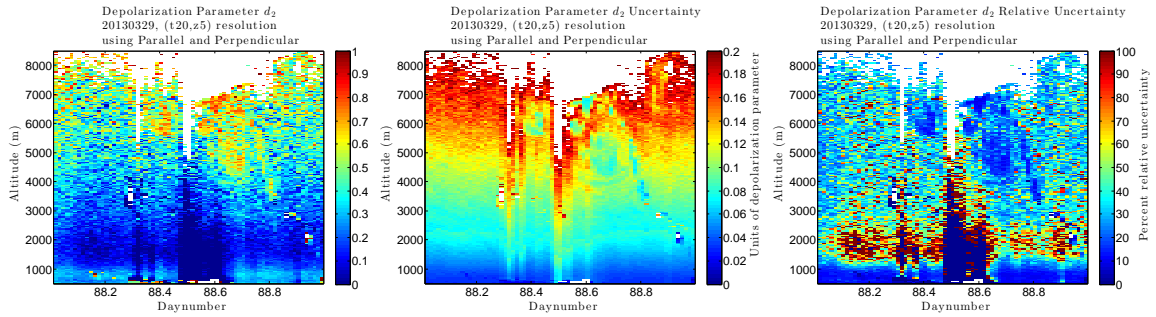


Figure 10.10: The d_2 depolarization values from 29 March 2013, with (t20,z5) resolution, excluding anywhere with more than 0.2 uncertainty in depolarization parameter units. Left: d_2 values. Centre: The uncertainties associated with the d_2 values in units of depolarization parameter. Right: The relative uncertainties are in units of percent. The calibration profile is based on (t20,z1) resolution calculations.

Finally at this resolution, most of the d_1 data creeps upward to 5000 metres in altitude. The clouds are clearly visible, although their morphologies and extents are not able to be discerned. More importantly, there is little ability to tell what the overall depolarization parameter value is for the cloud as a whole, much less for regions within the cloud. d_2 ex-

ceeds these capabilities on all counts. The larger features clearly have a high depolarization parameter, and it is possible to interpret some cloud shape information as well.

10.3 Using uncertainties to choose between d_1 and d_2

The d_2 values calculated with Option 2 clearly outperform d_1 values of the traditional method for the CRL most of the time. There are select situations in which the opposite might temporarily be true. One option which could be explored in future is to combine the results from both calculations in a procedure somewhat similar to the gluing processes of Section 5.7. The uncertainties could be compared for the two methods, and the data for each region could be selected based on whichever process boasts the smaller absolute uncertainty.

It is expected that most often the points with the lower uncertainty will be the Option 2 data, because of the count rates which are orders of magnitude larger in the contributing channels (R, \parallel) than are available in Option 1 (which uses \perp). Exceptions in some locations (such as the lowest count rates for which analogue channels are used) are expected. To verify this, it is possible to compare uncertainties for both depolarization methods ($\sigma_{d2} - \sigma_{d1}$) for measurements made at identical resolutions.

In the following example, (t20, z1) resolution is used. The uncertainties in d are calculated for each method as usual. For each data point, the uncertainties from the traditional method are subtracted from the uncertainties in the Option 2 method. Positive values indicate that the Traditional Method is more precise; Negative values indicate an improvement using the Option 2 method. Two plots are given: Figure 10.11 (left) is a colour plot showing the difference in uncertainties for each data point as a function of time and altitude. Figure 10.11 (right) plots all differences together as a function only of altitude.

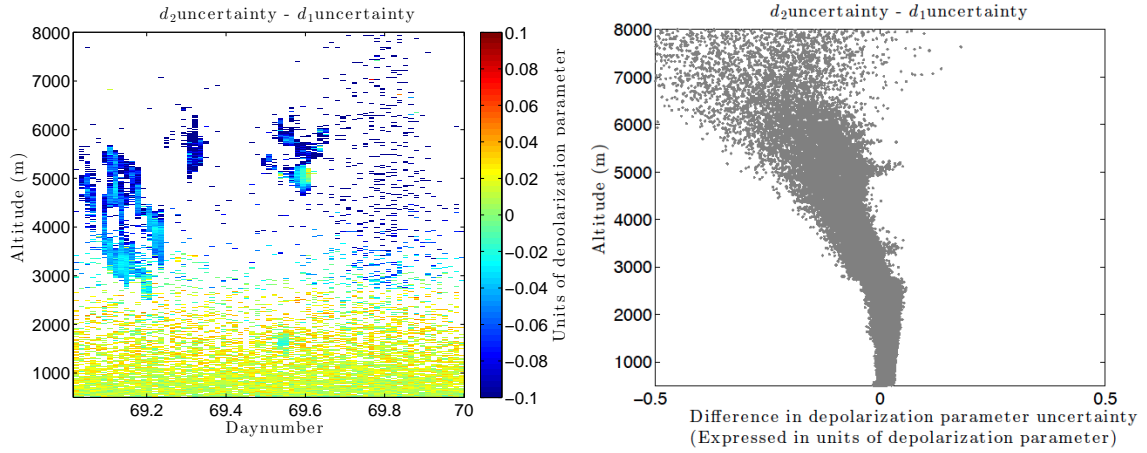


Figure 10.11: Compare uncertainties for both depolarization methods $\sigma_{d2} - \sigma_{d1}$. Positive values indicate that the Traditional Method is more precise; Negative values indicate an improvement using the Option 2 method.

The conclusion from either of the plots in Figure 10.11 is that at worst, the uncertainties are nearly identical (below 3000 m) and at best, d_2 has approximately 0.1 in depolarization parameter units, or 10 percent of the maximum possible depolarization value, lower uncertainty than does d_1 .

For routine operations, it is sensible to choose d_2 to express the depolarization parameter products, and not d_1 .

10.4 Summary of advantages of d_2 over d_1 and recommendations

The d_2 (Option 2) method of calculating depolarization parameters using the parallel and Rayleigh elastic channel exceeds the performance of d_1 (Traditional Method) calculations in almost every scenario for CRL. With Option 2,:

- High signal to noise ratios of channels contributing to d_2 mean lower uncertainty for each

d_2 data point in most cases.

- More time-altitude space is able to be given a depolarization parameter value than is possible with d_1
- Fine scale atmospheric structure is able to be examined because d_2 works well up to high temporal and spatial resolution.
- High altitude features are able to be examined because d_2 has sufficient contributing photocounts from these altitudes.

It is recommended that users of CRL depolarization measurements make use of the d_2 measurements. As these can be translated into depolarization ratio δ very easily (Chapter 6) should the user desire, there is no disadvantage to using the best depolarization expression possible. For CRL, this is a depolarization parameter calculated from the parallel and Rayleigh Elastic channels, calibrated nightly using contributions from the perpendicular channel.

Chapter 11

Conclusions

11.1 Summary of major results

The CANDAC Rayleigh-Mie-Raman lidar (CRL) at Eureka, Nunavut in the Canadian High Arctic has been upgraded with the addition of a linear depolarization system. This system contains a Polarotor spinning polarizer so that two measurement channels may share one photomultiplier tube. No measurements in other pre-existing lidar channels were negatively affected as a result of the installation.

Extensive analysis routines were written in MATLAB to take the depolarization channel measurements from raw binary data files to corrected, merged profiles of photons as a function of altitude.

Calibrated measurements of the depolarization ratio were produced according to the methods which are common in the depolarization lidar community. Calculations of the related depolarization parameter were also made. These methods use the Parallel and Perpendicular depolarization channel measurements in a ratio.

Detailed Mueller matrix calculations were made to develop the framework for validation tests of the CRL's optics. These tests demonstrated that the traditional calculation methods are valid for the CRL instrument.

The matrix calculations also opened up a new possibility for CRL's depolarization measurements: The use of a third, non-polarized Rayleigh Elastic lidar channel. Development of equations for the calculation of the depolarization parameter were made for four situations which are possible using combinations of the three available channels, and these were expressed in terms of the fewest calibration constants possible.

Numerous calibration protocols were developed, tested, and used for CRL depolarization. This included materials tests, installation tests, operational tests, and the interpretation of results. Several techniques will continue to be used at CRL, particularly during winter months.

For the most promising depolarization calculation option, full worked examples were presented using CRL data from 2013. In these examples, the Parallel and Perpendicular channel measurements are used at low resolution to calculate a calibration profile for the night. Then the Parallel and Rayleigh Elastic channels are used at high spatial-temporal resolution with the nightly calibration profile to produce measurements of depolarization parameter.

Because the nightly calibration profile does not vary much in time, it is possible to use a profile from one night to calculate another night's data, although this is less desirable. During the 2012 measurement campaign at CRL, the polarotor was removed for repairs. For 1.5 months, the lidar was run with a static Polaroid sheet polarizer in the place of the polarotor, and this was aligned in the parallel direction. With the advent of the three-channel method, after some modifications for a different type of calibration, the 2012 measurements should now be accessible for interpretation. The CRL group looks forward to retrieving these measurements which would have been impossible to use when relying only on the traditional methods.

The advantages of the new three-channel calculation technique are several: Better coverage of time and space when using the same measurement period, better signal to noise ratios, higher spatial and temporal resolution of derived depolarization parameter data prod-

ucts, and better cross-validation between channels.

CRL Depolarization measurements exist for 2010, 2011, 2012, 2013 and 2014, with at least one month (in some cases, more than two) of approximately 24h/day coverage in the polar sunrise season of each year. Now that measurements have been optimized and so have the calibrations, routine production of depolarization ratio and depolarization parameter plots for these years, with uncertainties, will be forthcoming.

Standard depolarization operating procedures for the CRL, looking forward, include processing using the new three-channel method with a fully-operational linear depolarization lidar system.

11.2 Future work

With the CRL's depolarization channel now in full operation, and with the new depolarization parameter calculation technique calibrated and validated, CRL's measurement products are ready for use in scientific studies.

Some of the first studies to be undertaken are an interpretation of the entire 2013 and 2014 Polar Sunrise season CRL data sets. Depolarization parameter and lidar ratio measurements will be examined in the context of temperature information from the Eureka radiosondes, and general descriptions of the clouds during each season will be presented. Cloud and aerosol particles will be grouped according to depolarization parameter and lidar ratio in order to determine whether various families of these particles are present (for example, desert dust particles tend to present differently to marine particles, differently again to volcanic ash, and ice particles). Backtrajectory calculation programs will be used to determine the origin of these families of particles where applicable. This will form the foundational work for a long-term climatology and observations of changes in these features, with CRL depolarization measurements anticipated to continue at Eureka for many years into the future.

An extension to this is the inclusion of radar measurements in the interpretation, as was carried out at Eureka in 2009, using data sets from 2005-2008. Then, an Arctic High Spectral Resolution Lidar (HSRL) was colocated with a Millimeter-wave Cloud Radar (MMCR), and these were used together to good effect to study the physical properties of Arctic clouds [43]. The AHSRL is no longer at Eureka, but CRL, with its new capabilities, can now take over the lidar portion of the measurements used in this study. Each technique is sensitive to different sizes and compositions of particles (e.g. aerosols, for the most part, being invisible to the radar but visible to the lidar), and the combination of these measurements. Charts plotting cloud data as a function of the ratio of radar backscatter to lidar backscatter on one axis, and depolarization ratio or depolarization parameter on the other, are helpful in classifying different atmospheric particles and mixtures thereof [43].

Well-calibrated depolarization lidar measurements can also be made in coordination with the Starphotometer group's measurements of aerosol abundance and size at Eureka. Diamond dust is an important component of the wintertime polar environment, and the combination of starphotometer and lidar is well equipped to investigate the microphysical properties of these tiny ice particles which precipitate from a cloud-free sky. Works following on to such publications as [121] will only benefit from the improved lidar depolarization parameter measurements made possible by this thesis. Improvements to the starphotometer's cloud screening algorithm are also possible using these data.

These examples are but a few planned studies which have been made possible by the depolarization upgrades to the CRL which have been described in this thesis. More are possible of course, using the other extensive local instrumentation at Eureka, and more still using satellite and aircraft measurements when the data exists for Arctic regions.

Eureka is not alone as a well-equipped Arctic atmospheric observatory. Cooperation with our international pan-Arctic community, with colleagues at the other pole, in the Antarctic, and with stations in between, will all serve to create a more complete global understanding of clouds and their climatic influences now, in the past, and into the future.

Bibliography

- [1] Ssolbergj, “Canada (orthographic projection) map. [https://commons.wikimedia.org/wiki/File:Canada_\(orthographic_projection\).svg](https://commons.wikimedia.org/wiki/File:Canada_(orthographic_projection).svg),” 2008.
- [2] G. Nott, T. Duck, J. Doyle, M. Coffin, C. Perro, C. Thackray, J. Drummond, P. Fogal, E. McCullough, and R. Sica, “A remotely operated lidar for aerosol, temperature, and water vapor profiling in the High Arctic,” *Journal of Atmospheric and Oceanic Technology*, vol. 29, no. 2, pp. 221–234, 2012.
- [3] W. J. Brennan, J. Kaye, T. Armstrong, A. Dearry, J. Elwood, M. Glackin, P. Gruber, W. Hohenstein, L. Lawson, J. Moyers, P. Neale, J. Schafer, J. Scheraga, H. Watson, G. Banks, M. Brandt, S. Eule, H. Frumkin, K. Gebbie, M. R. McCalla, and G. Whitney, *Our Changing Planet: The U.S. Climate Change Science Program for Fiscal Year 2008*. 2008.
- [4] W.-N. Chen, C.-W. Chiang, and J.-B. Nee, “Lidar ratio and depolarization ratio for cirrus clouds,” *Applied Optics*, vol. 41, no. 30, pp. 6470–6476, 2002.
- [5] A. Lampert, C. Ritter, A. Hoffmann, J.-F. Gayet, G. Mioche, A. Ehrlich, A. Dornbrack, M. Wendish, and M. Shiobara, “Lidar characterization of the arctic atmosphere during ASTAR 2007: four cases studies of boundary layer, mixed-phase and multi-layer clouds,” *Atmospheric Chemistry and Physics*, vol. 10, pp. 2847–2866, 2010.

- [6] IPCC Plenary XXVII, *Climate change 2007: Synthesis report summary for policy-makers. Technical report*, 2007, November 2007.
- [7] V. Noel, H. Chepfer, M. Haeffelin, and Y. Morille, “Classification of ice crystal shapes in midlatitude ice clouds from three years of lidar observations over the Sirta observatory,” *Journal of the Atmospheric Sciences*, vol. 63, pp. 2978–2991, 2006.
- [8] R. Cess, G. Potter, J. Blanchet, G. J. Boer, A. del Genio, M. Deque, V. Dymnikov, V. Galin, W. Gates, S. Ghan, J. Kiehl, A. Lacis, H. Le Treut, Z.-X. Li, X.-Z. Liang, B. McAvaney, V. Meleshko, J. Mitchell, J.-J. Morcrette, D. Randall, L. Rikus, E. Roeckner, J. Royer, U. Schlese, D. Sheinin, A. Slingo, A. Sokolov, K. Taylor, W. Washington, R. Wetherald, I. Yagai, and M.-H. Zhang, “Intercomparison and interpretation of climate feedback processes in 19 atmospheric general circulation models,” *Journal of Geophysical Research*, vol. 95, pp. 16601–16615, September 1990.
- [9] R. D. Cess, M. H. Zhang, W. J. Ingram, G. L. Potter, V. Alekseev, H. W. Barker, E. Cohen-Solal, R. A. Colman, D. A. Dazlich, A. D. D. Genio, M. R. Dix, V. Dymnikov, M. Esch, L. D. Fowler, J. R. Fraser, V. Galin, W. L. Gates, J. J. Hack, J. T. Kiehl, H. L. Treut, K. K.-W. Lo, B. J. McAvaney, V. P. Meleshko, J.-J. Morcrette, D. A. Randall, E. Roeckner, J.-F. Royer, M. E. Schlesinger, P. V. Sporyshev, B. Timbal, E. M. Volodin, K. E. Taylor, W. Wang, and R. T. Wetherald, “Cloud feedback in atmospheric general circulation models: An update,” *Journal of Geophysical Research: Atmospheres*, vol. 101, pp. 12791–12794, May 1996.
- [10] C. Platt, S. Young, P. Manson, G. Patterson, S. Marsden, and R. Austin, “The optical properties of equatorial cirrus from observations in the ARM pilot radiation observation experiment,” *Journal of the Atmospheric Sciences*, vol. 55, pp. 1977–1996, 1998.

- [11] A. Heymsfield and C. Platt, "A parameterization of the particle size spectrum of ice clouds in terms of the ambient temperature and ice water content.," *Journal of the Atmospheric Sciences*, vol. 41, no. 5, pp. 846–855, 1984.
- [12] L. Sauvage, H. Chepfer, V. Trouillet, P. Flamant, G. Brogniez, J. Pelon, and F. Albers., "Remote sensing of cirrus radiative parameters during EUCREX '94. Case study of 17 April 1994. part 1: Observations.," *Monthly Weather Review*, vol. 127, p. 486, 503 1999.
- [13] G. D. Boer, E. Eloranta, and M. Shupe, "Arctic mixed-phase stratiform cloud properties from multiple years of surface-based measurements at two high-latitude locations.," *Journal of the Atmospheric Sciences*, vol. 66, pp. 2874–2887, 2009.
- [14] M. Shupe, J. Daniel, G. de Boer, E. Eloranta, P. Kollias, C. Long, E. Luke, D. Turner, and J. Verlinde, "A focus on mixed-phase clouds: The status of ground-based observational methods," *Bulletin of the American Meteorological Society*, 2008.
- [15] S. Xie, J. Boyle, S. Klein, X. Liu, and S. Ghan, "Evaluation of mixed-phase cloud parameterizations in short-range weather forecasts with CAM3 and AM2 for mixed-phase Arctic cloud experiment," in *Third Quarter 2007 ARM Metric Report*, pp. 1–14, 2007.
- [16] J. Curry, W. Rossow, D. Randall, and J. Schramm, "Overview of Arctic cloud and radiation characteristics.," *Journal of Climate*, vol. 9, pp. 1731–1764, 1996.
- [17] Y. Takano and K.-N. Liou, "Solar radiative transfer in cirrus clouds. Part I: Single-scattering and optical properties of hexagonal ice crystals," *Journal of the Atmospheric Sciences*, vol. 46, pp. 3–19, January 1989.
- [18] Y. Takano and K.-N. Liou, "Solar radiative transfer in cirrus clouds. Part II: Theory and computation of multiple scattering in an anisotropic medium," *Journal of the Atmospheric Sciences*, vol. 46, pp. 20–36, January 1989.

- [19] Z. Sun and K. P. Shine, “Studies of the radiative properties of ice and mixed-phase clouds,” *Quarterly Journal of the Royal Meteorological Society*, vol. 120, no. 515, pp. 111–137, 1994.
- [20] D. Gregory and D. Morris, “The sensitivity of climate simulations to the specification of mixed phase clouds,” *Climate Dynamics*, vol. 12, pp. 641–651, 1996.
- [21] Z. Wang, “The seasonal interannual variations of mixed-phase cloud properties observed at the north shore of Alaska site.,” in *Sixteenth ARM Science Team Meeting Proceedings*, 2006.
- [22] G. de Boer and E. Eloranta, “Lidar-based retrievals of the microphysical properties of mixed-phase arctic stratus clouds and precipitation,” in *Sixteenth ARM Science Team Meeting Proceedings*, 2006.
- [23] T. Storelvmo, J. Kristjansson, and U. Lohmann, “Aerosol influence on mixed-phase clouds in CAM-OSLO,” *Journal of the Atmospheric Sciences*, vol. 65, pp. 3214–3230, 2008.
- [24] C. D. Westbrook and A. J. Illingworth, “The formation of ice in a long-lived supercooled layer cloud,” *Quarterly Journal of the Royal Meteorological Society*, vol. 139, pp. 2209–2221, October 2013.
- [25] P. Grenier, J.-P. Blanchet, and R. Munoz-Alpizar, “Study of polar thin ice clouds and aerosols seen by CloudSat and CALIPSO during midwinter 2007.,” *Journal of Geophysical Research*, vol. 114, pp. 1–19, 2009.
- [26] J. D. Spinhirne, M. Z. Hansen, and L. O. Caudill, “Cloud top remote sensing by airborne lidar,” *Applied Optics*, vol. 21, no. 9, pp. 1564–1571, 1982.
- [27] G. L. Stephens, D. G. Vane, R. J. Boain, G. G. Mace, K. Sassen, Z. Wang, A. J. Illingworth, E. J. O’Connor, W. B. Rossow, S. L. Durden, S. D. Miller, R. T. Austin,

- A. Benedetti, C. Mitrescu, and the CloudSat Science Team, “The CloudSat mission and the A-Train; a new dimension of space-based observations of clouds and precipitation,” *Bulletin of the American Meteorological Society*, vol. 83, no. 12, 2002.
- [28] T. Uttal, J. A. Curry, M. G. Mcphee, D. K. Perovich, R. E. Moritz, J. A. Maslanik, P. S. Guest, H. L. Stern, J. A. Moore, R. Turenne, A. Heiberg, M. C. Serreze, D. P. Wylie, O. G. Persson, C. A. Paulson, C. Halle, J. H. Morison, P. A. Wheeler, A. Makshtas, H. Welch, M. D. Shupe, J. M. Intrieri, K. Stamnes, R. W. Lindsey, R. Pinkel, W. S. Pegau, T. P. Stanton, Thomas, and C. Grenfeld, “Surface heat budget of the Arctic ocean,” *Bulletin of the American Meteorological Society*, pp. 255–275, 2002.
- [29] Earth System Research Laboratory, Physical Sciences Division, “Barrow, Alaska Observatory,” 2015.
- [30] National Science Foundation Office of Polar Programs, “Research: Greenland environmental observatory,” 2015.
- [31] Various Authors, “Summit Greenland project summaries 2014.” <http://www.geosummit.org>, 2014.
- [32] Earth System Research Laboratory, Physical Sciences Division, “Hydrometeorological observatory of Tiksi, Russia,” 2015.
- [33] Arctic Observing Summit 2013, *Advancing Arctic Atmospheric Science through Developing Collaborative , Targets for Large, International Observatories*, February 2013. Community White Paper.
- [34] I. A. Razenkov, E. W. Eloranta, J. P. Hedrick, R. E. Holz, R. E. Kuehn, and J. P. Garcia, “A high spectral resolution lidar designed for unattended operation in the Arctic,” in *21st International Laser Radar Conference*, July 8 - 12 2002.
- [35] E. W. Eloranta, I. A. Razenkov, J. P. Garcia, and J. Hedrick, “An automated high spectral resolution lidar for long term measurements in the Arctic: Observations with

- the University of Wisconsin Arctic high spectral resolution lidar,” in *2nd Symposium on Lidar Atmospheric Applications at the 85th Annual Meeting of the American Meteorological Society*, January 9 - 13 2005.
- [36] E. W. Eloranta, “Long-term continuous operation of the University of Wisconsin High Spectral Resolution Lidar in the High Arctic,” in *SPIE Asia-Pacific Remote Sensing 2006*, November 13-17 2006.
- [37] E. W. Eloranta, I. A. Razenkov, J. P. Garcia, and J. Hedrick, “Observations with the University of Wisconsin Arctic High Spectral Resolution Lidar,” in *22nd International Laser Radar Conference*, no. ESA SP-561, p. 305, July 2004.
- [38] M. D. Shupe, T. Uttal, S. Y. Matrosov, and A. S. Frisch., “Cloud water contents and hydrometeor sizes during the FIRE Arctic clouds experiment.,” *Journal of Geophysical Research*, 2001.
- [39] J. A. Curry, P. V. Hobbs, M. D. King, D. A. Randall, P. M. G. A. Isaac, J. O. Pinto, T. Uttal, A. Bucholtz, D. G. Cripe, H. Gerber, C. W. Fairall, T. J. Garrett, J. Hudson, J. M. Intrieri, C. Jakob, T. Jensen, P. Lawson, D. Marcotte, L. Nguyen, P. Pilewskie, A. Rangno, D. C. Rogers, K. B. Strawbridge, F. P. J. Valero, A. G. Williams, and D. Wyliep, “FIRE Arctic clouds experiment,” *Bulletin of the American Meteorological Society*, vol. 81, pp. 5–29, 2000.
- [40] J. Verlinde, J. Y. Harrington, G. M. McFarquhar, V. T. Yannuzzi, A. Avramov, S. Greenberg, N. Johnson, G. Zhang, M. R. Poellot, J. H. Mather, D. D. Turner, E. W. Eloranta, B. D. Zak, A. J. Prenni, J. S. Daniel, G. L. Kok, D. C. Tobin, R. Holz, K. Sassen, D. Spangenberg, P. Minnis, T. P. Tooman, M. C. Ivey, S. J. Richardson, S. M. C. P. Bahrmann, P. J. DeMott, A. J. Heymsfield, and R. Schofield, “The mixed phase Arctic cloud experiment,” *Bulletin of the American Meteorological Society*, pp. 205–211, 2007.

- [41] G. M. McFarquhar, G. Zhang, M. R. Poellot, G. L. Kok, R. McCoy, T. Tooman, A. Fridlind, and A. J. Heymsfield., “Ice properties of single-layer stratocumulus during the mixed-phase Arctic cloud experiment: 1. Observations,” *Journal of Geophysical Research*, vol. 112, pp. 1–19, 2007.
- [42] D. Turner and E. Eloranta, “Validating mixed-phase cloud optical depth retrieved from infrared observations with high spectral resolution lidar,” *IEEE Geoscience Remote Sensing Letters*, vol. 5, pp. 285–288, 2008.
- [43] L. Bourdages, T. J. Duck, G. Lesins, J. R. Drummond, and E. W. Eloranta, “Physical properties of High Arctic tropospheric particles during winter,” *Atmospheric Chemistry and Physics*, vol. 9, pp. 6881–6897, 2009.
- [44] J. E. Kristjansson, J. M. Edwards, and D. L. Mitchell, “Impact of a new scheme for optical properties of ice crystals on climates of two GCMs,” *Journal of Geophysical Research: Atmospheres*, vol. 105, pp. 10063–10079, April 2000.
- [45] D. Ivanova, D. L. Mitchell, W. P. Arnott, and M. Poellot, “A GCM parameterization for bimodal size spectra and ice mass removal rates in mid-latitude cirrus clouds,” *Atmospheric Research*, vol. 59-60, pp. 89–113, October-December 2001.
- [46] F. S. Boudala, G. A. Isaac, Q. Fu, and S. G. Cober, “Parameterization of effective ice particle size for high-latitude clouds,” *International Journal of Climatology*, vol. 22, no. 10, pp. 1267–1284, 2002.
- [47] H. R. Pruppacher and J. D. Klett, *Microphysics of Clouds and Precipitation*. Kluwer Academic, 1977.
- [48] U. Lohmann and B. Kärcher, “First interactive simulations of cirrus clouds formed by homogeneous freezing in the ECHAM general circulation model,” *Journal of Geophysical Research: Atmospheres*, vol. 107, no. D10, pp. AAC 8–1 –AAC 8–13, 2002.

- [49] I. Sednev, S. Menon, and G. McFarquhar, “Simulating mixed-phase Arctic stratus clouds: sensitivity to ice initiation mechanisms,” *Atmospheric Chemistry and Physics*, vol. 9, pp. 4747–4773, 2009.
- [50] E. Hecht, *Optics*. Addison Wesley, 4th ed., 2002.
- [51] G. Mie, “Contributions to the optics of turbid media, particularly of colloidal metal solutions (beitrage zur optik truber medien, speziell kolloidaler metallosungen). Royal Aircraft Establishment Library Translation 1983. Translator: B. Crossland. Translation editor: D.J. Rowley,” *Anallen der Physik, in translation*, vol. 25, no. 3, pp. 377–445, 1908.
- [52] H. C. van de Hulst, *Light scattering by small particles*. John Wiley and Sons, Inc., 1957.
- [53] J. Hovenier, H. van de Hulst, and C. van der Mee, “Conditions for the elements of the scattering matrix,” *Astronomy and Astrophysics*, vol. 157, pp. 301–310, 1986.
- [54] K. Liou and H. Lahore, “Laser sensing of cloud composition: a backscattered depolarization technique,” *Journal of Applied Meteorology*, vol. 13, pp. 257–263, March 1974.
- [55] K. N. Liou, “On depolarization of visible light from water clouds for a monostatic lidar,” in *Journal of Atmospheric Science*, vol. 29, pp. 1000–1003, 1972.
- [56] A. Lampert, *Airborne lidar observations of tropospheric Arctic clouds*. PhD thesis, Alfred-Wegener-Institut Für Polar- Und Meeresforschung, 2010.
- [57] M. Hayman and J. P. Thayer, “Explicit description of polarization coupling in lidar applications,” *Optics Letters*, vol. 34, pp. 611–613, March 2009.
- [58] U. Wandinger, *Lidar: Range-resolved optical remote sensing of the atmosphere*. Springer Science + Business Media Inc, 2005.

- [59] K. Sassen, "Polarization in lidar: a review," in *Polarization Science and Remote Sensing* (J. Shaw and J. Tyo, eds.), vol. 5158 of *Proceedings of SPIE*, 2003.
- [60] G. G. Gimmestad, "Reexamination of depolarization in lidar measurements," *Applied Optics*, vol. 47, pp. 3795 – 3802, July 2008.
- [61] K. F. G. Olofson, G. Witt, and J. B. C. Pettersson, "Bistatic lidar measurements of clouds in the Nordic Arctic region," *Applied Optics*, vol. 47, no. 26, pp. 4777–4786, 2008.
- [62] R. Schotland, K. Sassen, and R. Stone, "Observations by lidar of linear depolarization ratios for hydrometeors.," *Journal of Applied Meteorology*, vol. 10, pp. 1011–1017, 1971.
- [63] D. H. Hohn, "Depolarization of a laser beam at 6328 Angstroms due to the atmospheric transmission," *Applied Optics*, vol. 8, pp. 367–370, 1969.
- [64] K.-N. Liou and R. M. Schotland, "Multiple backscattering and depolarization from water clouds for a pulsed lidar system," *Journal of Atmospheric Science*, vol. 28, pp. 772–774, 1971.
- [65] P. K. Dubey, S. L. Jain, B. C. Arya, and P. S. Kulkarni, "Depolarization ratio measurement using single photomultiplier tube in micropulse lidar," *Review of Scientific Instruments*, vol. 80, no. 053111, 2009.
- [66] G. Larcheveque, I. Balin, R. Nessler, P. Quaglia, V. Simeonov, H. van den Bergh, and B. Calpini, "Development of a multiwavelength aerosol and water-vapour lidar at the Jungfrauoch Alpine Station (3580 m above sea level) in Switzerland," *Applied Optics*, vol. 41, no. 15, pp. 2781–2790, 2002.
- [67] S. R. Pal and A. I. Carswell, "Polarization properties of lidar backscattering from clouds," *Applied Optics*, vol. 12, pp. 1530–1535, July 1973.

- [68] J. Reichardt, R. Baumgart, and T. J. McGee, “Three-signal method for accurate measurements of depolarization ratio with lidar,” *Applied Optics*, vol. 42, no. 24, pp. 4909–4913, 2003.
- [69] J. Biele, A. Tsias, B. P. Luo, K. S. Carslaw, R. Neuber, G. Beyerle, and T. Peter, “Nonequilibrium coexistence of solid and liquid particles in Arctic stratospheric clouds,” *Journal of Geophysical Research*, vol. 106, no. 19, pp. 22991–23007, 2001.
- [70] J. Biele, *Polare stratosphärische Wolken: Lidar-Beobachtungen, Charakterisierung von Entstehung und Entwicklung, or Polar stratospheric clouds: Lidar-observations, characterization of formation and development*. PhD thesis, Alfred Wegener Institute for Polar and Marine Research, 303, 1999.
- [71] G. David, A. Miffre, B. Thomas, and P. Rairoux, “Sensitive and accurate dual-wavelength UV-VIS polarization detector for optical remote sensing of tropospheric aerosols,” *Applied Physics B Lasers and Optics*, vol. 108, no. 1, pp. 197–216, 2012.
- [72] M. Hayman and J. P. Thayer, “Lidar polarization measurements of PMCs,” *Journal of Atmospheric and Solar-Terrestrial Physics*, vol. 73, pp. 2110–2117, 2011.
- [73] J. M. Alvarez, M. A. Vaughan, C. A. Hostetler, W. H. Hunt, and D. M. Winker, “Calibration technique for polarization-sensitive lidars,” *American Meteorological Society*, vol. 23, pp. 683–699, 2006.
- [74] K. Sassen and S. Benson, “A midlatitude cirrus cloud climatology from the Facility for Atmospheric Remote Sensing. Part II: Microphysical properties derived from lidar depolarization,” *Journal of the Atmospheric Sciences*, vol. 58, pp. 2103–2112, 2001.
- [75] K. Sassen, “The polarization lidar technique for cloud research: a review and current assessment,” *Bulletin of the American Meteorological Society*, vol. 72, pp. 1848–1866, December 1991.

- [76] J. M. Intieri, M. D. Shupe, T. Uttal, and B. J. McCarty, "An annual cycle of Arctic cloud characteristics observed by radar and lidar at SHEBA," *Journal of Geophysical Research*, vol. 107, pp. SHE 5–1–SHE 5–15, October 2002.
- [77] K. Sassen, "Ice crystal habit discrimination with the optical backscatter depolarization technique," *Journal of Applied Meteorology*, vol. 16, pp. 425–431, 1977.
- [78] V. Noel, G. Ledanois, H. Chepfer, and P. H. Flamant, "Computation of a single-scattering matrix for nonspherical particles randomly or horizontally oriented in space," *Applied Optics*, vol. 40, no. 24, pp. 4365–4375, 2001.
- [79] V. Noel, D. M. Winker, M. McGill, and P. Lawson, "Classification of particle shapes from lidar depolarization ratio in convective ice clouds compared to in situ observations during CRYSTAL-FACE," *Journal of Geophysical Research*, vol. 109, no. D24213, pp. 1–13, 2004.
- [80] K. Sassen, "Polarization diversity lidar returns from virga and precipitation: Anomalies and the bright band analogy," *Journal of Applied Meteorology*, vol. 15, pp. 292–300, 1975.
- [81] T. Sakai, T. Nagai, Y. Zaizen, and Y. Mano, "Backscattering linear depolarization ratio measurements of mineral, sea-salt, and ammonium sulfate particles simulated in a laboratory chamber," *Applied Optics*, vol. 49, pp. 4441–2111, August 2010.
- [82] V. Noel, H. Chepfer, G. Ledanois, A. Delaval, and P. H. Flamant, "Classification of particle effective shape ratios in cirrus clouds based on the lidar depolarization ratio," *Applied Optics*, vol. 41, no. 21, pp. 4245–4257, 2002.
- [83] M. Hayman, S. Spuler, B. Morley, and J. VanAndel, "Polarization lidar operation for measuring backscatter phase matrices of oriented scatterers," *Optics Express*, vol. 20, pp. 29553–29567, December 2012.

- [84] M. Hayman and J. P. Thayer, “General description of polarization in lidar using Stokes vectors and polar decomposition of Mueller matrices vectors and polar decomposition of mueller matrices,” *Journal of the Optical Society of America*, vol. 29, pp. 400–409, 2012.
- [85] B. V. Kaul, I. V. Samokhvalov, and S. N. Volkov, “Investigating particle orientation in cirrus clouds by measuring backscattering phase matrices with lidar,” *Applied Optics*, vol. 43, pp. 6620–6628, December 2004.
- [86] C. J. Flynn^a, A. Mendoza^a, Y. Zheng^b, and S. Mathur^b, “Novel polarization-sensitive micropulse lidar measurement technique,” *Optics Express*, vol. 15, no. 6, pp. 2785–2790, 2008.
- [87] L. GmbH, “Rotating polarizer multispectral polarization measurements,” tech. rep., Licel lidar computing and electronics, June 2006.
- [88] L. GmbH, *LicelPolarotorManual: Licel Ethernet Controller – Installation and Reference Manual*. Licel GmbH, 2005.
- [89] Andover Corporation, “500-599nm standard bandpass optical filters technical specifications,” September 2015.
- [90] N. Shashar and T. W. Cronin, “Polarization contrast vision in octopus,” *The Journal of Experimental Biology*, vol. 199, pp. 999–1004, 1996.
- [91] S. Johnsen, “Extraocular sensitivity to polarized light in an echinoderm,” *Journal of Experimental Biology*, vol. 195, pp. 281–291, 1994.
- [92] D. D. Venable, D. N. Whiteman, M. Calhoun, A. O. Dirisu, R. Connell, and E. Landulfo, “A lamp mapping technique for independent determination of the water vapor mixing ratio calibration factor for a Raman lidar system,” *Applied Optics*, vol. 50, pp. 4622–4632, 2011.

- [93] Software Library and Utilities by The HDF Group, “Hdf5 website,” 2014.
- [94] L. GmbH, *Licel Transient Recorder and Ethernet-Controller Programming Manual*. Licel GmbH, February 2010.
- [95] L. GmbH, *TR20-160 Lidar transient recorder manual*. Licel lidar computing and electronics, December 2012.
- [96] L. GmbH, *Licel Ethernet Controller – Installation and Reference Manual*. Licel GmbH, October 2009.
- [97] B. Mielke, *Analogue + Photon Counting*. Licel lidar computing and electronics.
- [98] L. GmbH, *Licel PM-HV Photomultiplier Module R9880U Manual*. Licel lidar computing and electronics, December 2014.
- [99] Maxim Integrated Products, “INL/DNL Measurements for High-Speed Analog-to-Digital Converters (ADCs),” Tutorial APP 283, Maxim Integrated, <http://www.maximintegrated.com/an283>, November 2001.
- [100] L. GmbH, *Optical Transient Recorder*. Licel lidar computing and electronics, http://www.licel.com/datasheets/TransientRecorder2014_144dpi.pdf, February 2014.
- [101] Hamamatsu Photonics K.K., “Photon counting using photomultiplier tubes,” Tech. Rep. TPHO9001E02, Hamamatsu Photonics K.K., May 1998.
- [102] M. Walker, D. Venable, and D. N. Whiteman, “Gluing for Raman lidar systems using the lamp mapping technique,” *Applied Optics*, vol. 53, no. 36, pp. 8535–8543, 2014.
- [103] E. W. Eloranta, “Comments from CREATE-AAS Summer School,” July 2013.
- [104] D. Petty and D. Turner, “Combined Analog-to-Digital and Photon Counting detection utilized for continuous Raman lidar measurements,” in *Proceedings of the 23rd International Laser Radar Conference*, vol. 7574, 2006.

- [105] R. K. Newsom, D. D. Turner, B. Mielke, M. Clayton, R. Ferrare, and C. Sivaraman, “Simultaneous analog and photon counting detection for Raman lidar,” *Applied Optics*, vol. 48, no. 20, pp. 3903 – 3914, 2009.
- [106] Y. Zhang, F. Yi, W. Kong, and Y. Yi, “Slope characterization in combining analog and photon count data from atmospheric lidar measurements,” *Applied Optics*, vol. 53, no. 31, pp. 7312–7320, 2014.
- [107] D. Whiteman, B. Demoz, K. Rush, G. Schwemmer, B. Gentry, P. Di Girolamo, J. Comer, I. Veselovskii, K. Evans, S. Melfi, *et al.*, “Raman lidar measurements during the international H2O project. Part I: Instrumentation and analysis techniques,” *Journal of Atmospheric and Oceanic Technology*, vol. 23, no. 2, pp. 157–169, 2006.
- [108] D. Veberic, “Maximum-likelihood reconstruction of photon returns from simultaneous analog and photon-counting lidar measurements,” *Applied Optics*, vol. 51, no. 2, pp. 139–147, 2012.
- [109] G. Baumgarten, *Leuchtende Nachtwolken an der polaren Sommermesopause: Untersuchungen mit dem ALOMAR Rayleigh/Mie/Raman Lidar*. PhD thesis, Universitat Bonn Physikalisches Institut, Nussallee 12, 53115 Bonn, Germany, September 2001.
- [110] H. Mueller, “The foundation of optics,” in *Proceedings Of The Winter Meeting Of The Optical Society Of America*, no. 17, March 1948.
- [111] H. Mueller, “Theory of polarimetric investigations of light scattering. Parts I and II,” Tech. Rep. Contract W-18-035-CWS-1304. D.I.C 2-6467., Massachusetts Institute of Technology, 1946-47.
- [112] H. Mueller, “Lectures. course 8.262.” Cited by his student, N. Parke, in his dissertation., Fall term. 1946-47.

- [113] H. Mueller, “Development of a photoelastic shutter for modulating infrared light at audio frequencies,” Tech. Rep. Report No. 16.4-1. OEMsr-579; MIT Research Project DIC-6085., Massachusetts Institute of Technology, January 1943.
- [114] H. Mueller, “The polarization optics of the photoelectric shutter,” Tech. Rep. Report No. 16.4018. OEMsr-576; MIT Research Project DIC-6085., Massachusetts Institute of Technology, November 1943.
- [115] V. Bush, “Summary Technical Report of Division 16, NDRC, Volume 3: Non-Image Forming Infrared,” tech. rep., The National Defense Research Committee, 1946.
- [116] N. G. Parke III, *Matrix Optics*. PhD thesis, Massachusetts Institute of Technology, 1948.
- [117] M. I. Mishchenko and J. W. Hovenier, “Depolarization of light backscattered by randomly oriented nonspherical particles,” *Optics Letters*, vol. 20, no. 12, pp. 1356–1358, 1995.
- [118] W. A. Shurcliff and S. S. Ballard, *Polarized Light*. D. Van Nostrand Company, Inc, 1964.
- [119] E. Collett, *Field Guide to Polarization*, vol. FG05 of *SPIE Field Guides*. <http://ebooks.spiedigitallibrary.org/>: SPIE Press, 2005.
- [120] M. Snels, F. Cairo, F. Colao, and G. D. Donfrancesco, “Calibration method for depolarization lidar measurements,” *International Journal of Remote Sensing*, vol. 30, no. 21, pp. 5725 – 5736, 2009.
- [121] K. Baibakov, N. T. O’Neill, L. Ivanescu, T. J. Duck, C. Perro, A. Herber, K.-H. Schulz, and O. Schrems, “Synchronous polar winter starphotometry and lidar measurements at a High Arctic station,” *Atmospheric Measurement Techniques*, vol. 8, pp. 3789–3809, 2015.

Curriculum Vitae

Name:	Emily McCullough	
Post-Secondary Education and Degrees:	2009 - 2015	The University of Western Ontario London, Ontario, Canada PhD, Astronomy, Specialization in Planetary Science
	2007 - 2009	The University of Western Ontario London, Ontario, Canada MSc, Astronomy, Specialization in Planetary Science
	2003 - 2007	Saint Mary's University Halifax, Nova Scotia, Canada Honours BSc, Astrophysics
Honours and Awards:	2013 - 2014	The SOGS 125th Anniversary Scholarship
	2014	Top prize, doctoral students, oral presentation, NSERC CREATE Arctic Atmos. Sci. Research Symposium
	2013, 2015	NASA Group Achievement Awards (2 awards) for contributions to Mars Science Laboratory
	2010 - 2013	Ontario Graduate Scholarship (4 awards)
	2012	Malcolm Ramsay Memorial Award, Northern Scientific Training Program (NSTP)
	2012	William Henry Wehlau Prize in Astronomy, University of Western Ontario
	2011, 2012	Training Grant, Northern Scientific Training Program
Related Work Experience:	2011	Top prize, physical sciences oral presentation, Western Research Forum, University of Western Ontario
	2009	Student Paper Award, MST12 Intl. Radar Conference
	2007 - 2015	Research Assistant, The University of Western Ontario
	2007 - 2012	Teaching Assistant, The University of Western Ontario
	2006 - 2007	Teaching Assistant, Saint Mary's University
	2005 - 2007	Research Assistant, Saint Mary's University